Heterogeneous Nucleation of Solidification of Metals and Alloys

By De-Liang Zhang
B.Sc, M.Sc



Jesus College

A DISSERTATION SUBMITTED FOR
THE DEGREE OF DOCTOR OF PHILOSOPHY
IN THE UNIVERSITY OF OXFORD

Department of Materials

Trinity Term, 1990

Abstract

Deliang Zhang
Jesus College

D. Phil.
Trinity Term, 1990

Heterogeneous Nucleation of Solidification of Metals and Alloys

The main aim of this work is to investigate heterogeneous nucleation of solidification of metals and alloys by a combination of differential scanning calorimetry and transmission electron microscopy using a newly modified entrained particle technique. Attention is focused on investigating (a) heterogeneous nucleation of Cd, In and Pb particle solidification by Al in rapidly solidified Al-Cd, Al-In and Al-Pb binary alloys; (b) effects of various ternary additions such as Mg, Ge and Si on heterogenous nucleation of solidification of Cd and Pb solidification by Al; (c) heterogenous nucleation of solidification of Si by solid Al in hypoeutectic Al-Si alloys. In addition, the melting behaviour of Cd, In and Pb particles embedded in an Al matrix is investigated.

The rapidly solidified microstructures of melt spun Al-Cd, Al-In and Al-Pb alloys consist of faceted 5-200nm diameter Cd, In and Pb particles homogeneously distributed throughout an Al matrix. Cd particles exhibit an orientation relationship with the Al matrix which can be described as $\{111\}_{Al}//\{0001\}_{Cd}$ and $\langle 110\rangle_{Al}//\langle 11\bar{2}0\rangle_{Cd}$, and In and Pb particles exhibit a near cube-cube and cube-cube orientation relationship with the Al matrix respectively. Cd, In and Pb particles embedded in the Al matrix exhibit distorted truncated octahedral or truncated octahedral shapes surrounded by $\{111\}_{Al}$ and $\{100\}_{Al}$ facets. The solid Al-solid Cd, solid Al-solid In surface energy anisotropies are constant over the temperature range between room temperature and Cd and In melting points respectively. The solid Al-liquid Cd and solid Al-liquid In surface energy anisotropies decrease with increasing temperature above Cd and In melting points. Solidification of Cd, In, Pb particles embedded in an Al matrix is nucleated catalytically by the surrounding Al matrix on the $\{111\}_{Al}$ faceted surfaces with an undercooling of 56, 13 and 22K and a contact angle of 42°, 27° and 21° for Cd, In and Pb particles respectively.

Addition of Mg to Cd particles embedded in Al increases the lattice disregistry across the nucleating plane, but decreases the undercooling before the onset of Cd(Mg) particle solidification. Addition of Ge to Al decreases the lattice disregistry across the nucleating plane, but increases the undercooling before the onset of Pb particle solidification embedded in the Al(Ge) matrix. These results indicate that chemical interactions dominate over structural factors in determining the catalytic efficiency of nucleation solification in Al-Cd-Mg and Al-Pb-Ge alloys. Contact between Si precipitates and Pb particles embedded in an Al matrix decreases the undercooling before the onset of Pb particle solidification.

The equilibrium melting point of Cd particle in the melt spun Al-Cd alloy is depressed because of capillarity, and the depression of equilibrium melting point increases with decreasing particle size. In the melt spun Al-In and Al-Pb alloys, however, most of the In and Pb particles embedded within the Al matrix grains are superheated, and the superheating increases with decreasing particle size.

The heterogeneous nucleation temperature for Si solidification by Al depends sensitively on the purity of the Al. Na and Sr additions have different effects on the Si nucleation temperatures. With an Al purity of 99.995%, Na addition increases the Si nucleation temperature, while Sr addition does not affect or decreases the Si nucleation undercooling, depending on the amount of Sr addition. The solidified microstructure of liquid Al-Si eutectic droplets embedded in an Al matrix is affected by the Si nucleation undercooling. With low Si nucleation undercooling, each Al-Si eutectic liquid droplet solidifies to form one faceted Si particle, however, with high Si nucleation undercooling, each Al-Si eutectic liquid droplet solidifies to form a large number of non-faceted Si particles embedded in Al.

To my dear parents, wife
and motherland

PREFACE

This Dissertation describes work carried out in the Department of Materials, University of Oxford, from October 1987 to July 1990, under the supervision of Dr. B Cantor. It is submitted for the degree of Doctor of Philosophy at University of Oxford, and no part of it has been or is being submitted for a degree or any other qualification at any university. The dissertation is the result of my own work. The work described here is original, except where references are made to the work of others. Some of the work described in this dissertation has already been published or will be published soon (1-7), and some of the work will be submitted for publication (8,9). Some of the work described in this dissertation has also been read in three conferences (10-12).

I would like to thank all people who generously offer me help towards the production of this dissertation, unfortunately, it is not possible to name them all here, since the number of pages one can use in a dissertation is limited. In particular my thanks to the following.

I would like to thank my supervisor Dr. B Cantor for the invaluable discussions, encouragement and all the help he has given during the last three years. I am grateful to Professor Sir Peter Hirsch FRS for provision of laboratory facilities. I would also like to thank Professor Keqiang Gong in Northeast University of Technology in China for his encouragement during my study in Oxford. This work was supported by the British Council and the State Education Commission of China with Sino-British Friendship Scholarship Scheme.

I would like to thank Dr. W T Kim, Professor K Chattopadhyay for helpful discussions, Dr. M L Jenkins, Mr. G Dixon-Brown, Mr. R. Doole and Mr. C J Salter for technical assistant in electron microscopy and microprobe analysis.

It has been a great pleasure to work in the rapid solidification group with my fellow researchers. My special thanks are to Dr. W Gao, Dr. D H Kim, Dr. P Maher, I T H Chang, P Grant, K Mingard, K A O'Reilly and P Newbery for their help.

Finally, I am deeply grateful to my family for their encouragement, support and interest in my study.

Deliang Zhang

[Signature removed from online version of thesis]

July 1990

Publications

1. K. I. Moore, D. L. Zhang and B. Cantor: "Solidification of Pb particles embedded in Al", Acta Metall. Mater. 38 (1990), 1327
2. D. L. Zhang, K. Chattopadhyay and B. Cantor: "Heterogeneous nucleation of solidification of Cd particles embedded in an Al matrix", J. Mat. Sci. in the press
3. D. L. Zhang and B. Cantor: "Heterogeneous nucleation of solidification of In particles embedded in an Al matrix", Phil. Mag. in the press
4. D. L. Zhang and B. Cantor: "Effect of Si on the heterogenous nucleation of Pb solidification by Al", Scripta Metall. Mater. 24 (1990), 751
5. D. L. Zhang and B. Cantor: "Effect of Mg on the heterogeneous nucleation of Cd solidification by Al", Mat. Sci. Eng. in the press
6. D. L. Zhang and B. Cantor: "Effect of Ge on the heterogeneous nucleation of Pb solidification by Al", J. Cry. Growth in the press
7. D. L. Zhang, W. T. Kim and B. Cantor: "Melt spun Al bearing alloys", Proc. of Int. Conf. on Advanced Aluminium and Magnesium Alloys, Amsterdam, ASM International, in the press
8. D. L. Zhang and B. Cantor: "Melting behaviour of In and Pb particles embedded in an Al matrix", to be submitted
9. D. L. Zhang and B. Cantor: "Heterogeneous nucleation of the solidification of Si by solid Al in hypoeutectic Al-Si alloys", to be submitted

Conferences

10. U. K. Informal Conference on Rapid Solidification and Metastable Phases, 6-7 Sept. 1989, School of Materials, Sheffield University
11. TMS Annual Meeting, 18-22 Feb. 1990, Anaheim, California, USA
12. International Conference on Advanced Aluminium and Magnesium Alloys, 20 -22 June 1990, Amsterdam, Netherlands

CONTENTS

Chapter 1

Introduction

1.1 Background 1

1.2 Aim of the Present Work 3

Chapter 2

Literature Review

2.1 Nucleation ---------- 6

2.1.1 Introduction ---------- 6

2.1.2 Homogeneous nucleation theory ---------- 6

2.1.3 Heterogeneous nucleation theory ---------- 8

2.1.4 Experimental work ---------- 9

2.1.4(I) Introduction ---------- 9

2.1.4(II) Homogeneous nucleation ---------- 10

2.1.4(III) Heterogenous nucleation ---------- 12

2.2 Surface Energy ---------- 18

2.2.1 Introduction ---------- 18

2.2.2 Experimental methods for measuring σ_{SL} of pure metals and results ---------- 19

2.2.2(I) Homogeneous nucleation ---------- 19

2.2.2(II) Melting point depression of small particles ---------- 20

2.2.2(III) Dihedral angle ---------- 20

2.2.3 Anisotropy of σ_{SL} ---------- 21

2.2.3(I) σ-plot and Gibbs-Wulff theorem ---------- 21

2.2.3(II) Experimental work on anisotropy of σ_{SL} ---------- 22

2.3 Solidification of Monotectic Alloys ---------- 24

2.3.1 Introduction ---------- 24

2.3.2 Surface energy and critical wetting ---------- 25

2.3.3 Eutectic based model ---------- 27

2.3.4 Rapid solidification of monotectics ---------- 28

2.4 Solidification of Eutectic Alloys ---------- 28

2.4.1 Introduction ---------- 28
2.4.2 Classification of eutectic systems ---------- 29
2.4.3 Solidification of undercooled eutectic alloys ---------- 30
2.4.3 Modification of Al-Si Microstructure ---------- 31

Chapter 3

Experimental Techniques

3.1 Intorduction ---------- 33
3.2 Materials Preparation ---------- 33
3.2.1 Ingot preparation ---------- 33
3.2.2 Rapid solidification by melt spinning ---------- 34
3.3 Heat Treatment of the As-melt Spun Ribbons ---------- 34
3.4 X-ray Microprobe Analysis ---------- 35
3.5 Transmission Electron Microscopy ---------- 35
3.6 Differential Scanning Calorimetry ---------- 36

Chapter 4

Heterogeneous Nucleation of Solidification of Cd, In and Pb Particles Embedded in an Al Matrix

4.1 Introduction ---------- 38
4.2 Heterogeneous Nucleation of Solidification of Cd Particles Embedded in an Al Matrix ---------- 38
4.2.1 Alloy microstructure ---------- 38
4.2.2 Surface energy anisotropy ---------- 41
4.2.3 Cd particle solidification ---------- 42
4.3 Heterogeneous Nucleation of Solidification of In Particles Embedded in an Al Matrix ---------- 43
4.3.1 Alloy microstructure ---------- 43
4.3.2 Surface energy anisotropy ---------- 44
4.3.3 In particle solidification ---------- 45
4.4 Heterogeneous Nucleation of Solidification of Pb Particles Embedded in an Al matrix ---------- 46
4.4.1 Alloy microstructure ---------- 46

4.4.2 Pb particle solidification ---------- 46
4.5 Discussion ---------- 47
4.5.1 Alloy microstructures ---------- 47
4.5.2 Surface energy anisotropy ---------- 49
4.5.3 Particle solidification ---------- 50
4.5.4 Nucleation kinetics ---------- 51
4.5.5 Contact angle ---------- 52

Chapter 5

The Effect of Ternary Additions on the Heterogeneous Nucleation of Solidification of Cd and Pb Particles Embedded in an Al Matrix

5.1 Introduction ---------- 57
5.2 Preliminary Experimental Results ---------- 57
5.2.1 Al-Cd-X ternary alloys ---------- 57
5.2.2 Al-Pb-X ternary alloys ---------- 60
5.3 Effect of Mg on the Heterogeneous Nucleation of Cd Solidification by Al ---------- 62
5.3.1 Microstructure ---------- 62
5.3.2 Cd(Mg) particle solidification ---------- 65
5.3.3 Discussion ---------- 65
5.4 Effect of Ge on the Heterogeneous Nucleation of Pb Solidification by Al ---------- 67
5.4.1 Microstructures ---------- 67
5.4.2 Pb particle solidification ---------- 68
5.4.3 Discussion ---------- 69
5.4.3(I) Pb particle solidification ---------- 69
5.4.3(II) Nucleation kinetics ---------- 72
5.5 Effect of Si on the Heterogeneous Nucleation of Pb Solidification by Al ---------- 72
5.5.1 Microstructures ---------- 72
5.5.2 Pb particle solidification ---------- 74
5.5.3 Discussion ---------- 74

Chapter 6

Melting Behaviour of Cd, In and Pb Particles Embedded in an Al Matrix

6.1 Introduction ---------- 77

6.2 Melting Behaviour of Cd Particles Embedded in an Al Matrix ------ 77

6.2.1 Cd particle melting ---------- 77

6.2.2 Cd particle solidification ---------- 78

6.2.3 Discussion ---------- 78

6.3 Melting Behaviour of In and Pb Particles Embedded in an Al Matrix 80

6.3.1 In and Pb particle melting ---------- 80

6.3.2 In-situ heating experiments ---------- 82

6.3.3 In and Pb particle solidification ---------- 83

6.3.4 Discussion ---------- 83

Chapter 7

Heterogenous Nucleation of Solidification of Si by Solid Al in Hypoeutectic Al-Si Alloys

7.1 Introduction ---------- 87

7.2 Microstructures ---------- 87

7.3 Solidification of Al-Si Eutectic Liquid Droplets ---------- 89

7.4 Discussion ---------- 91

7.4.1 Solidification of binary Al-Si droplets ---------- 91

7.4.2 Solidification of ternary Al-Si alloys ---------- 93

7.4.3 Undercooling and microstructure ---------- 94

7.4.4 Modification of Al-Si by Na and Sr ---------- 95

Chapter 8

Conclusions

8.1 General Comments ---------- 96

8.2 Conclusions ---------- 97

8.3 Future Work ---------- 103

References

Chapter 1

Introduction

1.1 Background

Solidification is a very important process in metallurgical industry for the following reasons: (1) Most metals are produced from ores by processes of chemical and physical metallurgy, and the initial state of the metals is generally liquid. The liquid metals are either directly cast into specific shapes, or cast into ingots for subsequent mechanical shaping. (2) Large numbers of metallic parts used in various industries are produced by using casting processes, either because their shapes are too complicated to be produced by mechanical shaping, or because casting is the cheapest process. (3) Mechanical and physical properties of metallic products depend to a large extent upon the as-solidified microstructures. Subsequent treatments can only achieve limited improvement of the as-solidified microstructures and properties.

Solidification during casting occurs as a two stage process. The first stage is nucleation, when small solid particles, the nuclei, are formed and become energetically stable, and therefore will not decay. The second stage is growth of the solid, by addition of atoms to the nuclei. Desirable microstructures generally require control of the solidifying phases and the resulting grain shapes and sizes. The as-solidified microstructures are mainly determined by:

(1) The thermodynamics and kinetics of nucleation.

(2) The direction and rate of crystal growth.

Over the past 40 years, there has been much detailed investigation of the growth process, and understanding of the growth process is much more advanced than the understanding of nucleation. Since nucleation is such a small part of the overall solidification process, it is much more difficult to investigate experimentally.

Nucleation is thought to occur in two ways: (a) Heterogeneous nucleation, where nuclei are formed on some external surface which acts as a catalyst for the formation of the nuclei; (b) Homogeneous nucleation, where nuclei are formed within the liquid without any aid of an external catalyst. Heterogeneous nucleation is the most significant of these two nucleation mechanisms, since it is the mechanism by which most real solidification processes occur. Despite this, homogeneous nucleation has been investigated in more detail than heterogeneous nucleation.

The main difficulty associated with studying homogeneous nucleation is the exclusion of all extraneous impurities which could otherwise catalyse the nucleation. A method which was initially used to overcome this difficulty (Turnbull 1950) divides a mass of molten metal into a very large number of small droplets by using an organic foaming agent to coat the droplets. Any impurities are then contained in a very small number of the droplets, so that their effect is insignificant among the entire droplet population. Whether this method was successfully used in studying homogeneous nucleation is questionable, because of the unreproducible results obtained by different workers using the same method but different foaming agents. These experiments will be discussed further in chapter 2.

Heterogenous nucleation is even more difficult to investigate since it involves an extra phase, the catalyst, and it is therefore harder to control. It is necessary to keep a 'clean', i.e. impurity free, system to ensure that there is no interference caused by impurities, and that the catalyst under investigation is responsible for the nucleation. To determine the controlling factors of catalytic efficiency, it is also necessary to obtain morphological and crystallographic information of both the catalyst and nucleating materials.

A rather elegant technique for studying heterogeneous nucleation was devised by Wang and Smith (1950). This method involves the formation of a structure consisting of a large number of low melting point particles of one material

embedded in a matrix of a high melting point second material. The melting and solidification of the low melting point particles is then studied. This method is very similar to the liquid droplet method used in studying homogeneous nucleation. Small particles are produced to reduce in a similar way the effects of any impurities, so that the catalytic effect of the matrix which surrounds can be investigated under clean conditions.

The entrained particle technique of Wang and Smith was modified by Cantor and co-workers as follows (Moore et al, 1990, Kim and Cantor, 1990).

(i) Monotectic and near monotectic systems were chosen for study, with both metals practically insoluble in each other. This reduced complications in experimental interpretation caused by solubility effects.

(ii) Materials were prepared by rapid solidification by melt spinning. Rapid solidification produced a much smaller scale microstructure than conventional casting, ensuring that almost all the particles were impurity free, and making detailed observation less difficult.

(iii) The particles in the rapidly solidified materials were sufficiently small to enable direct observation of the melting and solidification of the small particles by using in-situ heating in the transmission elctron microscope.

(iv) Differential scanning calorimetry was used to investigate the nucleation of melting and solidification. This allowed detailed kinetic analysis of the nucleation process.

(v) The effect of doping on the nucleation process was investigated by adding small amounts of various ternary additions to the monotectic system.

1.2 Aim of the Present Work

The aim of the present work was to investigate the heterogeneous nucleation of solidification of metals and alloys, applying the modified entrained particle technique systematically to a variety of monotectic alloys, and extending its use to the heterogenous nucleation of solidification in eutectic alloys.

In order to perform a detailed study of heterogeneous nucleation, the research programme was divided into the following experimental stages:

(a) The size, shape, distribution and crystallography of the particles in as-solidified and heat treated binary monotectic alloys were characterised by using transmission electron microscopy.

(b) Nucleation experiments were performed to study melting and solidification of the particles by using a differential scanning calorimeter.

(c) The effect of heat treatment on the particles in the binary monotectic alloys was investigated by using in-situ heating in the transmission electron microscope. This enabled the measurement of the particle-matrix surface energy anisotropy as a function of temperature.

(d) The effects of doping with ternary elements on the microstructures and on the nucleation of particle solidification were investigated in a similar way, by a combination of transmission electron microscopy and differential scanning calorimetry.

(e) The microstructures of as-rapidly solidified and heat treated binary and ternary eutectic alloys were also investigated in a similar way by transmission electron microscopy, and the nucleation of particle solidification was again investigated by using differential scanning calorimetry.

The contents of the thesis are organised as follows:

Chapter 2 mainly reviews previous published work about aspects of the nucleation of solidification, surface energy, and solidification of monotectic and eutectic systems, and at the same time presents classical nucleation theory, outlines the technique used to measure surface energy anisotropy and describes the monotectic and eutectic systems.

Chapter 3 gives details of all the experimental techniques that were used in the present study.

Chapters 4, 5, 6 and 7 present the experimental data on binary monotectic alloys, ternary monotectic alloys, melting experiments, and binary and ternary eutectic alloys respectively. Each chapter includes discussion of the results that have been presented in relation to current theory and other relevant work that has been reported in the literature.

Chapter 8 presents a summary of the main conclusions, and proposals of future work in the field of heterogeneous nucleation of solidification.

Chapter 2

Literature Review

2.1 Nucleation

2.1.1 Introduction

Nucleation is the process by which the first small crystals form when a liquid solidifies. A great deal of work has been done to try to explain the nucleation mechanisms in molten metals, because the pattern of nucleation during solidification determines many important microstructural features such as phase composition, grain size, and structure and distribution of second phase particles, all of which influence the final material properties. However, the detailed nucleation mechanisms are still not clearly understood, and the control and prediction of nucleation are limited, because of serious fundamental and experimental difficulties (Christian, 1975, Cantor, 1990, Moore et al, 1990). These difficulties include the following. (1) The nuclei are too small to be viewed microscopically. (2) The formation of a nucleus involves rather too many atoms for simple atomistic modelling, and rather too few atoms for straight forward application of macroscopic thermodynamics. (3) Controlled and reproducible nucleation studies are difficult to achieve, because the nuclei are sensitive to the presence of trace impurities. (4) The way in which trace impurities affect the nucleation process is not known. Despite all of these difficulties, much valuable information has been generated from experimental work undertaken during the past 40 years and has led to an increase in the ability to control the morphology and distribution of phases formed under different nucleating conditions.

2.1.2 Homogeneous nucleation theory

When a liquid is progressively cooled, the atoms are in a state of constant motion, and some of the atoms form small clusters which have the structure of the solid phase. These clusters, called embryos, are potential nuclei. When

the embryos exceed a critical size, it is energetically favourable for them to grow. The theories developed by Volmer and Weber (1925) and Becker and Doring (1935) to describe the kinetics of homogenous nucleation of liquid droplets in a supersaturated vapour provide a basis for the theory of nucleation of solidification. The main assumptions made by Volmer and Weber and Becker and Doring have been incorporated into the theory of nucleation of solidification, though the validity of these assumptions are still a matter of debate. These assumptions are as follows. (1) The properties of microscopic embryos and nuclei are expressed in terms of macroscopic thermodynamic properties. (2) Embryos and nuclei are produced by thermally activated fluctuations, and grow or degrade by a series of bimolecular reactions. (3) The surface energy is assumed to be isotropic so that the nuclei are spherical to give a minimum surface area and minimum total surface energy. Based on these assumptions, the formation of a spherical solid particle of radius r at temperature T results in a free energy change ΔG given by

$$\Delta G=-(4/3)\pi r^3\Delta G_v+4\pi r^2\sigma_{SL} \qquad (2.1)$$

where σ_{SL} is the solid-liquid surface energy, $\Delta G_v=L_v(T_m-T)/T_m$ is the driving force for solidification per unit volume, T_m is the equilibrium melting temperature, T is the melt temperature, and L_v is the latent heat of fusion per unit volume. Differentiating equation (2.1) with respect to r and equating it to zero gives the critical radius r* and the work of nucleation ΔG^*

$$r^*=2\sigma_{SL}T_m/L_v(T_m-T) \qquad (2.2)$$

$$\Delta G^*=16\pi\sigma_{SL}{}^3T_m{}^2/3L_v{}^2(T_m-T)^2 \qquad (2.3)$$

Fig. 2.1 shows the free energy curve as a function of r from eq. (2.1), together with the critical radius r* and work of nucleation ΔG^*. Based upon the criterion that the sizes of the largest embryos should exceed the critical size for a liquid to nucleate and by applying Boltzman statistics, the nucleation rate I is given by

$$I=z\ \ n\exp(-\Delta G^*/kT) \qquad (2.4)$$

where z is the net rate of transfer of atoms across the interface between the liquid and the embryo, n is the total number of atoms per unit volume, and k is Boltzman's constant. Turnbull and Fisher (1949) inserted an expression for the rate of atom

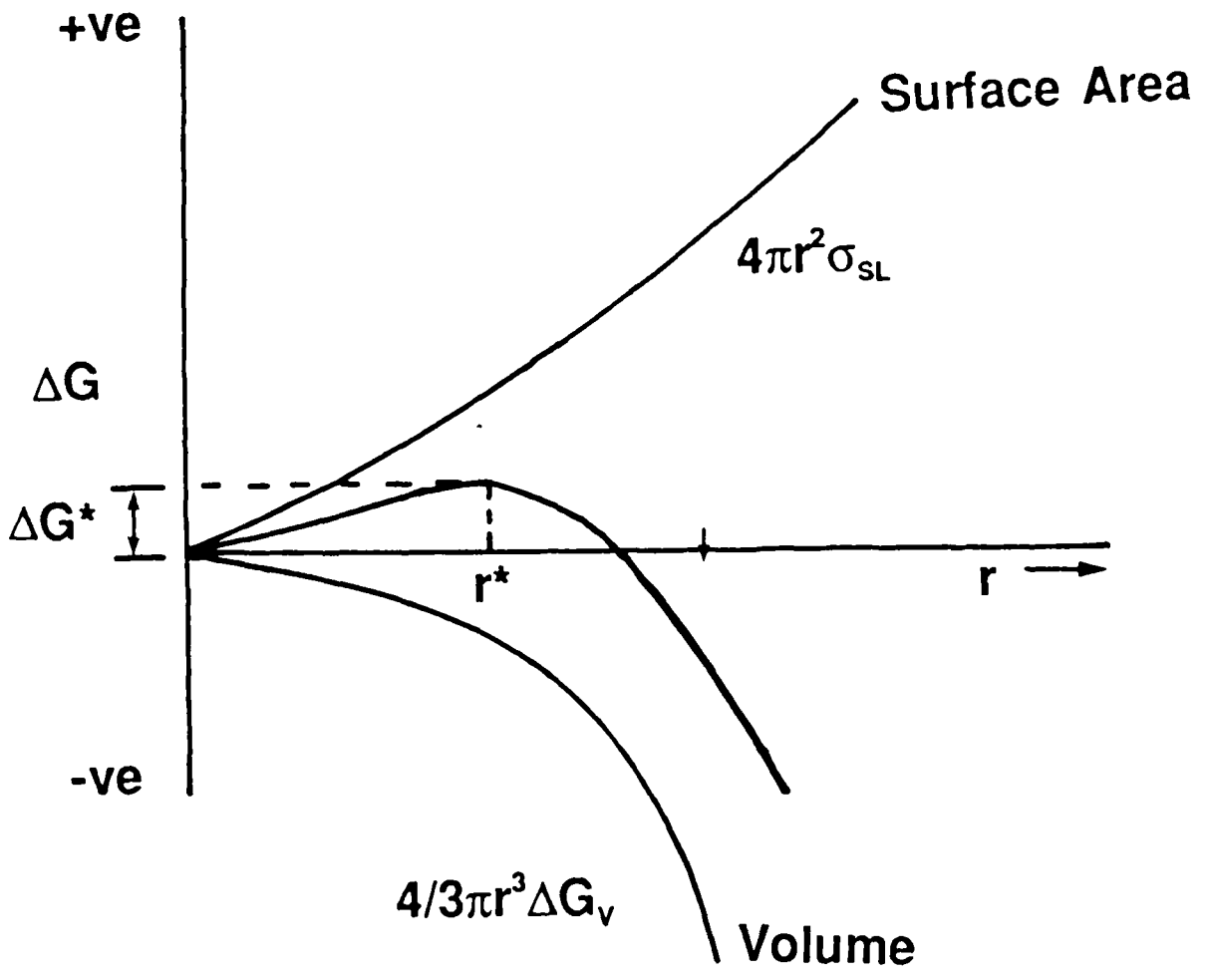


Fig. 2.1: The free energy change associated with homogeneous nucleation, showing the work of nucleation ΔG^* for the critical radius r^*.

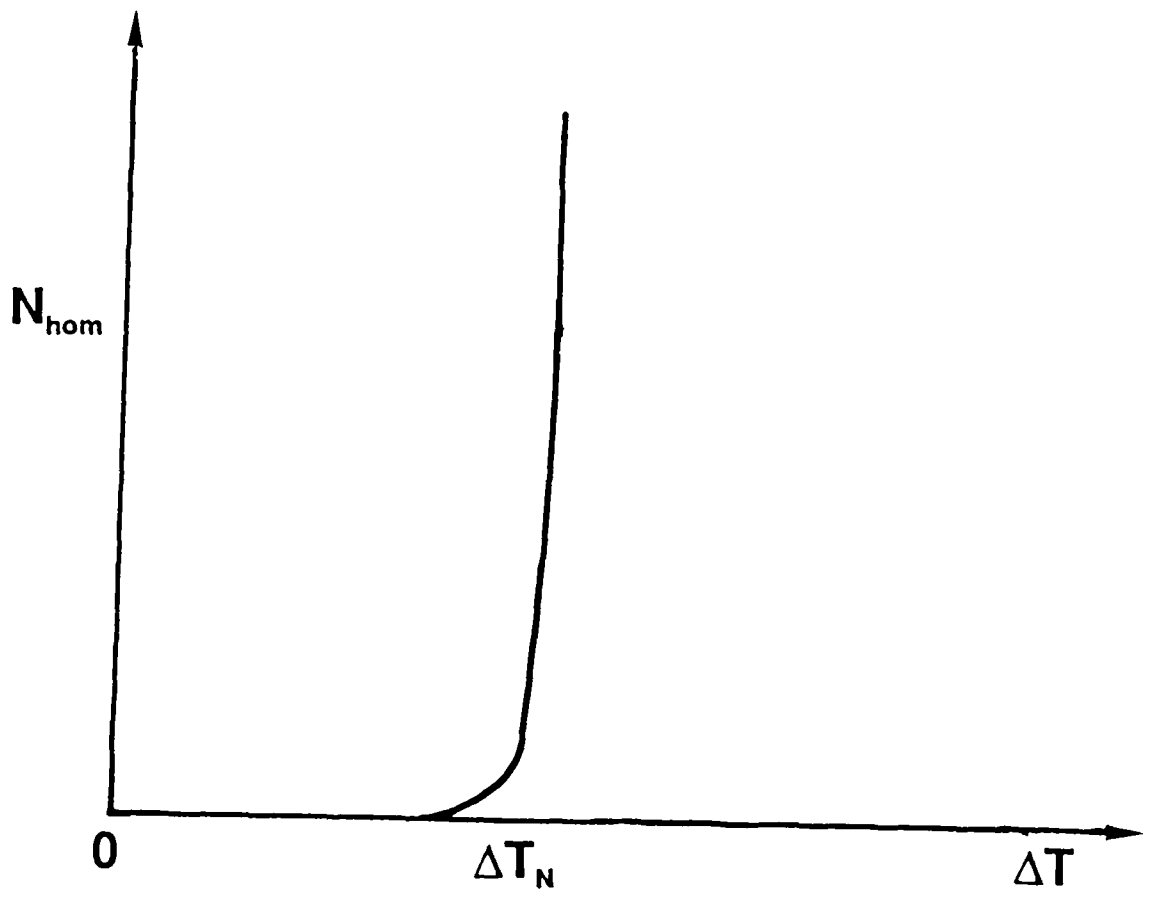


Fig. 2.2: Schematic plot of homogeneous nucleation rate as a function of undercooling showing ΔT_N, the critical undercooling for homogeneous nucleation.

transfer z, leading to

$$I=(kT/h)\ \ nexp\{(-\Delta G_A-\Delta G^*)/kT\} \qquad (2.5)$$

where h is Plank's constant and ΔG_A is the activation energy for growth, i.e. for an atom to add on to a critical nucleus. Fig. 2.2 shows a schematic plot of nucleation rate versus undercooling from eq. (2.5). The nucleation rate is virtually imperceptible until a critical value of undercooling $(T_m-T)_N$ is reached and the nucleation rate then increases sharply.

2.1.3 Heterogeneous nucleation theory

Heterogeneous nucleation theory is an extension of the homogeneous nucleation theory described above. Generally, metals solidify at much lower undercoolings than predicted by homogeneous nucleation theory, and this is thought to be due to the presence of impurities in the melt and to the mould wall which can act as catalysts of the nucleation process. Heterogeneous or catalytic nucleation is energetically more desirable since the surface energy barrier is reduced by the presence of the catalyst.

The spherical cap nucleus model of heterogeneous nucleation, as shown schematically in Fig. 2.3, can be used to describe these catalytic effects. The value of the contact angle at the solid-liquid-substrate triple junction point represents the catalytic efficiency of the substrate in stimulating the nucleation process. The contact angle Θ is determined by the following equation

$$\cos\Theta=(\sigma_{CL}-\sigma_{SC})/\sigma_{SL} \qquad (2.6)$$

where σ_{SC} is the surface energy between solid and catalyst, and σ_{SL} and σ_{CL} are the surface energies between liquid and solid, and catalyst and liquid respectively. For heterogeneous nucleation, the critical radius and the work of nucleation ΔG^*_{het}, are given by

$$r^*=2\sigma_{SL}T_m/L_v(T_m-T) \qquad (2.7)$$

$$\Delta G^*_{het}=16\pi\sigma_{SL}{}^3T_m{}^2f(\Theta)/3L_v{}^2(T_m-T)^2kT \qquad (2.8)$$

where $f(\Theta)=\{(2+\cos\Theta)(1-\cos\Theta)^2\}/4$. Comparing eq. (2.8) with eq. (2.3), it can be seen that the work of heterogeneous nucleation is the same as that for

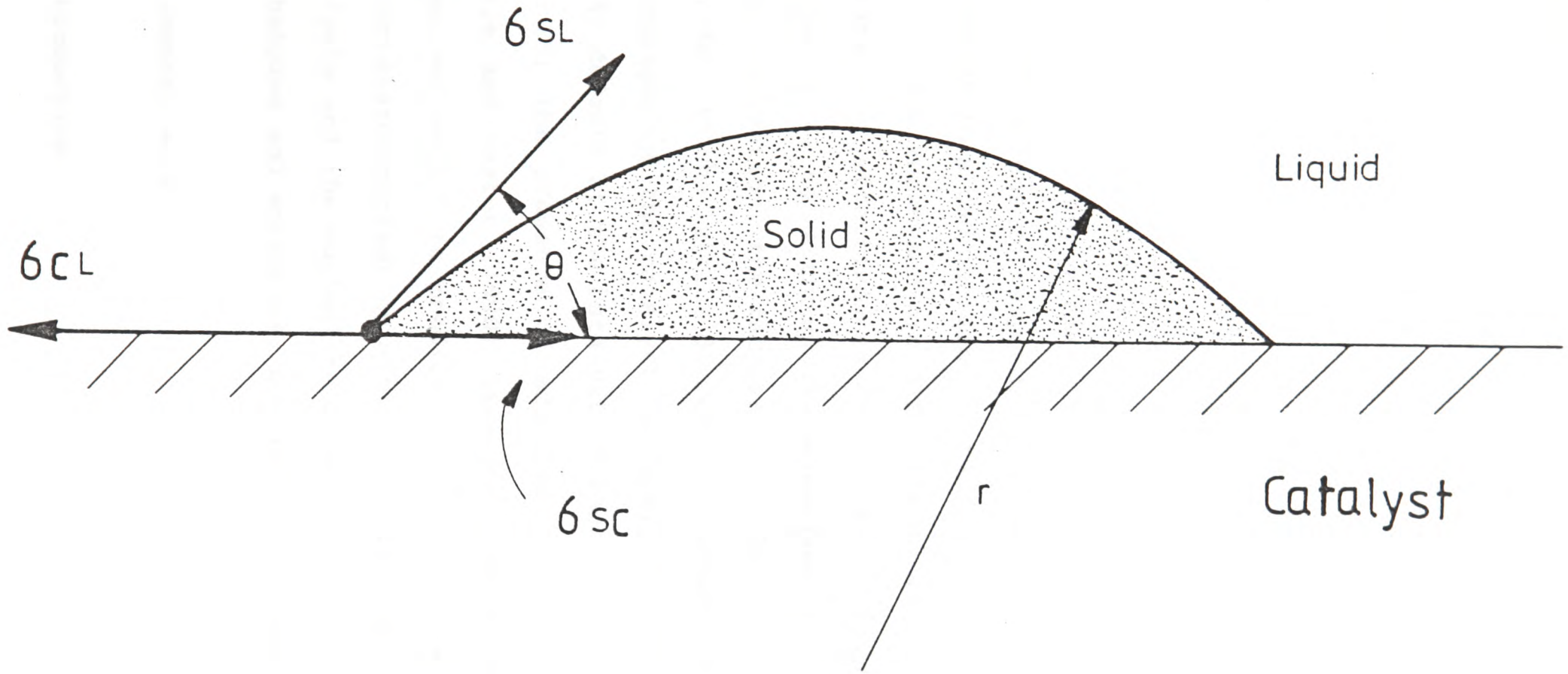


Fig. 2.3: Schematic diagram of a spherical cap on a flat catalytic nucleating surface.

homogeneous nucleation, except for the factor $f(\theta)$. The expression for heterogeneous nucleation frequency per unit area of catalyst has been given by Turnbull (1950(1)) as

$$I=n_s kT/h \cdot \exp\{(-\Delta G_A-\Delta G^*_{het})/kT\} \qquad (2.9)$$

where n_s is the number of atoms per unit area of surface between a liquid and catalyst. Here the assumption that all atoms on the surface between the liquid and catalyst can act as nucleation sites is doubtable. Again this expression is similar to that for homogeneous nucleation except for the term n_s and the insertion of $f(\theta)$ in the work of nucleation.

The action of the catalyst is to reduce the surface energy barrier to nucleation. θ can take any value from 0-180°. A small contact angle between the catalyst and nucleus corresponds to a good nucleant, and a large contact angle corresponds to a bad nucleant. Unfortunately, values of σ_{SC} and σ_{CL} are in general not well known and are difficult to measure directly, so that the potential catalytic effectiveness of a given nucleant can not be easily predicted from eq. (2.6). Although there has been a lot of work concerned with heterogeneous nucleation, the factors which determine θ are still not clear, and may include: (1) the lattice disregistry between the catalyst and nucleus; (2) the topography of the catalyst surface; (3) the chemical nature of the catalyst; (4) defects at the catalyst surface such as dislocations and grain boundaries; (5) the presence of adsorbed films on the catalyst surface. Recently, Kim and Cantor (1990) have proposed a new adsorption model of heterogeneous nucleation to predict the catalytic efficiency of nucleants. This model correlates nucleation efficiency with the thermodynamic properties of the catalysts and the nucleating materials, such as their melting point, melting enthalpies and entropies, and interaction energies.

2.1.4 Experimental work

2.1.4(I) Introduction

Moore (1986) reviewed the experimental work that has been done up to 1985 and her work has been used as the basis of the following. The work that has been

carried out can be divided into (1) the work concerning with homogeneous nucleation and (2) the work concerning with heterogeneous nucleation i.e. with the catalytic efficiency of nucleants. However, this division is not exact, since much work which originally was meant to be done on homogeneous nucleation may well have involved heterogeneous nucleation (Cantor and Doherty 1979).

The main difficulty associated with the experimental study of both homogeneous and heterogeneous nucleation is to exclude extraneous impurities from the system under investigation. Perepezko (1984) summarised various techniques that have been used for nucleation experiments, as shown in Fig. 2.4. (1) Droplet foam technique: a mass of liquid is emulsified into a large number of small droplets by an organic foaming agent, as shown in Fig. 2.4(a). (2) Droplet substrate technique: small individual droplets of liquid metal are studied on an inert glass substrate, as shown in Fig. 2.4(b). (3) Entrained droplet technique: a bulk alloy sample is equilibrated in the solid-liquid two phase field, so that small liquid droplets are in contact with the primary solid solution phase, which can act as a heterogeneous nucleant, as shown in Fig. 2.4(c). (4) Bulk liquid encasement technique: a bulk liquid sample is encased in an organic glass to remove active nucleation sites from the melt, as shown in Fig. 2.4(d). (5) Bulk melt levitation technique: a bulk liquid sample is levitated by induction forces to prevent contact between the melt and mould wall, as shown in fig. 2.4(e). Most of these techniques involve the use of calorimetry, dilatometry or microscopy to monitor the onset of solidification so as to determine the thermal driving force needed in the liquid to overcome any kinetic barrier to nucleation.

2.1.4(II) Homogeneous nucleation

The difficulty of excluding impurities was first overcome by Vonnegut (1948) who divided a bulk liquid into many small droplets (1-10μm in diameter) dispersed in an inert fluid so that the impurities present were isolated in a very small number of droplets. The remaining droplets should then be free

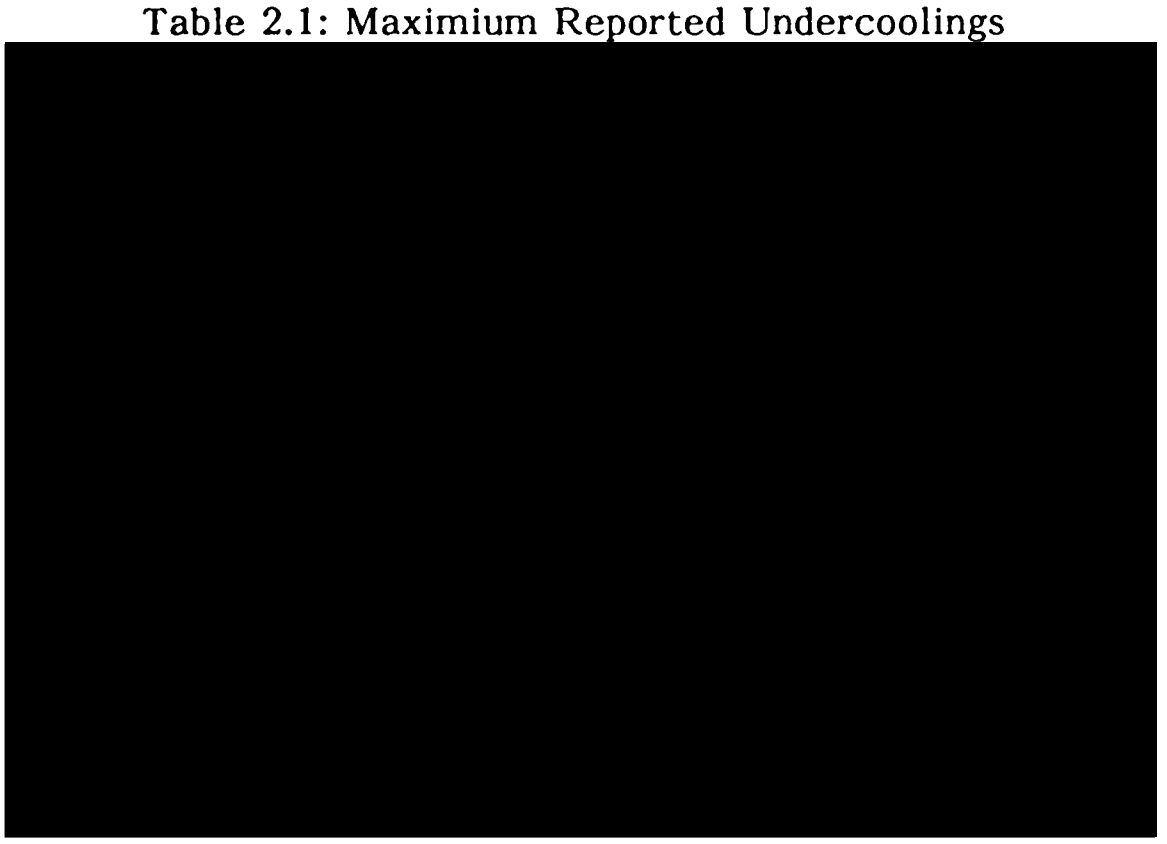


Fig. 2.4: Liquid undercooling methods that have been used for nucleation experiments (After Perepezko, 1984).

from impurities and homogeneous nucleation was thought to be possible. This droplet technique was later used by Turnbull and Cech (1950), Turnbull (1952) and Pound and LaMer (1952) to observe the undercoolings in a variety of different liquid metals. They found that the maximum undercooling was about $0.18T_m$. This figure was found to be largely unaffected by changes in droplet size or variations in cooling rate. The generalisation of maximum undercooling as a constant fraction of the melting point and the large measured undercoolings were generally accepted as being the results of homogenous nucleation. Turnbull (1950(2)) analysed the results of droplet experiments and found that for 12 out of 17 substances which were examined, the maximum undercooling was $0.185T_m$+/-0.02. For the whole range of substances, this ratio ranged from 0.133 for lead to 0.250 for gallium. The undercooling results were used to calculate interfacial energies, σ_{SL}, between the solid nucleus and liquid from eq. (2.5).

The resulting values of solid-liquid surface energy calculated from Turnbull's undercooling results were used extensively until 1970, when Stowell (1970) observed the undercooling for the nucleation of lead droplets in an electron microscope under vacuum and found a much greater undercooling than that seen by Turnbull. Stowell pointed out that the undercooling he observed was the lower limit of possible undercooling for homogeneous nucleation of lead and that Turnbull had not observed true homogeneous nucleation. Since 1978, Perepezko and co-workers have repeated Turnbull's experiments and studied a larger range of metals by using newly developed organic foaming agents (Peropezko and Rasmussen, 1978, Perepezko et al, 1979, 1982, 1985, 1986, Peropezko and Paik, 1982, 1984). A combination of in situ differential thermal analysis, x-ray diffraction on undercoooled droplets and post-solidification analysis of microstructure enabled much more detailed experimentation, and undercoolings of 0.3-0.4Tm were observed. Table 2.1 compares Perepezko's measurments for 10 molten metals with those obtained previously by Turnbull and co-workers and Pound and LaMer. The unreproducibility of these droplet results indicates the difficulty of achieving "true" homogeneous nucleation. In 1981, Turnbull (1981) reviewed

Table 2.1: Maximium Reported Undercoolings



After Perepezko, 1984

*(a) Turnbull and Cech, 1950
(b) Miyazawa and Pound, 1974
(c) Turnbull, 1952
(d) Pound and LaMer, 1952

his results in light of the most recent work, including a critical review of the pre-exponetial factors in eq. (2.5).

Most of the work concerning with homogeneous nucleation concentrates on the measurement of maximum undercooling and only a few authors have studied nucleation kinetics. Turnbull (1952) and Turnbull and Cormin (1960) used dilatometry to measure the nucleation rate in mercury and some organic liquid droplets in both isothermal and continuous cooling experiments. They claimed that the droplets solidified at rates which could be described within experimental uncertainty by the theory of either homogeneous or heterogeneous nucleation, depending upon the coating agents. However, Miyazawa and Pound (1974) pointed out that the 10^7 fold discrepency between the nucleation rates measured in Turnbull's experiments and those predicted by theory could not be due to experimental error. Miyazawa and Pound measured the nucleation rate in gallium by dilatometry and found that classical homogeneous nucleation theory could explain the available data more satisfactorily provided that one assumed a negative surface entropy, which could be theoretically justified. In a later study of homogeneous nucleation, Rasmussen and Loper (1975) suggested that a detailed kinetic study of nucleation should be able to determine whether the nucleation is homogenous or heterogenous.

2.1.4(III) Heterogenous nucleation

The work on heterogenous nucleation has mainly been concerned with the catalytical efficiency of various nucleants and the microstructural modifications that can be achieved. The earliest work that was undertaken to investigate heterogeneous nucleation is believed to be the work of Eborall (1949) and Cibula (1949) in 1949. They both investigated the effect of the addition of small concentrations of various elements and carbides to liquid metals and alloys. The main conclusion from their work was that good nucleants should have similar lattice structures and dimensions to those of the material to be nucleated. This conclusion was later justified theoretically by Turnbull and Vonnegut (1952). Further work by Reynolds and Tottle (1951) observing the

nucleating efficiency of metal powders when applied to the mould surface, gave evidence which supported this crystallographic misfit theory. They concluded that the lattice disregistry between solid nucleus and catalytic substrate should be less than 5-10%. It should be noted that these experiments, though simple to do, are very difficult to analyse, because of the presence of trace impurities and oxidation of the melt.

The lattice disregistry theory was further tested by other researchers (Sundquist and Mondolfo, 1961(1), Sang and Miller, 1970, Glicksman and Childs, 1962, Sundquist, 1963(1), (2)), and in all cases, the work suggested that lattice disregistry was not the dominant factor in determining the catalytic efficiency of nucleants. However, the techniques used by these researchers were incapable of eliminating the interference of oxidation or the formation of intermetallic compounds.

Eborall (1949) and Cibula (1949) also noted that good heterogeneous nucleation was often found to correspond to a peritectic reaction, and proposed that the peritectic reaction produces primary solid which can act as a nucleating site. Further investigation carried out by Crossley and Mondolfo (1951) on peritectic and eutectic Al alloys supported this argument. This model has, however been criticised because the cause of nucleation of the primary solid was not explained. Southin (1970) suggested that this could be due to the nucleant additions not being completely taken into solution when the alloy was melted. Experiments on grain refinement as a function of superheating of Al-Ti alloys have shown that increasing superheat decreased the degree of grain refinement (Davies et al, 1970). This result supports Southin's proposal.

Several variations of the droplet techniques used in homogeneous nucleation studies have been used by many authors to study heterogeneous nucleation. Hollomon and Turnbull (1951) and Sundquist and Mondolfo (1961 (1), (2)) observed the solidification of small alloy droplets on an inert subtrate using optical microscopy. Hollomon and Turnbull studied the nucleation of the

primary phase of Sn-Pb alloys as a function of composition. They claimed that the primary phase had a mild catalytic effect on the nucleation of the secondary phase. Sundquist and Mondolfo studied the catalytic effect of primary phase on the nucleation of secondary phase in over 60 binary alloys. They claimed to have found what they termed a "non-reciprocal" relationship, i.e. those metals that are difficult to nucleate are good nucleating agents, but those that nucleate easily are poor nucleating agents. This finding was supported by Powell and Colligan (1969 (1),(2)) who used a new technique based on the thermal analysis of bulk samples as a function of changing composition.

Sundquist and Mondolfo explained the non-reciprocal relationship in terms of surface energies, so that metals that are good nucleants have complex structures, high entropies of fusion and therefore high solid-liquid surface energies. The spherical cap model of heterogeneous nucleation based on relative surface energies requires that good nucleants have high solid-liquid interfacial energies, as shown in eqs. (2.6)-(2.9). Similarly metals that are poor nucleating agents should have simple structure, low surface entropies and low interfacial energies with metallic liquids. They found that measured values of undercooling seemed to be independent of orientation.

Chadwick (1965(1)) suggested that non-reciprocal nucleation behaviour could be explained in terms of a surface energy balance using the spherical cap nucleus model, as shown in Fig. 2.3. For a substrate catalyst to be an effective nucleant, it requires that

$$\sigma_{SC} < \sigma_{CL} - \sigma_{SL} \qquad (2.10)$$

For the solid to be an effective nucleant for the catalyst material it is required that

$$\sigma_{SC} < \sigma_{SL} - \sigma_{CL} \qquad (2.11)$$

Since both inequalities can not be satisfied simultaneouesly, non-reciprocal effects are to be expected. Non-reciprocal nucleation was further investigated by Crossley et al (1968) using the droplet technique. They stated that the requirements of a good nucleant were that it had a higher solid-liquid surface energy than that of the nucleus, and that there was

epitaxy between the nucleus and nucleant. Mondolfo (1989) recently reviewed the experimental evidence supporting non-reciprocal nucleation theory, and concluded that the balance of surface energies is a controlling factor.

Anderson and Perepezko (1983) used the droplet emulsion technique together with differential thermal analysis and microscopy to study the catalytic effects of primary phases such as Sn, Cd, Sb on the nucleation of the secondary Pb phase in Sn-Pb, Cd-Pb and Sb-Pb systems respectively. They found that the catalytic potency of Sn, Cd and Sb primary phases on Pb nucleation was proportional to L_v/δ, where the latent heat of fusion of the nucleant, L_v, represents chemical factors, and δ, the lattice disregistry between the nucleus and the nucleant, represents structural factors. They concluded that this combination of structural and chemical parameters may provide an improved method of predicting the relative activities of solidification catalysts.

The experimental technique used by researchers such as Sundquist and Mondolfo (1961(1), (2)) was criticised by Jackson (1965) who pointed out that the solids of both phases would be multiply re-entrant and full of cracks and crevices, so that it was unlikely that all of the secondary solid phase would melt.

Another variation of the droplet technique is to observe the nucleation of droplets on a substrate which acts as the nucleant. This technique was used by Bradshaw et al (1958-1959) to study the effect of various non-metallic substrates on the nucleation of Au droplets. They found that carbides and nitrides were the most effective known nucleants but none of them were as effective as unknown impurites. A more refined version of this technique was used by Wagner (1962). He studied the nucleation of liquid metal on a Ge substrate. Small particles of the alloy under investigation were deposited onto a Ge wafer, melted and then moved away from the surface into the bulk of the Ge by temperature-gradient zone-melting. This process removed any influence of surface films and pure metal droplets were embedded in the Ge. The undercoolings required to nucleate the particles by the Ge substrate were

measured, and in five of the seven alloys examined, Wagner found undercoolings close to or greater than those thought by Turnbull to represent homogeneous nucleation. Dislocation density and substrate orientation were not found to affect this process.

All of the techniques mentioned so far suffer from the fact that the substrate surface may be contaminated and most are open to the atmosphere. Prior to the above mentioned work on heterogeneous nucleation, Wang and Smith (1950) had described an experiment that was both simple and free from most of the defects of the other methods. Their technique consisted of studying chill cast binary alloys which contained a small amount of the second phase between fine dendritic arms of the matrix. The alloys were then annealed at temperatures between the solidus and liquidus of the alloy for sufficient time to ensure that the second phase became uniformly dispersed in the form of a large number of liquid droplets throughout the primary solid matrix. The principle of this technique is the same as that of the foam technique i.e. isolating impurities into an insignificant fraction of the droplets. The obvious advantages over the other methods are (1) that the droplets are formed internally, out of contact with the atmosphere, and (2) that the droplets form equilibrium shapes which are free of crevices. Experiments on the solidification of embedded particles of this type enabled the study of "clean" heterogeneous nucleation where the catalytic behaviour of the surrounding matrix material was under observation.

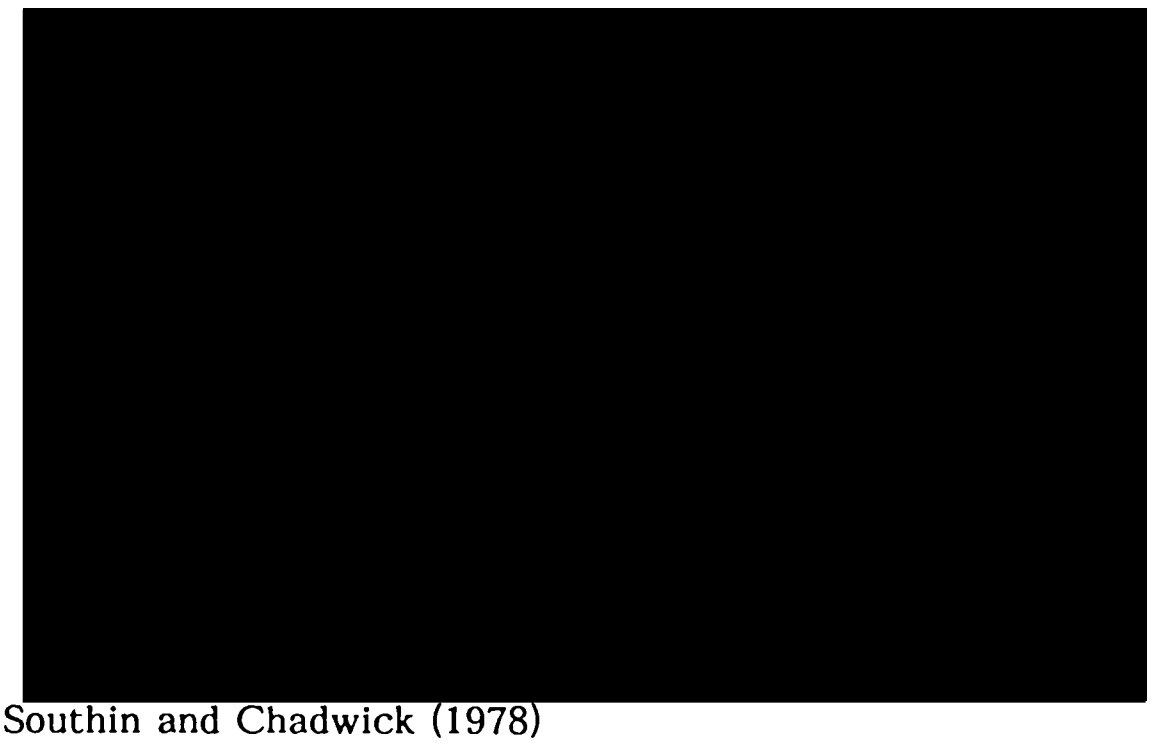
About twenty years after Wang and Smith (1950) described the entrained droplet technique, Chadwick and co-workers (Southin and Chadwick, 1978, Boswell et al, 1979, Boswell and Chadwick, 1980, Hunter and Chadwick, 1972) used the same technique together with differential thermal analysis to examine heterogeneous nucleation for a large range of pure metals and alloys. Southin and Chadwick (1978) found low undercoolings in binary alloys with similar crystal structures and bonding types and suggested that these factors were necessary but not sufficient for effective heterogeneous nucleation. The undercoolings they recorded for heterogenous nucleation were greater than those previously

reported for some systems, such as Zn-Sn, Bi-Sn, Zn-Bi and Al-Ge, as corresponding to homogeneous nucleation, as shown in Table 2.2. The analysis of their results did not support non-reciprocal nucleation or the electrostatic theory put forward by Tiller and Takahashi (1969). Southin and Chadwick also reported a correlation between the catalytic efficiency of a nucleant and its melting point. They concluded that the main factor controlling heterogeneous nucleation is the substrate-nucleus surface energy, although because of the difficulty in obtaining surface energy data, this could not be proved conclusively. Boswell and Chadwick (1980) measured the nucleation rate of entrained Sn droplets in contact with solid Bi, Zn and Al. Analysis of the data for the nucleation rate of Sn in contact with Bi gave a pre-exponential factor which was in good agreement with that predicted for pure Sn by eq. (2.9) using the spherical cap model. The nucleation rates of Sn droplets in contact with Zn and Al were more complicated and this was thought to be due to modification of the Sn structure formed on the surface of the Sn droplets.

Cantor and Doherty (1979) have analysed in detail the experimental results obtained by Southin and Chadwick (1978) by calculating the driving force for solidification in order to determine the contact angles. The equilibrium phase was generally assumed to form on solidification, but this should be treated with care since both metastable and stable products are thermodynamically possible at high undercoolings. By analysing the results of heterogeneous nucleation, Doherty (1978) suggested a correlation between catalytic potency and the melting point ratio between substrate and nucleus.

Cantor and co-workers (Moore et al, 1990, Kim and Cantor, 1990) have recently modified the entrained droplet technique by using monotectic and near monotectic binary alloys prepared by rapid solidification, and monitoring the solidification behaviour by differential scanning calorimetry and transmission electron microscopy. A monotectic alloy ensures that the embedded particles are highly insoluble in the matrix at low temperatures, so that the thermodynamics of solidification are not influenced significantly by

Table 2.2: Maximium Undercooling Coefficient Found by Turnbull (1950) and Southin and Chadwick (1978)



After Southin and Chadwick (1978)

solubility effects. Alloy preparation by rapid solidification ensures that the embedded particles are extremely small, so that their morphology and crystallography relative to the matrix can be examined in detail by transmission electron microscopy. Differential scanning calorimetry allows direct examination of the solidification kinetics, unlike previous dilatometry, differential thermal analysis and microscopy techniques. Moore et al (1990) investigated the melting and soldification behaviour of Pb particles embedded in an Al matrix in melt spun hypermonotectic Al-5wt%Pb, as well as the influence of several ternary element dopants in the binary alloy. They found that liquid Pb droplets exhibited a truncated octohedral shape just above the melting point of Pb, and this shape was maintained after the Pb particles solidified at an undercooling of 22K with an epitaxial cube-cube orientation relationship with the Al matrix. They concluded that the heterogeneous nucleation of solidification of Pb occurs on the {111} facets which have lower solid Al-solid Pb energies. As for the effect of ternary elements, they found that about 2wt%Si strongly enhanced the nucleation of Pb. Kim and Cantor (1990) performed a similar investigation on Sn particles embedded in an Al matrix by using a melt-spun Al-Sn alloy. They claimed that the kinetic analysis of the experimental results was in good agreement with the classical nucleation model.

2.2 Surface Energy

2.2.1 Introduction

According to the classical nucleation theory of solidification, the solid-liquid surface energy plays a very important role in the process of nucleation, so reliable values of these surface energies and a detailed understanding of surface structure is of great interest. A great deal of work has been published in this field over the last 40 years and a detailed review is not possible in the present work. However, there are several good reviews available, by Woodruff (1973), Jones (1974), Eustathopoulos (1983) and Gunduz (1984). The most relevent aspects of the study of interfacial energy to the

present work are the methods used for the measurement of interfacial energy, the values available and the interfacial energy anisotropy. The following brief review is, therefore, concerned with these aspects.

2.2.2 Experimental methods for measuring σ_{SL} of pure metals and results

2.2.2(I) Homogeneous nucleation

As mentioned in section 2.1.4.(II), most of the published values of solid-liquid interfacial energies for pure metals were obtained by means of homogeneous nucleation experiments. Combining eqs. (2.3) and (2.5), the following equation is obtained for the nucleation rate

$$I=K_v\exp(-16/3\pi\sigma_{SL}^{3}T_m^{2}/L_v^{2}(T_m-T)^{2}kT) \qquad (2.13)$$

where $K_v=(nkTs^*/h)\exp(-\Delta G_A/kT)$ and is insensitive to small changes of temperature. As shown in fig. 2.2, I remains equal to zero up to a critical value of undercooling, after which it increases very rapidly with a further small decrease in temperature. As a consequence, measurement of I as a function of (T_m-T) is generally possible only in a very narrow temperature range. The σ_{SL} value can be obtained from the slope of the straight line of a logI versus $1/T(T_m-T)^2$ plot, as shown in Fig. 2.5 for the nucleation of Ga (Miyazawa and Pound, 1974). When nucleation frequency is not available over a range of temperature, an approximate value of σ_{SL} can be deduced from simple maximum undercooling $(T_m-T)_{max}$ measurements performed during continuous cooling. Assuming that at $(T_m-T)_{max}$ the homogeneous nucleation rate of liquid droplets (i.e. the product IV, where V is the volume of a liquid droplet) is the same for all metals, I can be estimated, and by inserting I and (Tm-T) values into equation (2.13), an approximate value of σ_{SL} can then be obtained. The main criticism of the homogeneous nucleation experiments is the use of macroscopic quantities to describe systems containing a few hundred atoms. The unreproducibity of the undercooling values of homogeneous nucleation, as shown in table 2.1, indicates that the σ_{SL} values obtained with this method should be treated with care.

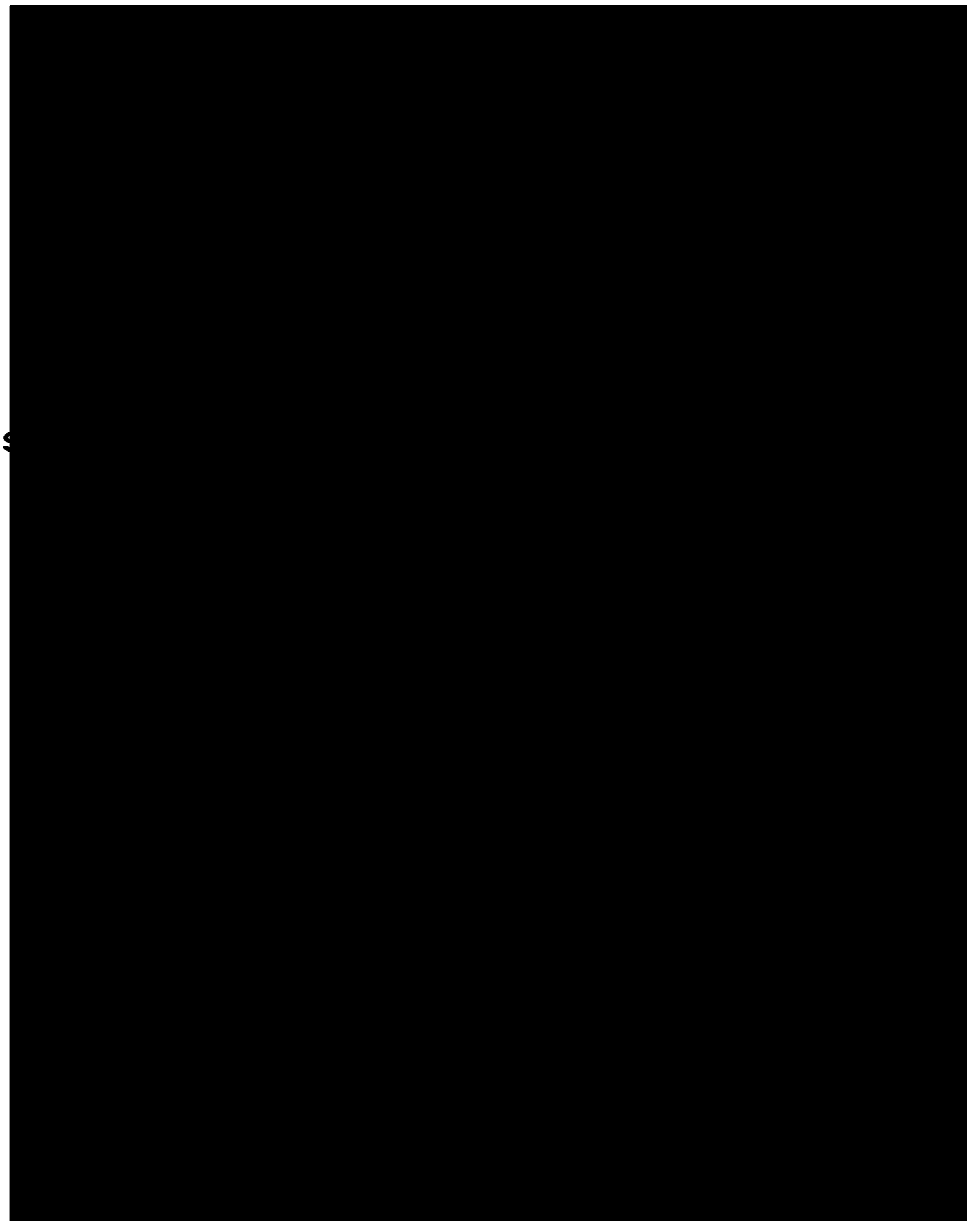


Fig. 2.5: Nucleation plot for Ga (After Miyazawa and Pound, 1974).

2.2.2(II) Melting point depression of small particles

This method is based on the well known Gibbs-Thomson equation which gives the size dependence of equilibrium melting point. The theory of melting of small particles was given by Reiss and Wilson (1948) and modified by Hanszen (1960) and Wronski (1967). Assuming the melting of a small crystal begins at the surface, Wronski (1967) considered the equilibrium of a solid particle of radius (r-t) surrounded by a thin liquid shell of inner radius (r-t) and thickness t. In the absence of any energy barrier to the formation of shell melting, which would start when the concentric liquid shell reaches a critical value, the melting point of small particles is described by the equation

$$(T_m-T)/T_m=2/L_v\{(\sigma_{SL}/(r-t) + \sigma_{LV}/r(1-\rho_s/\rho_l)\} \qquad (2.14)$$

where σ_{LV} is the liquid-vapour surface energy, ρ_s and ρ_l are the densities of the solid and liquid respectively. Experimentally, small crystals (r<50nm) of metal are formed on an amorphous non-reactive substrate by vapour deposition in a vacuum and the melting of the crystals is detected either by electron diffraction (Wronski, 1967, Coombes, 1972) or by the change of evaporation rate (Samples, 1971). The two unknown parameters σ_{SL} and t are then obtained by fitting experimental values of T as a function of r, into eq. (2.14) (Fig. 2.6). This liquid-skin model of melting requires perfect wetting of the solid by its own melt and is not universally accepted (Scripov et al, 1981).

2.2.2(III) Dihedral angle

This method of measuring σ_{SL} involves the measurement of the dihedral angle formed at a grain boundary when a liquid is equilibrated with a solid as shown schematically in Fig. 2.7. From the value of dihedral angle, the ratio between σ_{SL} and σ_{GB} can be obtained. σ_{GB} is the surface energy of a grain boundary. If the value of σ_{GB} is well established, the value of σ_{SL} can be calculated easily. This method has been used by several researchers (Eustathopoulos et al, 1974, Passerone et al, 1977, 1979, Passerone, 1979, Mondolfo et al, 1984-1985) and is considered as the most direct and reliable method (Mondolfo et al, 1984-1985). The main drawbacks are that (1) alloying elements introduce



Fig. 2.6: Melting point of Pb particles as a function of particle radius (After Coombes, 1972; Reproduced from Eustathopoulos, 1983).

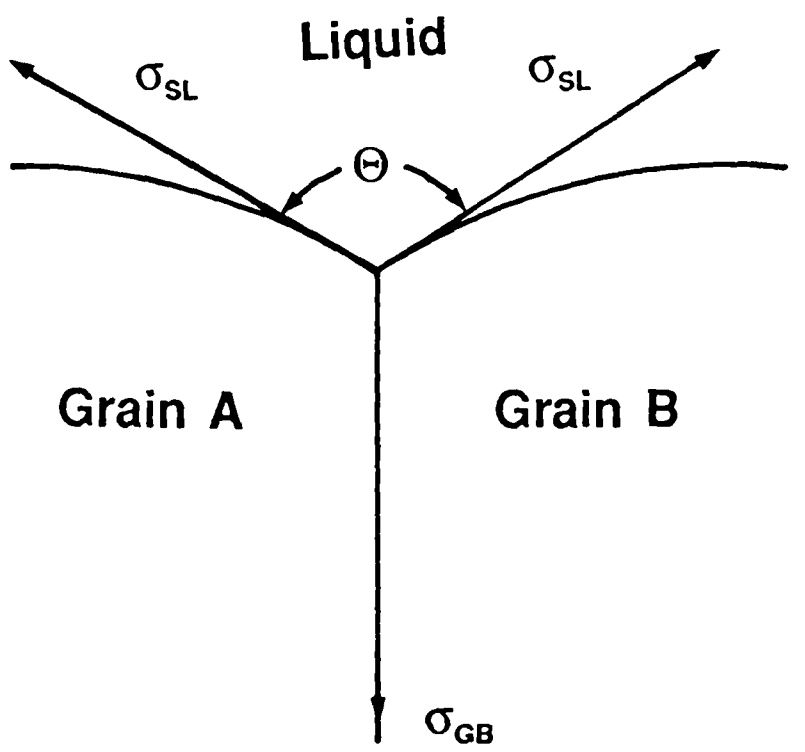


Fig. 2.7 Schematic diagram showing the equilibrium solid-liquid interface at grain boundary.

chemical contributions to the grain boundary energy, with the possiblity of segregation to the grain boundaries, and (2) the grain boundary energy is a strong function of crystallographic orientation which has never been well established. These effects must be allowed for in calculating or measuring the value of σ_{GB}.

Table 2.3 summarises the σ_{SL} values which have been obtained by the three methods mentioned above.

2.2.3 Anisotropy of σ_{SL}

2.2.3(I) σ-plot and Gibbs-Wulff theorem

For a solid-liquid surface, the surface energy is a function of the bonds which are modified in forming a surface from a region of perfect crystal. Different surfaces will have different packing densities and thus different surface energies, i.e. σ_{SL} is anisotropic for a crystalline solid. The study of anisotropy of σ_{SL} is generally based upon the σ-plot and the Gibbs-Wulff theorem, which were originally used for solid-vapour surface energy anisotropy. A polar plot of the angular variation of surface energy per unit area for a crystal is usually called the σ-plot. The conventional representation of the variation of σ with the orientation of the surface plane as a section through the polar σ-plot was suggested by Wulff (1901). The equilibrium shape for a particle will be the shape with minimum total surface free energy, thus the equilibrium shape requires that the value of $\int \sigma dA$ is a minimium, where A is the surface area. Wulff suggested the construction as shown in Fig. 2.8. From the origin O of the σ-plot draw a line to cut the σ-plot at a point B, then draw a plane, MBC, normal to OB, this plane is termed a Wulff plane. Repeat this construction for all possible orientations of the line OB. The Wulff theorem is that the equilibrium shape of the corresponding crystal is bounded by all parts of the set of Wulff planes that can be reached from the origin without crossing any other Wulff planes, i.e. the inner envelope of the set of Wulff planes. For an observed equilibrium

Table 2.3: Published Values of Solid-liquid Surface Energy of Pure Metals (Ref. in Brackets)

Metal	Solid-liquid Surface Enegies σ_{SL} (mNm^{-1}) Determined by the Following Methods			
	NF	ΔT	DMP	DA
Bi	62.5(a)	54(b) 84(c) 61(g) >45(h)	55-80(d)	74(e) 84(f)
Cd				87(f)
Pb		33(b) 46(c) 33(i) 55(j) 69(k)	40(d)	76(f)
Sb		103(b)		80-130(l) 124(f)
Sn		55(b) 69(c) 59(c) 62(n) >58.5(o)	62(m)	84(f)
Tl				67(f)
Zn				117(p) 90(q) 100(r) 87(s) 123(f)
Hg	37.2(f) 23.0(a)			
Ga(α)	67.7(u)			
Ga(β)	40.0(a)			
In	30.0(a)			
Al		>121(v)	131-153(w)	158+/-30(e)
Ge	251(a)			
Ag	143(a)			
Au		>132(x)	270+/-10(y)	
Cu	200(a)		237+/-26(p)	

(to be continued)

Table 2.3 (continued)

NF: Nucleation Frequency; ΔT: Maximium Undercooling;
DMP: Melting Point Depression; DA: Dihedral Angle

*(a) Scripov, 1977
(b) Turnbull, 1950
(c) Perepezko, 1979
(d) Coombes, 1972
(e) Eustathopoulos et al, 1976
(f) Mondolfo et al, 1984-85
(g) Scripov et al, 1973
(h) Bosio et al, 1961
(i) Takagi, 1954
(j) Cladkihk et al, 1974
(k) Skapski, 1956
(l) Crossley et al, 1968
(m) Wronski, 1967
(n) Berman and Curzon, 1974
(o) Pound and LaMer, 1952
(p) Eustathopoulos et al, 1974
(q) Passerone et al, 1974
(r) Passerone, 1979
(s) Passerone et al, 1979
(t) Turnbull, 1952
(u) Miyazawa and Pound, 1974
(v) Falkenhagen and Hofmann, 1952
(w) Quinson et al, 1979
(x) Turnbull and Cech, 1950
(y) Samples, 1971



Fig. 2.8: The Wulff construction (After Martin and Doherty, 1976).

shape in a crystal, measurement of the perpendicular distance between each set of planes, L, on the Wulff plot is proportional to σ for that surface. Comparison of measurements in different orientations gives the surface energy anisotropy.

According to Mullins (1963) the Gibbs-Wulff theorem can only be proved if it is first assumed that the equilibrium shape is convex. However, non-convex equilibrium shapes have not been reported so far. Sundquist (1964) calculated the 3-dimensional σ-plot for an fcc crystal, considering the different bond energy effects of nearest and second nearest neighbours. Cusps in the σ-plot were found at low index planes. Fig. 2.9 shows Sundquist's σ-plot in a (100)-(110)-(111) stereographic triangle, together with the corresponding equilibrium crystal shapes, where ρ is the ratio of the energy of a second-nearest neighbor bond to the energy of a first-nearest neighbour bond.

2.2.3(II) Experimental work on anisotropy of σ_{SL}

Since the high mobility of solid-liquid surfaces in pure metals makes them highly sensitive to small fluctuations of heat, reliable data for the anisotropy of σ_{SL} in pure metals are not easy to obtain. Glicksman and Vold (1969, 1971) constructed a partial σ_{SL} plot for Bi, but it is not clear if this plot refers to equilibrium or growth forms. Naidich et al (1983) found that at equilibrium or near equilibrium conditions, the contact angle formed on Ge by its own melt exhibited a strong orientation dependence, but the anisotropy of σ_{SL} in this case is masked by the anisotropy of solid-vapour surface energy.

Studies of solid-liquid surface energy anisotropy mainly refer to simple binary eutectic and monotectic systems. Miller and Chadwick (1968, 1969) determined the anisotropy of σ_{SL} in some binary alloys. The technique used by Miller and Chadwick involved determining the shape of small (10-30um diameter) liquid droplets of a metal B, entrained in a matrix of polycrystalline metal A. The material was equilibrated in the solid-liquid region of the phase diagram and then quenched. The cross sectional shape of the B particles was

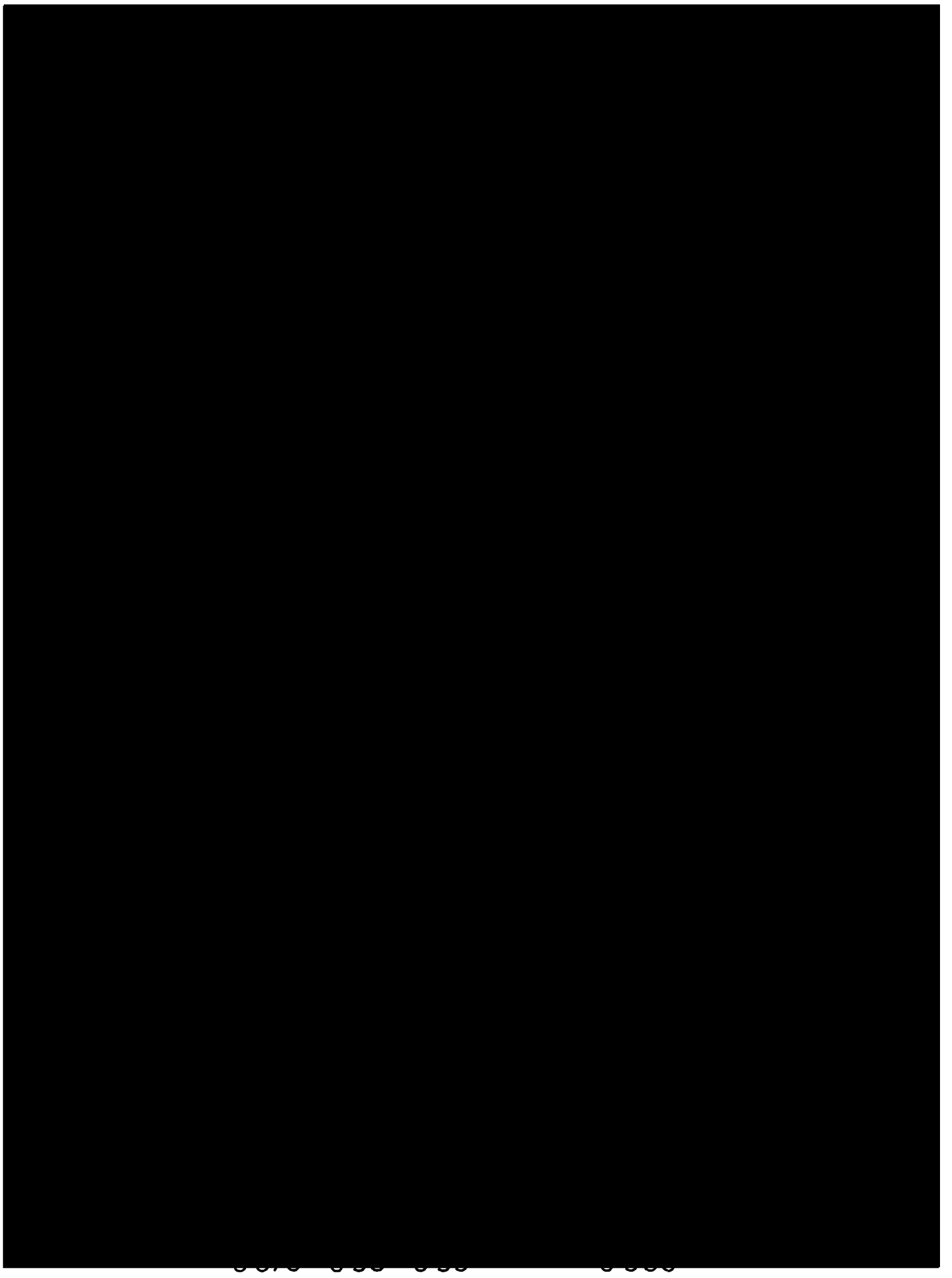


Fig. 2.9: σ-plots in a stereographic triangle (100, 110 and 111) with the corresponding equilibrium shapes for an fcc crystal with (a)ρ=0; and (b) ρ=0.1 (After Sundquist, 1964).

examined by optical microscopy, and the anisotropy of surface energy was determined by measurement of the distance of each surface from the centre as shown in Fig. 2.10. They found that the hcp metals Zn and Cd had a large anisotropy in equilibrium with various eutectic liquids. Mg formed spherical particles in equilibrium with liquid Ni or Zn, which indicated that σ_{SL} is isotropic. Detailed reviews of this work have been published elsewhere (Chadwick, 1969, Basterfield et al, 1970).

Passerone (1981) and Passerone and Eustathopoulos (1980, 1982) studied the change in equilibrium shape of droplets of In, Sn, Bi and Pb in solid Zn as a function of temperature and/or composition with a similar technique to that of Miller and Chadwick. The quenched droplets were liberated by selective etching of the matrix and then observed under a scanning electron microscope. A maximum anisotropy of σ_{SL} as high as 100% was found at low temperatures for Zn-In alloys. Extrapolation of the variation of anisotropy with temperature to the melting point of Zn gave a σ_{SL} anisotropy of 30% for pure Zn. The maximum σ_{SL} anisotropy of fcc metals in binary alloys is low and so the departures of the equilibrium shape from sphericity can not be easily detected. However, Camel et al (1980) have used scanning and transmission electron microscopy to measure the surface energy anisotropy of fcc and other metals by the same technique as used by Miller and Chadwick. They examined liquid Sn and Zn droplet shapes in Al and liquid Pb droplet shapes in Ag. The shapes were bounded with {111} facets separated by smoothly curved areas. Several other workers (McCormick, 1986) have done similar experiments on the equilibrium shapes of small particles of Pb in Al.

The most recent contribution to this field has been made by Moore et al (1987) who examined the shape change of small Pb particles (<60nm diameter) embedded in an Al matrix in a melt spun hypermonotectic Al-5wt%Pb as a function of temperature, by in-situ heating in a transmission electron microscope. Unlike other workers who quenched the alloy and observed the shape of the frozen particles, Moore et al observed the shape change directly in the in-situ experiments. The detailed crystallographic and morphological information

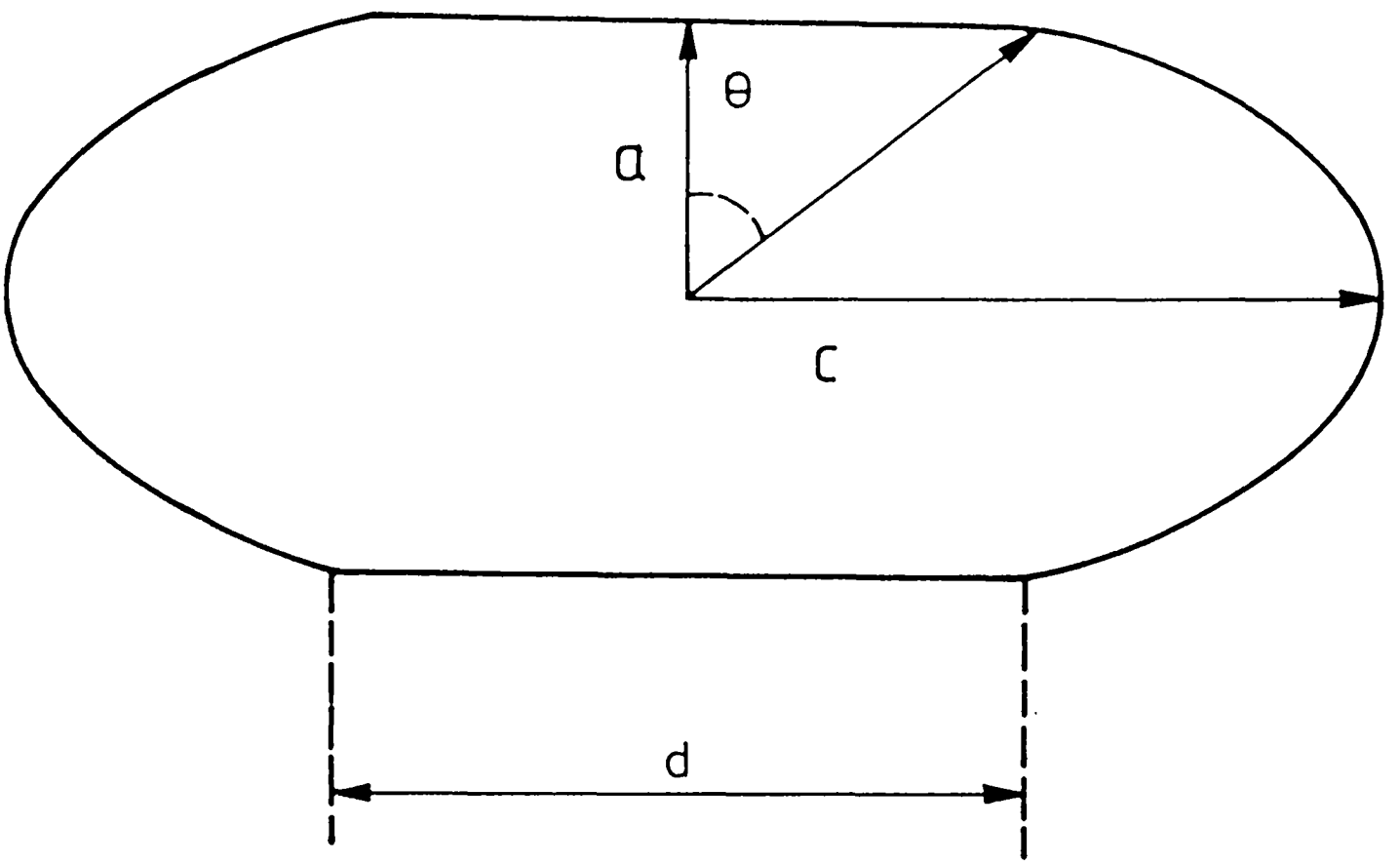


Fig. 2.10: Schematic diagram of the equilibrium particle shape, showing that the surface energy anisotropy of the particle can be determined from the ratio c/a.

available by transmission electron microscopy showed clearly the three-dimensional shape of the Pb particles, and therefore made the surface energy anisotropy measurements more accurate and more convincing. The solid Al-solid Pb surface energy anisotropy was found to be constant up to the Pb melting point, and the solid Al-liquid Pb surface energy anisotropy decreased gradually as the temperature increased above the melting point, from $\sigma_{100}/\sigma_{111}=1.14$ at 327°C to $\sigma_{100}/\sigma_{111}=1.0$ at about 550°C.

2.3 Solidification of Monotectic Alloys

2.3.1 Introduction

A monotectic system is a binary alloy in which the two components are immiscible for part of both the liquid and solid regions. Fig. 2.11 shows a schematic phase diagram for a monotectic system. Above T_c, the critical temperature, the two components are liquid and miscible at all compositions. Below T_c, two immiscible liquids L_1 and L_2 are formed over part of the composition range. At the monotectic temperature T_m, the monotectic reaction occurs:

$$L_1 \rightarrow S_1 + L_2 \qquad (2.15)$$

and liquid L_1 of composition C_m decomposes to give a solid phase S_1 of composition C_1 and a liquid phase L_2 of composition C_2. At the eutectic temperature T_E, the eutectic reaction occurs:

$$L_2 \rightarrow S_1 + S_2 \qquad (2.16)$$

and liquid L_2 of composition C_E, decomposes to give a solid phase S_1 of composition C_3 and a second solid phase S_2 of composition C_4.

The microstructures obtained during solidification of monotectic alloys are determined by a combination of process and material parameters. A large portion of the work that has been reported for monotectic systems has involved directional solidification experiments. In this type of experiment, growth is unidirectional, and the solidification velocity and temperature gradient at the solid-liquid interface can be independently controlled.

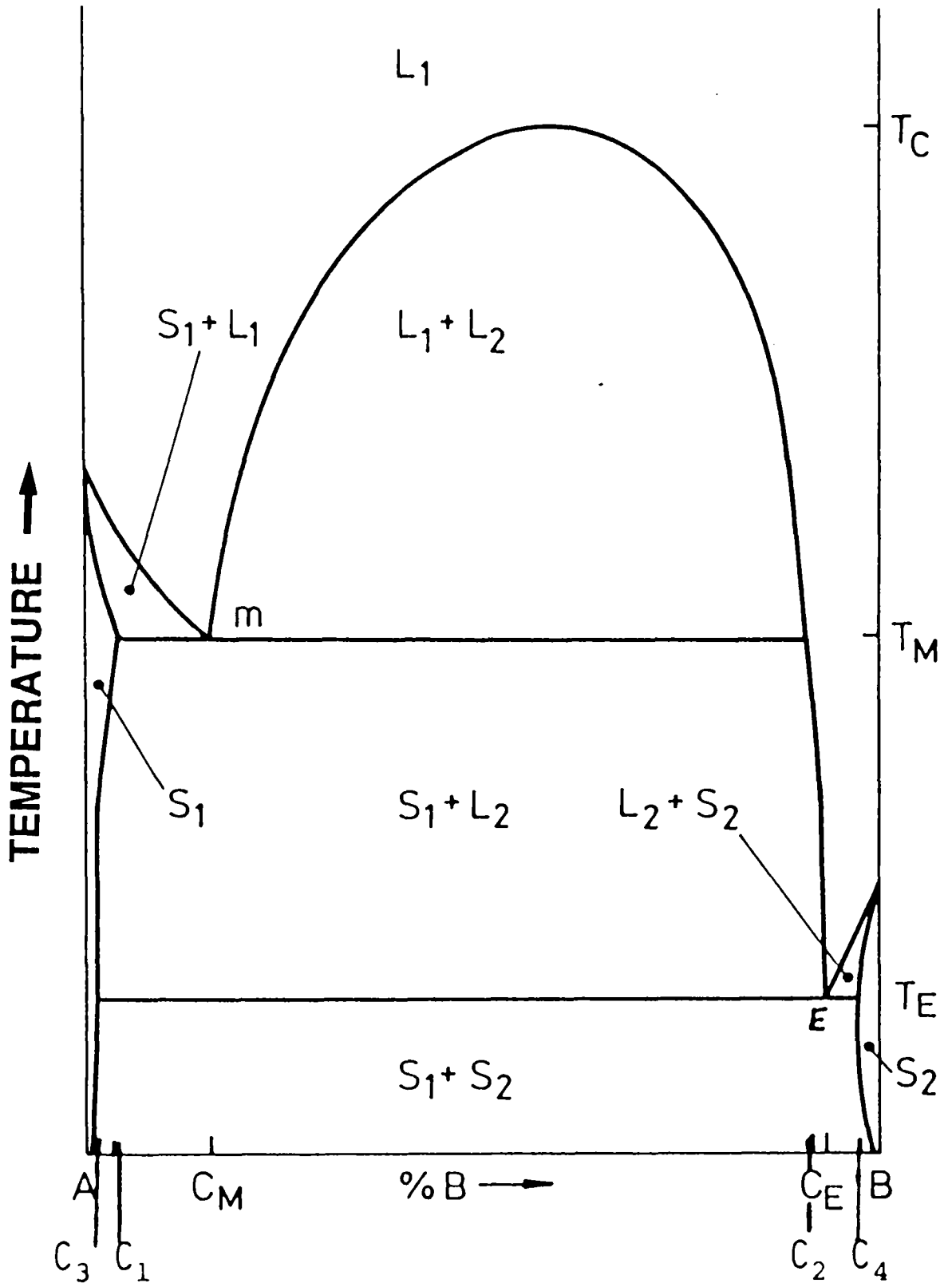


Fig. 2.11: Schem atic phase diagram for a monotectic system.

The types of microstructure observed are found to fall into two broad catagories, referred to as type A and type B. Type A microstructures are charateristic of systems with a high miscibilty gap, i.e. a large value of T_c-T_m. Figs. 2.12(a), (b) and (c) show schematic diagrams of the microstructures that are found at different growth rates. At low growth rates, the microstructure consists of uniform diameter, close packed rods of S_2 embedded in a matrix of S_1, as shown in Fig. 2.12(a). Over a small range of intermediate growth rates, the microstructure consists of regular sized and uniformly spaced S_2 particles embedded in a matrix of S_1, as shown in Fig. 2.12(b). At high growth rates, the microstructure consists of irregular S_2 particles embedded in the S_1 matrix, as shown in fig. 2.12(c).

Type B microstructures are characteristic of systems with a low miscibility gap, and are irregular at all growth rates. Figs. 2.13(a), (b) and (c) show schematic diagrams of the microstructures that are formed at different growth rates. Fig. 2.13(a) shows the random S_2 particle distribution formed at low growth rates, Fig 2.13(b) shows coarse interconnected "globules" of S_2 which are found at intermediate growth rates, and Fig. 2.13(c) shows the irregular fibrous microstructure formed at high growth rates. Toloui et al (1984) investigated the range of solidification conditions for obtaining the three different type A microstructures shown in Fig. 2.12, using the high miscibility gap monotectic system Al-In. The resulting conditions of V and G for obtaining the different microstructures are plotted schematically in Fig. 2.14, where V is the growth velocity and G is the temperature gradient at the solid-liquid interface.

2.3.2 Surface energy and critical wetting

Chadwick (1965(2)) first explained the microstructure of monotectic alloys grown from the melt in terms of surface energies and the resultant wetting conditions. He used similar arguments to those which he proposed to explain certain microstructural features of eutectic alloy solidification (Chadwick, 1962). At the monotectic point, there are two possible situations dependent

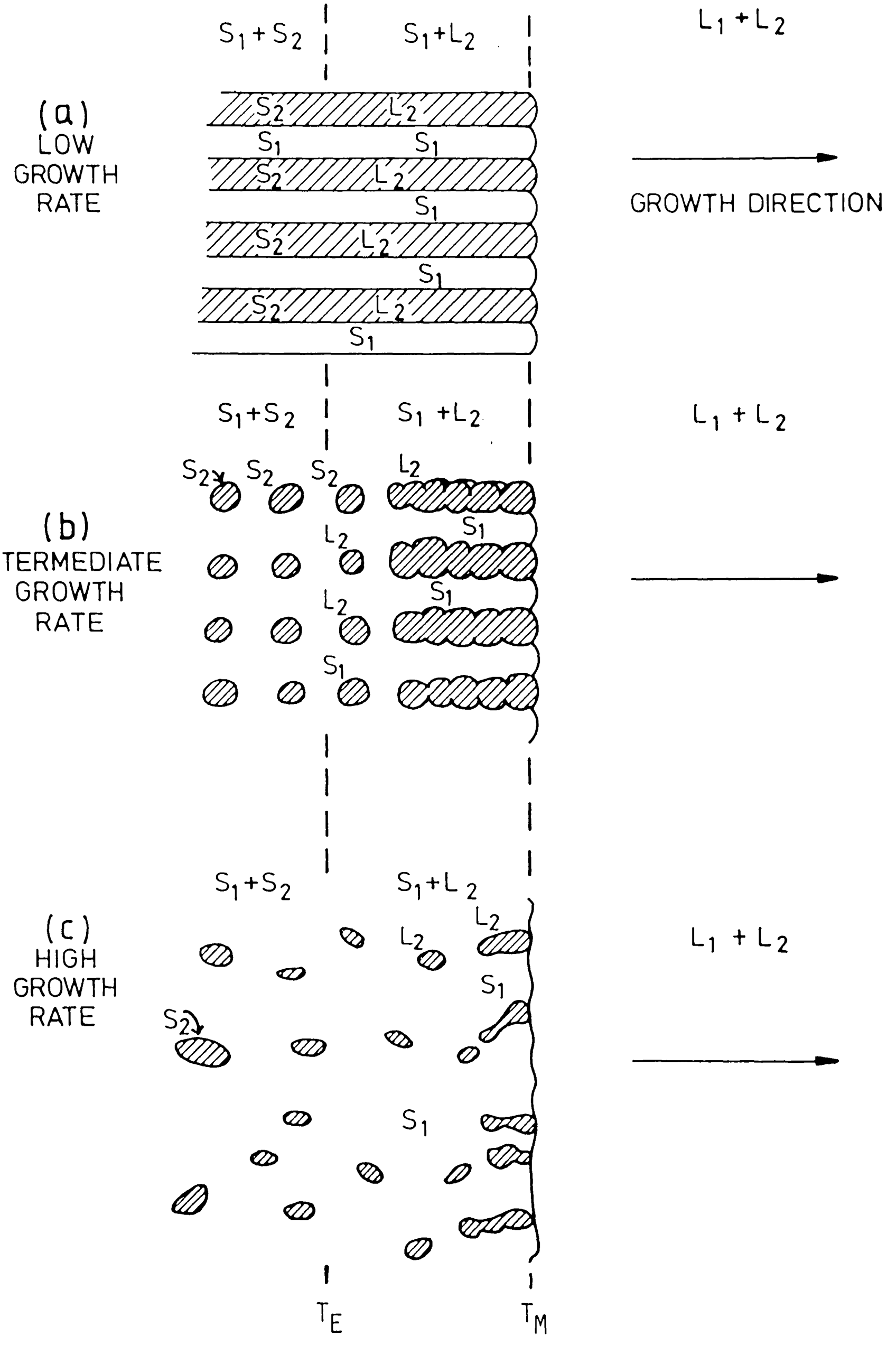


Fig. 2.12: Schematic diagrams of typical microstructure formed at different growth rate in a monotectic system with a high miscibility gap.

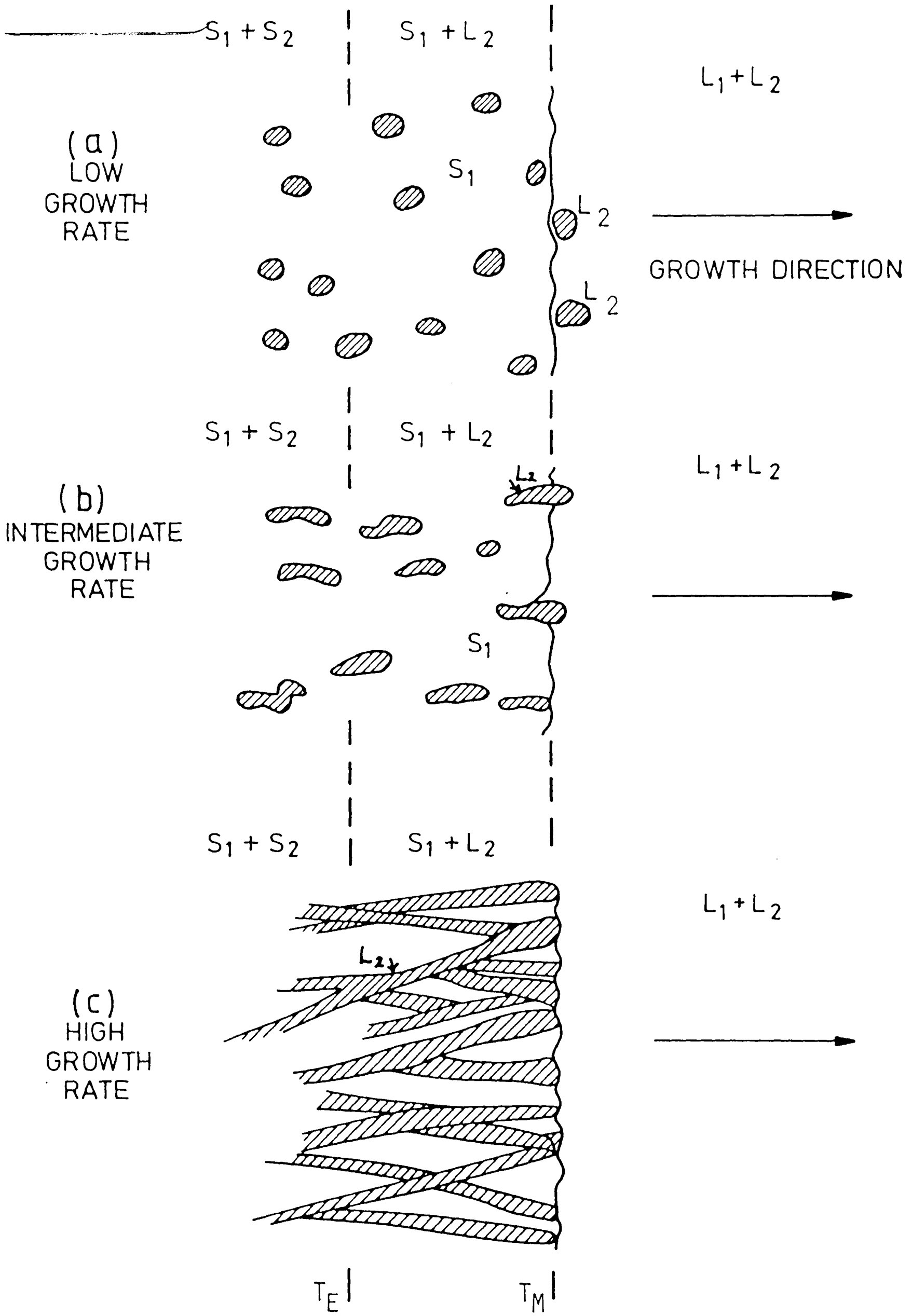


Fig. 2.13 Schematic diagrams of typical microstructures formed at different growth rate in a monotectic system with a low miscibility gap.

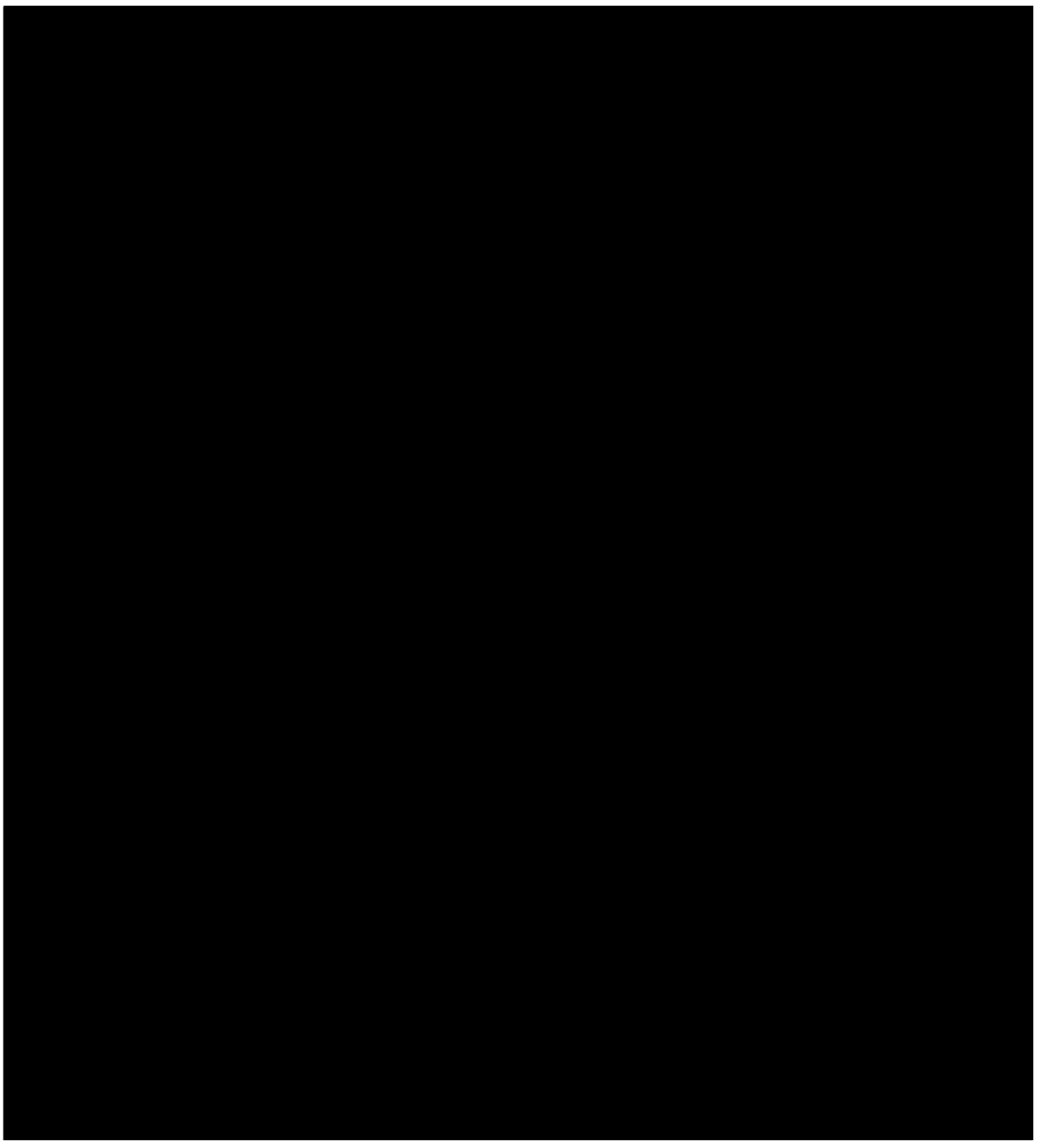


Fig. 2.14: Microstructures obtained in Al-In under different solidification conditions (After Derby, 1984).

upon the balance between $\sigma_{S_1L_1}$, $\sigma_{S_1L_2}$ and $\sigma_{L_1L_2}$, as shown schematically in Figs. 2.15(a) and (b), where $\sigma_{S_1L_1}$ and $\sigma_{S_1L_2}$ are the surface energies between solid S_1 and liquid L_1 and L_2 respectively, and $\sigma_{L_1L_2}$ is the surface energy between L_1 and L_2 . When

$$\sigma_{S_1L_2} < \sigma_{S_1L_1} + \sigma_{L_1L_2} \qquad (2.17a)$$

a stable triple point can form, as shown in Fig. 2.15(a). Under these conditions, a stable coupled growth front can develop and propagate into the melt to produce type A microstructures. Alternatively, if

$$\sigma_{S_1L_2} > \sigma_{S_1L_1} + \sigma_{L_1L_2} \qquad (2.17b)$$

S_1 is wetted by L_1 with the exclusion of L_2 as shown in Fig. 2.15(b). Under these conditions a stable coupled growth front is impossible and type B microstructures are produced.

Cahn (1977, 1979) discussed in more detail the way in which the surface energies and resultant wetting conditions are related to the miscibity gap in the monotectic system. His explanation is summarised schematically in Fig. 2.16. At T_c the liquid is completely miscible so that L_1 and L_2 are the same:

$$\sigma_{S_1L_1} = \sigma_{S_1L_2} \quad \text{and} \quad \sigma_{L_1L_2}=0 \qquad (2.18)$$

Below T_c, the two liquids L_1 and L_2 have an increasing composition difference with decreasing temperature, so that $\sigma_{L_1L_2}$ rises, and at the same time $\sigma_{S_1L_1}$ and $\sigma_{S_1L_2}$ increasingly diverge. As shown in Fig. 2.13, this predicts a critical wetting temperature T_w at which

$$\sigma_{S_1L_2} = \sigma_{S_1L_1} + \sigma_{L_1L_2} \qquad (2.19)$$

For a monotectic system with a high miscibility gap, T_m is much lower than T_c and is also therefore likely to be below T_w, i.e.

$$Tm/Tc<<1 \qquad Tm<Tw<Tc \qquad (2.20)$$

Under these circumstances, Fig. 2.16 shows that equation (2.17a) is fulfilled at T_m and type A microstructures are formed during solidification. With a low miscibility gap, T_m is only slightly smaller than Tc and is therefore likely to be above Tw, i.e.

$$Tm/Tc=1 \qquad Tw<Tm<Tc \qquad (2.21)$$

Under these circumstances, Fig. 2.16 shows that equation (2.17b) is fulfilled at T_m and type B microstructures are formed during solidification.



Fig. 2.15: Possible three phase profiles at the monotectic growth front showing (a) balanced wetting of S_1 by L_1 and L_2; and (b) perfect wetting of S_1 by L_1 (After Hellawell and Grugel, 1978).

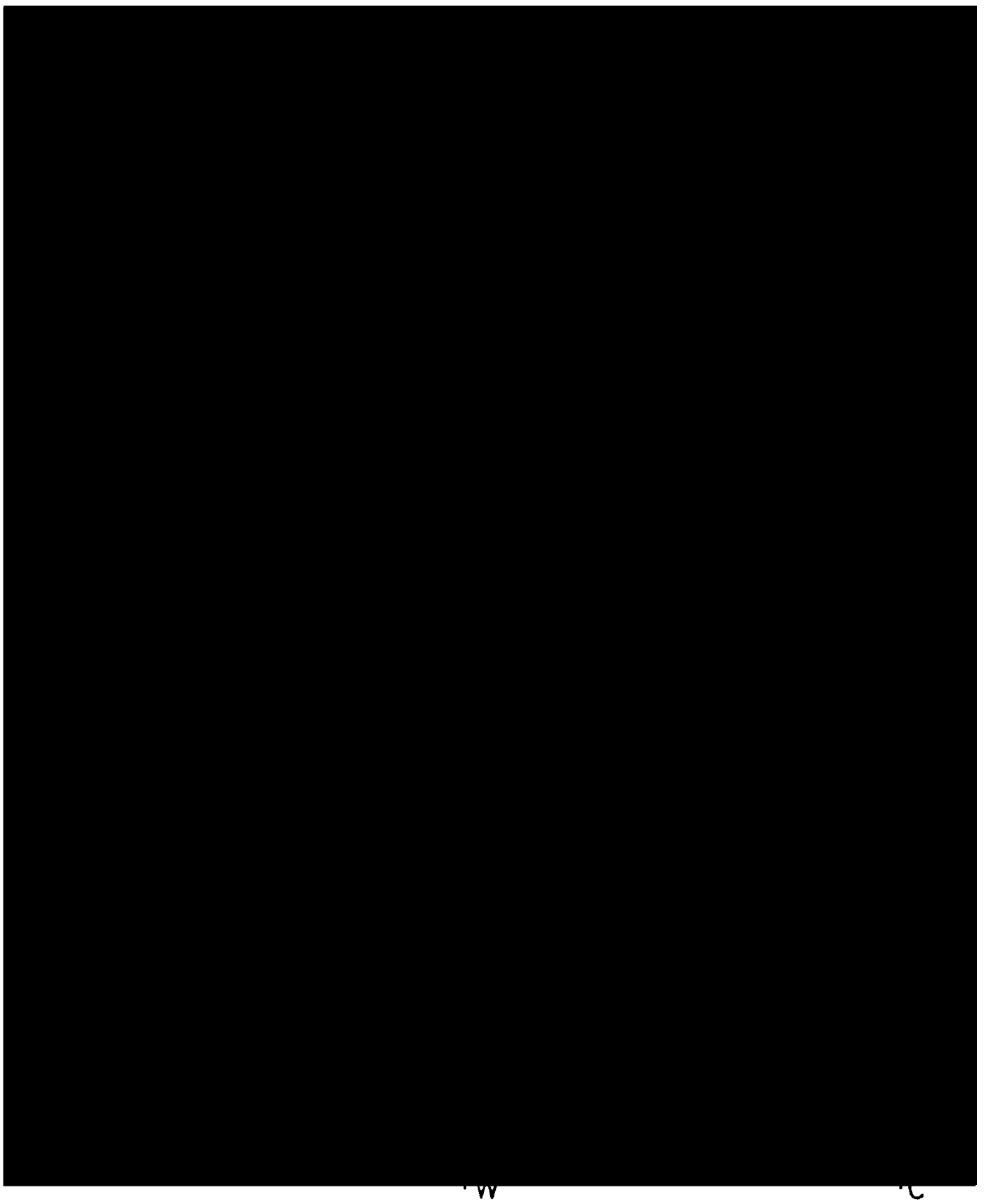


Fig. 2.16: Schematic representation of variation of interfacial energies with temperature (After Cahn, 1979).

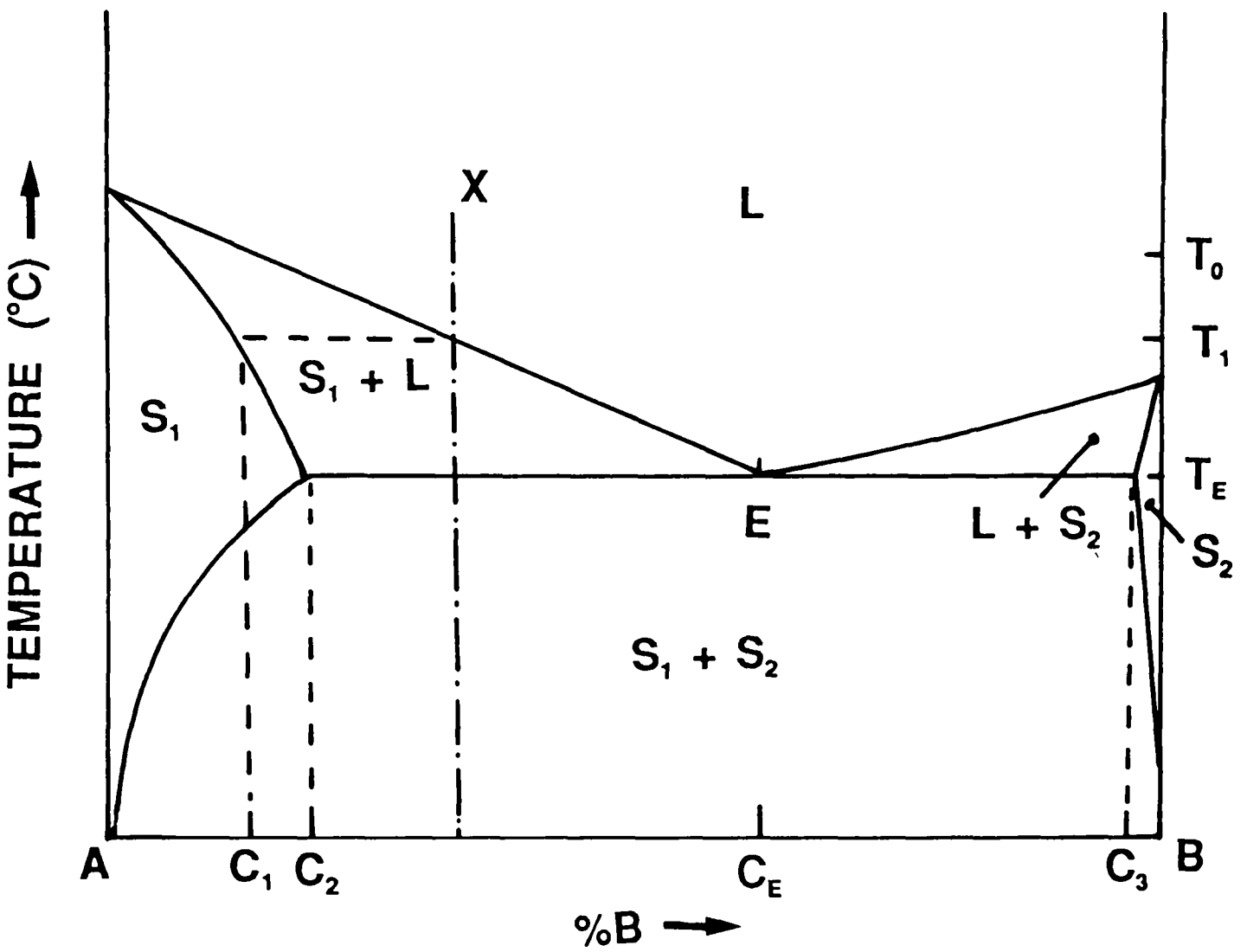


Fig. 2.17 Schematic phase diagram for a eutectic system.

Grugel and Hellawell (1981) have shown that varying the height of the miscibility gap by suitable ternary additions does result in a transition in the type of microstructure. Grugel et al (1984) noted that the critical point for the transition between type A and type B microstructures is T_m/T_c=0.9. Type A microstructures are found in binary monotectic systems with T_m/T_c below 0.9 and type B microstructures are found in binary system with Tm/Tc greater than 0.9. Perepezko et al (1982) have detected the undercooling prior to liquid phase separation for some compositions of Bi-Ga and Cu-Pb monotectic systems. They concluded that this was consistent with the operation of a critical wetting behaviour as put forward by Cahn (1977).

2.3.3 Eutectic based model

Derby and Favier (1983) and Derby et al (1983) checked the wetting model by comparing surface energies obtained by various empirical extrapolation rules and the solidification morphologies observed in different monotectic systems. They claimed that the wetting model does not explain the morphologies that are found experimentally. They therefore proposed a new model for monotectic morphologies based upon the model of eutectic growth developed by Jackson and Hunt (1966). For a regular eutectic, Jackson and Hunt found that nonfaceted/nonfaceted eutectic alloys obey the relation

$$\lambda V^{1/2} = \text{constant} \qquad (2.22)$$

where λ is the phase spacing, and the constant is a material parameter. Derby et al (1983) found that type A monotectic microstructures also obey equation (2.22) to a reasonable degree, whereas type B microstructures follow

$$\lambda V^{1/2} G^{1/3} = \text{constant} \qquad (2.23)$$

more closely than equation (2.22). They therefore concluded that type B monotectic alloys and faceted/nonfaceted eutectic alloys have similar mechanisms of solidification, with similar growth laws and similar microstructures (Toloui and Hellawell 1976, Hellawell and Grugel 1978, Fisher and Kurz 1981, Carlgerg and Bergman 1985).

2.3.4 Rapid solidification of monotectics

Despite great interests in the rapid solidification of eutectic alloys, there has been very little work reported in the literature concerning the microstructure of rapidly solidified monotectic alloys. The work that has been reported only involves rapid solidification of monotectic alloys which exhibit type A microstructures.

Work on rapidly solidified Al-In, Al-Cd and Al-Pb has been reported by Ojha and Chattopadhyay (1978), Chattopadhyay and Ramachandrao (1980) and Moore and Cantor (1988) respectively. The microstructures formed by rapid solidification of these monotectics were found to consist of a bi-modal distribution of particles embedded in a matrix. For monotectic Al-Cd, Chattopadhyay and Ramachandrao (1980) suggested that the larger Cd particles were formed by the monotectic reaction whereas the small Cd particles were formed by solid state Cd precipitation from the as-solidified supersaturated solid solution of Cd in Al. For the melt spun hypermonotectic Al-Pb, however, Moore and Cantor (1988) suggested that the larger Pb particles were formed by liquid phase separation, whereas the smaller Pb particles are formed by the monotectic reaction. The irregular monotectic microstructure was reasonably consistent with the approximate values of G and V during melt spinning, as expected from Fig. 2.14. All these researchers found that the rapidly solidified monotectic microstructures were of much smaller scale than the corresponding directionally solidified microstructures. Due to lack of data no detailed theory of the rapid solidification of monotectic alloys is available.

2.4 Solidification of Eutectic Alloys

2.4.1 Introduction

A eutectic system is a binary alloy in which addition of either component metal to the other causes a lowering of the melting point, and for which the liquidus curve passes through a temperature minimum known as the "eutectic

point". Fig. 2.17 shows a schematic phase diagram for a eutectic system. Assuming that the alloy composition X is in the hypoeutectic region, the course of equilibrium solidification is as follows. At temperature T_o, the alloy is molten. Upon cooling the alloy to temperature T_1, solidification begins with the formation of primary solid S_1, having the composition C_1. At the eutectic temperature, the eutectic reaction occurs:

$$L \rightarrow S_1 + S_2 \qquad (2.24)$$

and liquid L of composition C_E decomposes to give a solid S_1 of composition C_2 and a second solid phase S_2 of composition C_3.

As with monotectic alloys, the microstructures obtained during solidification of eutectic alloys are determined by a combination of process and material parameters. A large amount of work reported for eutectic systems has involved unidirectional solidification experiments. Unlike monotectic alloys, the solidification of eutectic alloys has been extensively investigated experimentally and theoretically. A detailed and complete review of the solidification of eutectic alloys is beyond the range of this thesis. However, there are several good reviews available by Elliot (1985), Minkoff (1986), and Flood (1985). The work relevant to the present thesis is on (a) the classification of eutectic systems and the governing equations for the corresponding microstructures; (b) the solidification of undercooled eutectic liquids, and (c) modification of Al-Si eutectic alloy microstructures.

2.4.2 Classification of eutectic systems

Hunt and Jackson (1966) proposed that eutectic systems may be classified into three groups: nonfaceted/nonfaceted alloys in which both phases have low entropies of melting; faceted/nonfaceted alloys in which one phase has a high and the other phase a low entropy of melting; and faceted/faceted alloys in which both phases have high entropies of melting. Lamellar or rod like structures are formed in nonfaceted/nonfaceted alloys. Irregular or complex regular structures are formed in faceted/nonfaceted alloys. In faceted/faceted eutectic alloys, each phase grows independently with a faceted solid-liquid

interface, leading to an irregular structure. The Al-Si alloys studied in the present investgation belong to the second group, i.e. they are faceted/nonfaceted eutectics.

For a regular nonfaceted/nonfaceted eutectic alloy, the relation found by Jackson and Hunt (1966),

$$\lambda V^{1/2} = \text{constant} \qquad (2.25)$$

predicts with good accuracy the phase spacing λ as a function of solidification rate V during unidirectional solidification (Tassa and Hunt, 1976, Clark and Elliott, 1976(1), (2)). However, for irregular faceted/nonfaceted eutectic alloys such as Al-Si very little comparable progress has been made in predicting the dendritic spacing, despite irregular eutectic alloys being of greater practical importance. The reason for the neglect of irregular eutectics has been because the growth mechanism is very complicated, and not well understood. Based on experimental observations, several authors (Toloui and Hellawell, 1976, Fisher and Kurz, 1981) found a relation as follows:

$$\lambda V^{1/2} G^{1/3} = \text{constant} \qquad (2.26)$$

In spite of the difficulties confronting the theoreticians, some theoretical models have been proposed based on the criterion of minimum interfacial undercooling, or the criterion of morphological stability (Sato and Sagama, 1974, Fisher and Kurz, 1980).

2.4.3 Solidification of undercooled eutectic alloys

Since the time when Hollomon and Turnbull (1951) investigated the solidification behaviour of undercooled Pb-Sn eutectic alloy droplets, many authors have studied the solidification behaviour of undercooled eutectic alloys in the form of bulk liquid or liquid droplets (e.g. Powell and Hogan, 1965, Powell and Colligan, 1969 (1), (2), Kattamis and Flemings, 1970, Cooper et al, 1982, Levi and Mehrabian, 1982(1), Chu et al, 1984). It has been established that with high undercooling before nucleation, the initial solidification rate is very high during recalescence, resulting in

supersaturation of solid solution, refinement of grains and even metastable phases. After recalescence, the solidification rate of the remaining liquid is determined by external cooling conditions. Apart from experimental work, several authors have done theoretical modelling of the solidification process of undercooled droplets (e.g. Shiohara and Flemings, 1984, Levi, 1986, Levi and Mehrabian, 1982(2)).

2.4.3 Modification of Al-Si Microstructure

The commercial importance of Al-Si casting alloys has attracted the interests of many researchers in studying the solidification of Al-Si alloys. In the early 1920s (Pacz, 1921), it was found that a transition in the shape of the Si phase from coarse flakes to fine fibres could improve dramatically the mechanical properties of Al-Si castings. This transition is known as the modification of Al-Si alloy microstructures. Modification can be achieved by either chill casting or impurity additions such as Na and Sr. Recent reviews of modification can be found in the work by Kanani and Abbaschian (1984) and Hanna et al (1984).

There are two types of proposed mechanism of modification caused by impurity addition: changes in Si growth mode; changes in Si nucleation temperature. Hellawell and co-workers (Day and Hellawell, 1968, Steen and Hellawell, 1972, 1975, Hanna et al, 1984, Lu and Hellawell, 1985, 1987) and Hogan and co-workers (Kobayashi and Hogan, 1985, Hogan and Song, 1987, Hogan and Shamsuzzoha, 1987, Shamsuzzoha and Hogan, 1986(1) (2), 1989(1) (2)) have done a lot of crystallographic work to understand the Si growth mode with and without impurity additions. In all cases additions of impurities such as Na and Sr dramatically increases the number of twins in the Si phase. It is therefore proposed that the increase in the number of twins causes the change of Si growth mode and therefore the modification of the Si morphology.

In contrast, little work has been done to understand the effects of impurity additions on the Si nucleation temperature, which might also affect the Si

morphology. However, it has been consistently reported that thermal analysis shows that Na increases the undercooling of Al-Si solidification. Southin (1970) showed that Na additions increase the undercooling required for Si nucleation and therefore also increase the undercooling during Si growth, leading to modification of the Si morphology. Thus, Southin (1970) and Flood and Hunt (1981) both suggested that a combination of nucleation and growth mechanisms are operative in the modification of Al-Si by Na additions.

Chapter 3

Experimental Techniques

3.1 Introduction

In this chapter, the experimental techniques used in the present investigation are described. The results that have been obtained will be presented and discussed in later chapters.

3.2 Materials Preparation

Binary Al-4.5wt%Cd, Al-7wt%In, Al-2wt%Pb, Al-5wt%Pb, and Al-3wt%Si alloys, and ternary Al-Cd-X, Al-Pb-X (X=Zn, Ga, Ge, Cu, Si, Mg), and Al-Si-X (X=Na, Sr) alloys were manufactured using induction melting, chill casting or normal casting and melt spinning.

3.2.1 Ingot preparation

10-30g binary and ternary alloy ingots were prepared using metals with 99.9%-99.9999% purity. The metals were cleaned in a dilute NaOH solution and weighed according to the nominal compositions. The cleaned and weighed metals were placed in a recrystallised alumina crucible, which was placed inside a copper R. F. heating coil. When preparing ingots of Al-Cd binary and ternary alloys, and ingots of Al-Si-Na, Al and the other metals with low vapour pressure were melted first, and then the metals with higher vapour pressure were added to the melt to reduce evaporation. To prevent contamination, all ingot melting was carried out under a dynamic argon atmosphere . The temperature was monitored during melting with a chromel-alumel thermocouple which remained immersed in the alloy throughout heating. Fig. 3.1 shows a schematic diagram of the apparatus used for the ingot preparation.

Each of the alloys was induction heated to a temperature in the miscible liquid region, and then held for at least 600s to ensure homogeneous mixing.

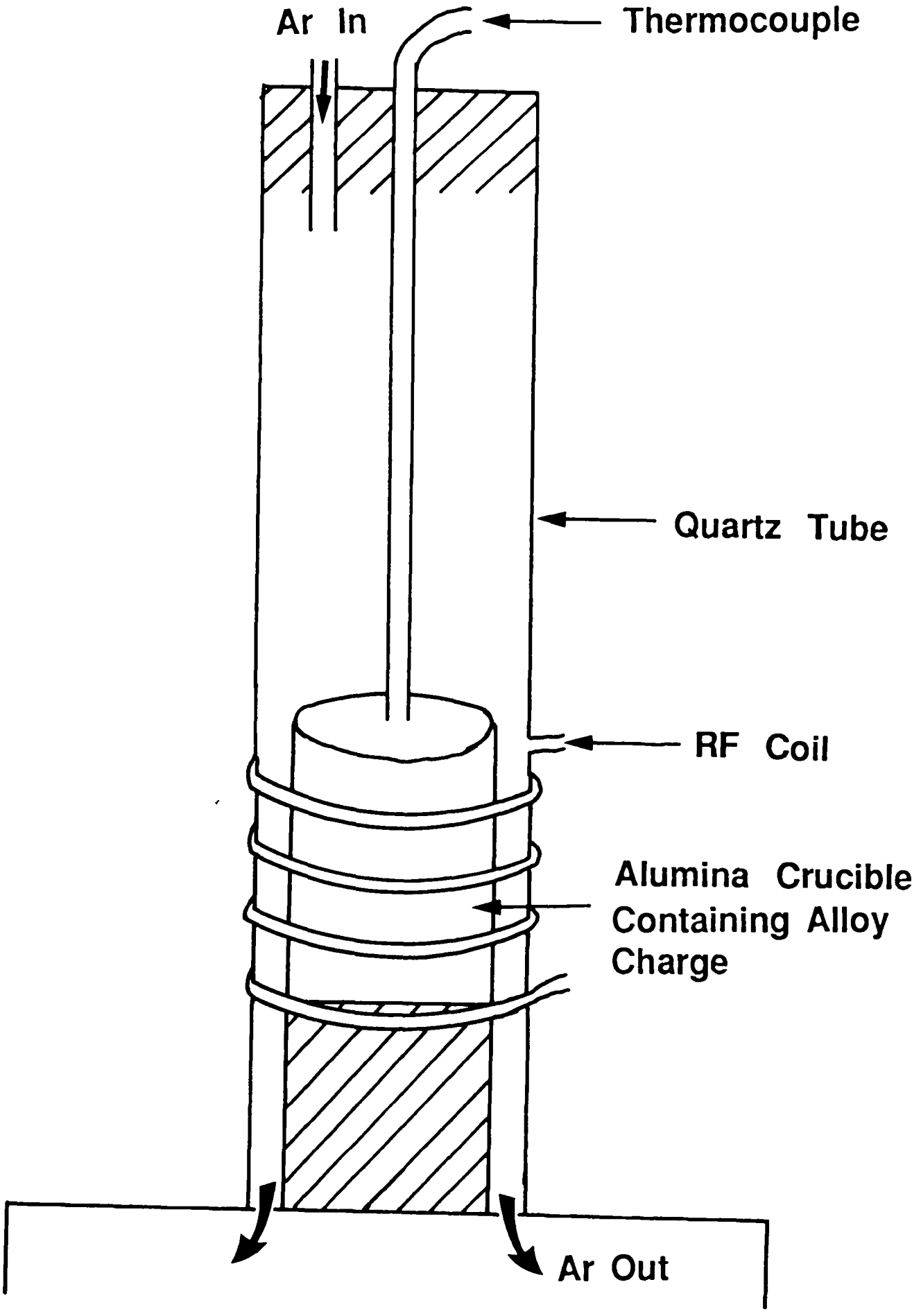


Fig. 3.1: Schematic diagram of the apparatus used for ingot preparation.

Finally the ingot was either quenched into water to minimise the effect of gravity segregation or slowly cooled by switching off the heater. The latter process was used for those alloys such as Al-Si where gravity segregation was not a problem in their solidification. Table 3.1 gives details of the conditions of preparation of all the alloys.

3.2.2 Rapid solidification by melt spinning

From all the rapid solidification routes which have been developed over the last 30 years, melt spinning was used in the present study (Gillen and Cantor, 1985). In melt spinning, a jet of molten liquid is converted very rapidly into a thin layer in contact with a rotating metal "chill block" to produce thin solidified foil or ribbon. Typical cooling rates during melt spinning are of the order of 10^6 K/s.

The melt spun alloys were in the form of ribbon, typical dimensions being 0.05-0.1mm in thickness, 3-10mm in width and up to several metres in length. Fig. 3.2 shows a schematic diagram of the melt spinning apparatus . Approximately 5g charges from each alloy ingot were remelted in a quartz crucible under a dynamic argon atmosphere, held at a temperature in the miscible liquid region, for at least 200s to ensure homogeneous mixing, and then ejected with an argon overpressure of 20KPa through a 1mm diameter orifice, onto the outer surface of a polished Cu wheel rotating with a tangential surface speed in the range 7-70m/s. Table 3.2 gives details of the manufacturing conditions of the melt spun ribbons.

3.3 Heat Treatment of the As-melt Spun Ribbons

To check for possible nonequilibrium solidification effects, some specimens of the as-melt spun ribbons were equilibrated by annealing under a vacuum of 10^{-6} torr or a dynamic argon atmosphere at temperatures just below or just above the second phase melting point. Annealing at temperatures below the second phase melting point ensured equilibrium in the solid state, and

Table 3.1: Conditions of Ingot Preparation

Composition (wt%)	Purity	Holding Time (mins)	Hold Temperature (°C)	Casting
Al4.5Cd	99.999%	10	750	Quench
Al3Cd1.5Zn	99.999% Al, Cd 99.99% Zn	10	750	Quench
Al2Cd1.5Ga	99.999%	10	750	Quench
Al2Cd0.5Ge	99.999%	10	750	Quench
Al2Cd0.5Cu	99.999%	10	750	Quench
Al2Cd1Si	99.999%	10	750	Quench
Al9Cd1.5Mg	99.999% Al, Cd 99.97% Mg	10	750	Quench
Al2Pb	99.999%	10	1000	Quench
Al5Pb	99.999%	10	1000	Quench
Al4Pb1Zn	99.999% Al, Pb 99.99% Zn	10	1000	Quench
Al2Pb1Ga	99.999%	10	1000	Quench
Al2Pb0.5Cu	99.999%	10	1000	Quench
Al5Pb0.5Ge	99.999%	10	1000	Quench
Al5Pb1Ge	99.999%	10	1000	Quench
Al5Pb1.5Ge	99.999%	10	1000	Quench
Al5Pb2Ge	99.999%	10	1000	Quench
Al5Pb0.2Si	99.999%	10	1000	Quench
Al5Pb0.5Si	99.999%	10	1000	Quench
Al5Pb0.7Si	99.999%	10	1000	Quench
Al5Pb1Si	99.999%	10	1000	Quench
Al3Si	99.995% Al 99.999% Si	10	750	Slow cool
Al3Si	99.999% Al 99.999% Si	10	750	Slow cool
Al3Si	99.9999% Al 99.999% Si	10	750	Slow cool
Al3SiNa	99.995% Al 99.999% Si 99.9% Na	10	750	Slow cool
Al3Si0.15Sr	99.995% Al 99.999% Si Al-Sr Master Alloy	10	750	Slow cool
Al3Si0.3Sr	99.995% Al 99.999% Si Al-Sr Master Alloy	10	750	Slow cool

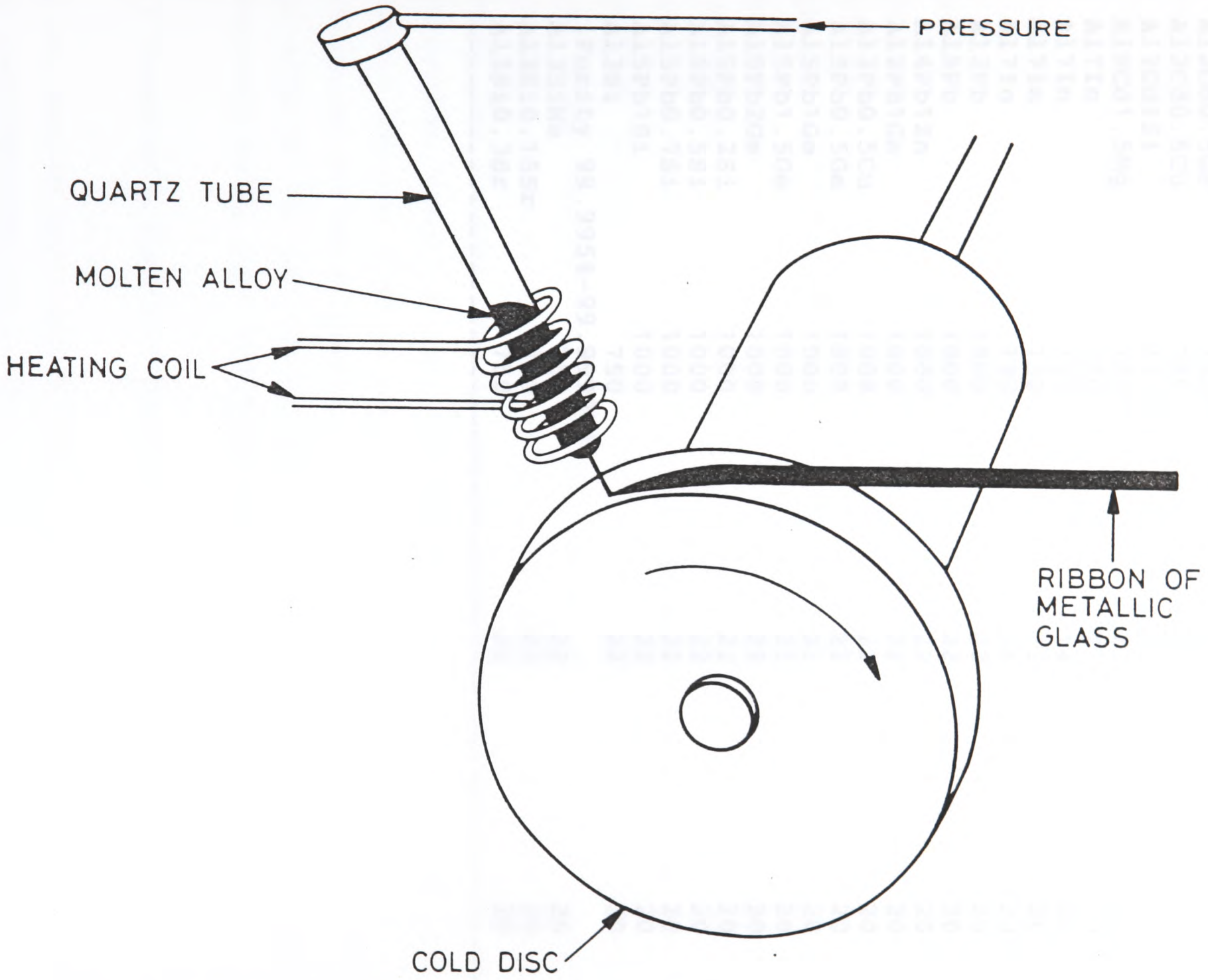


Fig. 3.2: Schematic diagram of the melt spinning apparatus.

Table 3.2: Conditions of Melt Spinning

Compositions (wt%)	Ejection Temperature (°C)	Wheel Speed (m/s)	Ejection Pressure (kPa)
Al4.5Cd	730	22	20
Al3Cd1.5Zn	730	22	20
Al2Cd1.5Ga	730	22	20
Al2Cd0.5Ge	730	22	20
Al2Cd0.5Cu	730	22	20
Al2Cd1Si	730	22	20
Al9Cd1.5Mg	730	22	20
Al7In	730	7	20
Al7In	730	14	20
Al7In	730	33	20
Al7In	730	65	20
Al2Pb	1000	22	20
Al5Pb	1000	22	20
Al4Pb1Zn	1000	22	20
Al2PB1Ga	1000	22	20
Al2Pb0.5Cu	1000	22	20
Al5Pb0.5Ge	1000	22	20
Al5Pb1Ge	1000	22	20
Al5Pb1.5Ge	1000	22	20
Al5Pb2Ge	1000	22	20
Al5Pb0.2Si	1000	22	20
Al5Pb0.5Si	1000	22	20
Al5Pb0.7Si	1000	22	20
Al5Pb1Si	1000	22	20
Al3Si	750	22	20
(Purity 99.995%-99.9999%)			
Al3SiNa	750	22	20
Al3Si0.15Sr	750	22	20
Al3Si0.3Sr	750	22	20

annealing at temperatures above the second phase melting point ensured equilibrium in the solid-liquid region. Table 3.3 gives details of the solid state heat treatment of the melt spun ribbons, which was carried out in a tube furnace. Details of the solid-liquid heat treatment of the melt spun ribbons, which was carried out in a calorimeter furnace, will be described in section 3.6.

3.4 X-ray Microprobe Analysis

Samples taken from the as-melt spun ribbons were mounted in thermal-setting resin with the cross sections of the ribbons exposed. The sections were ground with silica papers, polished to 1/4μm with diamond paste, coated with an approximately 30nm thick layer of carbon to prevent localised charging, and then examined in a Cameca Camebax electron microprobe analyser. The electron beam was set to scan a small area typically 2μm square, and characteristic X-rays were collected by the wave length dispersive spectrometers for 2s-30s depending upon the signal intensity. The K ratios between the intensity of each element measured from the sample and the intensity from a corresponding standard gave the measured compositions. In each case, 20-30 positions on each sample were analysed, and the average value was taken to be the measured composition. Table 3.4 lists the measured compositiions of the melt spun ribbons. For the Al-Si-Na alloy, the composition of Na in the melt spun ribbons was too low to produce a measurable X-ray peak, although 1wt% of Na was added to the melt during ingot casting. Presumably, most of the Na evaporated during ingot casting and melt spinning.

3.5 Transmission Electron Microscopy

As-melt spun and heat treated ribbon samples were abraded using silica papers, jet electropolished in a mixture of 25vol% nitric acid and 75vol% methanol at -40°C, and then examined in either a Philips CM12 or JEOL 100C transmission electron microscope, operating at 120 and 100kV respectively. The Philips CM12 was generally used to perform detailed morphological and crystallographic

Table 3.3: Heat Treatment of Melt Spun Ribbons

Alloy (wt%)	Annealing Temprature (°C)	Anealing Time (s)	Atmosphere
Al4.5Cd	300	10^5	Argon
Al7In	145	10^5	Vacuum
Al9Cd1.5Mg	345	10^5	Vacuum
Al3Si (purity 99.995%-99.9999%)	595	600 then quenching	Argon
Al3SiNa	595	600 then quenching	Argon
Al3Si0.15Sr	595	600 then quenching	Argon
Al3Si0.3Sr	595	600 then quenching	Argon

Table 3.4: Measured Composition of Alloys

Nominal Compositions (wt%)	Measured Compositions (wt%)
Al4.5Cd	Al4.47Cd
Al3Cd1.5Zn	Al3.40Cd1.78Zn
Al2Cd1.5Ga	Al2.40Cd1.60Ga
Al2Cd0.5Ge	Al1.90Cd0.51Ge
Al2Cd0.5Cu	Al2.10Cd0.80Cu
Al2Cd1Si	Al2.50Cd1.20Si
Al9Cd1.5Mg	Al8.79Cd1.45Mg
Al7In	Al7.20In
Al2Pb	Al2.38Pb
Al5Pb	Al4.20Pb
Al4Pb1Zn	Al4.17Pb1.12Zn
Al2Pb1Ga	Al1.67Pb1.25Ga
Al2Pb0.5Cu	Al2.40Pb0.60Cu
Al5Pb0.5Ge	Al5.53b0.31Ge
Al5Pb1Ge	Al4.64Pb1.01Ge
Al5Pb1.5Ge	Al3.03Pb1.57Ge
Al5Pb2Ge	Al4.28Pb2.03Ge
Al5Pb0.2Si	Al6.13Pb0.24Si
Al5Pb0.5Si	Al6.93Pb0.54Si
Al5Pb0.7Si	Al5.29Pb0.72Si
Al5Pb1Si	Al3.74Pb1.11Si
Al3Si (99.995% pure)	Al3.45Si
Al3Si (99.999% pure)	Al2.90Si
Al3Si (99.9999% pure)	Al3.58Si
Al3SiNa	Al3.70SiNa
Al3Si0.15Sr	Al3.30i0.19Sr
Al3Si0.3Sr	Al3.18Si0.35Sr

examination, while the JEOL 100C was used to perform in-situ heating experiments.

For in-situ heating, specimens from melt spun Al-4.5wt%Cd equilibrated by annealing for 10^5s at 300°C, melt spun Al-7wt%In equilibrated by annealing for 10^5s at 145°C, as-melt spun Al-7wt%In and as-melt spun Al-5wt%Pb were prepared for observation in the transmission electron microscope by jet electropolishing as described above. The specimens were sandwiched between two nickel grids and mounted on an appropriate heating stage. The temperature was measured with a thermocouple placed close to the specimen, and calibrated against the second phase melting point measured in the differential scanning calorimeter. Heating runs were performed by heating from room temperature to 420°C in steps of 20-50K for melt spun Al-4.5wt%Cd, from room temperature to 280°C in steps of 10-20K for melt spun Al-7wt%In, and from room temperature to 380°C in steps of 10-20K for melt spun Al-5wt%Pb. The specimens were held for at least 600s at each temperature below the second phase melting point, and 180s above the second phase melting point, to compensate for any thermal lag. The specimens were then allowed to cool down. The melting and solidification behaviour, and the change in shape of the low melting point second phase particles were observed and recorded on films.

3.6 Differential Scanning Calorimetry

Differential scanning calorimetry involves measurements of the difference in heat flow from a known reference that does not undergo any transformation and a sample whose thermal stability is being investigated, while both the reference and the sample are subject to the same controlled heating or cooling programme.

The solidification behaviour of Cd, Pb, In and Si particles in the melt spun binary and ternary Al alloys were investigated in a DuPont 1090 thermal analyser fitted with 910 differential scanning calorimeter module. Figs. 3.3 and 3.4 show the cross-section and schematic diagram of the DuPont



Fig. 3.3: Differential scanning calorimeter cell cross-section (Reproduced from DuPont Manual).



Fig. 3.4: Temperature servo cell schematic diagram (Reproduced from DuPont Manual).

differential scanning calorimeter cell. Individual 15-20mg samples were sealed in Al cans, and then heated and cooled under a dynamic argon atmosphere. During each heating and cooling cycle, the differences in heat flow to and from the sample and a similarly heat treated reference were continuously recorded at maximium sensitivity on a microcomputer for subsequent detailed examination. Heating and cooling programmes for the different alloys were as follows.

(1) Al-4.5wt%Cd and Al-Cd-X alloys: Samples were heated from 230°C to a temperature in the range 310-400°C at a rate of 10K/min, held for 600s and then re-ccoled to 230°C at a rate in range 0.5-10K/min.

(2) Al-7wt%In: Samples were heated from 100°C to a temperature in the range 150-210°C at a rate of 10K/min, held for 600s, and then re-cooled to 120°C at a rate in the range 1-2K/min.

(3) Al-5wt%Pb and Al-Pb-X alloys: Samples were heated from 250°C to a temperature in the range 310-380°C at rate of 10K/min, held for 600s and then re-cooled to 200°C at a rate in the range 0.5-10K/min.

(4) Al-3wt%Si and Al-Si-X alloys: Samples were heated from 450°C to 595°C at heating rate of 10K/min, held for a time in the range 300-3600s, and then re-cooled to 450°C at a rate of 10K/min.

Chapter 4

Heterogeneous Nucleation of Solidification of Cd, In and Pb Particles Embedded in an Al Matrix

4.1 Introduction

In this chapter, the results of experimental work to investigate the heterogeneous nucleation of solidification of Cd, In and Pb particles embedded in an Al matrix are presented together with the as-melt spun and heat treated microstructures of Al-4.5wt%Cd, Al-7wt%In and Al-5wt%Pb monotectic alloys. Based on the microstructural information, the results of the nucleation experiments are discussed in relation to the current theory of heterogeneous nucleation kinetics. The experiments used to obtain the results presented in this chapter include the following.

(a) Transmission electron metallography to investigate the shape, size, spatial distribution and crystallographic orientation of Cd, In and Pb particles in the melt spun ribbons.

(b) In-situ heating experiments in a transmission electron microscope to investigate the change of Cd and In particle shape, and therefore the change of surface energy anisotropy, during heating and melting and cooling and solidification.

(c) Heating and cooling experiments in a differential scanning calorimeter to investigate the solidification behaviour of Cd, In and Pb particles embedded in an Al matrix.

4.2 Heterogeneous Nucleation of Solidification of Cd Particles Embedded in an Al Matrix

4.2.1 Alloy microstructure

Fig. 4.1 shows a typical transmission electron micrograph of the microstructure of as-melt spun hypomonotectic Al-4.5wt%Cd, consisting of small Cd particles homogeneously distributed throughout a matrix of Al. Figs. 4.2(a)

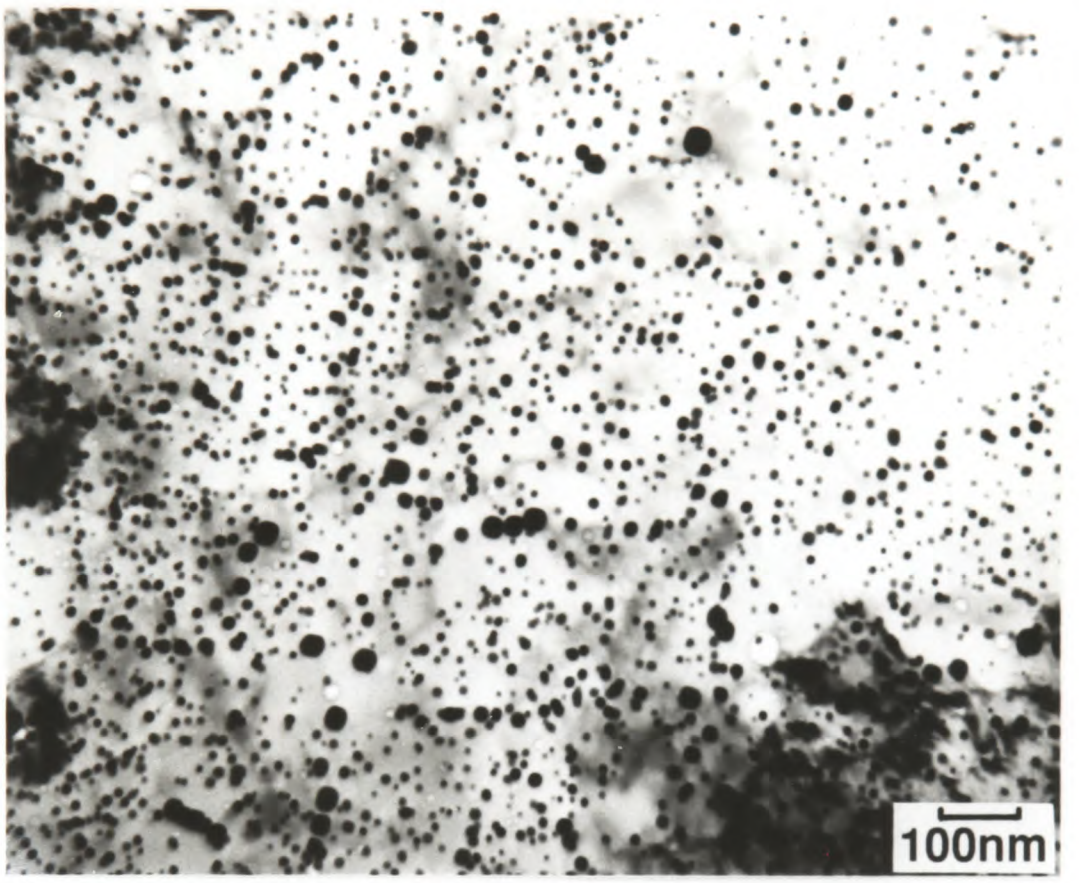


Fig. 4.1: Bright field transmission electron micrograph of the microstructure of as-melt spun hypomonotectic Al-4.5wt%Cd, showing a homogeneous distribution of Cd particles embedded in an Al matrix.

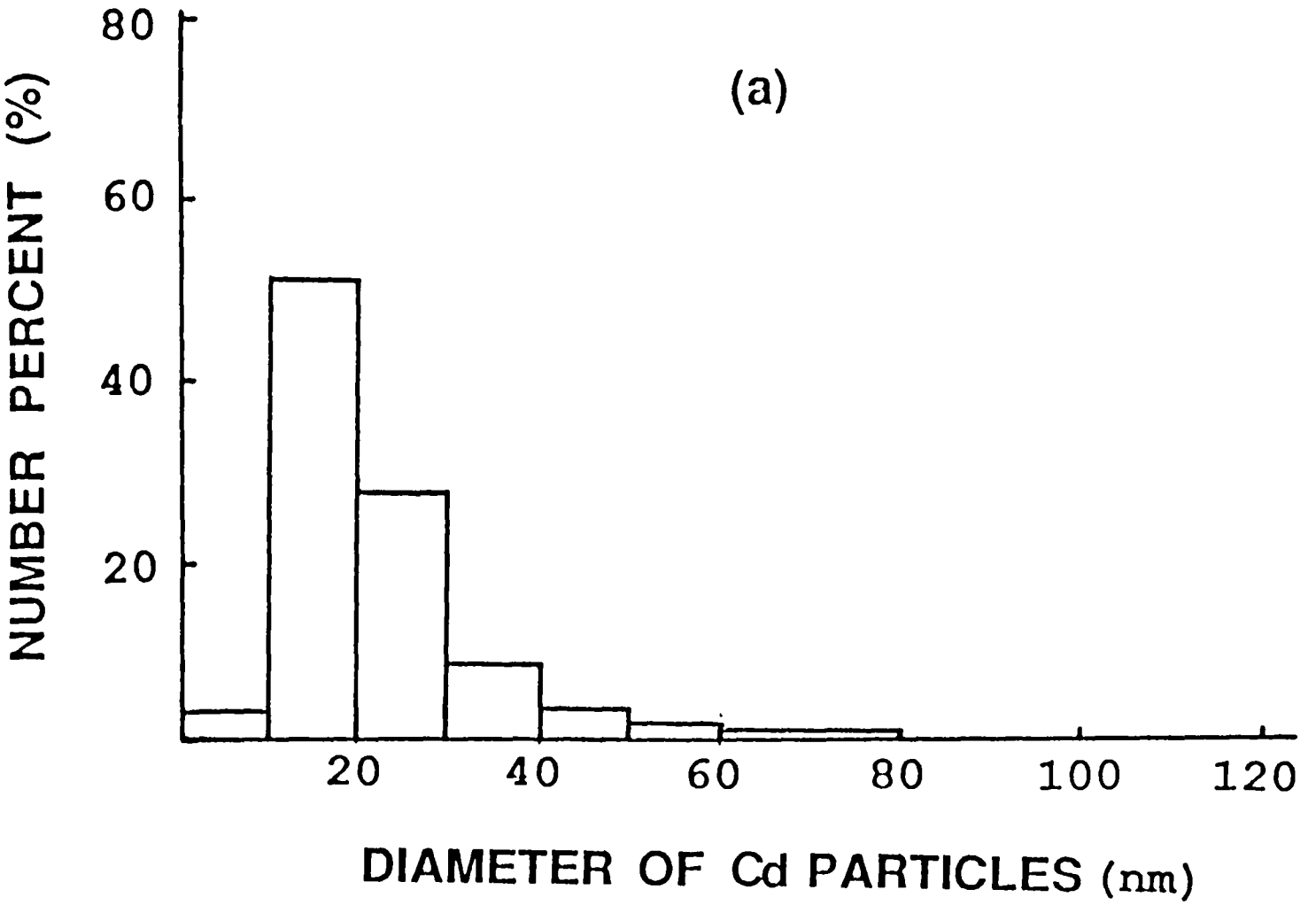


Fig. 4.2: Size distribution of Cd particles in as-melt spun Al-4.5wt%Cd by (a) number and (b) volume.

and (b) show the as-melt spun Cd particle size distribution by number and volume respectively. The Cd particles ranged from 5-120nm in diameter, with an average particle diameter of 20nm, and an average inter particle spacing of 140nm. The Cd particles were resistant to heat treatment, with insignificant coarsening after 300s at 350°C or 10^5s at 300°C.

The Cd particles were faceted in as-melt spun Al-4.5wt%Cd. To establish the facet crystallography, superimposed Al and Cd electron diffraction patterns were generated to determine the Al-Cd orientation relationship, and then the Cd particle cross sectional shape was examined as a function of Al matrix crystallographic orientation. This was achieved by tilting until a low index Al zone axis was parallel to the electron beam, as shown by a symmetrical distribution of Kikuchi lines and/or diffraction spots, followed by recording the diffraction pattern together with the corresponding bright field and dark field images.

The hcp Cd particles were found to have an orientation relationship with the fcc Al matrix which can be described as:

$$\{111\}_{Al}//\{0001\}_{Cd}$$

$$\langle 110\rangle_{Al}//\langle 11\bar{2}0\rangle_{Cd}$$

Each Cd particle was a single crystal, and in each Al grain there were four different Cd particle variants depending upon which of the four $\{111\}_{Al}$ planes was parallel to the $\{0001\}_{Cd}$ plane. Fig. 4.3(a) shows a typical selected area electron diffraction pattern with superimposed $[111]_{Al}$, $[0001]_{Cd}$, $[03\bar{3}1]_{Cd}$, $[3\bar{3}01]_{Cd}$ and $[30\bar{3}1]_{Cd}$ zones from the Al matrix and the four Cd particle variants respectively. This orientation shows the $\{220\}_{Al}$ diffraction spots from the $[111]_{Al}$ zone, and the $\{10\bar{1}0\}$ diffraction spots from the $[0001]_{Cd}$ zone, but diffraction spots from the other three Cd particle variants were obscured by the $\{220\}_{Al}$ diffraction spots, as can be seen on the schematic diffraction pattern in Fig. 4.3(b). Fig. 4.3(c) shows a bright field image corresponding to the diffraction pattern in Fig. 4.3(a), and Figs. 4.3(d) and (e) show dark field images from the same region taken with the $(10\bar{1}0)_{Cd}$ and $(02\bar{2})_{Al}$ diffraction spots from the $[0001]_{Cd}$ and $[111]_{Al}$ zones respectively. As expected

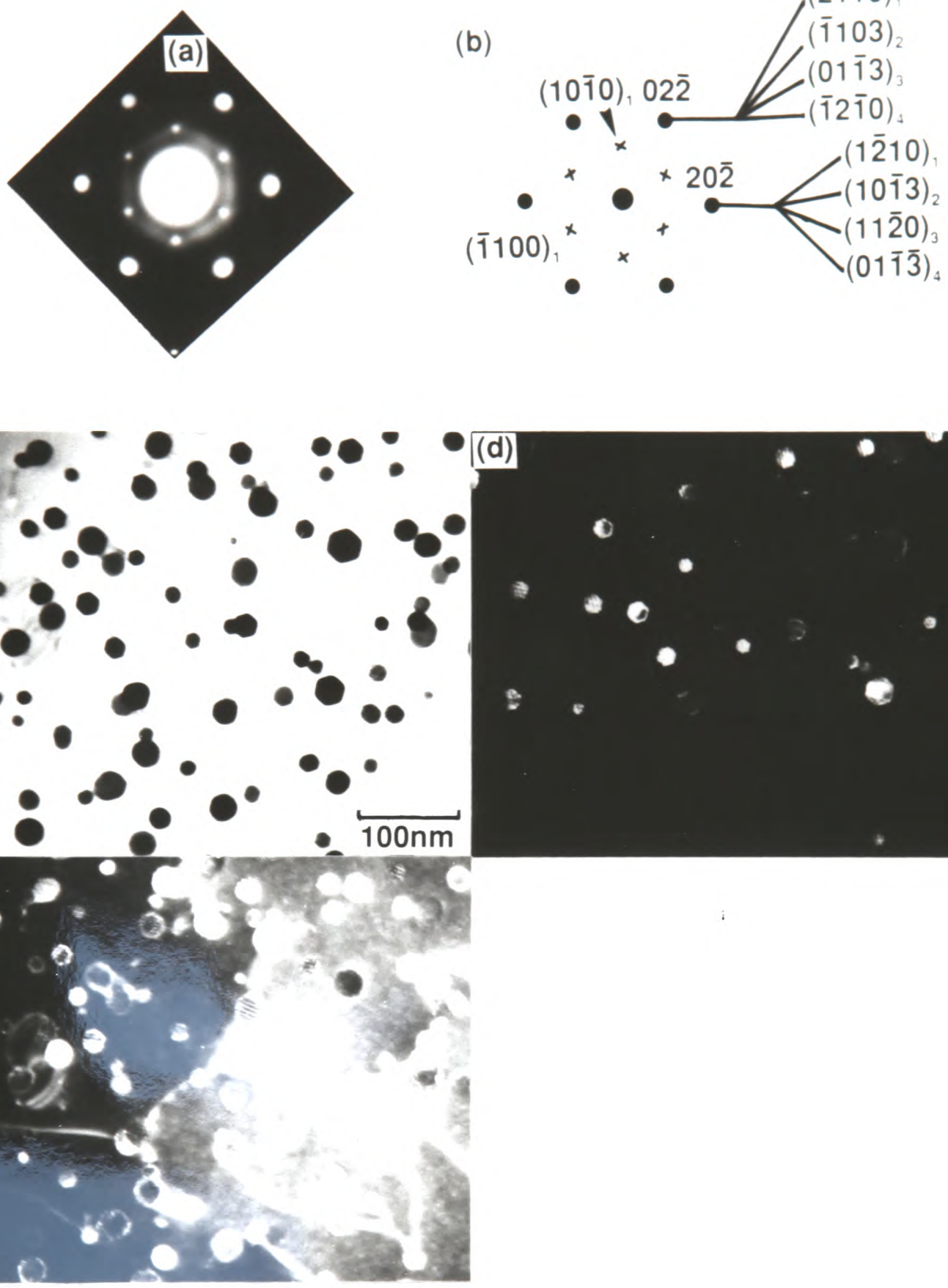
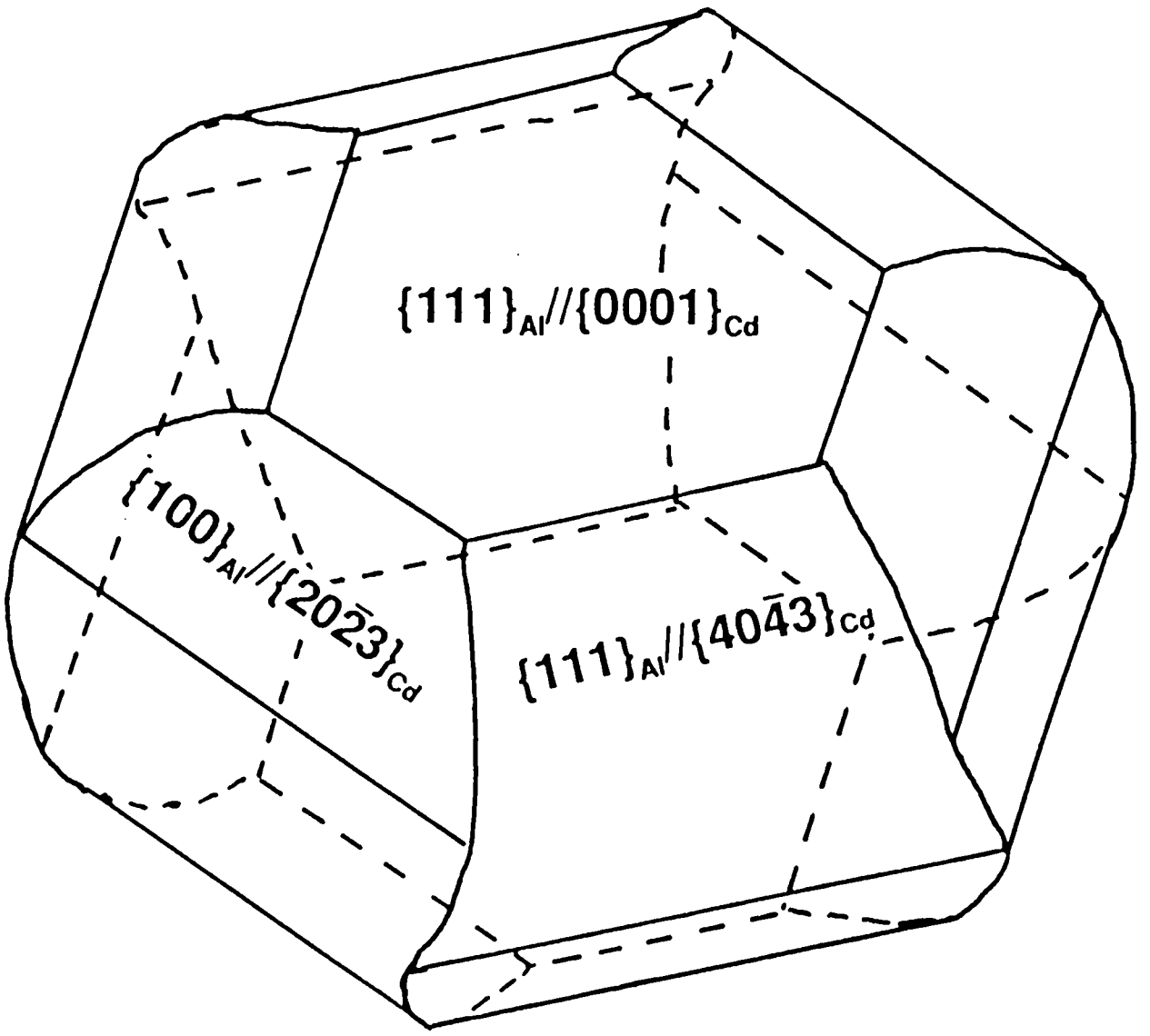


Fig. 4.3: (a) Selected area diffraction pattern from as-melt spun Al-4.5wt%Cd, showing superimposed $[111]_{Al}$, $[0001]_{Cd}$, $[03\bar{3}1]_{Cd}$, $[3\bar{3}01]_{Cd}$ and $[30\bar{3}1]_{Cd}$ zones from the Al matrix and Cd particle variants 1-4 respectively; (b) schematic diffraction pattern corresponding to (a) with crosses corresponding to diffraction spots from the $[0001]_{Cd}$ zone, and circles corresponding to superimposed diffraction spots from the $[111]_{Al}$ zone and all four Cd particle variants; (c) bright field transmission electron micrograph corresponding to (a); and (d) and (e) dark field transmission electron micrographs from the same area as (c) and formed with the $(10\bar{1}0)_{Cd}$ and $(2\bar{2}0)_{Al}$ spots respectively.

from the schematic diffraction pattern in Fig. 4.3(b), only a quarter of the Cd particles in the bright field image in Fig. 4.3(c) were illuminated in the $(10\bar{1}0)_{Cd}$ dark field image in Fig. 4.3(d), since the $\{10\bar{1}0\}_{Cd}$ diffraction spots were generated by only one of the four Cd particle variants. However, all Cd particles in the bright field image in Fig. 4.3(c) were illuminated in the $(02\bar{2})_{Al}$ dark field image in Fig. 4.3(e), since $\{022\}_{Al}$ spots obscured diffraction spots from all Cd particles.

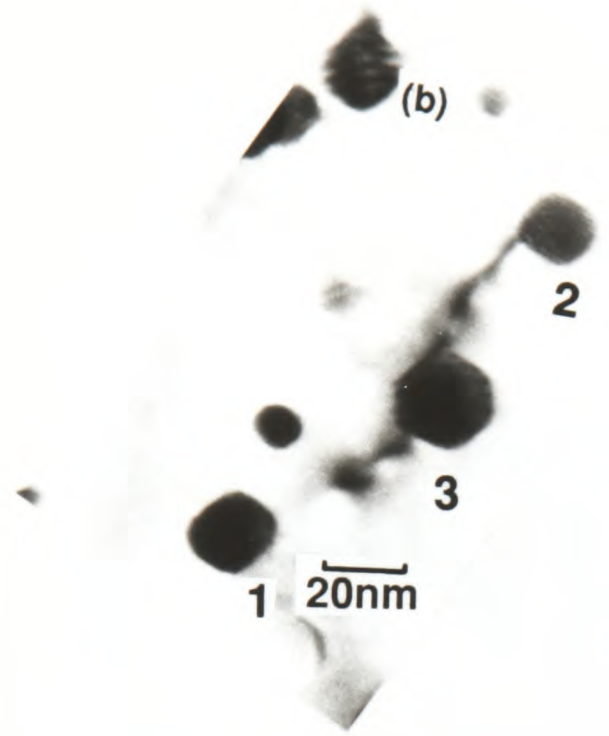
The as-melt spun Cd particle shape was found to be distorted truncated octahedral, bounded by six curved $\{100\}_{Al}//\{20\bar{2}3\}_{Cd}$ facets, six curved $\{111\}_{Al}//\{40\bar{4}3\}_{Cd}$ facets, and the two flat $\{111\}_{Al}//\{0001\}_{Cd}$ facets, as shown schematically in Fig. 4.4(a). Typical as-melt spun Cd particle cross sectional shapes with the electron beam parallel to the $[\bar{1}10]_{Al}$ zone are shown in Fig. 4.4(b), with corresponding selected area and schematic diffraction patterns in Figs. 4.4(c) and (d). Three types of Cd particle cross sectional shape can be seen in Fig. 4.4(b). The particle marked 1 in Fig. 4.4(b) belonged to variant 1, with a distorted hexagonal shape bounded by pairs of $(111)_{Al}//(0001)_{Cd}$, $(11\bar{1})_{Al}//(\bar{4}403)_{Cd}$ and $(001)_{Al}//(\bar{2}203)_{Cd}$ facets; the particle marked 2 in Fig. 4.4(b) belonged to variant 2, with a distorted hexagonal shape bounded by pairs of $(11\bar{1})_{Al}//(0001)_{Cd}$, $(111)_{Al}//(\bar{4}403)_{Cd}$ and $(001)_{Al}//(2\bar{2}03)_{Cd}$ facets; the particle marked 3 in Fig. 4.4(b) belonged to variant 3 or 4, with a distorted hexagonal shape bounded by pairs of $(111)_{Al}//(0\bar{4}43)_{Cd}$, $(11\bar{1})_{Al}//(40\bar{4}3)_{Cd}$ and $(001)_{Al}//(20\bar{2}3)_{Cd}$ facets.

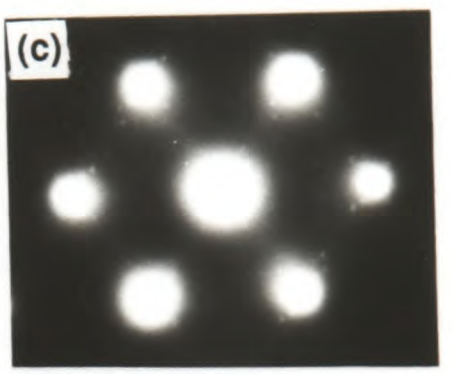
After heat treatment for 300s at 350°C, above the Cd melting point, there was no change in either the Cd particle shape, or the orientation relationship between the Cd particles and the Al matrix. However, after heat treatment for 10^5s at 300°C, below the Cd melting point, the Cd particles became elongated to increase the surface area and decrease the separation of the two $\{111\}_{Al}//\{0001\}_{Cd}$ facets, as shown schematically in Fig. 4.5(a). Typical annealed Cd particle cross sectional shapes with the electron beam parallel to the $[\bar{1}10]_{Al}$ zone are shown in Fig. 4.5(b), with corresponding selected area and schematic diffraction patterns in Figs. 4.5(c) and (d). Again, three types



(a)

Fig. 4.4(a)





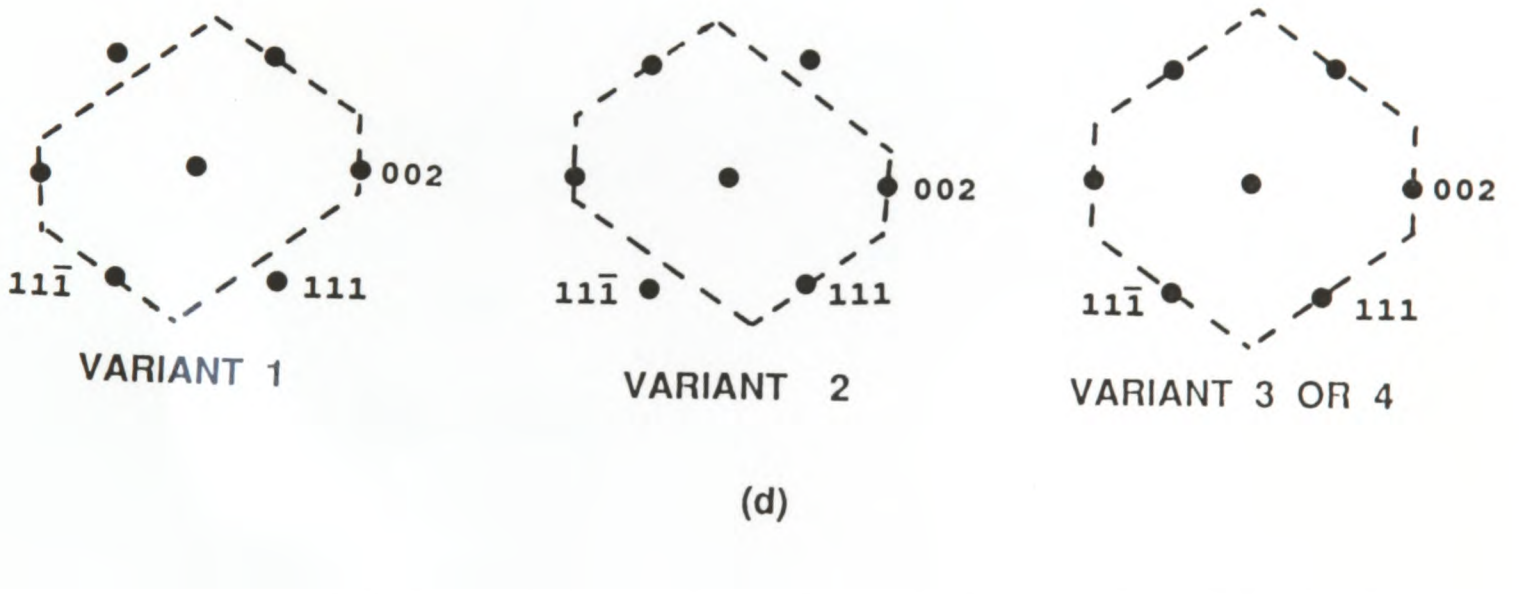
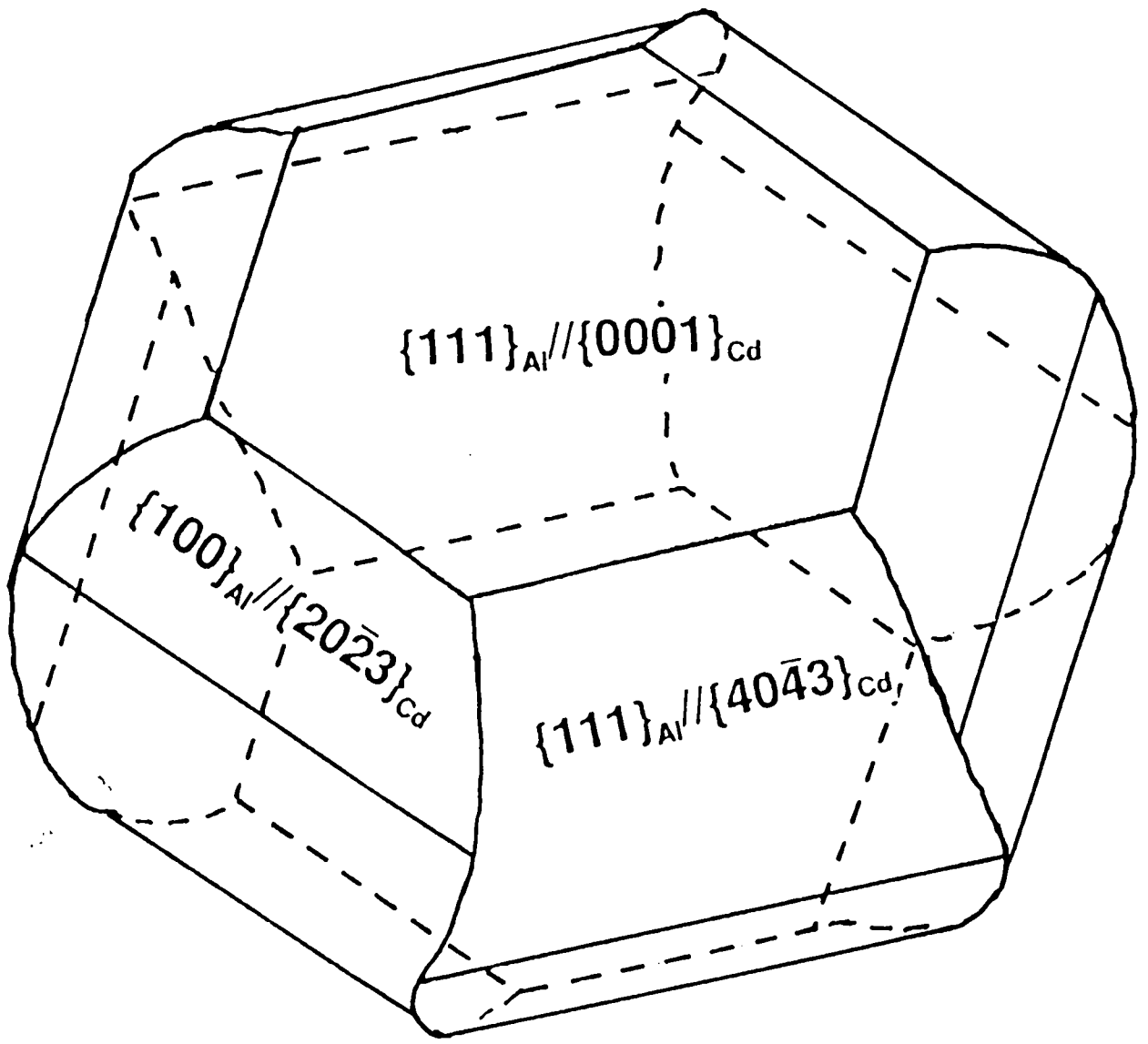


Fig. 4.4: (a) Schematic diagram of as-melt spun Cd particle distorted truncated octahedral shape; (b) bright field transmission electron micrograph from as-melt spun Al-4.5wt%Cd showing the distorted hexagonal cross sections of Cd particles perpendicular to the $[\bar{1}10]_{Al}$ zone axis; (c) selected area diffraction pattern corresponding to (b) showing $[\bar{1}10]$ zone of Al matrix; (d) schematic diffraction pattern and Cd particle cross sections.



(a)

Fig. 4.5(a)

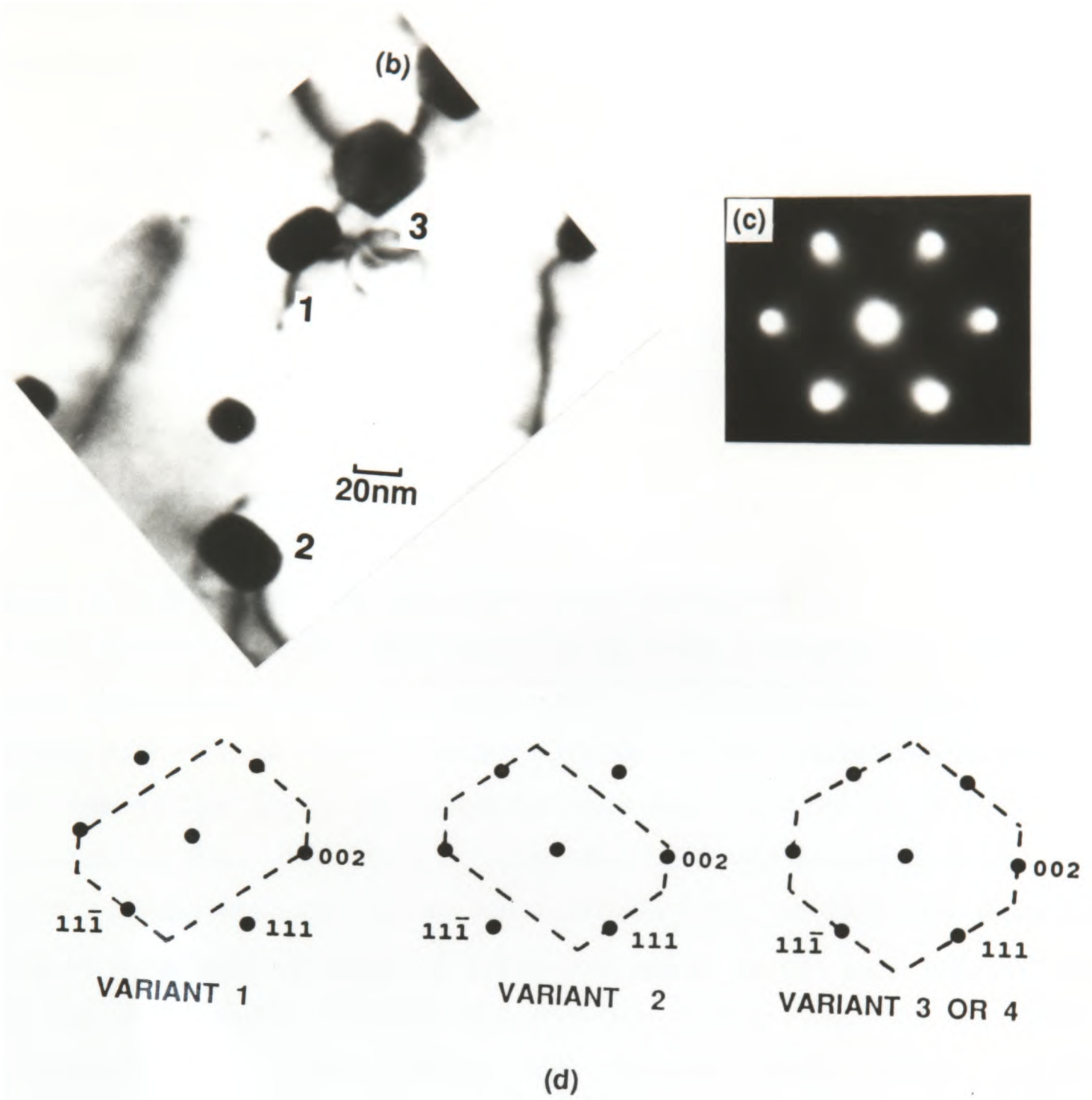


Fig. 4.5: (a) Schematic diagram of equilibrium Cd particle distorted truncated octahedral shape; (b) bright field transmission electron micrograph from melt spun Al-4.5wt%Cd after heat treatment for 10^5s at 300°C, showing the distorted hexagonal cross sections of Cd particles perpendicular to the $[\bar{1}10]_{Al}$ zone axis; (c) selected area diffraction pattern corresponding to (b) showing $[\bar{1}10]$ zone of Al matrix; (d) schematic diffraction pattern and Cd particle cross sections.

of Cd particle shape can be seen in Fig. 5(b). The particle marked 1 in Fig. 4.5(b) belonged to variant 1, with a distorted hexagonal shape bounded by pairs of $(111)_{Al}//(0001)_{Cd}$, $(11\bar{1})_{Al}//(\bar{4}403)_{Cd}$ and $(001)_{Al}//(\bar{2}203)_{Cd}$ facets; the particle marked 2 in Fig. 4.5(b) belonged to variant 2, with a distorted hexagonal shape bounded by pairs of $(11\bar{1})_{Al}//(0001)_{Cd}$, $(111)_{Al}//(\bar{4}403)_{Cd}$ and $(001)_{Al}//(2\bar{2}03)_{Cd}$ facets; the particle marked 3 in Fig. 4.5(b) belonged to variant 3 or 4, with a distorted hexagonal shape bounded by pairs of $(111)_{Al}//(0\bar{4}43)_{Cd}$, $(11\bar{1})_{Al}//(40\bar{4}3)_{Cd}$ and $(001)_{Al}//(20\bar{2}3)_{Cd}$ facets.

4.2.2 Surface energy anisotropy

The shapes of individual Cd particles were monitored as a function of temperature during in-situ step heating in the transmission electron microscope, using specimens of the melt spun Al-4.5wt%Cd alloy equilibrated by annealing for 10^5s at 300°C. Before heating in the electron microscope, specimens were tilted until the electron beam was parallel to an Al ‹110› zone. As shown in Figs. 4.4 and 4.5, with this specimen orientation all the Cd particle facets were parallel to the electron beam, so that the observed separation of each pair of opposite facets was equal to the true separation, and from the Gibbs-Wulff theorem was directly proportional to the facet surface energy (Wulff, 1901, Martin and Doherty, 1976). After careful orientation in this way, specimens were heated in steps of 20-50K up to a maximum temperature of 420°C, with the Cd particle shape recorded at each temperature, after an equilibrating anneal of either 600s below or 180s above the Cd melting point of 321°C. Approximate diffusion calculations indicated that these times were sufficient for equilibration of the 5-120nm Cd particles at all temperatures above about 200°C. This was confirmed by in-situ step cooling experiments, in which the Cd particles changed shape in a reverse sequence to that seen during heating. During step cooling, the different Cd particle shape variants all re-appeared after solidification, with no time lag from insufficient equilibration during annealing.

Fig. 4.6 shows a selected area diffraction pattern and two typical series of bright field images of the Cd particle shapes as a function of temperature during in-situ heating in the transmission electron microscope. The Cd particle shape in series 1 corresponded to variant 3 or 4, ie was similar to the Cd particle marked 3 in Fig. 4.5(b). The Cd particle shape in series 2 corresponded to variant 1, ie was similar to the Cd particle marked 1 in Fig. 4.5(b). Almost identical results were obtained for a number of different Cd particles during heating, and Fig. 4.7 shows the resulting variation of average surface energy anisotropy as a function of temperature. The Cd particle shape was constant between room temperature and the Cd melting point of 321°C, with the $\{100\}_{Al}//\{20\bar{2}3\}_{Cd}$ surface energy on average 40% greater than the $\{111\}_{Al}//\{0001\}_{Cd}$ surface energy, and 10% greater than the $\{111\}_{Al}//\{40\bar{4}3\}_{Cd}$ surface energy. When the Cd particles melted, the $\{100\}_{Al}//\{20\bar{2}3\}_{Cd}$ facet disappeared, and the $\{111\}_{Al}//\{40\bar{4}3\}_{Cd}$ and $\{111\}_{Al}//\{0001\}_{Cd}$ surface energies became equal. However, the $\{111\}_{Al}$ facets did not disappear when the Cd particles melted, and the surface energy anisotropy decreased gradually from 1.1 to 1.0, as the temperature increased above the Cd melting point from 321°C to ~450°C.

4.2.3 Cd particle solidification

Figs. 4.8(a)-(c) show typical Cd solidification exotherms from melt spun Al-4.5wt%Cd obtained at cooling rates of 10, 5 and 2K/min respectively in the differential scanning calorimeter. The Cd particles always solidified with a single sharp exotherm at an onset temperature close to 265°C, but the shape of the Cd particle solidification exotherms depended upon the imposed cooling rate in the calorimeter. Table 4.1 gives full details of the measured onset, peak and end temperatures and peak heights of the Cd particle solidification exotherms, obtained from a series of differential scanning calorimeter experiments similar to those shown in Figs. 4.8(a)-(c). At each cooling rate, the onset, peak and end temperatures of the Cd particle solidification exotherms were reproducible to within +/-0.2-0.3K from specimen to specimen, as can be seen in Figs. 4.8(a)-(c) and Table 4.1. Figs. 4.9(a) and (b) show

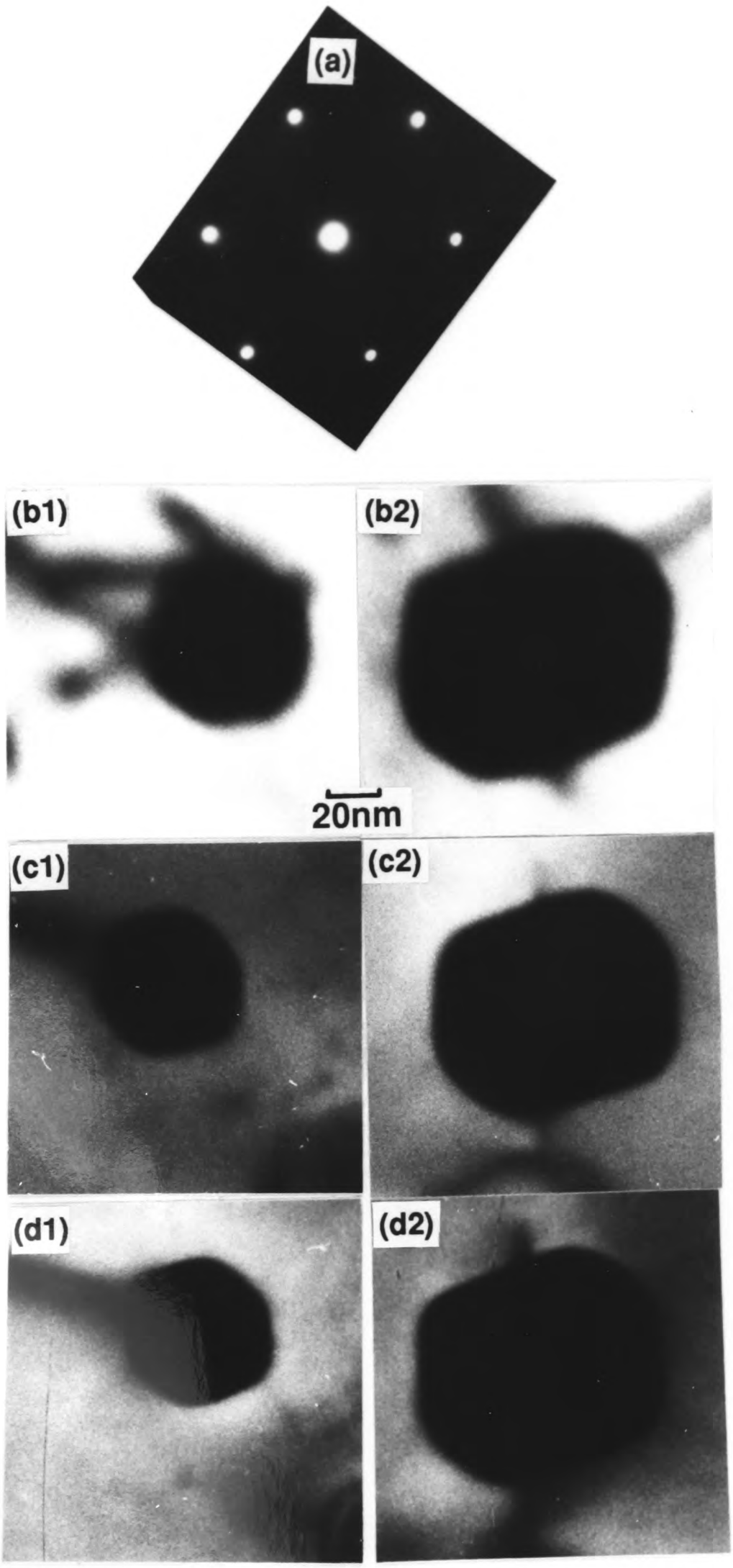


Fig. 4.6 (to be continued)

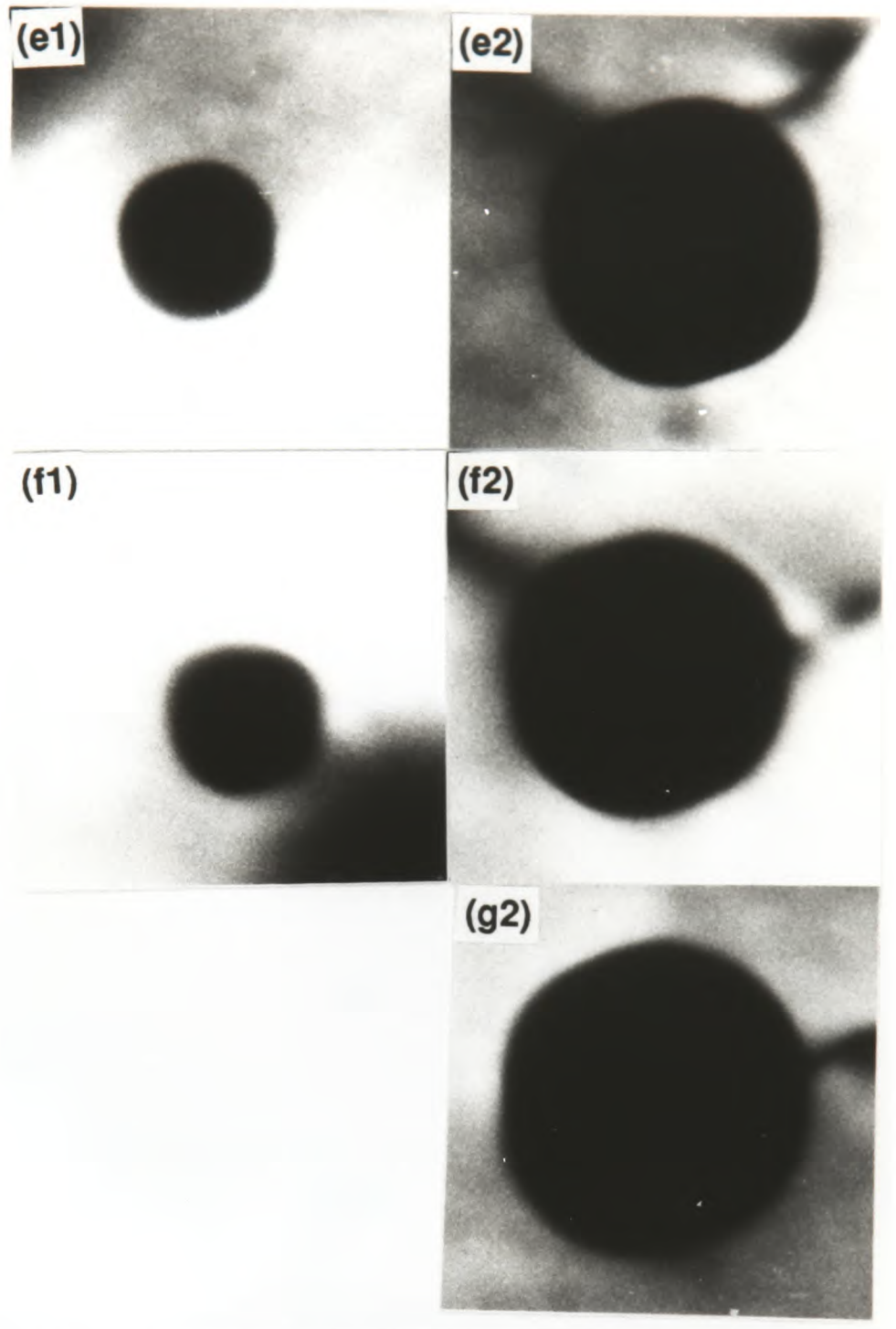


Fig. 4.6: Sequence of transmission electron micrographs showing the variation in shape of two Cd particles in melt spun Al-4.5wt%Cd after heat treatment for 10^5s at 300°C, as a function of temperature during subsequent in-situ heating: (a) selected area diffraction pattern showing [$\bar{1}$10] zone of Al matrix; (b1) and (b2) room temperature; (c1) and (c2) 220°C; (d1) and (d2) 270°C; (e1) and (e2) 320°C; (f1) and (f2); 350°C; (g2) 370°C.

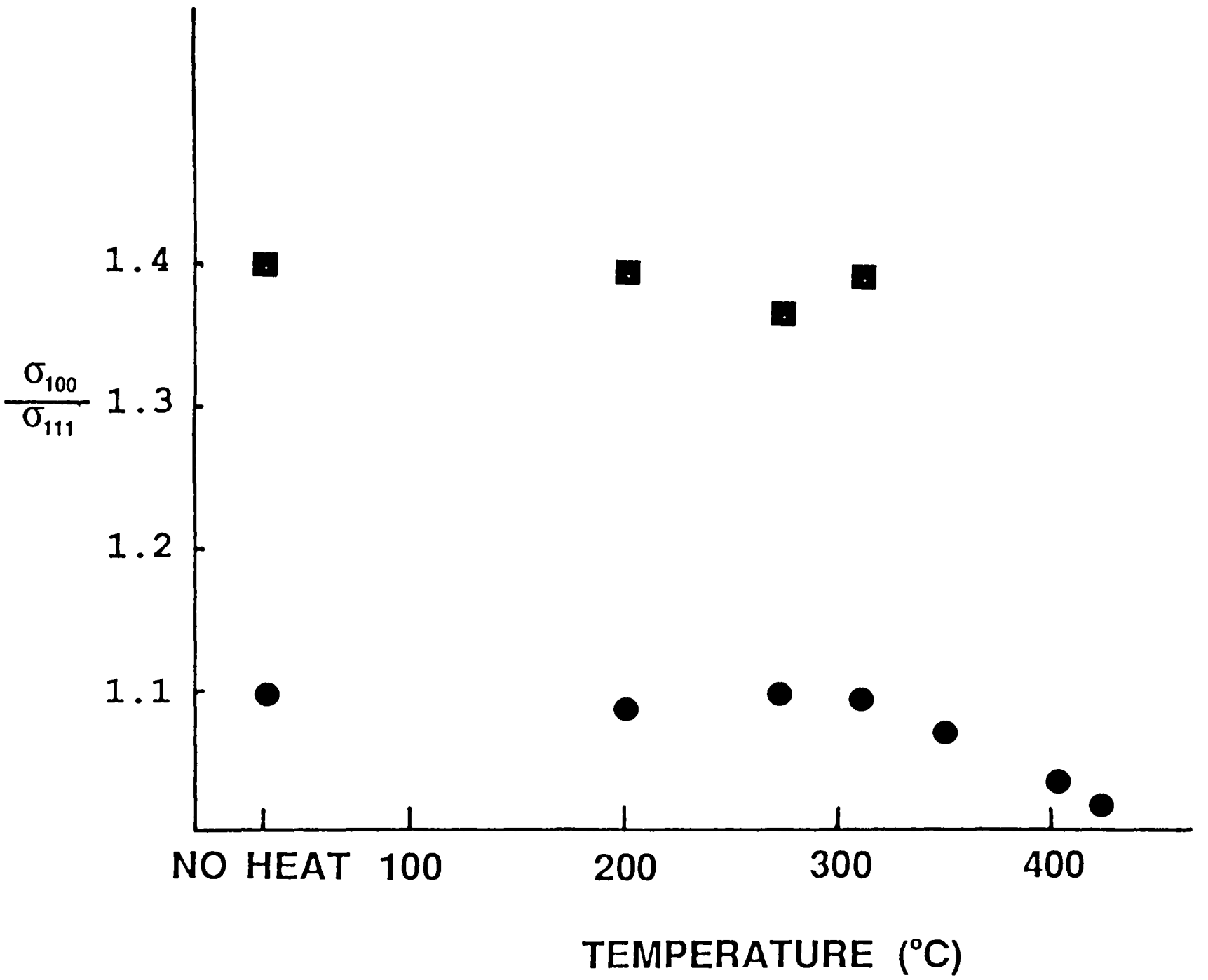


Fig. 4.7: Al-Cd surface energy anisotropy as a function of temperature from measurements of facet separation in melt-spun Al-4.5wt%Cd after heat treatment for 10^5s at 300°C during subsequent in-situ heating in the transmission electron microscope. With squares corresponding to $\{111\}_{Al}//\{0001\}_{Cd}$ facets, and circles correspond to $\{111\}_{Al}//\{40\bar{4}3\}_{Cd}$ facets.

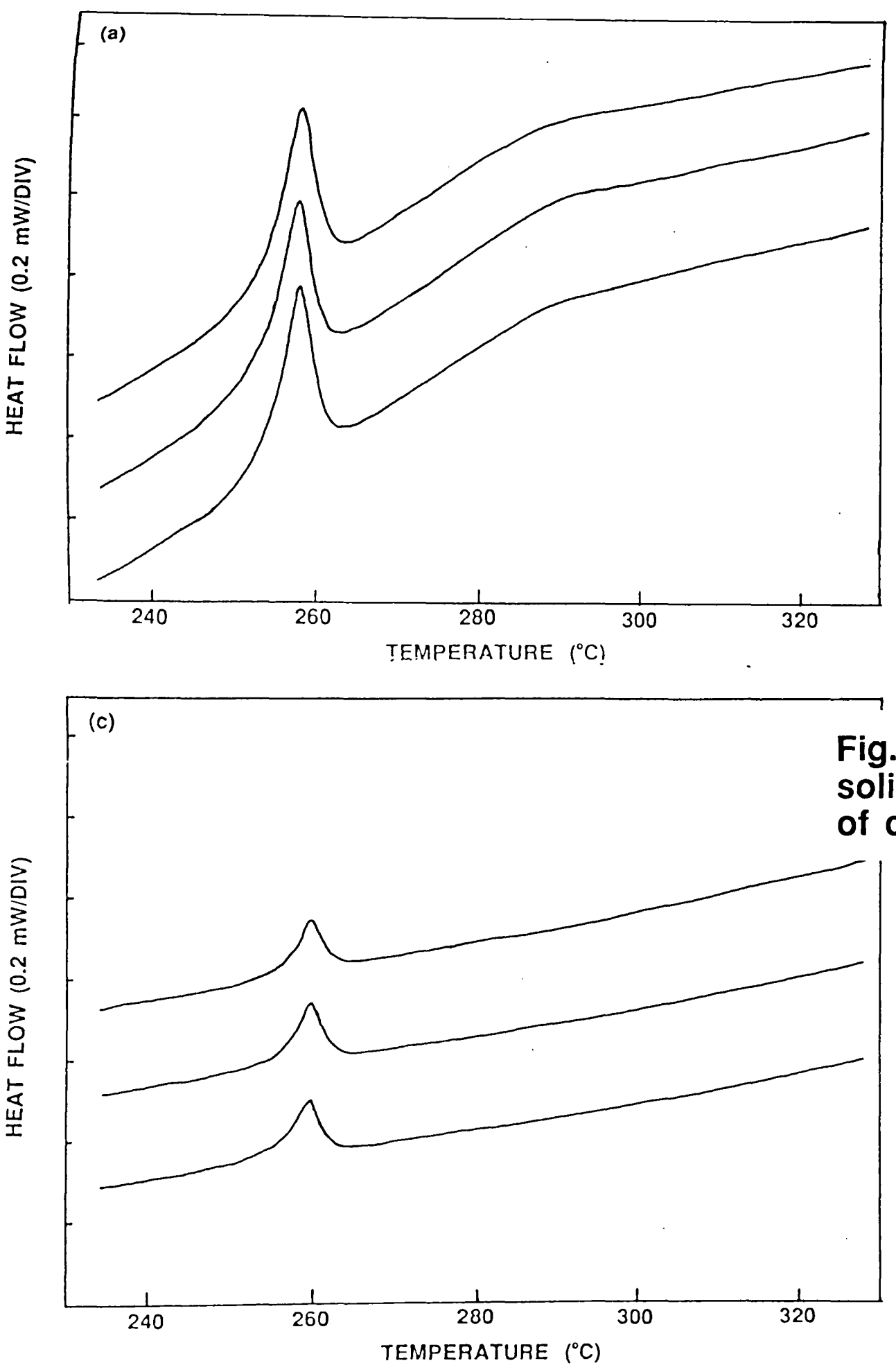


Fig. 4.8: Differential scanning calorimeter traces of Cd particle solidification exotherms from melt spun Al-4.5wt%Cd as a function of cooling rate: (a) 10K/min; (b) 5K/min; and (c) 2K/min.

Table 4.1: Onset, peak and end temperatures and peak heights of Cd particle solidification exotherms during cooling melt spun hypomonotectic Al-4.5wt%Cd in the differential scanning calorimeter

Cooling Rate (K/min)	No. of Specimens	Onset Temperature (°C)	Peak Temperature (°C)	End Temperature (°C)	Peak Height (mW/g)
10.0	8	264.7+/-0.2	258.0+/-0.2	248.1+/-0.3	44+/-2.5
5.0	8	265.0+/-0.3	258.6+/-0.2	249.7+/-0.3	31+/-2.5
2.0	8	265.1+/-0.3	259.5+/-0.2	252.6+/-0.3	14+/-1.0
1.0	5	264.8+/-0.2	260.2+/-0.1	254.5+/-0.3	7.5+/-0.5
0.5	2	265.4+/-0.1	260.6+/-0.1	256.0+/-0.3	4.4+/-0.2

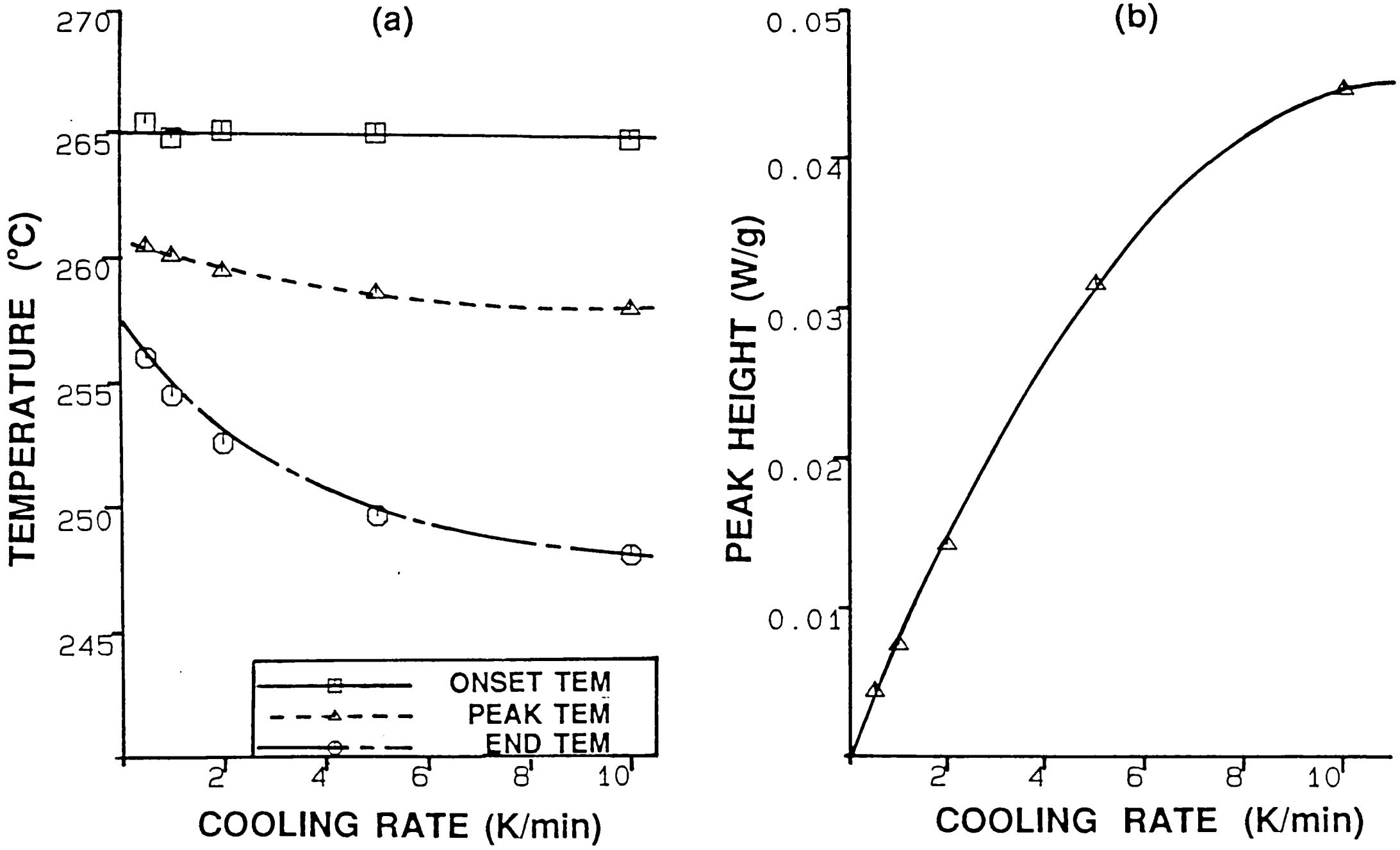


Fig. 4.9 Exothermic peak shape from Cd particle solidification in melt spun Al-4.5wt%Cd as a function of cooling rate in the differential scanning calorimeter: (a) solidification onset, peak and end temperatures; and (b) exothermic peak height.

the variation of the solidification onset, peak and end temperatures and exothermic peak height as functions of cooling rate in the calorimeter. The solidification onset temperature was independent of cooling rate, but the peak and end temperatures decreased and the peak height increased with increasing cooling rate.

4.3 Heterogeneous Nucleation of Solidification of In Particles Embedded in an Al Matrix

4.3.1 Alloy microstructure

Figs. 4.10(a)-(c) show typical transmission electron micrographs of the microstructure of as-melt spun hypomonotectic Al-7wt%In as a function of wheel speed during melt spinning. The microstructure consisted of small faceted 10-200nm diameter In particles homogeneously distributed throughout a matrix of Al. The average In particle size decreased from 40nm to 20nm and the average In particle spacing decreased from 140nm to 70nm, as the wheel speed increased from 7m/s to 65m/s. No obvious coarsening of the In particles was detected after heat treatment for either 600s at 210°C or 10^5s at 145°C.

The In particles were found to have an orientation relationship with the Al matrix which can be described as

$$\{111\}_{Al}//\{111\}_{In}$$

$$\langle 110\rangle_{Al}//\langle 110\rangle_{In}$$

using a face centred tetragonal Bravais lattice for the crystal structure of In.[1] Fig. 4.11 shows a typical electron diffraction pattern with superimposed Al and In ⟨111⟩ zones. There were twelve In particle variants in each

---

[1] Body centred tetragonal and face centred tetragonal Bravais lattices can be used as alternative descriptions of the same crystal structure, with a different unit cell in each case. By convention, the body centred tetragonal Bravais lattice and unit cell are usually selected to describe the crystal structure. For In, the body centred tetragonal c/a ratio is 1.52 and the face centred tetragonal c/a ratio is 1.07 (Hume-Rothery et al, 1969). In the present thesis, the face centred tetragonal Bravais lattice and unit cell are used to describe the crystal structure of In, in order to emphesise the near-cubic atomic structure and simplify the resulting crystallographic relationships.

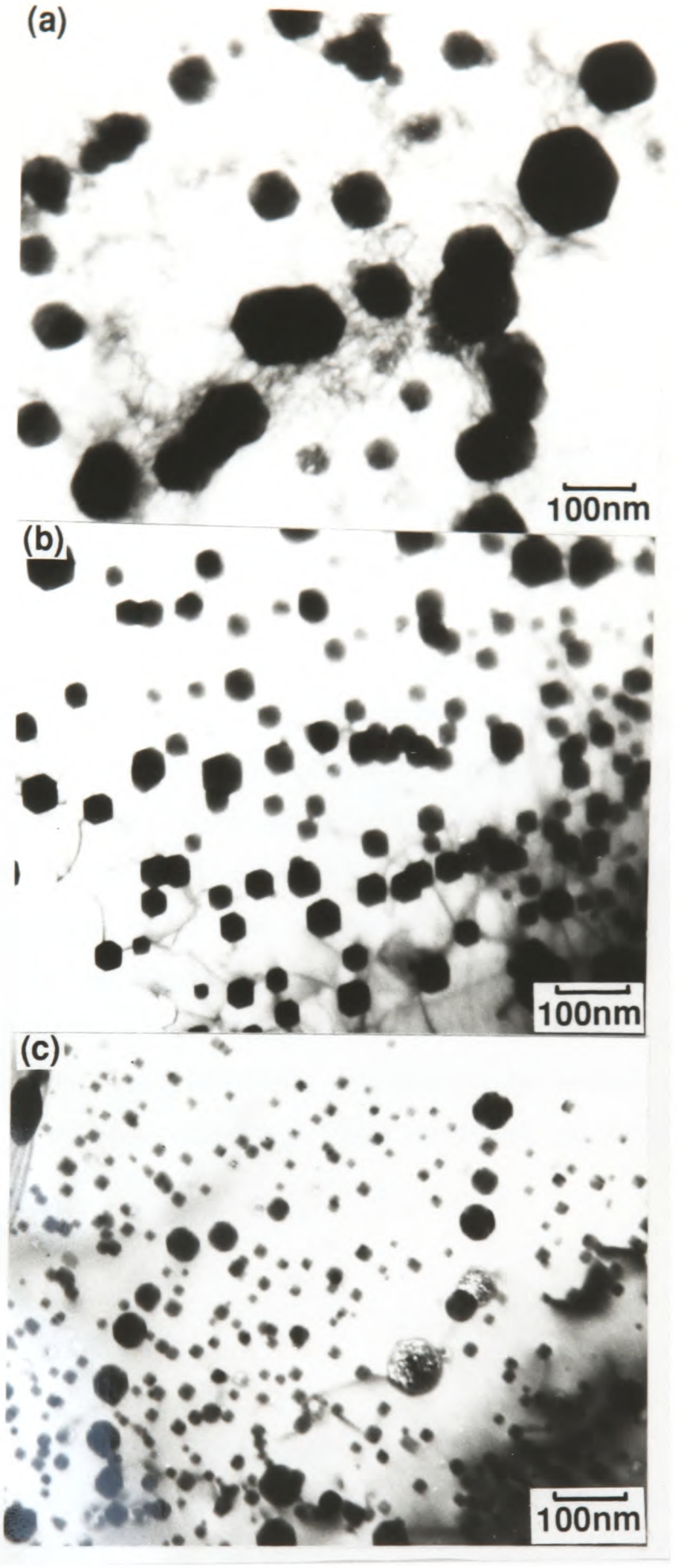


Fig. 4.10: Bright field transmission electron micrographs of as-melt spun Al-7wt%In, showing the homogeneous distribution of In particles at different melt spinning wheel speeds: (a) 7m/s; (b) 14m/s; and (c) 65m/s.

grain of the Al matrix, depending upon which of the {111} planes and ‹110› directions were parallel. However, the face centred tetragonal In crystal structure is very nearly cubic, with a c/a ratio of 1.07. Individual diffraction spots from the different In particle variants can not therefore easily be distinguished, although the In diffraction spots are relatively diffuse, as shown in Fig. 4.11. The as-melt spun In particle shape was found to be truncated octahedral, bounded by $\{111\}_{Al}$ and $\{100\}_{Al}$ facets, as shown schematically in Fig. 4.12. Figs. 4.13 and 4.14 show typical examples of the distorted hexagonal and octagonal cross sections of the truncated octahedral In particles, obtained with the electron beam parallel to $\langle 110\rangle_{Al}$ and $\langle 001\rangle_{Al}$ zones respectively.

After heat treatment for 600s at 210°C, above the In melting point, there was no change in either the In particle shape or the orientation relationship between the In particles and the Al matrix. However, after heat treatment for 10^5s at 145°C , below the In melting point, the In particles became elongated to increase the surface area and decrease the separation of the two $\{111\}_{Al}//\{111\}_{In}$ facets, as shown schematically in Fig. 4.15. Figs. 4.16 and 4.17 show typical examples of the distorted hexagonal and distorted octagonal cross sections of the equilibrated elongated truncated octahedral In particles, obtained with the electron beam parallel to $\langle 110\rangle_{Al}$ and $\langle 001\rangle_{Al}$ zones respectively.

4.3.2 Surface energy anisotropy

The shapes of individual In particles were monitored as a function of temperature during in-situ step heating in the transmission electron microscope, using specimens of melt spun Al-7wt%In equilibrated by heat treatment for 10^5s at 145°C. Before heating in the electron microscope, the specimens were tilted until the electron beam was parallel to a $\langle 110\rangle_{Al}$ zone. After careful orientation in this way, specimens were heated in steps of 10-20K upto a maximum temperature of 280°C, with the In particle shape recorded

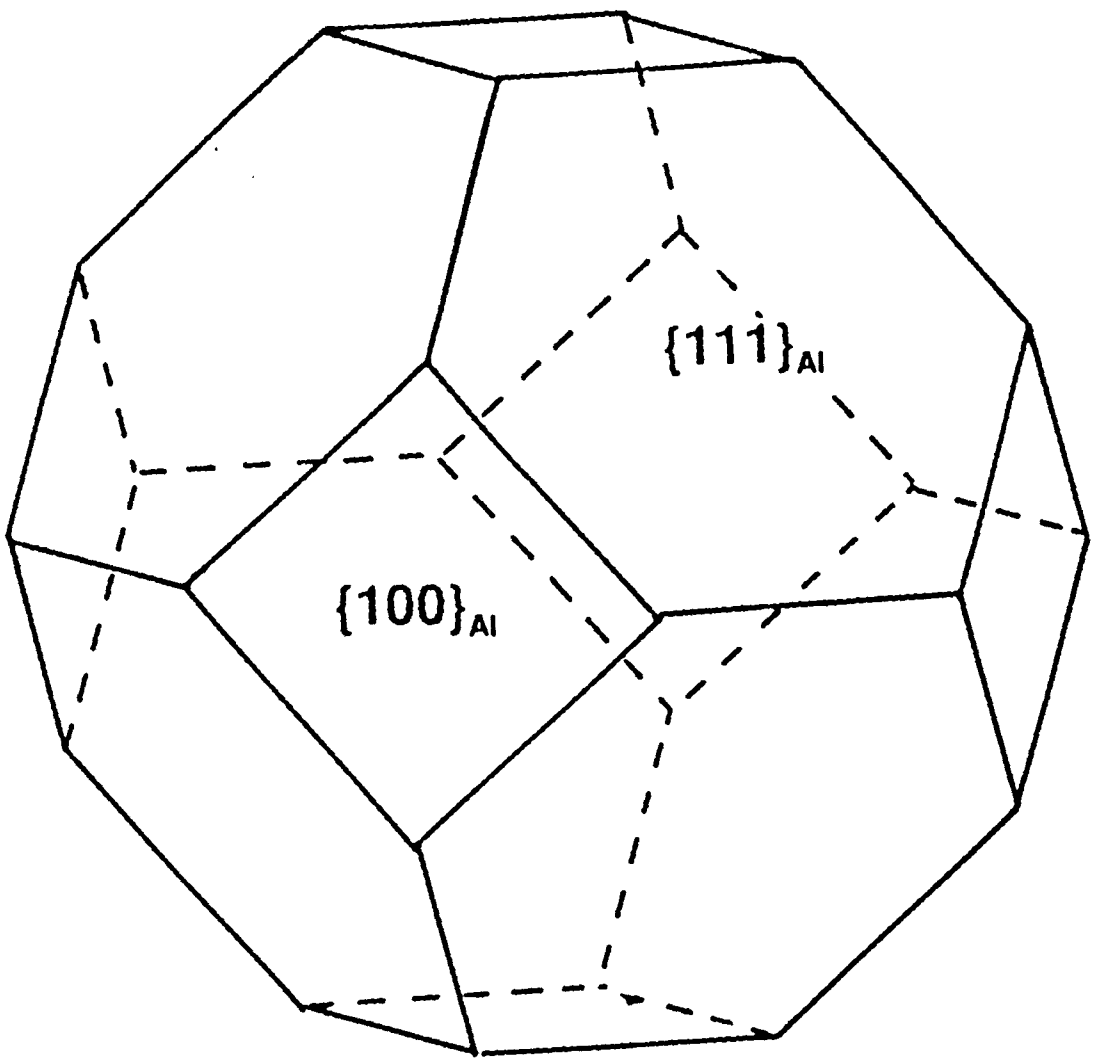


Fig. 4.12: Schematic diagram of the truncated octahedral as-melt spun In particle shape.

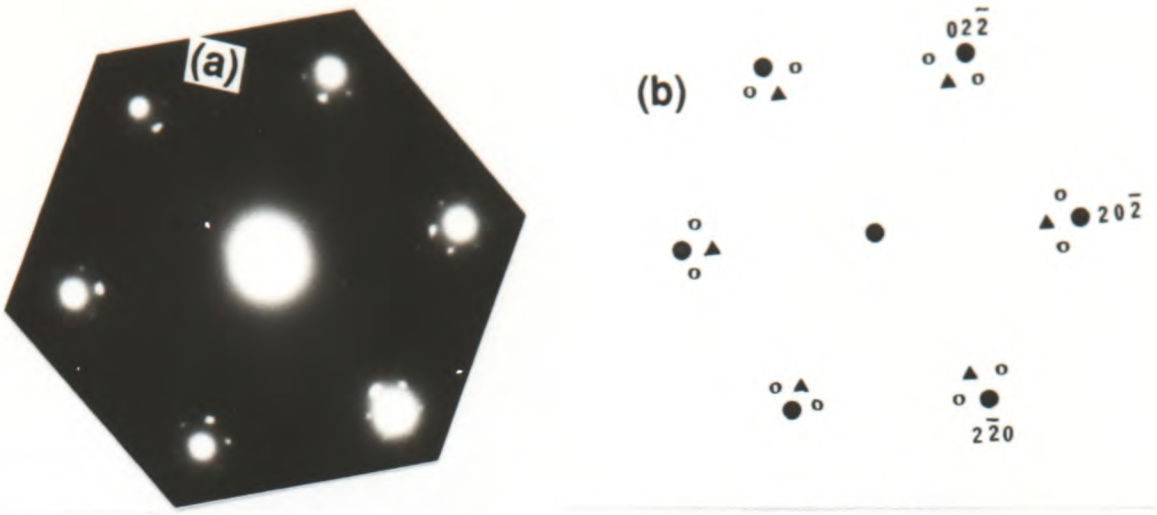


Fig. 4.11: (a) Selected area diffraction pattern showing superimposed <111> Al and In zones from as-melt spun Al-7wt%In; (b) corresponding schematic diffraction pattern. Filled circles correspond to Al diffraction spots, filled triangles correspond to In diffraction spots, and open circles correspond to double diffraction.

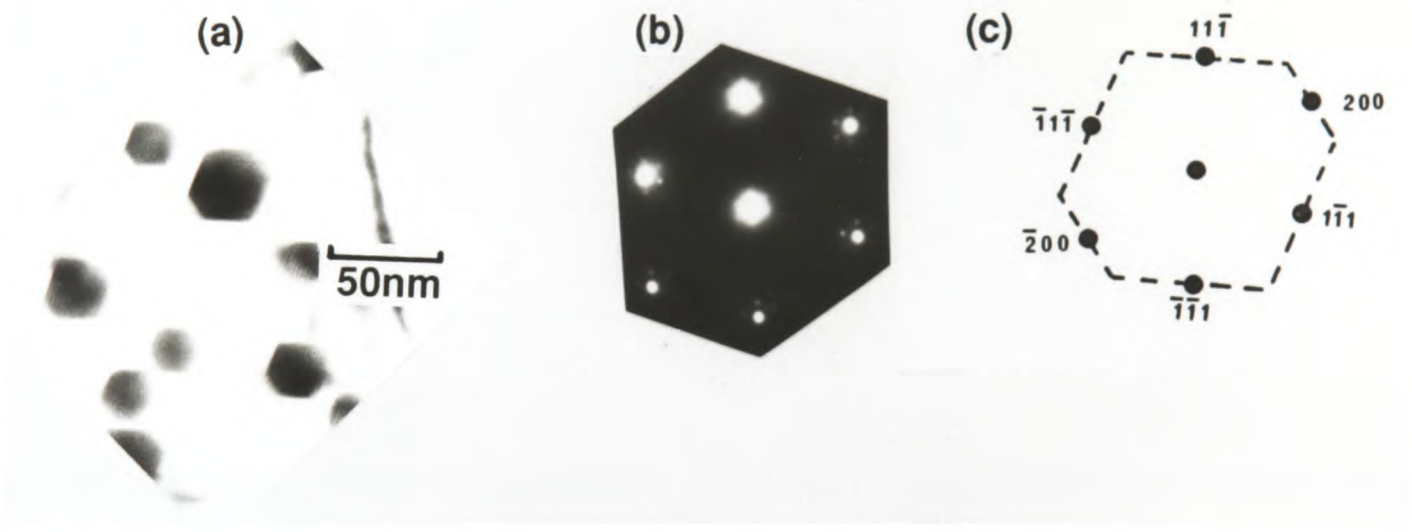


Fig. 4.13: (a) Bright field transmission electron micrograph from as-melt spun Al-7wt%In, (b) corresponding selected area diffraction pattern, and (c) corresponding schematic diffraction pattern, showing the distorted hexagonal cross sectional shape of In particles normal to the $<110>_{Al}$ zone axis.

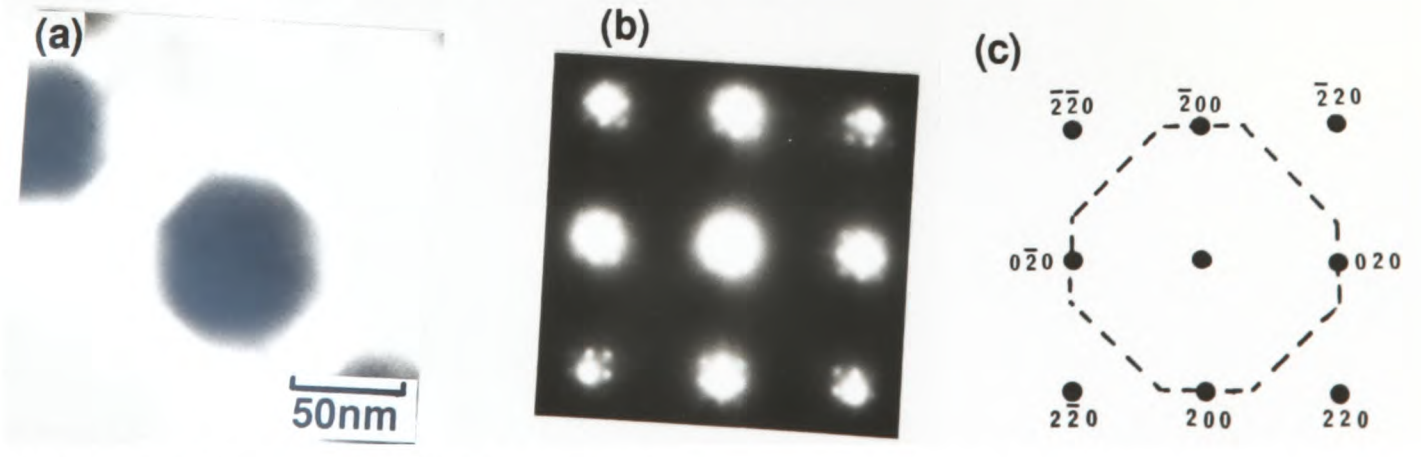


Fig. 4.14: (a) Bright field transmission electron micrograph from as-melt spun Al-7wt%In, (b) corresponding selected area diffraction pattern, and (c) corresponding schematic diffraction pattern, showing the octagonal cross sectional shape of In particles normal to the $<001>_{Al}$ zone axis.

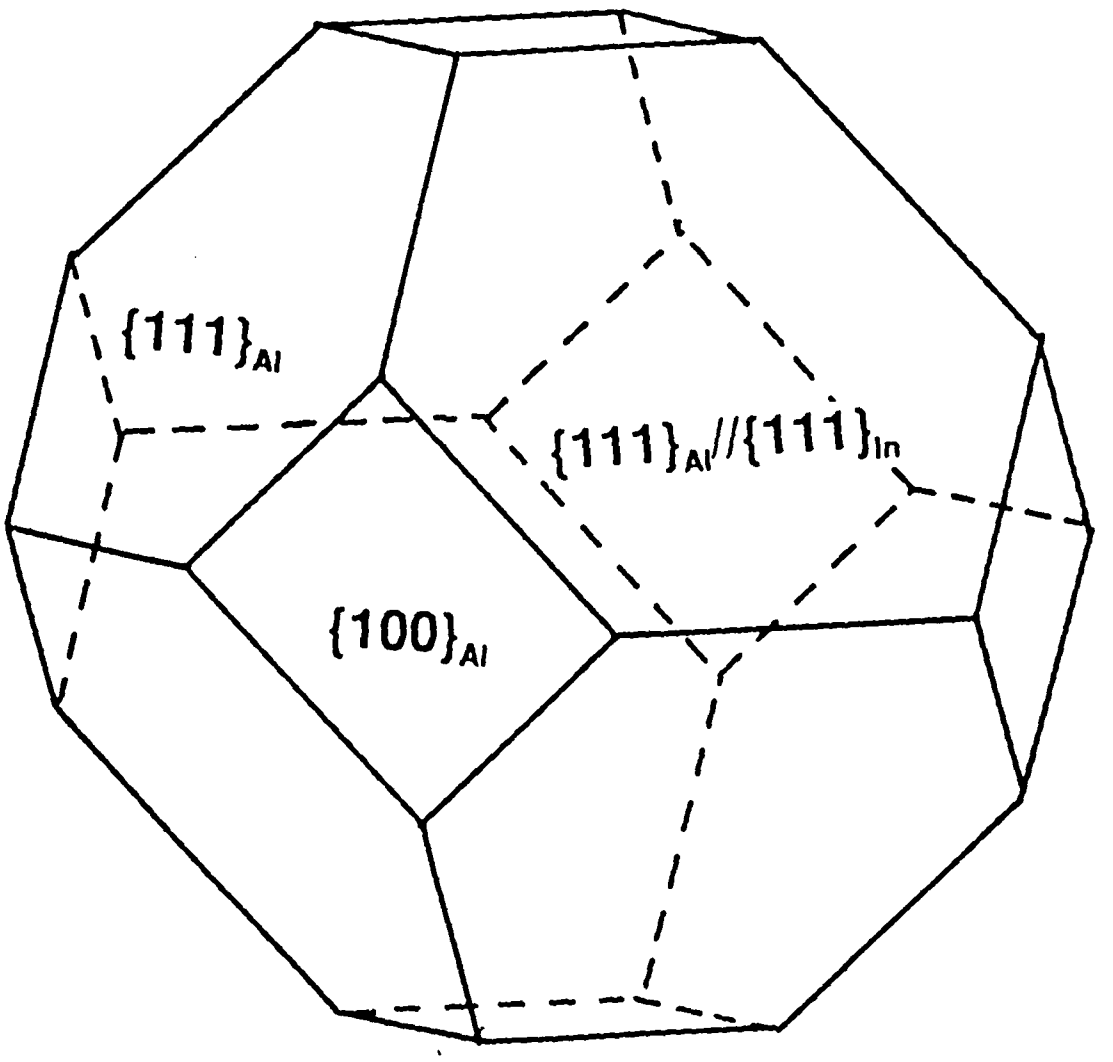


Fig. 4.15: Schematic diagram of the equilibrated elongated truncated octahedral In particle shape.

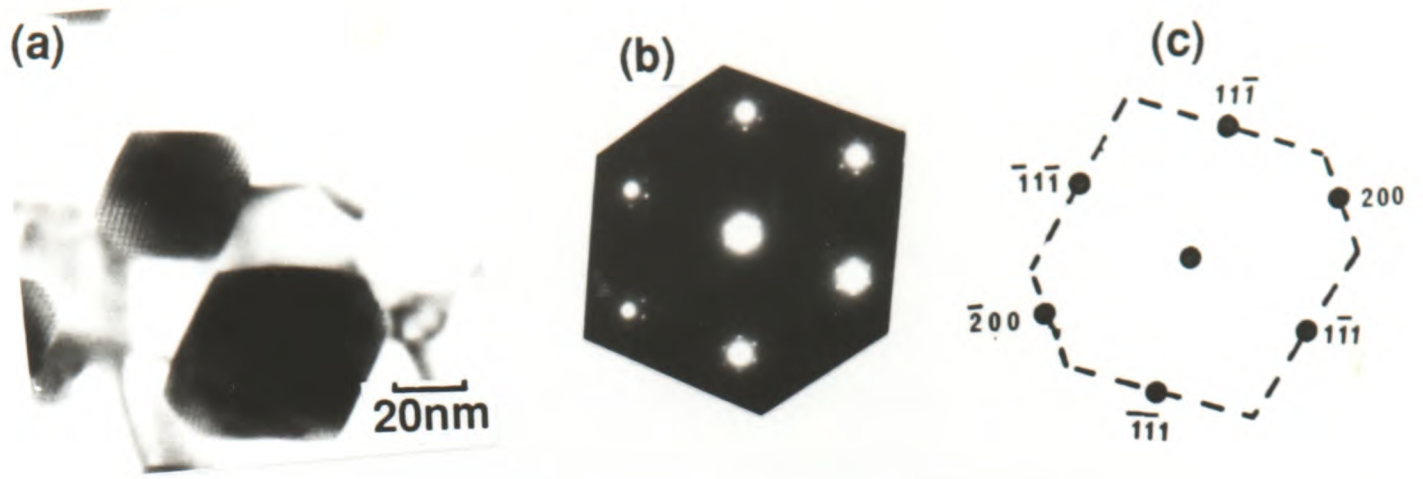


Fig. 4.16: (a) Bright field transmission electron micrograph from melt spun Al-7wt%In after heat treatment for 10^5s at 145°C, (b) corresponding selected area diffraction pattern, and (c) corresponding schematic diffraction pattern, showing the distorted hexagonal cross sectional shape of In particles normal to the $<110>_{Al}$ zone axis.

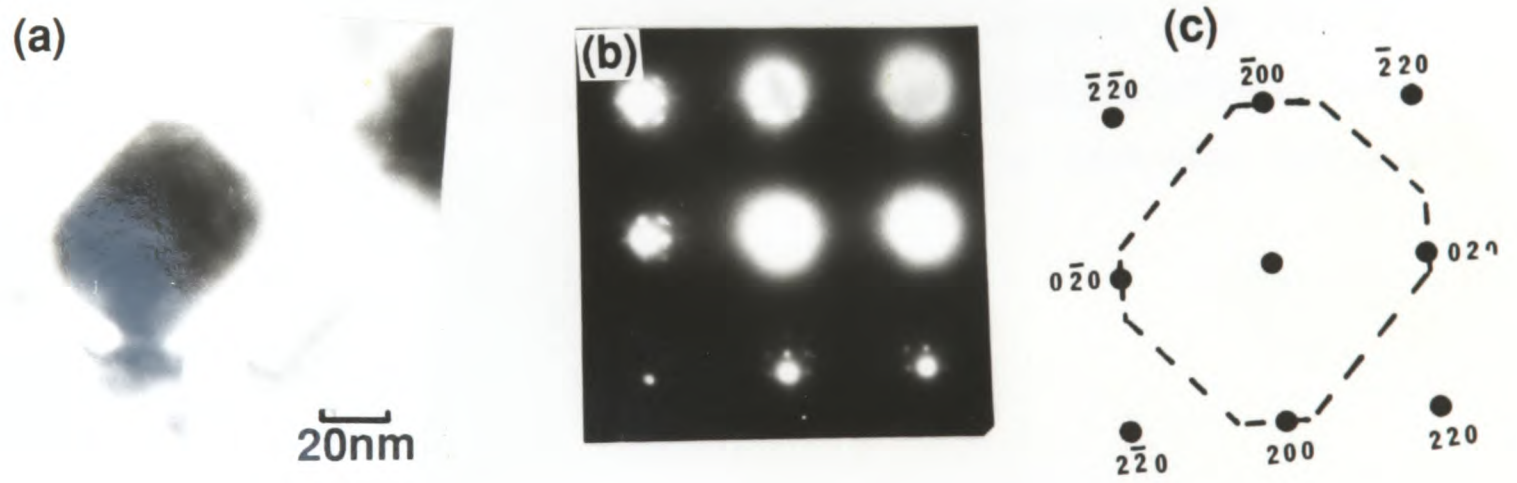


Fig. 4.17: (a) Bright field transmission electron micrograph from melt spun Al-7wt%In after heat treatment for 10^5s at 145°C, (b) corresponding selected area diffraction pattern, and (c) corresponding schematic diffraction pattern, showing the distorted octagonal cross sectional shape of In particles normal to the $<001>_{Al}$ zone axis.

at each temperature after an equilibrating anneal of 900s. Approximate diffusion calculations indicated that this time was sufficient for equilibration of the 10-200nm In particles at all temperatures above about 130°C.

Fig. 4.18 shows a typical series of bright field images of the In particle shape as a function of temperature during in-situ heating in the transmission electron microscope. Almost identical results were obtained for a number of different In particles during heating, except that In particles of different sizes melted at slightly different temperatures. Fig. 4.19 shows the resulting variation of surface energy as a function of temperature averaged over 4 In particles of ~40nm in diameter. The In particle shape was constant between room temperature and the In particle melting temperature, with the $\{100\}_{Al}$ surface energy on average 36% greater than the $\{111\}_{Al}//\{111\}_{In}$ surface energy and 25% greater than the other $\{111\}_{Al}$ surface energy. When the In particles melted, the $\{100\}_{Al}$ facets disappeared and all the $\{111\}_{Al}$ surface energies became equal. However the $\{111\}_{Al}$ facets did not disappear when the In particles melted, and the surface energy anisotropy decreased gradually from 1.25 to 1.0 as the temperature increased above the In particle melting temperature.

4.3.3 In particle solidification

Fig. 4.20 shows typical differential scannning calorimeter traces of In particle solidification exotherms from hypomonotectic Al-7wt%In melt spun at different wheel speeds. The In particle solidification exotherms were independent of the wheel speed during melt spinning, and exhibited a characteristic shape. A broad solidification exotherm extended over approximately 10-12K below the In equilibrium melting point of 156°C, followed by a sharp solidification exotherm at an onset temperature of approximate 143°C, ie. at an undercooling of 13K below the In melting point. Table 4.2 gives full details of the measured onset, peak and end temperatures and peak heights of the In particle solidification exotherms, obtained from a series

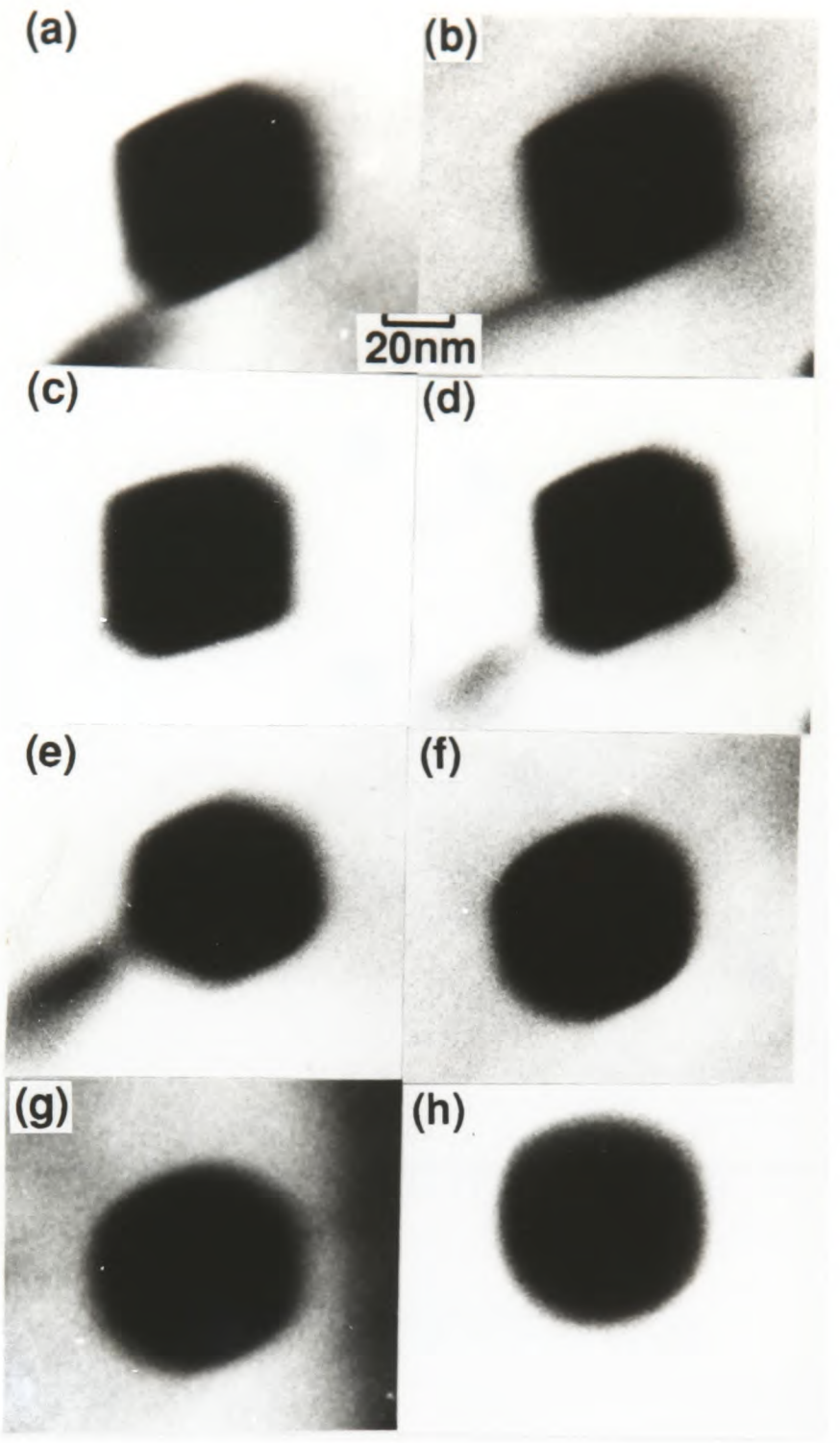


Fig. 4.18: Sequence of transmission electron micrographs showing the variation in shape of In particles in melt spun Al-7wt%In after heat treatment for 10^5s at 145°C, as a function of temperature during subsequent in-situ heating: (a) room temperature; (b) 135°C; (c) 145°C; (d) 160°C; (e) 170°C; (f) 190°C; (g) 215°C; (h) 235°C.

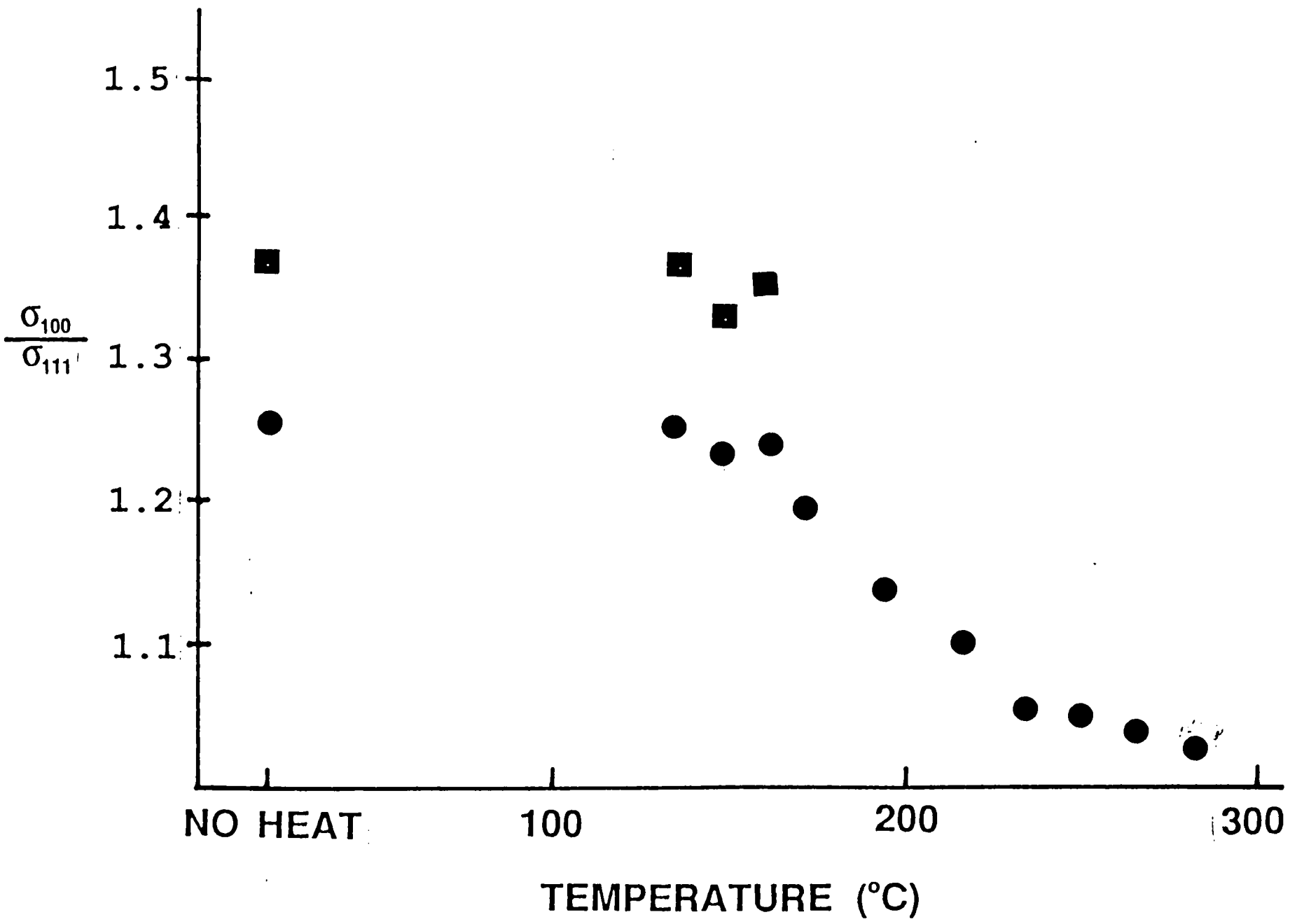


Fig. 4.19: Al-In surface energy anisotropy as a function of temperature from measurements of facet separations in melt spun Al-7wt%In after heat treatment for 10^5s at 300°C, during subsequent in-situ heating in the transmission electron microscope. Filled squares correspond to the $\{111\}_{Al}//\{111\}_{In}$ facets and filled circles correspond to the other $\{111\}_{Al}$ facets.

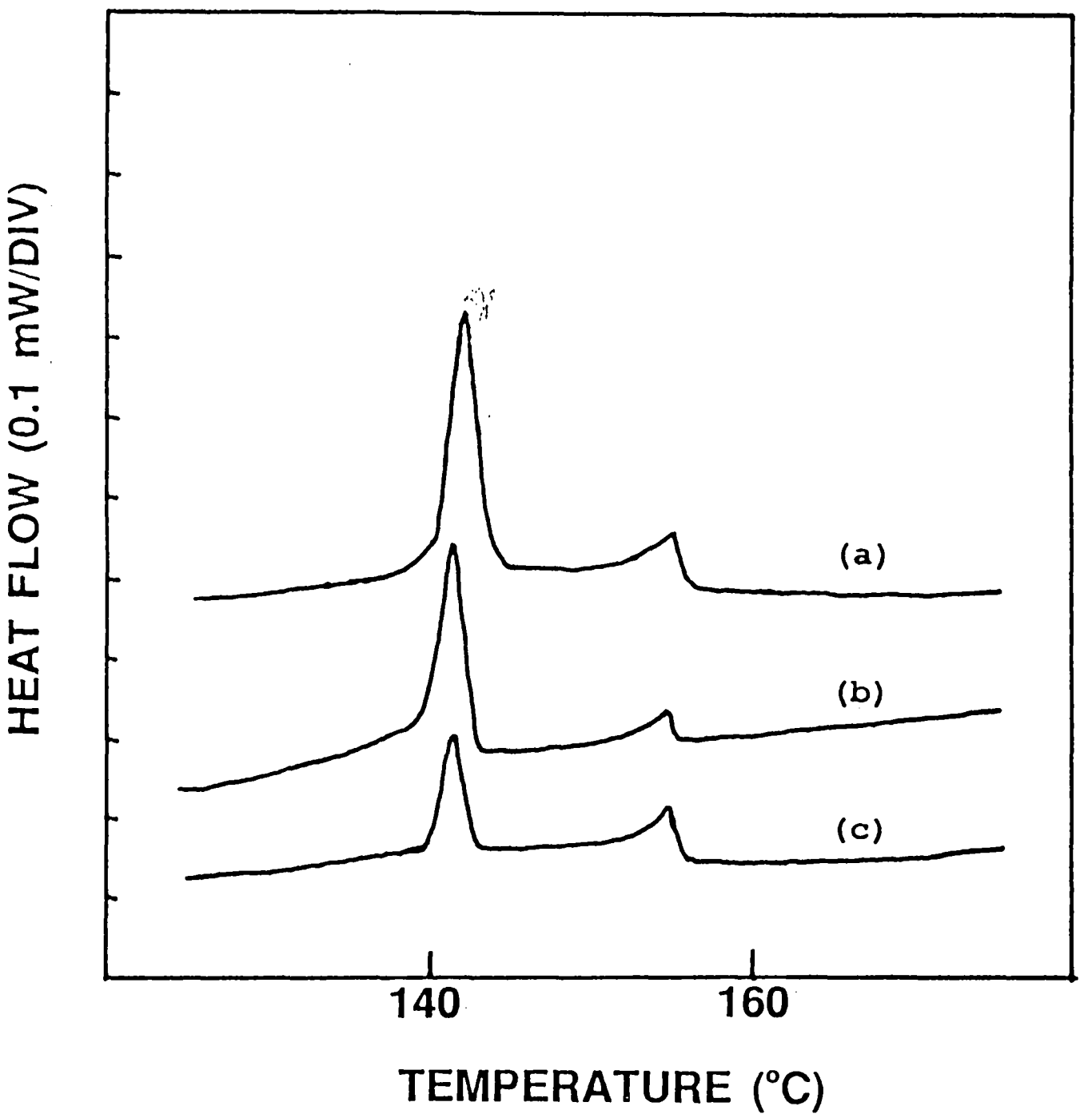


Fig. 4.20: Differential scanning calorimeter traces of In particle solidification exotherms from Al-7wt%In melt spun with different wheel speeds: (a) 7.0m/s; (b) 14m/s; and (c) 65m/s.

Table 4.2: Onset, peak and end temperatures and peak heights of In particle solidification exotherms during cooling melt spun hypomonotectic Al-7wt%In in the differential scanning calorimeter.

CR (K/min)	No.	Sharp Exotherms				Broad Exotherms		
		T_{on}(°C)	T_p(°C)	T_{end}(°C)	PH(mW/g)	T_{on}(°C)	T_p(°C)	PH(mW/g)
2.0	5	143.3+/-0.2	140.6+/-0.1	126.4+/-0.5	15+/-3	154.6+/-0.2	153.6+/-0.1	4.0+/-0.5
1.0	6	143.3+/-0.3	141.1+/-0.2	131.0+/-0.5	9.0+/-0.5	154.9+/-0.2	153.9+/-0.1	2.6+/-0.5
0.5	3	143.3+/-0.2	141.4+/-0.5	134.5+/-0.5	5.0+/-0.2	155.0+/-0.2	154.0+/-0.1	1.6+/-0.2

CR: Cooling Rate
No.: Number of Specimens
T_{on}: Onset Temperature
T_p: Peak Temperature
T_{end}: End Temperature
PH: Peak Height

of differential scanning calorimeter experiments similar to those shown in Fig. 20. At same cooling rate, the onset, peak and end temperatures of the sharp In particle solidification exotherm were reproducible to within +/-0.3-0.4K, as can be seen in Table 4.2. The solidification onset temperature was independent of cooling rate, but the peak and end temperatures decreased and peak height increased with increasing cooling rate, as shown in Table 4.2.

4.4 Heterogeneous Nucleation of Solidification of Pb Particles Embedded in an Al matrix

4.4.1 Alloy microstructure

Fig. 4.21 shows a typical transmission electron micrograph of the microstructure of as-melt spun hypermonotectic Al-5wt%Pb. The microstructure consisted of a bimodal distribution of small faceted Pb particles embedded in an Al matrix. The smaller Pb particles ranged from 5-10nm in diameter and the larger Pb particles ranged from 50-100nm in diameter. Figs. 4.22(a) and (b) show a selected area diffraction pattern of ‹110› Al and Pb zones and corresponding transmission electron micrograph from as-melt spun hypermonotectic Al-5wt%Pb respectively. Fig. 4.22(c) shows the schematic analysis of the diffraction pattern. These results are in good agreement with Moore et al's results (1987), and indicated that Pb particles exhibited a cube-cube orientation relationship with the Al matrix and a truncated octahedral shape bounded by {100} and {111} facets as shown schematically in Fig. 4.12. After heat treatment for 600s at 380°C, above the Pb melting point, there was no change in either the Pb particle shape or the orientation relationship between the Pb particles and Al matrix.

4.4.2 Pb particle solidification

Figs. 4.23(a)-(c) show typical Pb solidification exotherms from melt spun Al-5wt%Pb obtained at cooling rates of 10, 5 and 2K/min respectively in the differential scanning calorimeter. The Pb particles always solidified with a

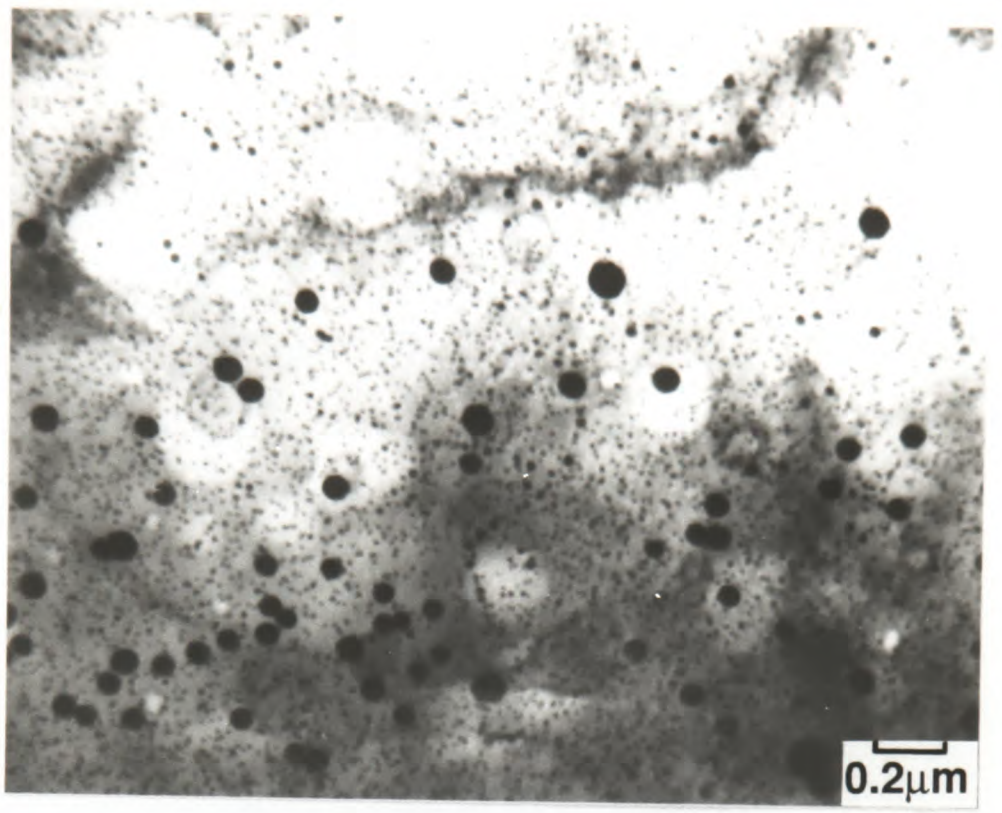


Fig. 4.21: Bright field transmission electron micrograph of the microstructure of as-melt spun hypermonotectic Al-5wt%Pb, showing a bi-modal distribution of Pb particles embedded in an Al matrix.

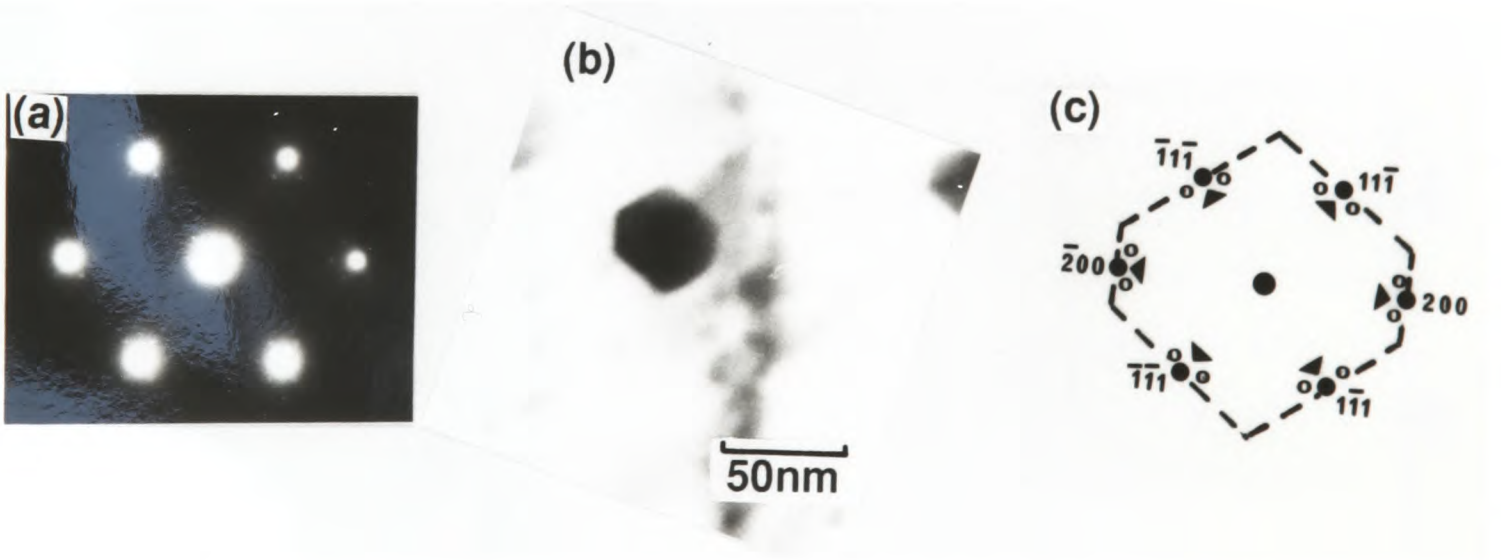


Fig. 4.22: (a) Selected area diffraction pattern from as-melt spun Al-5wt%Pb showing superimposed [011] zones from the Al matrix and the Pb particles; (b) bright field transmission electron micrograph corresponding to (a), showing the distorted hexagonal cross section of Pb particles perpendicular to the [011] Al and Pb zone axis; and (c) schematic diffraction pattern and Pb particle cross section.

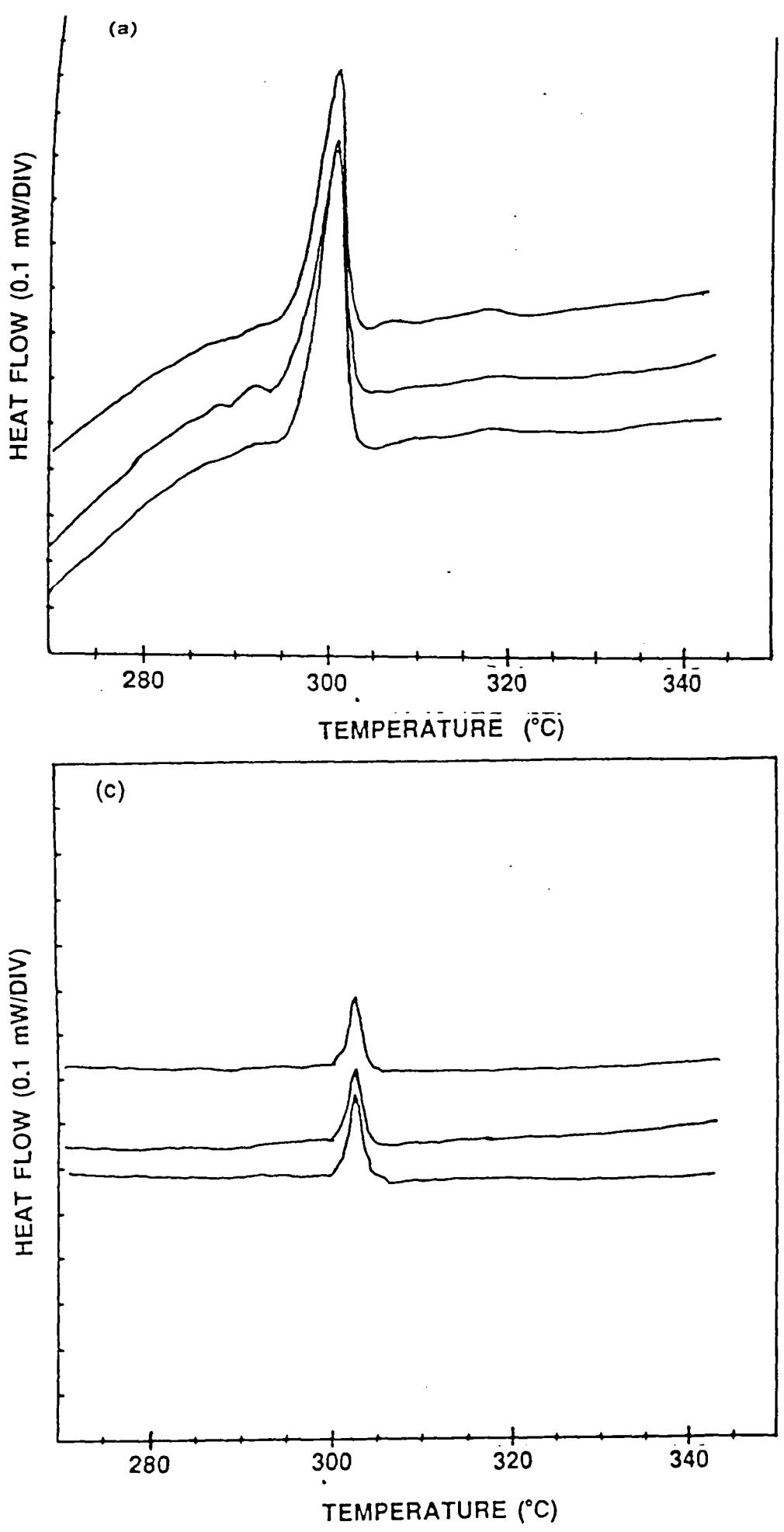


Fig. 4.23: Differential scanning calorimeter traces of Pb particl solidification exotherms from melt spun Al-5wt%Pb as a functio of cooling rate: (a) 10K/min; (b) 5K/min; and (c) 2K/min.

single sharp exotherm at an onset temperature close to 305°C, but the shape of Pb particle solidification exotherms depended upon the imposed cooling rate in the calorimeter. Table 4.3 gives full details of the measured onset, peak and end temperatures and peak heights of the Pb particle solidification exotherms, obtained from a series of differential scanning calorimeter experiments similar to those shown in Figs. 4.23(a)-(c). At each cooling rate, the onset, peak and end temperatures of the Pb particle solidification exotherms were reproducible to within +/-0.2-0.3K from specimen to specimen, as can be seen in Figs. 4.23(a)-(c) and Table 4.3. Figs. 4.24(a) and (b) show the variation of solidification onset, peak and end temperatures and exothermic peak height as functions of cooling rate in the calorimeter. The solidification onset temperature was independent of cooling rate, but the peak and end temperatures decreased and the peak height increased with increasing cooling rate.

4.5 Discussion

4.5.1 Alloy microstructures

The rapidly solidified microstructure of melt spun hypermonotectic Al-5wt%Pb has been discussed in details by Moore (1986), and the following discussion on microstructural features is mainly concerned with melt spun hypomonotectic Al-4.5wt%Cd and Al-7wt%In. The rapidly solidified microstructures of melt spun hypomonotectic Al-4.5wt%Cd and Al-7wt%In are shown in Figs. 4.1 and 4.10, and correspond to a solidification sequence which can be described as follows:

(1) Monotectic solidification: For compositions of 4.2wt%Cd and 7.2wt%In, the gap between the liquidus and monotectic temperatures is less than 10K, as shown in the phase diagrams of Fig. 4.25 (Massalski et al, 1986). During rapid solidification, primary Al dendritic solidification is either suppressed completely or limited to an insignificant extent. On cooling below the monotectic temperature (650°C for Al-4.5wt%Cd and 639°C for Al-7wt%In) the liquid solidifies at high speed by a duplex monotectic reaction, producing

Table 4.3: Onset, peak and end temperatures and peak height of Pb particles soldification exotherms during cooling melt spun hypermonotectic Al-5wt%Pb in the differential scanning calorimeter

Cooling Rate (K/min)	No. of Specimens	Onset Temperature (°C)	Peak Temperature (°C)	End Temperature (°C)	Peak Heights (mW/g)
10.0	5	304.6+/-0.2	300.6+/-0.2	294.0+/-0.3	34+/-4
5.0	7	304.7+/-0.3	301.5+/-0.2	295.8+/-0.3	19+/-3
2.0	5	305.0+/-0.2	302.3+/-0.1	299.8+/-0.3	10+/-2
1.0	5	304.7+/-0.3	302.9+/-0.1	300.6+/-0.3	7+/-1
0.5	4	304.8+/-0.3	303.2+/-0.1	301.4+/-0.3	3.0+/-0.5

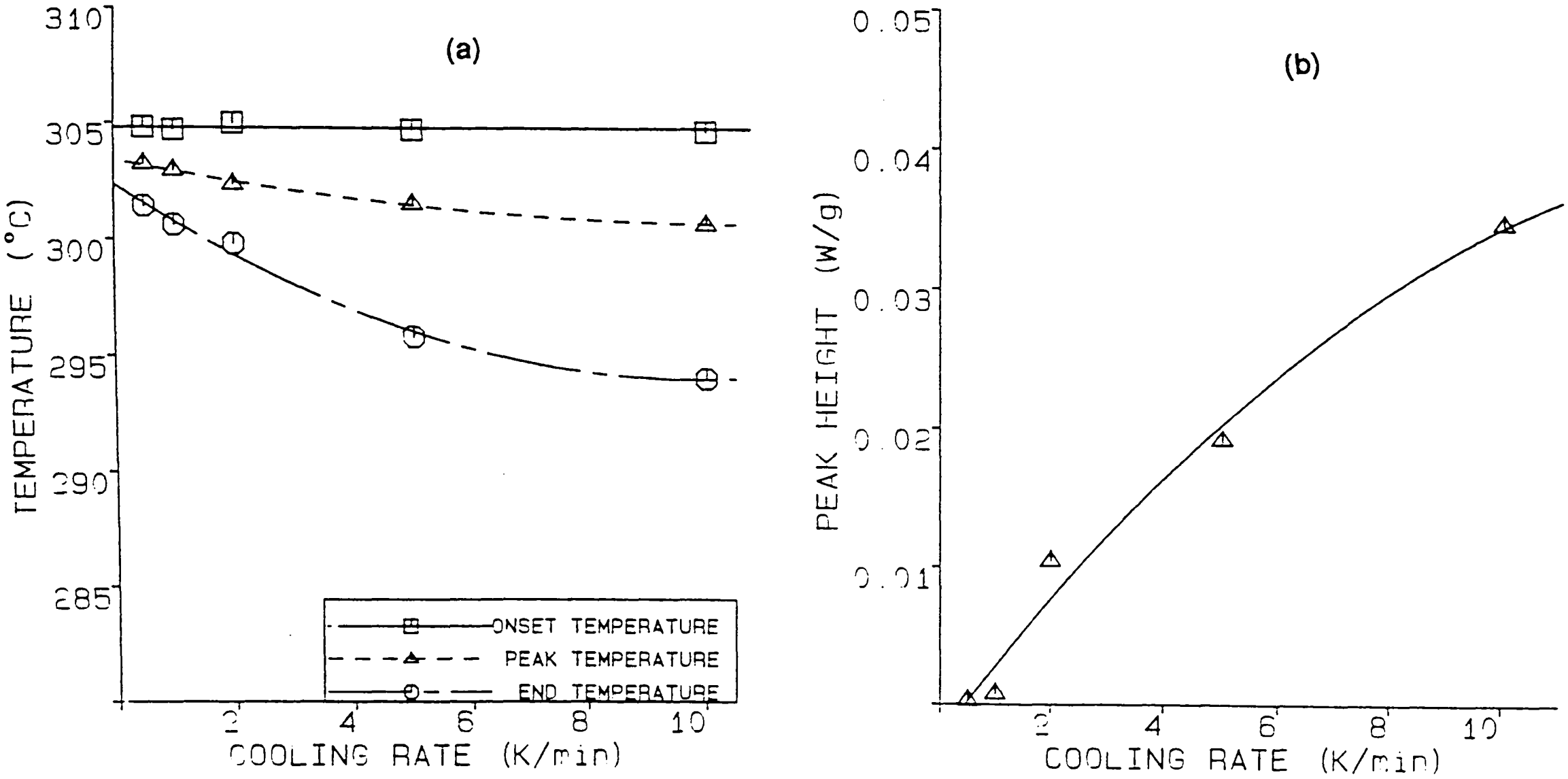


Fig. 4.24: Exotherm peak shape from Pb particle solidification in melt spun Al-5wt%Pb as a function of cooling rate in the differential scanning calorimeter: (a) solidification onset, peak and end temperatures: and (b) exothermic peak height.

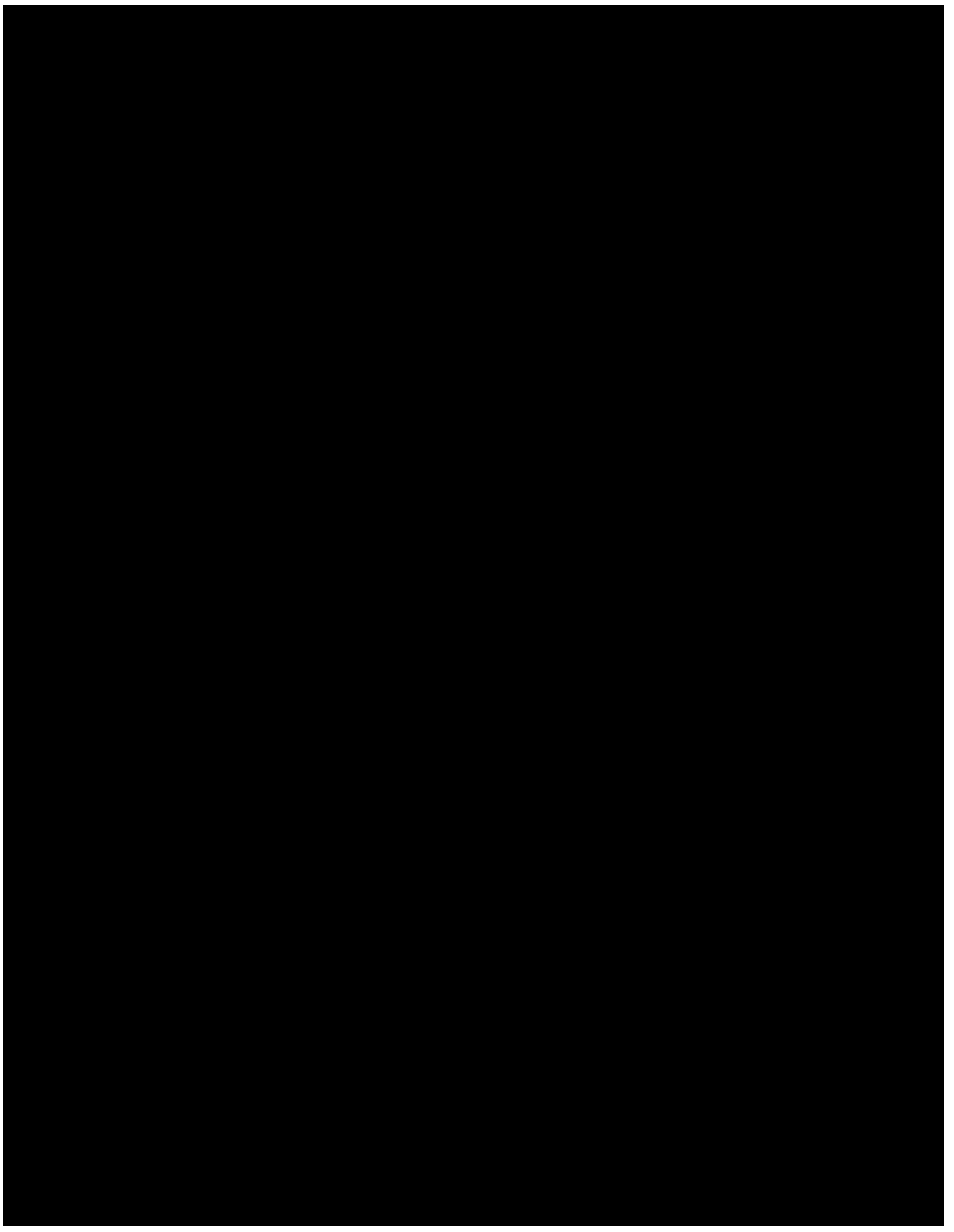


Fig. 4.25: Binary phase diagrams of (a) Al-Cd and (b) Al-In systems (After Massalski et al, 1986).

small 5-200nm sized Cd-1.3wt%Al or In-3wt%Al liquid droplets embedded in a matrix of solid Al. As shown in Fig. 4.10, the average droplet size decreases with increasing wheel speed and solidification rate during melt spinning. The irregular Cd and In particle monotectic microstructures in Figs. 4.1 and 4.10 are consistent with a relatively low value of ~100Ks/mm^2 for the ratio of thermal gradient to solidification velocity G/V during melt spinning, estimated from

$$G/V=(T-Tr)t/y^2 \qquad (4.1)$$

where T is the melt temperature, Tr is room temperature, y is the section size and t is the solidification time (Derby and Favier, 1983, Derby, 1984).

(2) Droplet coarsening: During cooling from the monotectic temperature to the eutectic temperature (320°C for Al-4.5wt%Cd and 156°C for Al-7wt%In), the average diffusion distance X of Cd and In in solid Al is approximately 10nm, estimated from:

$$X^2=4Dt \qquad (4.2)$$

where D is the average Cd or In diffusivity in solid Al and t is the cooling time (Shewmon, 1963). The diffusion distance is relatively small compared with the corresponding interparticle spacings of 140nm for Cd particles and 70-140nm for In particles. Thus, there is insufficient time for significant particle coarsening to take place. During cooling from the monotectic temperature to the eutectic temperature, the solubility of Al in the Cd rich and In rich droplets decreases to zero by deposition on the surrounding Al matrix.

(3) Droplet solidification: On cooling below the eutectic temperature, the Cd and In droplets solidify by heterogeneous nucleation on the {111} facets of the surrounding Al matrix as shown in Figs. 4.6 and 4.18, with epitaxial orientation relationships of $\{111\}_{Al}//\{0001\}_{Cd}$ and $\langle 110\rangle_{Al}//\langle 11\bar{2}0\rangle_{Cd}$ as shown in Fig. 4.3, and $\{111\}_{Al}//\{111\}_{In}$ and $\langle 110\rangle_{Al}//\langle 110\rangle_{In}$ as shown in Fig. 4.11. For Al-4.5wt%Cd, four Cd particle variants are formed in each Al grain, depending upon which of the four $\{111\}_{Al}$ planes is parallel to $\{0001\}_{Cd}$. Transmission electron micrographs and electron diffraction patterns such as

Figs. 4.4(a)-(d) show that the resulting solid Cd particles embedded in the Al matrix have a distorted truncated octahedral shape, bounded by six curved $\{100\}_{Al}//\{20\bar{2}3\}_{Cd}$ facets, six curved $\{111\}_{Al}//\{40\bar{4}3\}_{Cd}$ facets and two flat $\{111\}_{Al}//\{0001\}_{Cd}$ facets. For Al-7wt%In, twelve In particle variants are formed in each Al grain, depending upon which of {111} planes and ‹110› zone axis are parallel. Transmission electron micrographs and electron diffraction patterns such as Figs. 4.13 and 4.14 show that the resulting solid In particles embedded in the Al matrix have a truncated octahedral shape, bounded by $\{100\}_{Al}$ and $\{111\}_{Al}$ facets. Details of the particle solidification behaviours are clarified by the differential scanning calorimeter results obtained during subsequent heat treatment, and are discussed further in sections 4.5.3-4.5.5.

4.5.2 Surface energy anisotropy

As shown in Figs. 4.4, 4.5 and 4.12-4.17, the Cd and In particles become further elongated after annealing in the solid state, indicating that the as-melt spun particle shapes are metastable. Measurements of facet separations during in-situ heating in the transmission electron microscope are shown in Figs. 4.6 and 4.7 for the Cd particles and Figs. 4.18 and 4.19 for the In particles, and indicate that the small particles can equilibrate quickly during either heating and melting or cooling and solidification, even when the temperature changes rapidly. Liquid Cd and In particle shapes embedded in an Al matrix above the Cd and In melting points are very similar to each other and also similar to those seen for other liquid particles embedded in an Al matrix (Moore et al, 1987, Kim and Cantor, 1990, Camel et al, 1980). Thus, the solid Al-liquid Cd and solid Al-liquid In surface energy anisotropies are controlled by the crystallography and atomic structure of the different Al surfaces at temperatures just above the Cd and In melting points.

The anisotropy of solid Al-solid Cd surface energy in melt spun Al-4.5wt%Cd is complicated, because of the complicated disordered structure of some of the curved facets which bound the Cd particles. The anisotropy of solid Al-solid In surface energy in melt spun Al-7wt%In is simple, because the In

particles are bounded by low index facets. The In particle surface energy anisotropy can therefore be estimated by using a simple near-neighbour bond energy calculation applied previously by Sundquist (1964) to solid-vapor surface energies in fcc and bcc metals, and by Moore et al (1987) to solid Al-solid Pb surface energy in melt spun Al-5wt%Pb. The surface internal energy u_{hkl} of a general {hkl} solid Al-solid In facet can be estimated from:

$$2u_{hkl} = n_{hkl}b_{hkl}(2e_{Al\text{-}In} - e_{Al\text{-}Al} - e_{In\text{-}In}) \qquad (4.3)$$

where n_{hkl} is the number of surface atoms per unit area, b_{hkl} is the number of near-neighbour bonds per surface atom, and $e_{Al\text{-}In}$ $e_{Al\text{-}Al}$ and $e_{In\text{-}In}$ are the Al-In, Al-Al and In-In near neighbour bond energies respectively. The ratio of $\{100\}_{Al}/\{111\}_{Al}$ surface energies is therefore given by:

$$u_{100}/u_{111}=n_{100}b_{100}/n_{111}b_{111} \qquad (4.4)$$

For the fcc Al and fct In, $b_{100}=4$, $b_{111}=3$, $n_{100}=1/d^2$ and $n_{111}=2/3^{0.5}d^2$, where d is the near-neighbour separation. Equation (4.4) then gives the $\{100\}_{Al}/\{111\}_{Al}$ anisotropy of surface internal energy as $u_{100}/u_{111}=2/3^{0.5}=1.15$, This is lower than the measured ratio of 1.36 between the $\{100\}_{Al}$ and $\{111\}_{Al}//\{111\}_{In}$ surface energies, because of approximately 2^{o} misorientation between the $\{100\}_{Al}$ and $\{100\}_{In}$ planes.

4.5.3 Particle solidification

Differential scanning calorimeter traces such as in Figs. 4.8, 4.20 and 4.23 give detailed information about the Cd, In and Pb particle solidification kinetics in melt spun Al-4.5wt%Cd, Al-7wt%In and Al-5wt%Pb. The large number of particles ensures reproducibility in the differential scanning calorimeter traces. The small size of the particles ensures that their solidification kinetics are dominated by nucleation, since each particle must be nucleated independently during cooling below the melting point in the differential scanning calorimeter. The particle solidification behaviour in the melt spun alloys can be described as follows. On cooling below the melting point, particles containing catalytic trace impurities nucleate and solidify with a variable undercooling because of the variable catalytic potency of the trace impurities. For the Cd and Pb particles, too few are nucleated by catalytic

trace impurities to be detected in the differential scanning calorimeter. For In particles, the number of the particles which are nucleated by catalytic trace impurities is large enough to be detected in the differential scanning calorimeter, producing a broad exotherm extending upto approximately 10-12K below the equilibrium In melting point as shown in Fig. 4.20. Below a critical temperature, all the particles which have not been nucleated by catalytic trace impurities are nucleated by the surrounding Al matrix, with an epitaxial orientation relationship and a sharp exothermic peak in the differential scanning calorimeter. This critical temperature is 265°C for Cd particles, 143°C for In particles and 305°C for Pb particles. As shown in Figs. 4.6, 4.7, 4.18 and 4.19 and in Moore et al's work (1987), particle nucleation can take place on the {111} Al facets which survive above the Cd, In and Pb melting points.

4.5.4 Nucleation kinetics

The equilibrium melting point of Cd, In and Pb particles in the melt spun alloys may not be the same as the corresponding bulk equilibrium melting points, because of pressure effects caused by a combination of differential thermal contraction, solidification shrinkage and capillarity. However, the particle melting behaviour (presented and discussed in Chapter 6) shows that (a) differential thermal contraction and solidification shrinkage stresses are relieved by a combination of cavitation and vacancy creep, (b) capillarity forces have an insignificant effect, and (c) nucleation of In and Pb melting is delayed kinetically to temperatures above the equilibrium In and Pb melting points for the smallest In and Pb particles.

In the melt spun alloys, the 5-200nm sized particles begin to nucleate and solidify at a critical temperature , i.e. at a critical undercooling below the melting point, as shown in Fig. 4.8 for the Cd particles, Fig. 4.20 for the In particles and Fig. 4.23 for the Pb particles. Complete particle solidification is expected to follow almost instantaneously after nucleation for such small particles at relatively high undercooling. At any temperature

T below the particle melting point, the fraction of solid particles Z is therefore given by the differential equation (Kim et al, 1990):

$$dZ/dt=I(1-Z) \qquad (4.5)$$

where I is the nucleation frequency within each particle. With decreasing temperature below the particle melting point, the particle solidification rate dZ/dt increases with increasing nucleation frequency I, reaches a maximum, and then decreases as the fraction of solid particles Z approaches 1. At a constant cooling rate $\dot{T}$, the particle solidification rate has its maximum value when $d/dT(dZ/dt)=-\dot{T}^{-1}d^2Z/dt^2=0$, which by differentiating equation (4.5) is equivalent to:

$$dI/dt = -\dot{T}\, dI/dT=I^2 \qquad (4.6)$$

Fig. 4.26 shows schematically the heterogeneous nucleation of a spherical cap of solid Cd, In or Pb on a catalytic {hkl} facet of the Al matrix surrounding a liquid particle in the melt spun alloys. The nucleation frequency I within each particle is given by (Turnbull, 1950, Cantor and Doherty, 1979):

$$I = A\exp\{-B/(Tm-T)^2T\} \qquad (4.7)$$

where Tm is the particle melting point, $A=Nc(kT/h)\exp(-Q/kT)$, Nc is the number of potential catalytic nucleation sites per particle, k and h are Boltzmann's and Plank's constants respectively, Q is the activation free energy for transporting an atom of the particle across the solid nucleus-liquid interface, $B=K\sigma_{SL}{}^3Tm^2f(\Theta)/kL^2$, K is a shape factor equal to $16\pi/3$ for a spherical cap shaped nucleus, σ_{SL} is the solid nucleus-liquid surface energy, $f(\Theta) = (2-3\cos\Theta+\cos^3\Theta)/4$, Θ is the contact angle at the solid Al-solid nucleus-liquid triple point as shown in Fig. 2.24, and L is the Cd latent heat of solidification per unit volume.

4.5.5 Contact angle

On differential scanning calorimeter traces such as shown in Fig. 4.8 for Cd particles, Fig. 4.20 for In particles and Fig. 4.23 for Pb particles, the particle solidification rate dZ/dt at each temperature is directly proportional to the measured excess heat flow, i.e. to the height of the

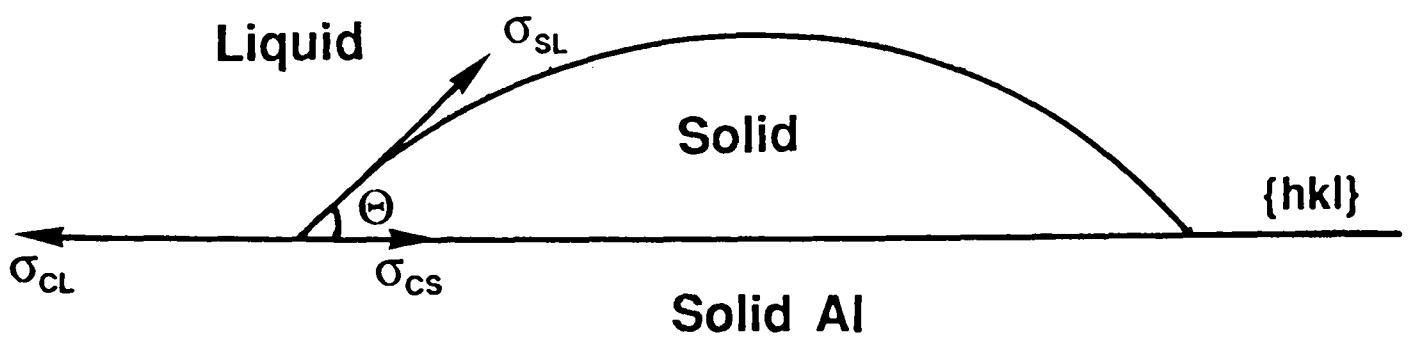


Fig. 4.26: Schematic diagram of the heterogeneous nucleation of particle solidification on a catalytic {hkl} facet of the surrounding Al matrix during heating and cooling of the melt spun Al alloys in the differential scanning calorimeter.

exothermic solidification peak. The fraction of solid particles Z can also be obtained at each temperature by partial integration of the exothermic solidification peak. Equations (4.5)-(4.7) and the differential scanning calorimeter traces can then be used in several different ways to calculate the contact angle Θ at the solid Al-solid nucleus-liquid triple point, and the number of potential catalytic nucleation sites per particle Nc (Kim et al, 1990):

(1) From equations (4.5) and (4.7), the particle solidification onset temperature is independent of cooling rate in the differential scanning calorimeter, in agreement with the experimental measurements shown in Fig. 4.9 for melt spun Al-4.5wt%Cd, and Fig. 4.24 for melt spun Al-5wt%Pb. From equations (4.5) and (4.7), the Cd particle solidification onset temperature is given by $(dZ/dt)onset = (dZ/dt)_{Z=0} = I = (dZ/dt)^*$, where $(dZ/dt)^*$ is the detection limit of the calorimeter. The calorimeter traces were obtained with a typical specimen size of 18mg and a calorimeter sensitivity of 0.01mW, corresponding to a detection limit of $2.2x10^{-3}$/s, $2.7x10^{-3}$/s and $1.5x10^{-3}$/s for Cd, In and Pb particles respectively. Assuming that all the Al atoms at the surface of the $\{111\}_{Al}$ facets of the particles can act as catalytic nucleation sites, $Nc=1.4x10^4$ for an average Cd particle diameter of 20nm, $Nc=2.0x10^4$ for an average In particle diameter of 30nm, and $Nc=1.9x10^4$ for an average Pb particle diameter of 20nm. Taking $\exp(-Q/kT)=10^{-2}$ (Turnbull, 1950, Cantor and Doherty, 1979), $\sigma_{SL}=87mJ/m^2$, $30mJ/m^2$ and $55mJ/m^2$ for Cd, In and Pb respectively (Mondolfo et al, 1984-1985, Johns, 1974), and $L=441MJ/m^3$, $200MJ/m^3$ and $250MJ/m^3$ for Cd, In and Pb respectively (Brandes and Smithells, 1983), the measured solidification onset temperatures give $f(\Theta)=0.048$ and $\Theta=43^\circ$ for Cd, $f(\Theta)=0.019$ and $\Theta=33^\circ$ for In, and $f(\Theta)=0.010$ and $\Theta=28^\circ$ for Pb.

(2) Equations (4.5) and (4.7) can also be used to describe the shape of individual particle solidification exotherms in the differential scanning calorimeter. Combining equations (4.5) and (4.7), $\ln\{(dZ/dt)/(1-Z)\}$ varies linearly with $1/(Tm-T)^2T$, with a slope and intercept of -B and ln A respectively. Figs. 4.27-4.29 show particle solidification exotherms from

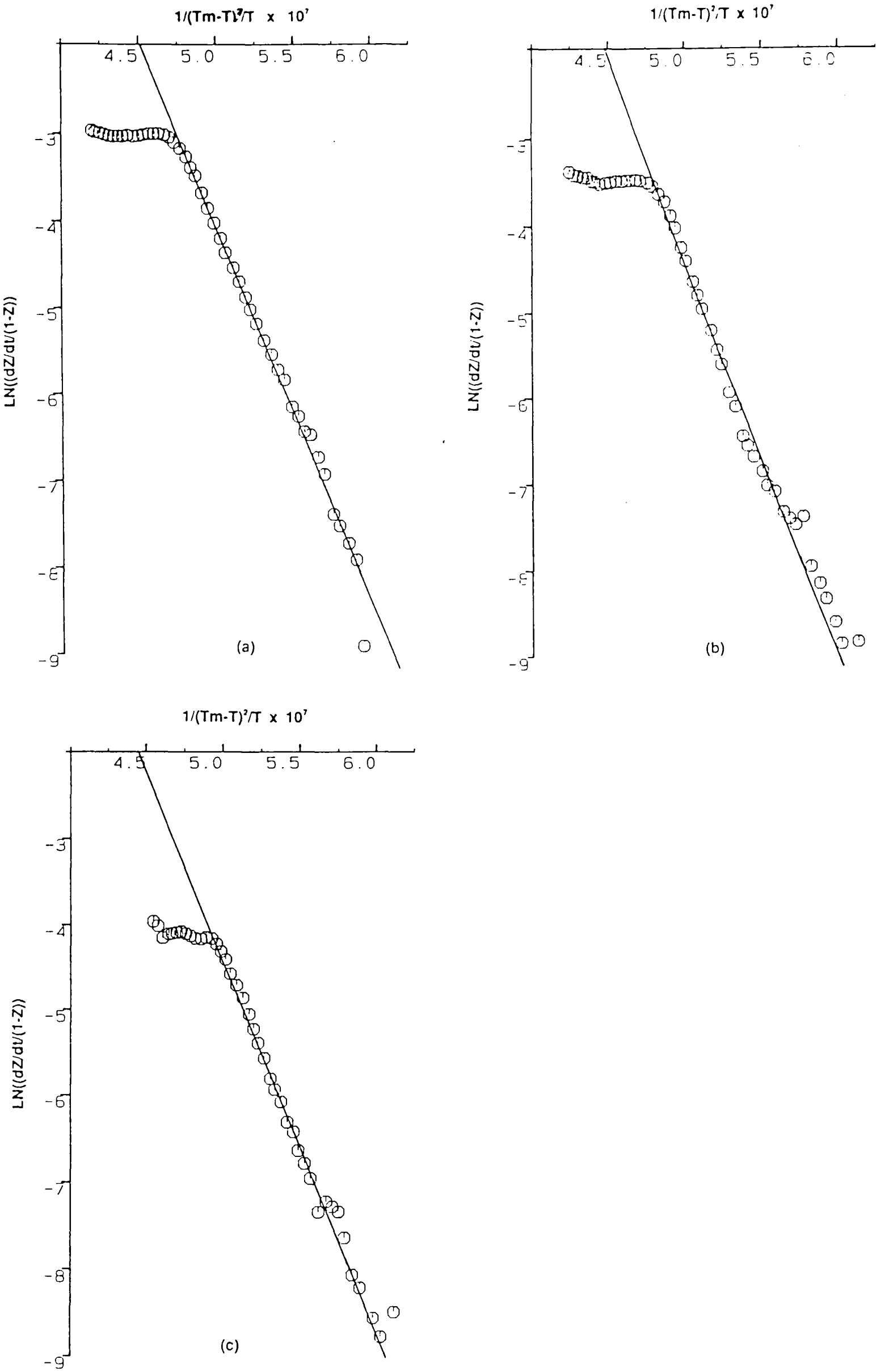
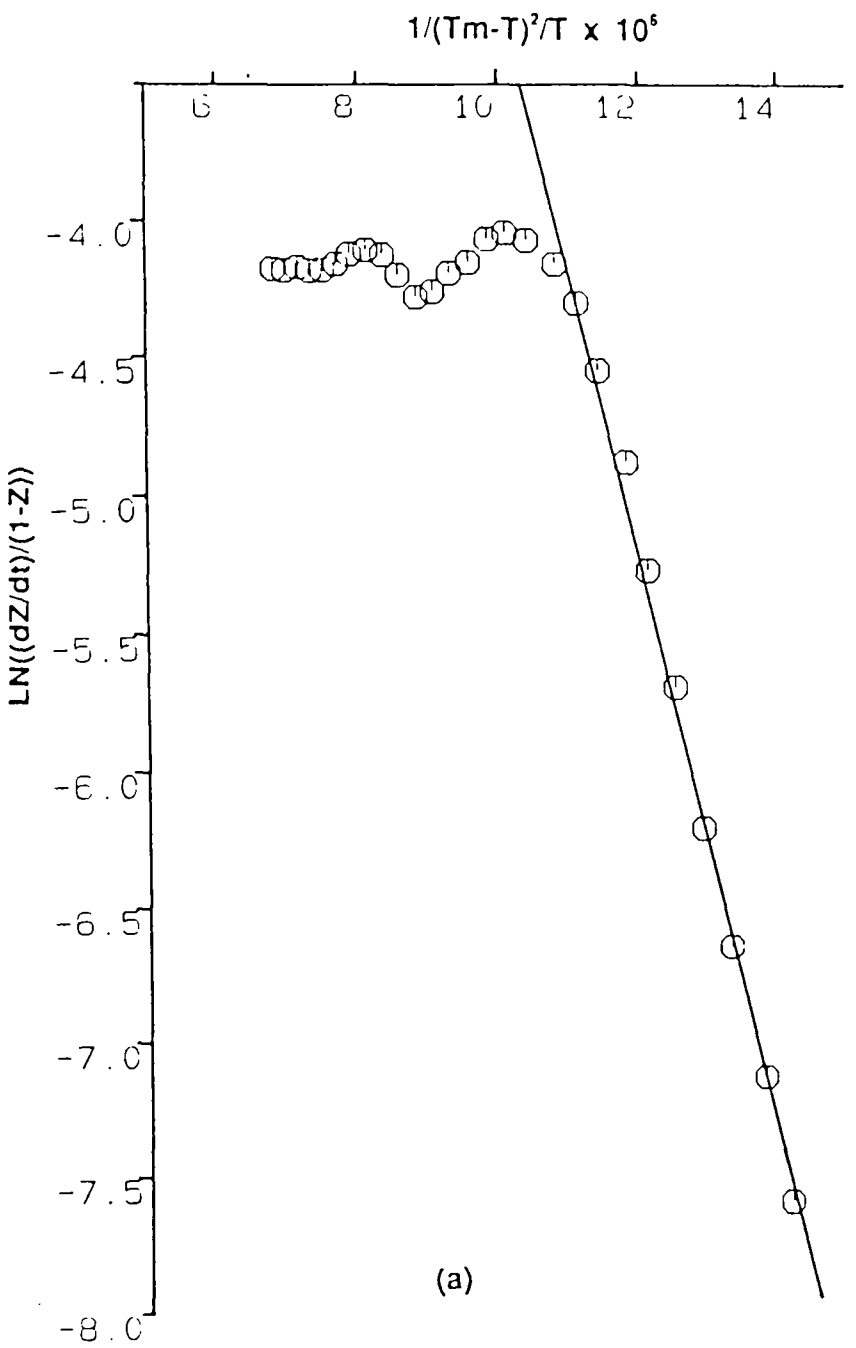


Fig. 4.27: Differential scanning calorimeter traces of Cd particle solidification exotherms from melt spun Al-4.5wt%Cd, re-plotted according to equations (4.5) and (4.7) in the form ln{(dZ/dt)/(1-Z)} versus $1/(Tm-T)^2T$: (a) 10K/min; (b) 5K/min; and (c) 2K/min.



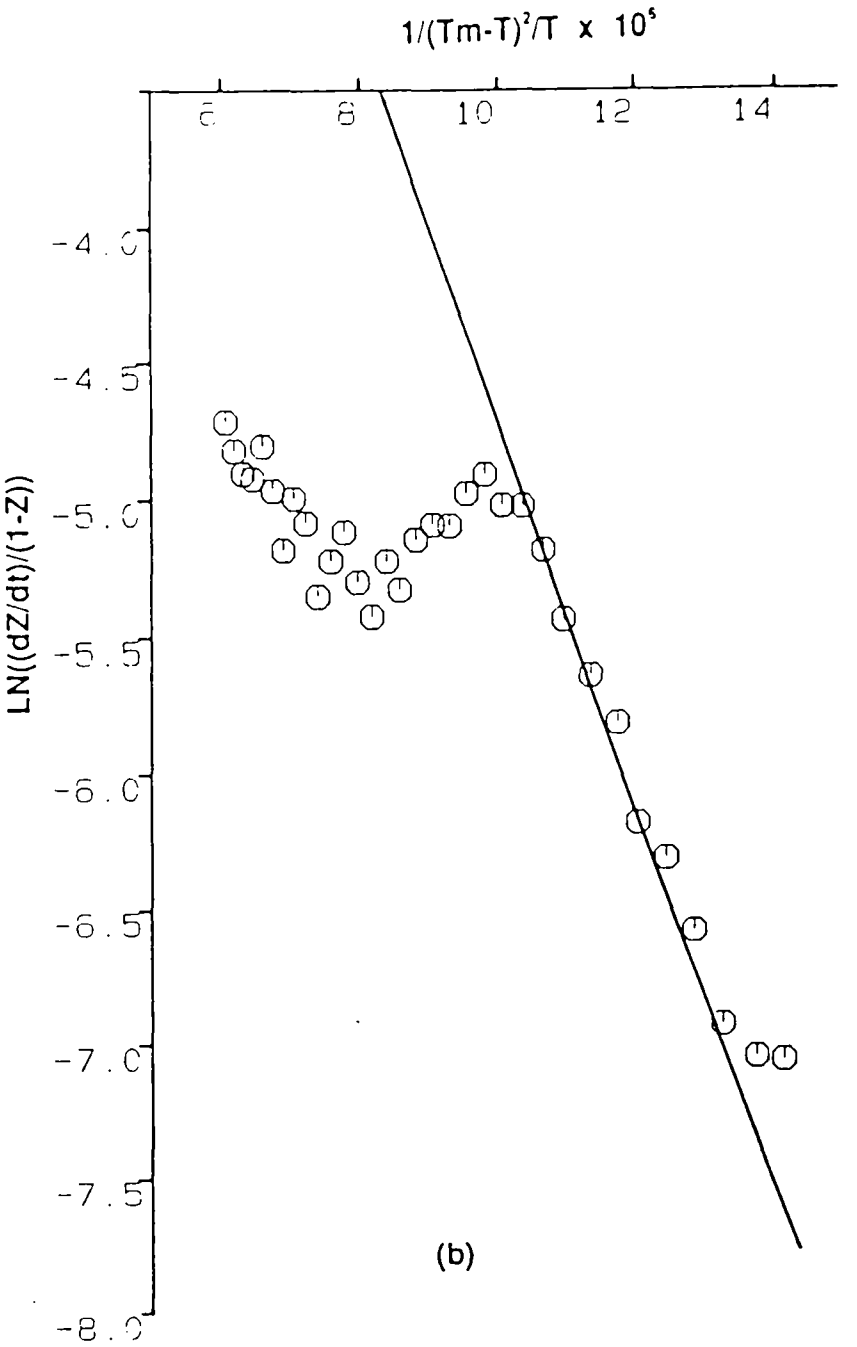
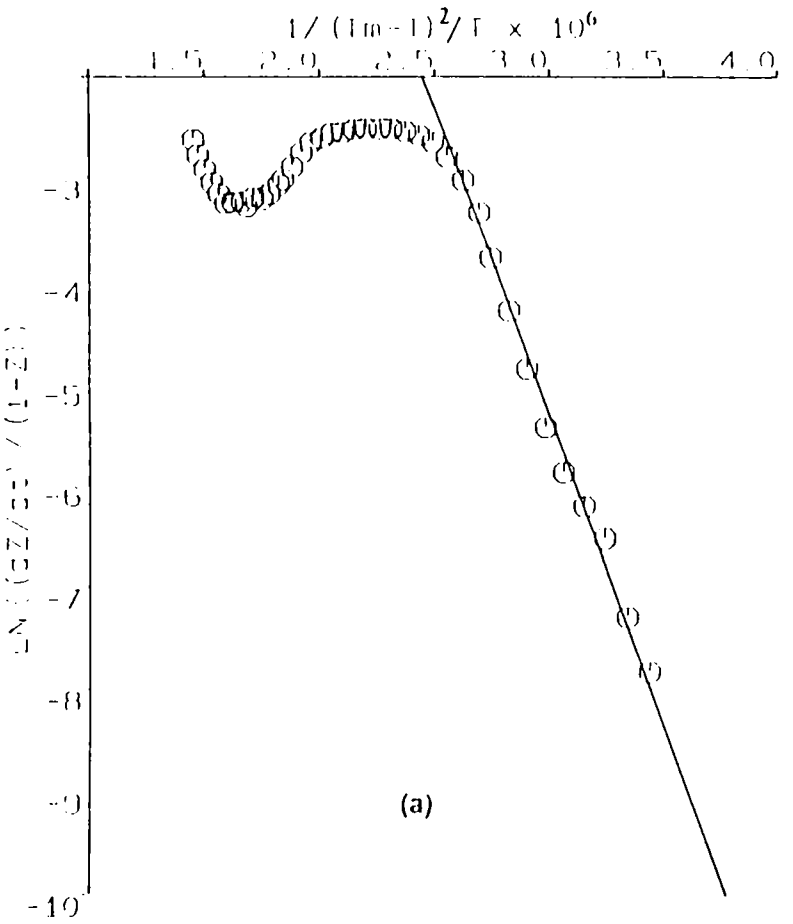
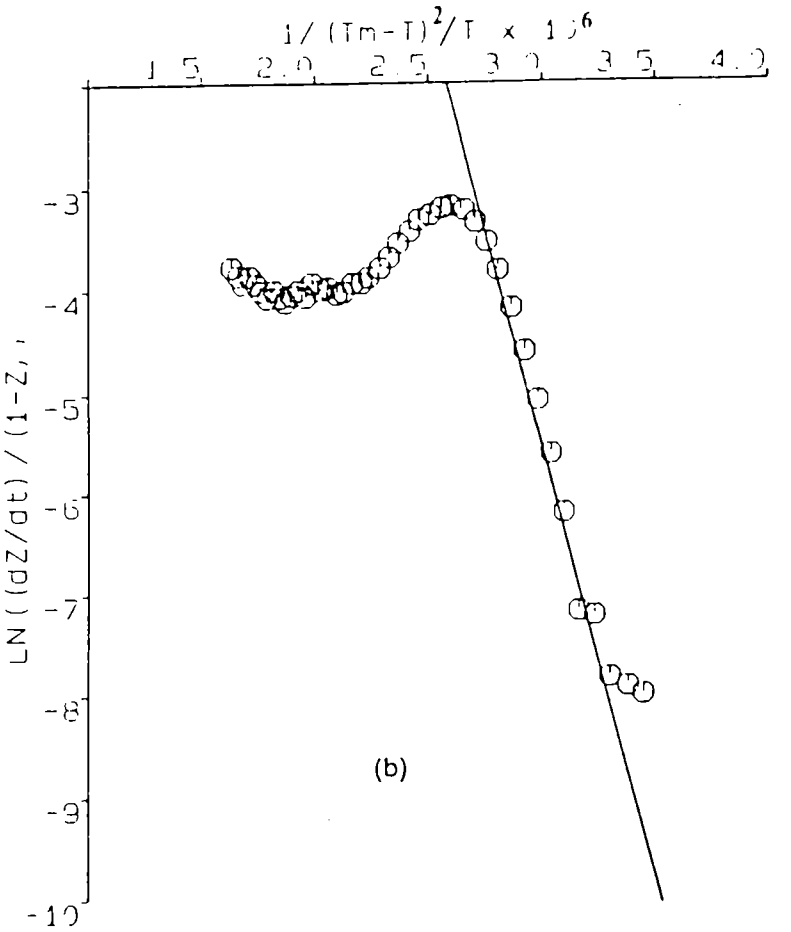


Fig. 4.28: Differential scanning calorimeter traces of In particle solidification exotherms from melt spun Al-7wt%In, replotted according to equations (4.5) and (4.7) in the form ln {(dZ/dt)/(1-Z)} versus $1/(Tm-T)^2T$; (a) 2K/min; and (b) 1K/min.





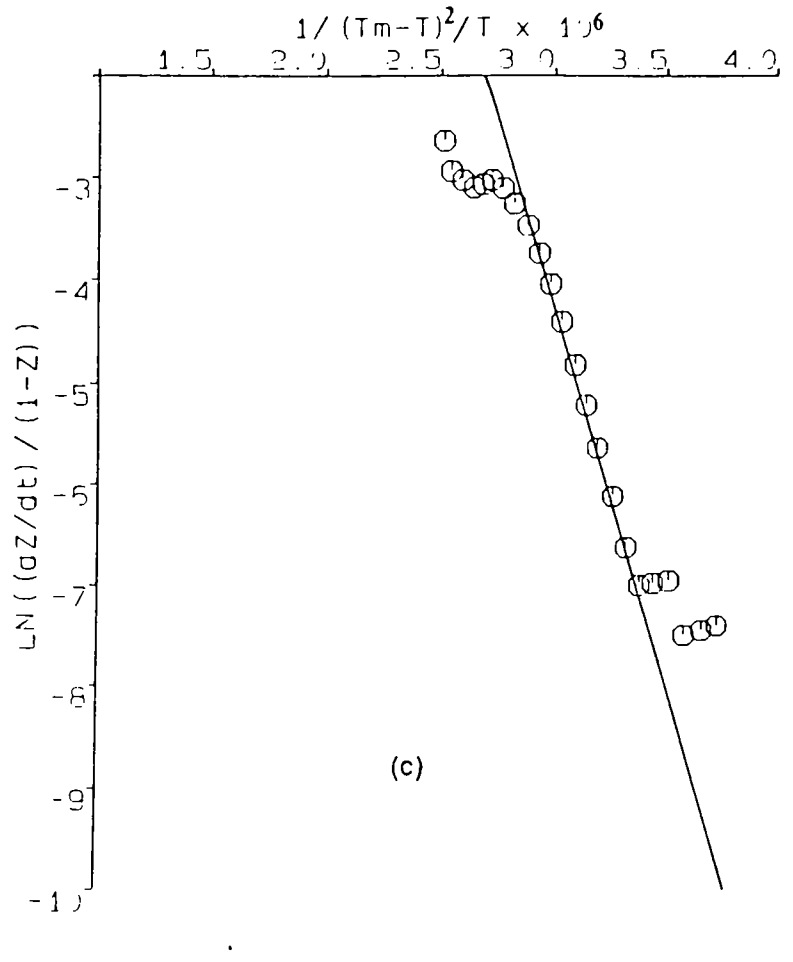


Fig. 4.29: Differential scanning calorimeter traces of Pb particle solidification exotherms from melt spun Al-5wt%Pb, re-plotted according to equations (4.5) and (4.7) in the form ln{(dZ/dt)/(1-Z)} versus $1/(Tm-T)^2T$: (a) 10K/min; (b) 5K/min; and (c) 2K/min.

melt spun Al-4.5wt%Cd, Al-7wt%In and Al-5wt%Pb respectively, obtained at different cooling rates in the differential scanning calorimeter, and re-plotted in the form $\ln\{(dZ/dt)/(1-Z)\}$ versus $1/\{Tm-T)^2T$. The linear variation predicted by equations (4.5) and (4.7) is obeyed well over the temperature range between the solidification onset and peak temperatures. Best fit slopes and intercepts give values of A and B which correspond to contact angles Θ in the range 38°-40° for Cd, 26°-28° for In, and 23°-27° for Pb, and numbers of potential catalytic nucleation sites per particle Nc in the range 7.5×10^{-4}-0.1 for Cd, 1.3×10^{-8}-1.0×10^{-6} for In, and 2.6×10^{-6}-0.5. for Pb.

(3) From equations (4.5) and (4.7), the maximum Cd particle solidification rate (dZ/dt)max is given by (Kim et al, 1990):

$$(dZ/dt)max = A(1-Zmax)\exp\{-B/(Tm-Tmax)^2Tmax\} \qquad (4.8)$$

and corresponds to a temperature Tmax, which can be obtained from equation (4.6) after differentiating equation (4.7) with A approximately independent of temperature (Kim et al, 1990, Turnbull, 1950, Cantor and Doherty, 1979):

$$B\dot{T}(3Tmax-Tm)/A(Tm-Tmax)^3Tmax^2 = \exp\{-B/(Tm-Tmax)^2Tmax\} \qquad (4.9)$$

Equations (4.8) and (4.9) describe the variation in shape of the particle solidification exotherms as a function of cooling rate in the differential scanning calorimeter, as shown in Figs. 4.8, 4.9, 4.23 and 4.24. From equations (4.8) and (4.9), the particle solidific ation peak temperature Tmax decreases and the exothermic peak height (dZ/dt)max increases with increasing cooling rate, in agreement with the experimental results shown in Figs. 4.9 and 4.24. From equation (4.8), $\ln\{(dZ/dt)max/(1-Zmax)\}$ varies linearly with $1/(Tm-Tmax)^2Tmax$, with a slope and intercept of -B and ln A respectively; from equation (4.9), $\ln\{\dot{T}(3Tmax-Tm)/(Tm-Tmax)^3Tmax^2\}$ also varies linearly with $1/(Tm-Tmax)^2Tmax$, with a slope and intercept of -B and ln (A/B) respectively. Figs 4.30 and 4.31 show the cooling rate variation of particle solidification peak temperature and exothermic peak height for Cd and Pb particles respectively, re-plotted from Figs. 4.9 and 4.24 according to equations (4.8) and (4.9) respectively. For the Cd particles, best fit slopes and intercepts give values of A and B which correspond to contact angles Θ of 43° and 41° and

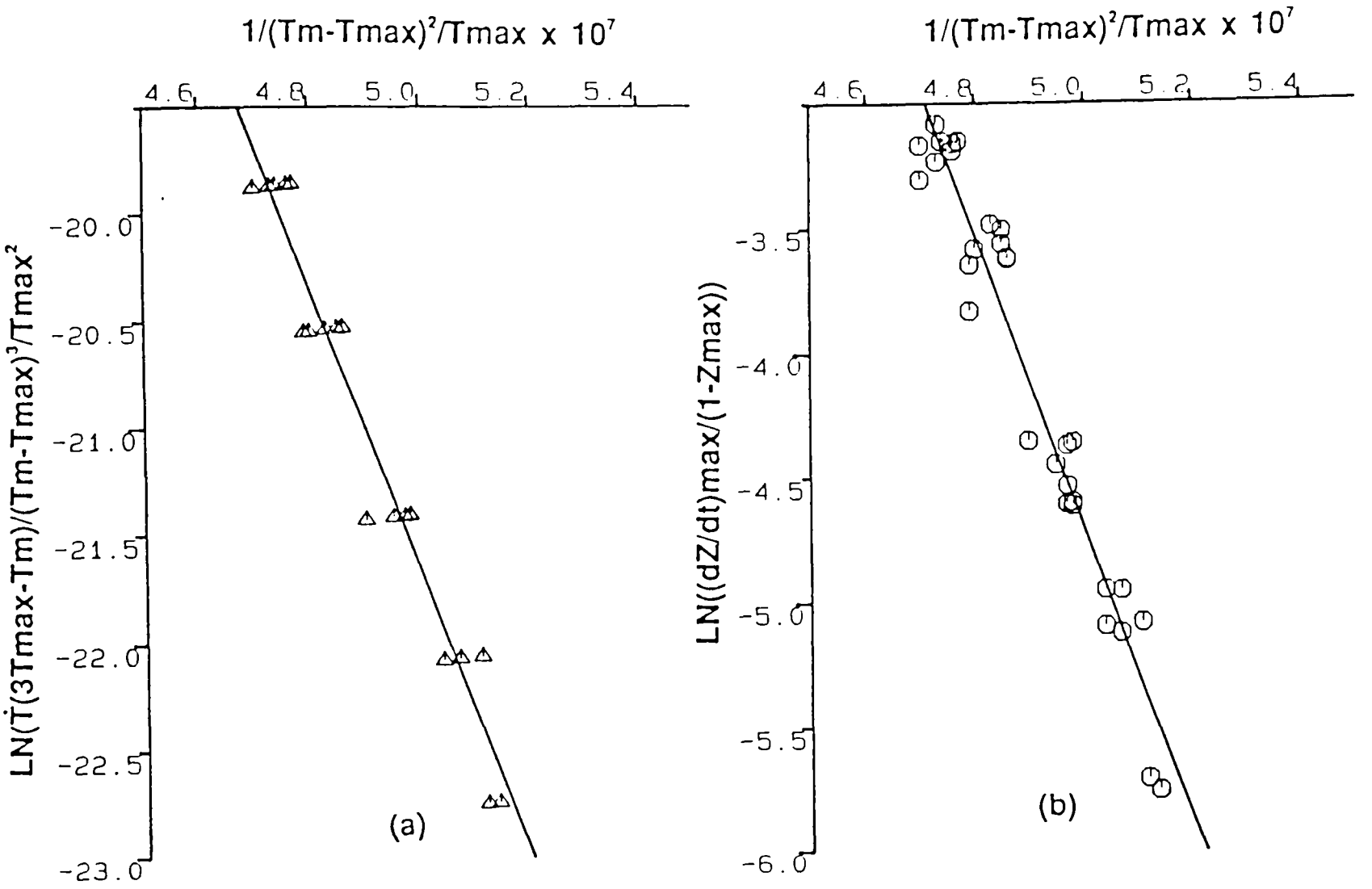


Fig. 4.30: Cd particle solidification peak temperature and exothermic peak height for melt spun Al-4.5wt%Cd as a function of cooling rate in the differential scanning calorimeter, re-plotted from Fig. 4.9 according to equations (4.8) and (4.9) in the form: (a) ln $\{\dot{T}(3T_{max}-T_m)/(T_m-T_{max})^3T_{max}^2\}$ versus $1/(T_m-T_{max})^2T_{max}$; and (b) ln $\{(dZ/dt)_{max}/(1-Z_{max})\}$ versus $1/(T_m-T_{max})^2T_{max}$

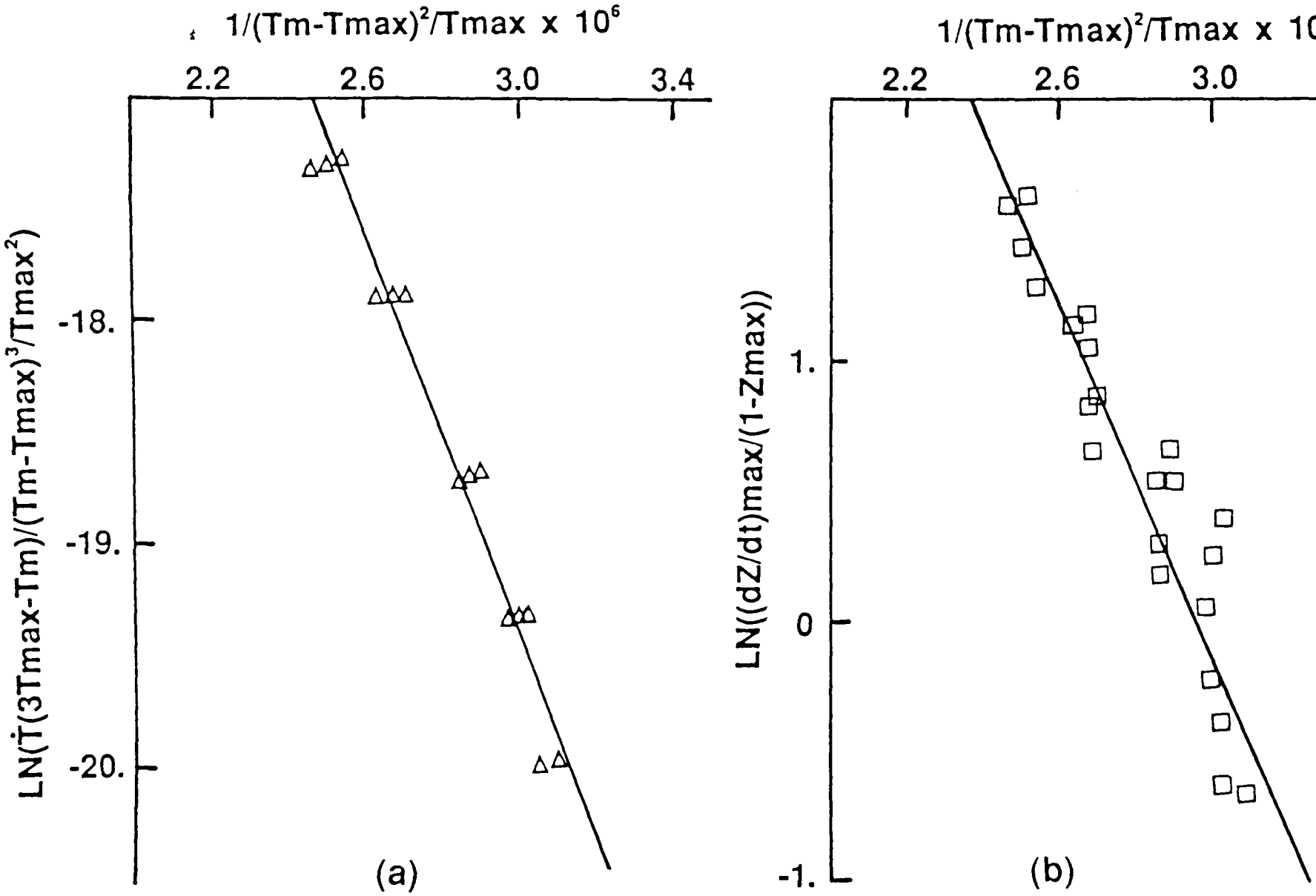


Fig. 4.31: Pb particle solidification peak temperature and exothermic peak height for melt spun Al-5wt%Pb as a function of cooling rate in the differential scanning calorimeter, re-plotted from Fig. 4.24 according to equations (4.8) and (4.9) in the form: (a) ln $\{\dot{T}(3Tmax-Tm)/(Tm-Tmax)^3Tmax^2\}$ versus $1/(Tm-Tmax)^2Tmax$; and (b) ln $\{(dZ/dt)max/(1-Zmax)\}$ versus $1/(Tm-Tmax)^2Tmax$

numbers of potential catalytic nucleation sites per particle Nc of 29.8 and 0.1 for the peak temperature and peak height variations respectively. For the Pb particles, best fit slopes and intercepts give values of A and B which correspond to contact angles Θ of 22° and 20°, and numbers of potential catalytic nucleation sites per particle Nc of 1.1×10^{-7} and 1.8×10^{-7} for the peak temperature and peak height variation respectively.

The best method of analysing the Cd and Pb particle solidification exotherms from differential scanning calorimeter traces such as shown in Figs. 4.8 and 4.23 is probably the cooling rate variation of peak shape shown in Figs. 4.30 and 4.31, which averages over a large number of independent differential scanning calorimeter experiments. The best measured value of contact angle Θ at the solid Al-solid nucleus-liquid triple point is therefore 42° for Cd and 21° for Pb. The best method which is used to analyse the Cd and Pb particle solidification exotherms can not be used to analyse the In particle solidification, because the limited accessible range of cooling rates. The best measured value of contact angle Θ for In particles is, therefore, 27° obtained by averaging after re-plotting the differential scanning calorimeter traces as shown in Fig. 4.28 according to equations (4.5)-(4.7).

The measured values of the number of potential catalytic nucleation sites per Cd particle Nc are considerably smaller than the number of Al atoms on the $\{111\}_{Al}$ facets surrounding each Cd particle, indicating that catalytic nucleation can only take place at special sites such as steps or dislocations on the $\{111\}_{Al}$ facets. However, the measured values of the number of potential catalytic nucleation sites per In and Pb particle are unreasonably low by several orders of magnitude, a common observation for pre-exponential factors by analysing nucleation kinetics during solidification (Turnbull, 1950, Cantor and Doherty, 1979). The present results, taken together with the results obtained through investigation of the solidification of Sn particles in an Al matrix by Kim and Cantor (1990), indicate that measured Nc values become more unreasonable as nucleation catalysis become more efficient. As discussed elsewhere (Kim et al, 1990), this effect may be associated with a progressive

breakdown of the classical spherical cap model of heterogeneous nucleation at the low values of contact angle corresponding to efficient catalysis.

As shown in Fig. 4.26 the contact angle Θ at the solid Al-solid nucleus-liquid triple point during particle solidification is determined by the relative magnitudes of the solid Al-liquid, solid Al-solid nucleus and solid nucleus-liquid surface energies, σ_{CL}, σ_{CS} and σ_{SL} respectively:

$$\cos\Theta = (\sigma_{CL}-\sigma_{CS})/\sigma_{SL} \qquad (4.10)$$

The surface energies σ_{CL} and σ_{CS} in equation (4.10) depend upon the crystallography of the {hkl} Al facet which catalyses the nucleation of solidification. Liquid Cd, In and Pb particles can nucleate on the atomically ordered {111} Al facets which survive above the Cd, In and Pb melting points, giving relatively small values of σ_{CS} and Θ, and a strong orientation relationship of $\{111\}_{Al}//\{0001\}_{Cd}$ and $\langle 110\rangle_{Al}//\langle 11\bar{2}0\rangle_{Cd}$ for Cd, $\{111\}_{Al}//\{111\}_{In}$ and $\langle 110\rangle_{Al}//\langle 110\rangle_{In}$ for In, and a cube-cube orientation relationship for Pb. Taking the best values of $\Theta = 42^{\circ}$, 27° and 21° for Cd, In and Pb respectively, equation (4.10) gives the difference in solid Al-liquid and solid Al-solid nucleus surface energies as $\sigma_{CL}-\sigma_{CS} = 65mJ/m^2$, $26.7mJ/m^2$ and $51mJ/m^2$ on the {111} Al facets for Cd, In and Pb respectively.

Chapter 5

The Effect of Ternary Additions on the Heterogeneous Nucleation of Solidification of Cd and Pb Particles Embedded in an Al Matrix

5.1 Introduction

In this chapter the results of experimental work investigating the effect of ternary additions on the heterogeneous nucleation of solidification of Cd and Pb particles embedded in an Al matrix are presented and discussed in relation to current heterogeneous nucleation theory. The experiments used to obtain the results presented in this chapter include the following:

(a) Transmission electron metallography to investigate the shape, size and crystallographic orientation of Cd rich and Pb rich particles embedded in an Al rich matrix in a variety of melt spun ternary alloys.

(b) Heating and cooling experiments in a differential scanning calorimeter to investigate the solidification behaviour of Cd and Pb rich particles in the melt spun ternary alloys.

5.2 Preliminary Experimental Results

In this section, preliminary results on a series of Al-Cd-X (X=Zn, Ga, Ge, Cu, Si) and Al-Pb-X (X=Zn, Ga, Cu) ternary alloys are described and briefly discussed. The results of more detailed experimental work on Al-Cd-Mg, Al-Pb-Ge and Al-Pb-Si will be described and discussed in the following sections.

5.2.1 Al-Cd-X ternary alloys

Figs. 5.1(a)-(e) show transmission electron micrographs of the microstructures of as-melt spun Al-Cd-X (X=Zn, Ga, Ge, Cu, Si) ternary alloys. The ternary elements did not significantly affect the Al-Cd alloy microstructure. Similar to the microstructure of as-melt spun Al-4.5wt%Cd, all the as-melt spun ternary alloy microstructures consisted of a homogeneous distribution of 5-120nm Cd rich particles embedded in an Al rich matrix. No precipitates were

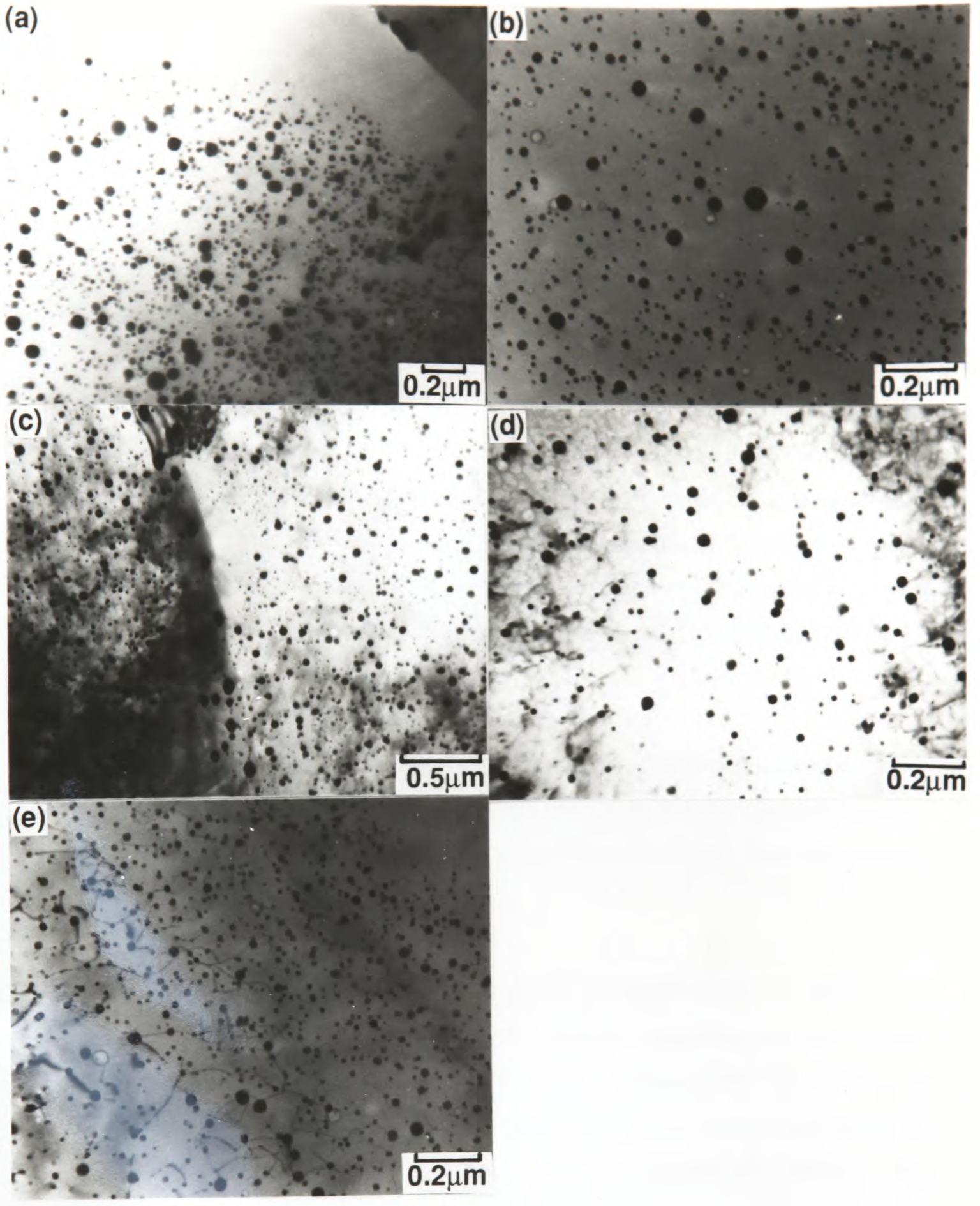


Fig. 5.1: Bright field transmission electron micrographs of the microstructures of as-melt spun Al-Cd-X ternary alloys: (a) Al-3wt%Cd-1.5wt%Zn; (b) Al-2wt%Cd-1.5wt%Ga; (c) Al-2wtCd-0.5wt%Ge; (d) Al-2wt%Cd-0.5wt%Cu; and (e) Al-2wt%Cd-1wt%Si.

observed in the as-melt spun microstructures, indicating that the ternary element atoms were fully dissolved in the Al matrix and the Cd particles.

Heat treated microstructures of three of the Al-Cd-X ternary alloys were also examined using transmission electron microscopy. Fig. 5.2 shows a transmission electron micrograph of the microstructure of Al-2wt%Cd-0.5wt%Ge after heat treatment for 600s at 350°C, No Ge precipitates were observed, indicating that in the equilibrium state the Ge atoms were fully dissolved in the Al matrix and the Cd particles. Fig. 5.3 shows a transmission electron micrograph of the microstructure of Al-2wt%Cd-0.5wt%Cu after heat treatment for 5.4×10^4s at 300°C. Precipitation of Al_2Cu was observed with some of the Al_2Cu precipitates in contact with the pre-existing Cd particles. Fig. 5.4 shows a transmission electron micrograph of the microstructure of Al-2wt%Cd-1wt%Si after heat treatment for 600s at 350°C. As with heat treated Al-Cd-Cu, Si precipitates appeared in the heat treated microstructure, with some of the precipitates in contact with the pre-existing Cd particles.

Figs. 5.5(a)-(e) and 5.6(a)-(e) show typical differential scanning calorimeter traces of Cd solidification exotherms and melting endotherms respectively, from all the melt spun Al-Cd-X ternary alloys. These traces are described individually as follows.

(1) As shown in Fig. 5.5(a) and 5.6(a), The Cd rich particles in melt spun Al-3wt%Cd-1.5wt%Zn solidified with a single, sharp exotherm at an onset temperature close to 257°C, and melted with an onset temperature of 313°C, 8K lower than the equilibrium melting point of pure Cd. This indicated that Zn was dissolved partly in the Cd particles and partly in the Al matrix. The onset of Cd(Zn) particle solidification was at an undercooling of 56K below the melting point, the same as the undercooling required to initiate the nucleation of pure Cd particles in Al, as discussed in chapter 4. In other words, doping of Zn in the Al-Cd alloy does not affect the catalytic efficiency of Al as a heterogenous nucleant for Cd solidification.

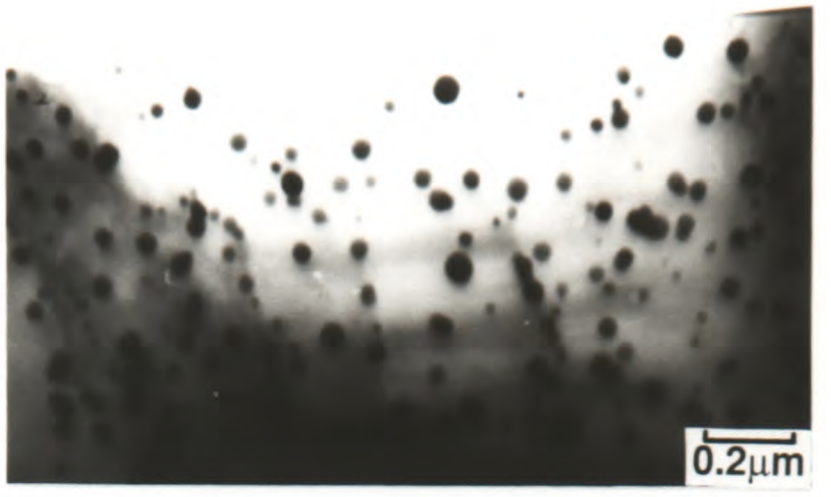


Fig. 5.2: Bright field transmisson electron micrograph of the microstructure of melt spun Al-2wt%Cd-0.5wt%Ge after heat treatment for 600s at 350°C.



Fig. 5.3: Bright field transmission electron micrograph of the microstructure of melt spun Al-2wt%Cd-0.5wt%Cu after heat treatment for $4x10^4$s at 300°C. Al_2Cu precipitates are arrowed.



Fig. 5.4: Bright field transmission electron micrograph of the microstructure of melt spun Al-2wt%Cd-1wt%Si after heat treatment for 600s at 350°C. Si precipitates are arrowed.

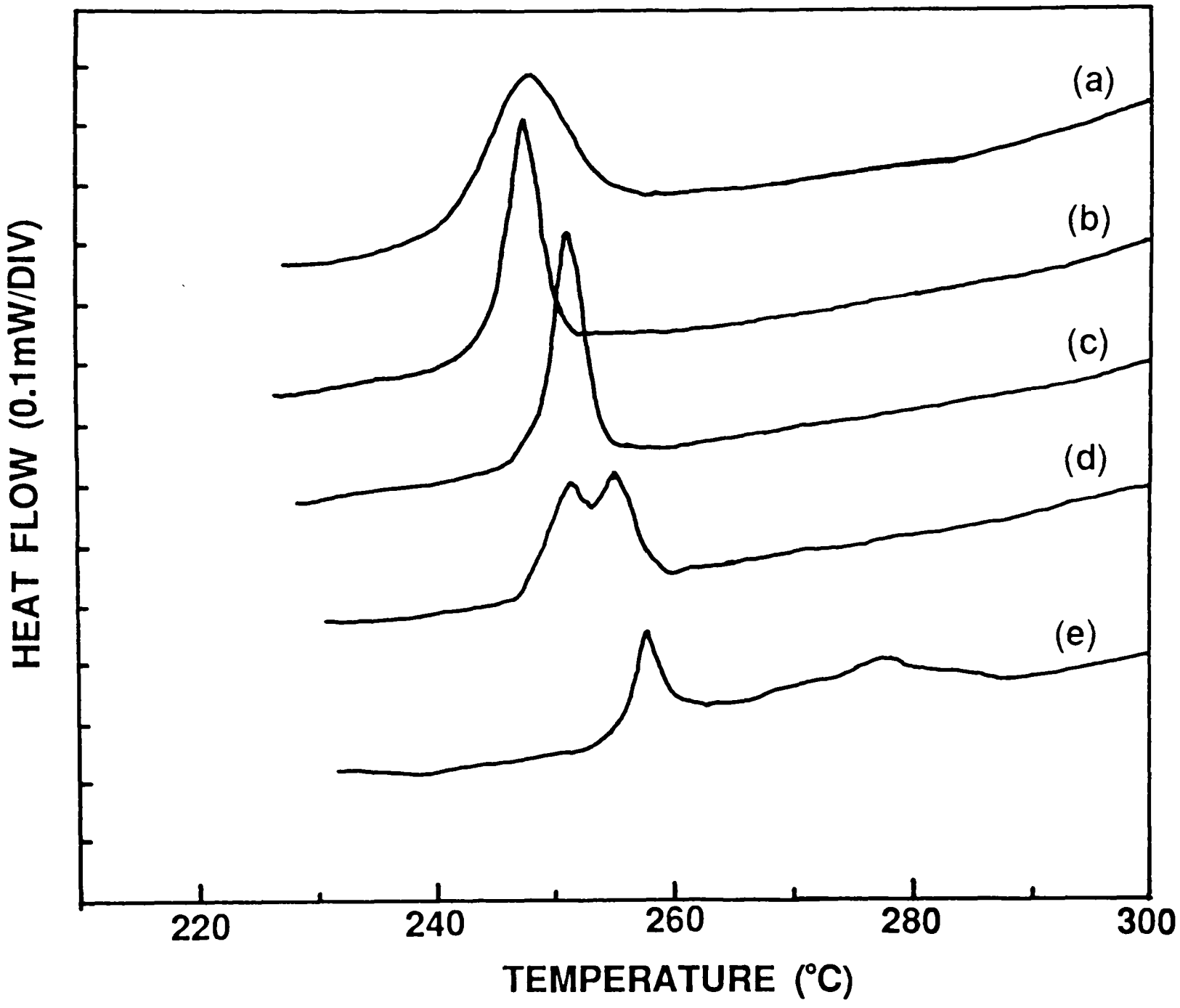


Fig. 5.5: Differential scanning calorimeter traces of Cd solidification exotherms from melt spun ternary Al-Cd-X alloys: (a) Al-3wt%Cd-1.5wt%Zn; (b) Al-2wt%Cd-1.5wt%Ga; (c) Al-2wt%Cd-0.5wt%Ge; (d) Al-2wt%Cd-0.5wt%Cu; and (e) Al-2wt%Cd-1wt%Si.

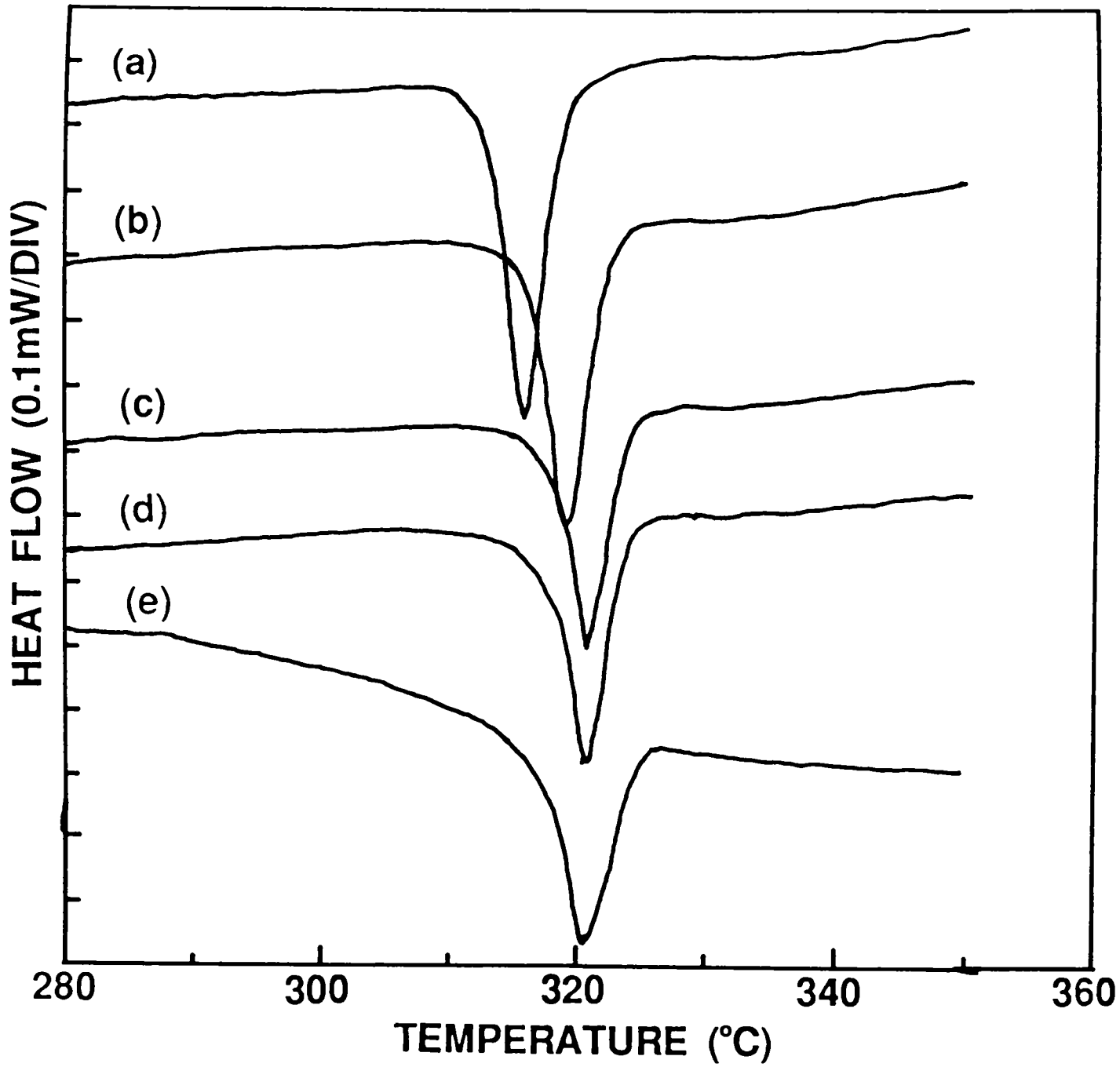


Fig. 5.6: Differential scanning calorimeter traces of Cd melting endotherms from melt spun ternary Al-Cd-X alloys: (a) Al-3wt%Cd-1.5wt%Zn; (b) Al-2wt%Cd-1.5wt%Ga; (c) Al-2wt%Cd-0.5wtGe; (d) Al-2wt%Cd-0.5wt%Cu; and (e) Al-2wt%Cd-1wt%Si.

(2) As shown in Figs. 5.5(b) and 5.6(b), the Cd rich particles in melt spun Al-2wt%Cd-1.5wt%Ga solidified with a single, sharp exotherm at an onset temperature of approximately 256°C, and melted with an onset temperature of 316°C, 5K lower than the equilibrium melting point of pure Cd. This indicated that Ga was dissolved partly in the Cd particles and partly in the Al matrix. The onset of Cd(Ga) particle solidfication was at an undercooling of 60K below the melting point, 4K larger than the undercooling required to initiate the nucleation of pure Cd particles in Al, as discussed in Chapter 4. In other words, doping of Ga in the Al-Cd alloy slightly decreased the catalytic efficiency of Al as a heterogeneous nucleant for Cd solidification.

(3) As shown in Figs. 5.5(c) and 5.6(c), the Cd rich particles in melt spun Al-2wt%Cd-0.5wt%Ge solidified with a single, sharp exotherm at an onset temperature close to 256°C, and melted at an onset temperature of 320°C, only slightly different from the equilibrium melting point of pure Cd. This indicated that a negligible amount of Ge was dissolved in the Cd particles. The onset of Cd particle solidification was at an undercooling of 64K, below the melting point, about 8K larger than the undercooling required to initiate the nucleation of pure Cd particles in Al, as discussed in chapter 4. Doping of 0.5wt%Ge into the Al-Cd alloy decreased the catalytic efficiency of Al as a heterogeneous nucleant for Cd solidification. With increased doping of Ge, the nucleation undercooling of Cd is probably increased further.

(4) As shown in Fig. 5.5(d), the Cd rich particles in the melt spun Al-2wt%Cd-0.5wt%Cu solidified with two overlapping exotherms, the higher temperature exotherm at an onset temperature close to 260°C, and the lower temperature exotherm at an onset temperature close to 256°C. As shown in Fig 5.6(d), the Cd rich particles melted with an onset temperature of 320°C, only slightly different from the equilibrium melting point of pure Cd. This indicated that a negligible amount of Cu was dissolved in the Cd rich particles. The high and low temperature exotherms were at undercoolings of 60K and 64K below the melting point. More detailed work is needed to identify the two exothermic peaks, but one peak may correspond to solidification of Cd particles in

contact with Al_2Cu precipitates as shown in Fig. 5.3, and the other peak may correspond to Cd particles not in contact with Al_2Cu precipitates. Both exotherms were at higher undercooling than that required to initiate the nucleation of pure Cd particles in Al, as discussed in chapter 4. Doping of Cu in the Al-Cd alloy decreased the catalytic efficiency of Al as a heterogeneous nucleant for the Cd solidification.

(5) As shown in Fig. 5.6(e), the Cd rich particles in melt spun Al-2wt%Cd-1wt%Si solidified with a broad exotherm extending between 264°C and 285°C, and a sharp exotherm at an onset temperature close to 264°C. As shown in Fig. 5.6(c), the Cd rich particles melted with an onset temperature of 320°C, only slightly different from the equilibrium melting point of pure Cd. This indicated that the amount of Si dissolved in the Cd particles was negligible. The broad exotherm, extended between 35K and 56K undercooling and the sharp exotherm was at 56K undercooling below the melting point. The broad exotherm may correspond to solidification of Cd particles in contact with Si precipitates, as shown in Fig. 5.4, while the sharp exotherm may correspond to solidification of Cd particles not in contact with Si precipitates. If this explanation is valid, the present results indicate that doping of 0.2wt%Si in the Al-Cd alloy does not affect the catalytic efficiency of Al as a heterogeneous nucleant for Cd solidification, but that contact between Cd particles and Si precipitates stimulate the nucleation of Cd solidification. Detailed work is needed to clarify the nucleation mechanism.

5.2.2 Al-Pb-X ternary alloys

Figs. 5.7(a)-(c) show transmission electron micrographs of the microstructures of as-melt spun Al-Pb-X (X=Zn, Ga and Cu) ternary allloys. Similar to the as-melt spun Al-5wt%Pb, all the as-melt spun ternary alloy microstructures consisted of a homogeneous distribution of 5-100nm Pb rich particles embedded in an Al rich matrix. No precipitates were observed in the as-melt spun microstructures, indicating that the ternary element atoms were fully dissolved in the Al matrix and the Pb particles. Fig. 5.8 shows an electron

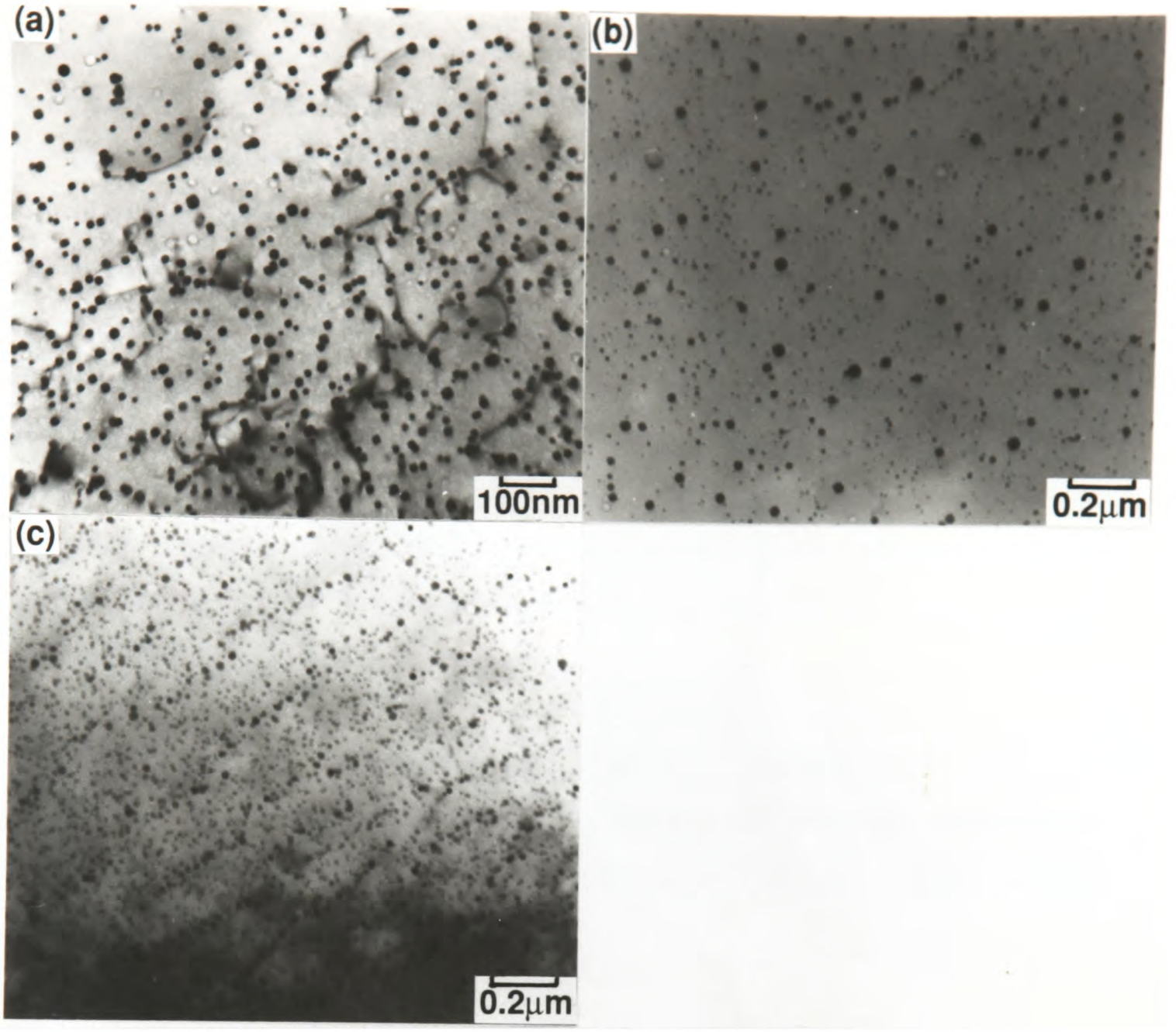


Fig. 5.7: Bright field transmission electron micrographs of the microstructures of as-melt spun Al-Pb-X ternary alloys: (a) Al-4wt%Pb-1wt%Zn; (b) Al-2wt%Pb-1wt%Ga; and (c) Al-2wt%Pb-0.5wt%Cu.

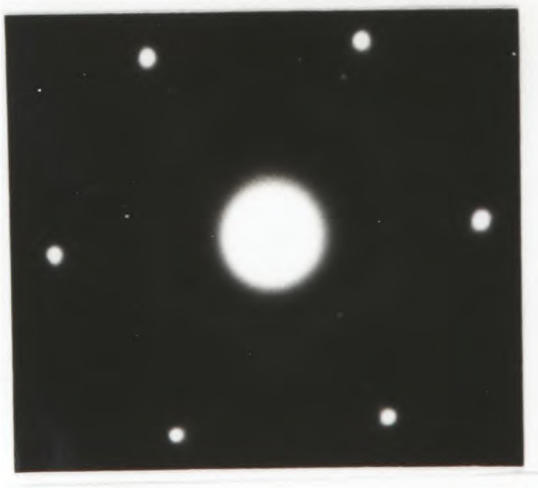


Fig. 5.8: Selected area diffraction pattern from as-melt spun Al-2wt%Pb-1wt%Ga, showing superimposed <111> zones from the Al(Ga) matrix and the Pb(Ga) particles.

diffraction pattern of an Al ‹111› zone from as-melt spun Al-2wt%Pb-1wt%Ga, and Figs. 5.9(a) and (b) show electron diffraction patterns of Al ‹110› zones from as-melt spun Al-4wt%Pb-1wt%Zn and Al-2wt%Pb-0.5wt%Cu respectively. All these diffraction patterns indicate that the Pb rich particles exhibited a cube-cube orientation relationship with the Al rich matrix, without being affected by the ternary additions (Moore et al, 1987). The heat treated microstructure of melt spun Al-2wt%Pb-1wt%Ga was also examined by transmission electron microscopy. Fig. 5.10 shows the microstructure of melt spun Al-2wt%Pb-1wt%Ga after heat treatment for 1200s at 380°C. Once again, no precipitates were observed in the heat treated microstructure, indicating that in the equilibrium state the Ga atoms were fully dissolved in the Al matrix and the Pb particles.

Figs. 5.11(a)-(c) and 5.12(a)-(c) show typical differential scanning calorimeter traces of Pb solidification exotherms and melting endotherms respectively from the three melt spun Al-Pb-X ternary alloys. These traces are described individually as follows.

(1) As shown in Figs. 5.11(a) and 5.12(a), the Pb rich particles in melt spun Al-4wt%Pb-1wt%Zn solidified with a single, sharp exotherm at an onset temperature of 299°C, and melted with an onset temperature of 320°C, 7K lower than the equilibrium melting point of pure Pb. This indicated that Zn was dissolved partly in the Pb particles and partly in the Al matrix. The onset of Pb(Zn) solidification was at an undercooling of 21K below the melting point, only 1K lower than the undercooling required to initiate the nucleation of pure Pb particles in Al as dicussed in chapter 4. Doping of Zn in the Al-Pb alloy does not affect the catalytic efficiency of Al as a heterogeneous nucleant for Pb solidification.

(2) As shown in Figs. 5.11(b) and 5.12(b), the Pb rich particles in melt spun Al-2wt%Pb-1wt%Ga solidified with a single sharp exotherm at an onset temperature close to 293°C, and melted at an onset temperature of 325°C, 2K lower than the equilibrium melting point of pure Pb. This indicated that only

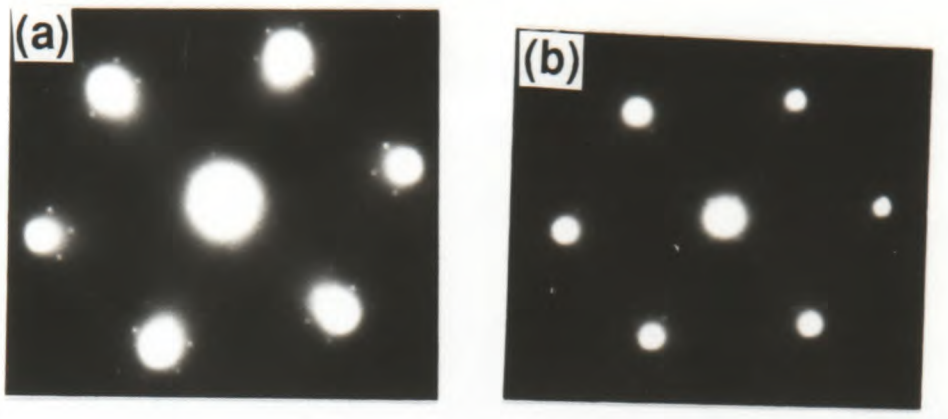


Fig. 5.9: Selected area diffraction patterns from as-melt spun (a) Al-4wt%Pb-1wt%Zn and (b) Al-2wt%Pb-0.5wt%Cu, showing superimposed <110> zones from the Al(Zn) or Al(Cu) matrix and the Pb particles.

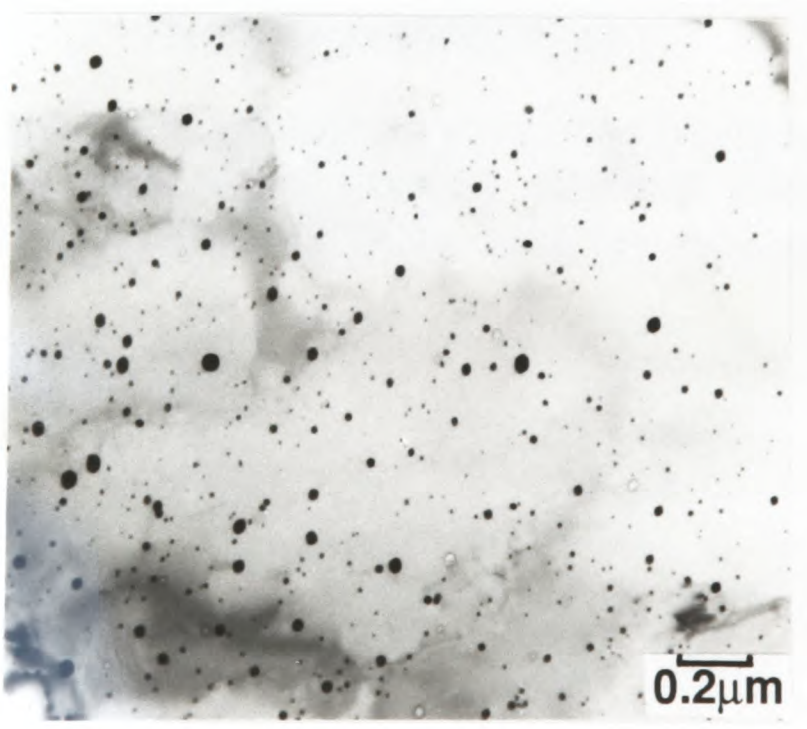


Fig. 5.10: Bright field transmission electron micrograph of the microstructure of melt spun Al-2wt%Pb-1wt%Ga after heat treatment for 1200s at 380°C.

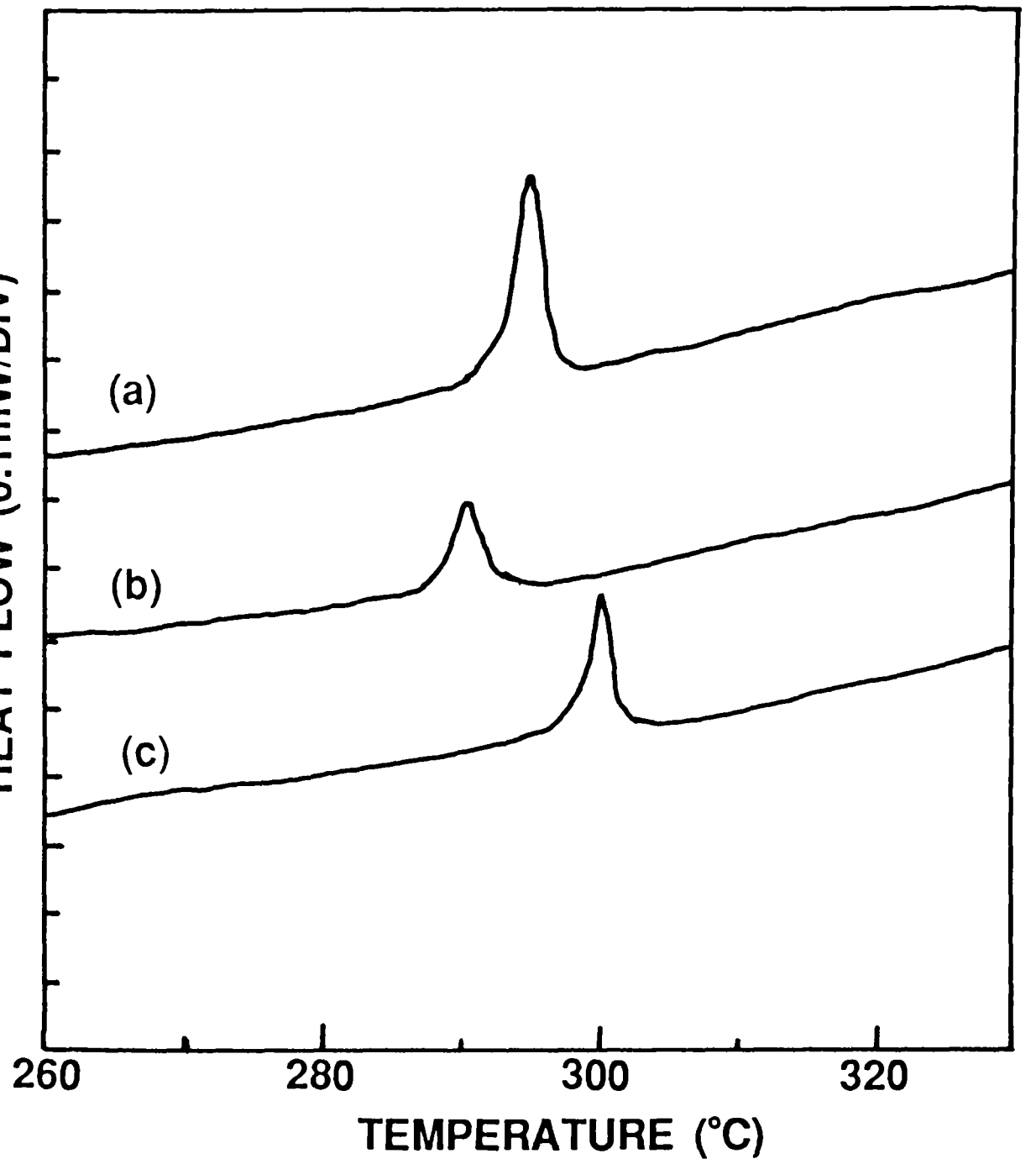


Fig. 5.11 Diferential scanning calorimeter traces of Pb solidification exotherms from melt spun ternary Al-Pb-X alloys: (a) Al-4wt%Pb-1wt%Zn; (b) Al-2wt%Pb-1wt%Ga; and (c) Al-2wt%Pb-0.5wt%Cu.

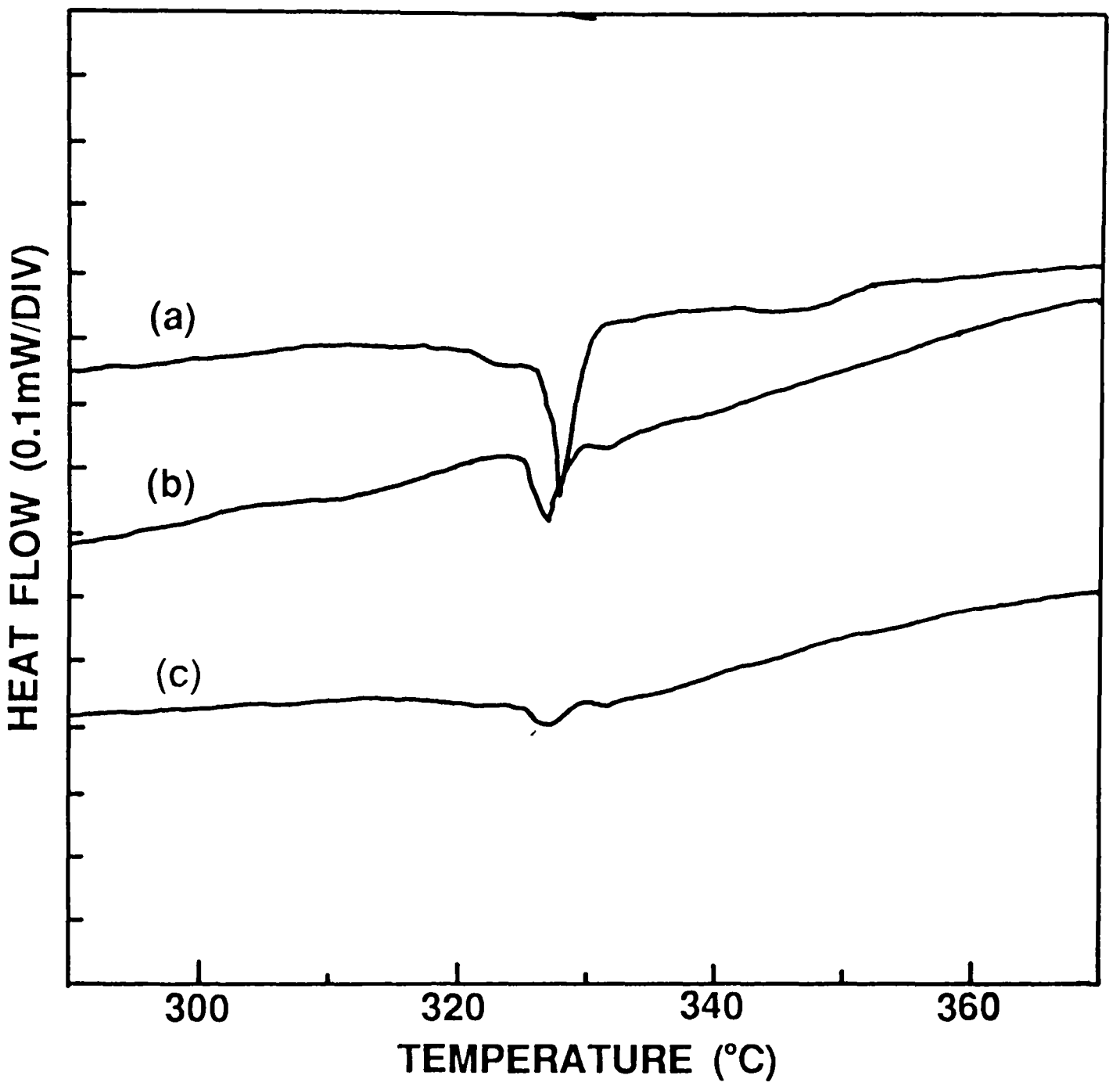


Fig. 5.12: Differential scanning calorimeter traces of Pb melting endotherms from melt spun ternary Al-Pb-X alloys: (a) Al-4wt%Pb-1wt%Zn; (b) Al-2wt%Pb-1wt%Ga; and (c) Al-2wt%Pb-0.5wt%Cu.

a small amount of Ga was dissolved in the Pb particles. The onset of Pb(Ga) solidification was at an undercooling of 32K below the melting point, about 10K higher than the undercooling required to initiate the nucleation of pure Pb particles in Al, as discussed in chapter 4. Doping of 1.2wt%Ga into the Al-Pb alloy clearly decreased the catalytic efficiency of Al as a heterogeneous nucleant for Pb solidification.

(3) As shown in Figs. 5.11(c) and 5.12(c), the Pb rich particles in melt spun Al-2wt%Pb-0.5wt%Cu solidified with a single sharp exotherm at an onset temperature close to 304°C, and melted with an onset temperature of 326°C, only slightly different from the equilibrium melting point of pure Pb. This indicated that the amount of Cu dissolved in the Pb particles was negligible. The onset of Pb solidification was at an undercooling of 22K below the melting point, the same as the undercooling required to initiate the nucleation of pure Pb particles in Al as discussed in chapter 4. Doping of Cu in the Al-Pb alloy does not affect the catalytic efficiency of Al as a heterogeneous nucleant for Pb solidification.

5.3 Effect of Mg on the Heterogeneous Nucleation of Cd Solidification by Al

5.3.1 Microstructure

Fig. 5.13 shows a typical transmission electron micrograph of the microstructure of as-melt spun Al-9wt%Cd-1.5wt%Mg, consisting of small Cd(Mg) particles homogeneously distributed throughout a matrix of Al(Mg). The Cd(Mg) particle sizes ranged from 10-150nm with an average of 30nm. The Cd(Mg) particles in Al-9wt%Cd-1.5wt%Mg coarsened gradually during heat treatment, with the average particle diameter increasing to 70nm after 600s at 400°C, and 80nm after 10^5s at 345°C respectively. This is different from the Cd particles in melt spun Al-4.5wt%Cd, which were resistant to heat treatment with insignificant coarsening after 600s at 350°C, or 10^5s at 300°C.

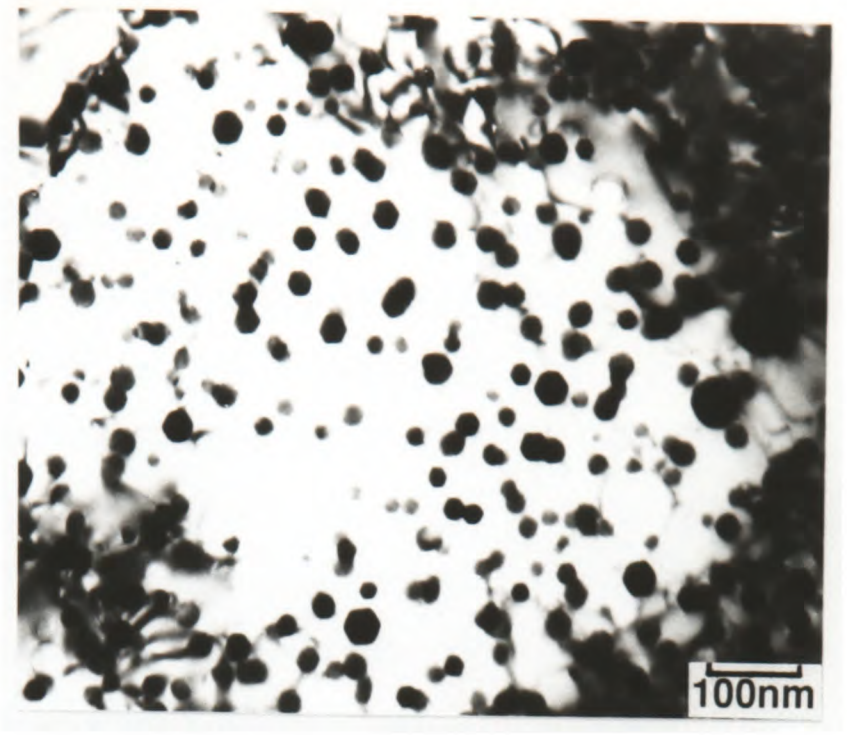
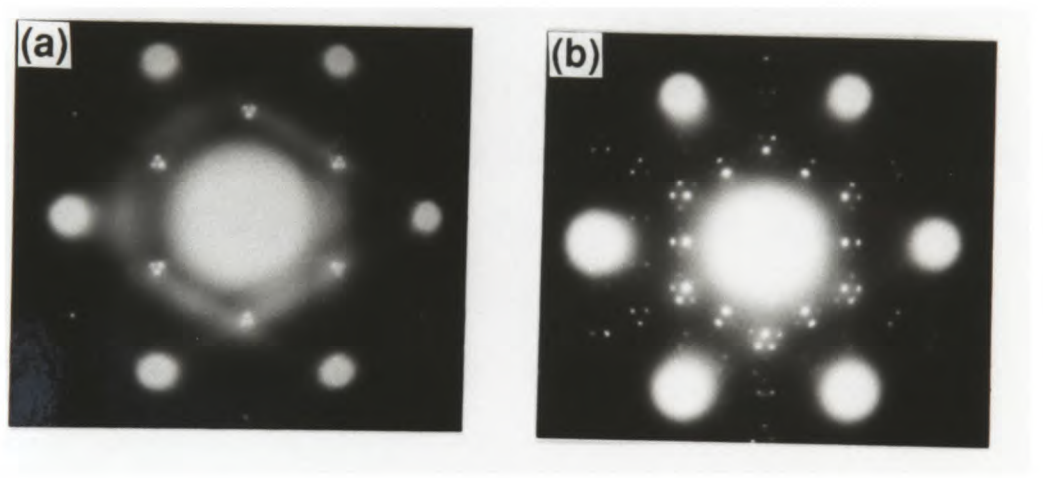


Fig. 5.13: Bright field transmission electron micrograph of the microstructure of as-melt spun Al-9wt%Cd-1.5wt%Mg, showing a homogeneous distribution of Cd(Mg) particles embedded in an Al(Mg) matrix.



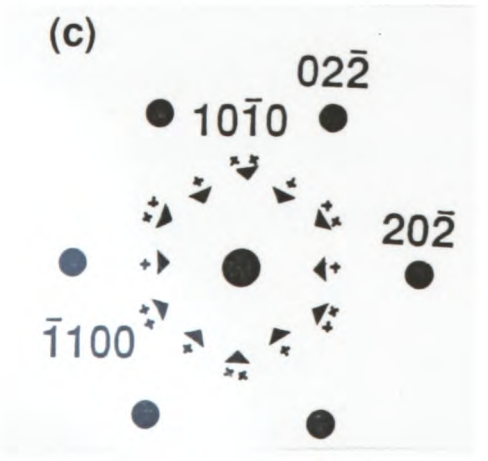


Fig. 5.14: Selected area diffraction patterns showing superimposed $<111>_{Al(Mg)}$ and $<0001>_{Cd(Mg)}$ zones from the Al(Mg) matrix and Cd(Mg) particles: (a) as-melt spun Al-4.5wt%Cd; (b) as-melt spun Al-9wt%Cd-1.5wt%Mg; and (c) corresponding schematic analysis with filled triangles corresponding to diffraction spots from $[0001]_{Cd(Mg)}$ zone, filled circles corresponding to diffraction spots from $[111]_{Al(Mg)}$ zone, and crosses corresponding to double diffraction.

Figs. 5.14(a) and (b) compare typical selected area electron diffraction patterns of superimposed $\langle 111\rangle_{Al(Mg)}$ and $\langle 0001\rangle_{Cd(Mg)}$ zones from as-melt spun Al-4.5wt%Cd and Al-9wt%Cd-1.5%Mg respectively. Fig. 5.14(c) shows a corresponding schematic analysis of the diffraction patterns in Figs. 5.14(a) and (b). Figs. 5.14(a) and (b) are similar, except for some extra superlattice diffraction spots from the Cd(Mg) particles in Al-9wt%Cd-1.5wt%Mg in Fig. 5.14(b). Diffraction patterns such as shown in Fig. 5.14 indicated that the orientation relationship between the Cd(Mg) particles and the Al(Mg) matrix in as-melt spun Al-9wt%Cd-1.5wt%Mg was the same as in as-melt spun Al-4.5wt%Cd, and can be described as follows:

$$\{111\}_{Al(Mg)}//\{0001\}_{Cd(Mg)}$$

$$\langle 110\rangle_{Al(Mg)}//\langle 11\bar{2}0\rangle_{Cd(Mg)}$$

Each Cd(Mg) particle was a single crystal, and there were four particle variants in each Al(Mg) grain depending upon which of the four $\{111\}_{Al(Mg)}$ planes was parallel to the $\{0001\}_{Cd(Mg)}$ plane.

Figs. 5.15(a) and (b) show typical selected area diffraction patterns of superimposed $\langle 001\rangle_{Al}$ and $\langle 30\bar{3}2\rangle_{Cd(Mg}$ zones from as-melt spun Al-4.5wt%Cd and Al-9wt%Cd-1.5wt%Mg respectively. In diffraction patterns such as shown in Fig. 5.15, the separation between corresponding $\{11\bar{2}0\}_{Cd(Mg)}$ and $\{110\}_{Al(Mg)}$ diffraction spots was clearly larger in Al-9wt%Cd-1.5wt%Mg than in Al-4.5wt%Cd, indicating a greater lattice disregistry in the ternary alloy. A similar effect can be seen on the $\langle 111\rangle_{Al(Mg)}//\langle 0001\rangle_{Cd(Mg)}$ diffraction patterns of Fig. 5.14, with an increased separation between each $\{10\bar{1}0\}_{Cd(Mg)}$ diffraction spot and its nearby double diffraction spots for Al-9wt%Cd-1.5wt%Mg.

The lattice parameter of the Al(Mg) matrix in both Al-4.5wt%Cd and Al-9wt%Cd-1.5wt%Mg is virtually identical to that of pure Al (Pearson, 1958), and can therefore be used as a standard to calculate directly the lattice parameters of the Cd(Mg) particles from diffraction patterns such as in Figs. 5.14 and 5.15. In Al-4.5wt%Cd, the Cd particle lattice parameters were calculated to be a=0.300nm and c=0.557nm, in good agreement with lattice parameters of a=0.298nm and c=0.562nm for pure Cd (Pearson, 1958). In Al-

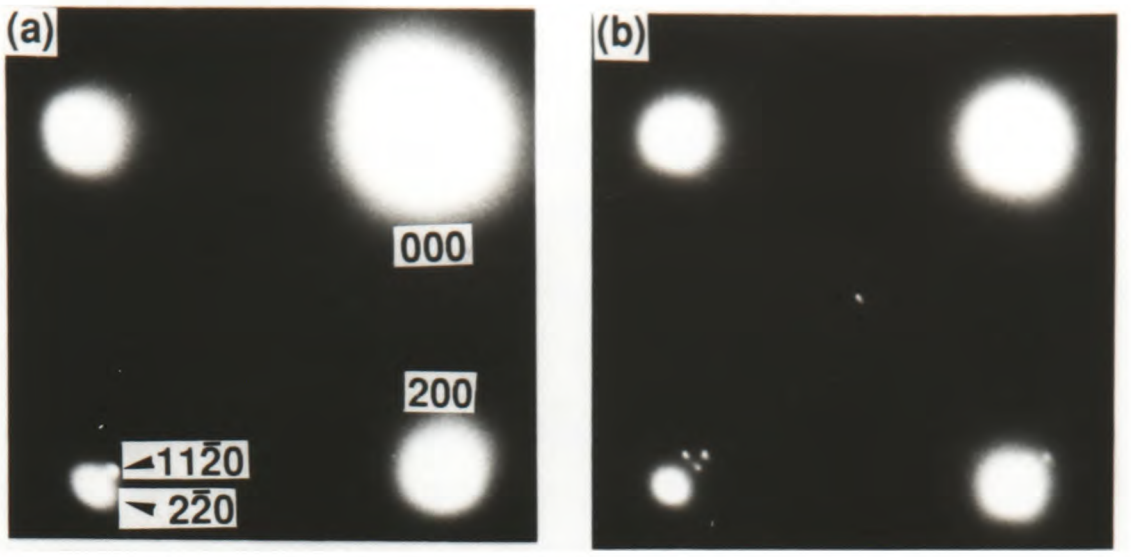


Fig. 5.15: Selected area diffraction patterns showing superimposed $<001>_{Al(Mg)}$ and $<30\bar{3}2>_{Cd(Mg)}$ zones from the Al(Mg) matrix and Cd(Mg) particles: (a) as-melt spun Al-4.5wt%Cd; (b) as-melt spun Al-9wt%Cd-1.5wt%Mg.

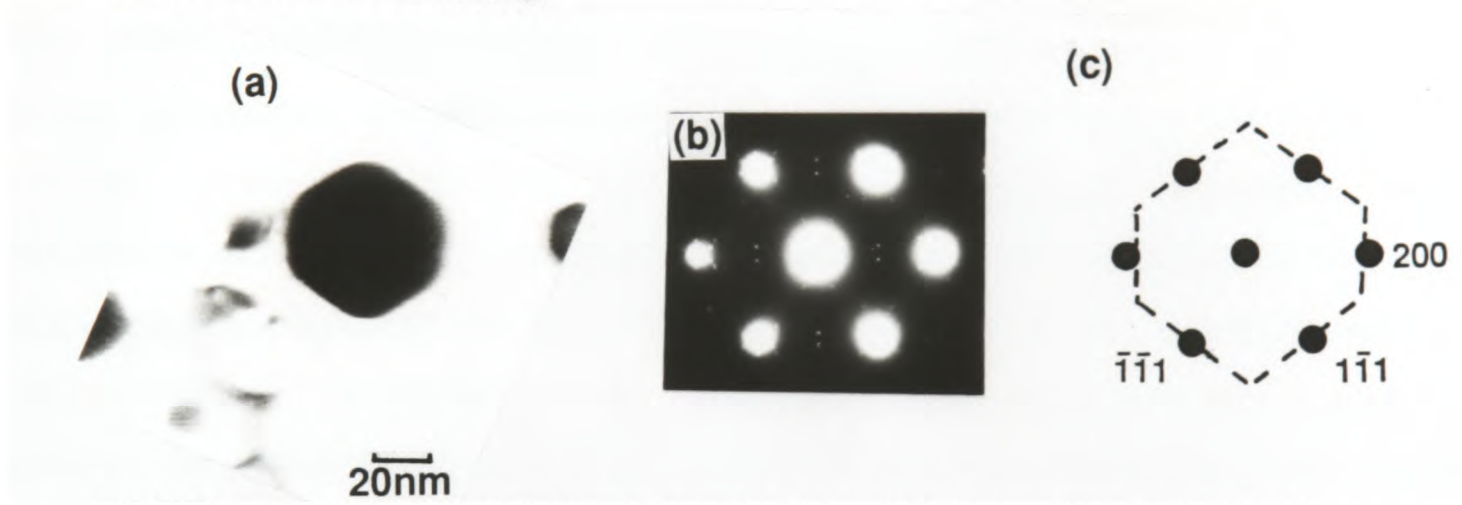


Fig. 5.16: (a) Bright field transmission electron micrograph from as-melt spun Al-9wt%Cd-1.5wt%Mg, showing the distorted hexagonal cross sectional shape of Cd(Mg) particles normal to the $<110>_{Al(Mg)}$ zone axis; (b) selected area diffraction pattern corresponding to (a), showing the <110> zone of the Al(Mg) matrix; and (c) schematic diffraction pattern and Cd(Mg) particle cross sectional shape.

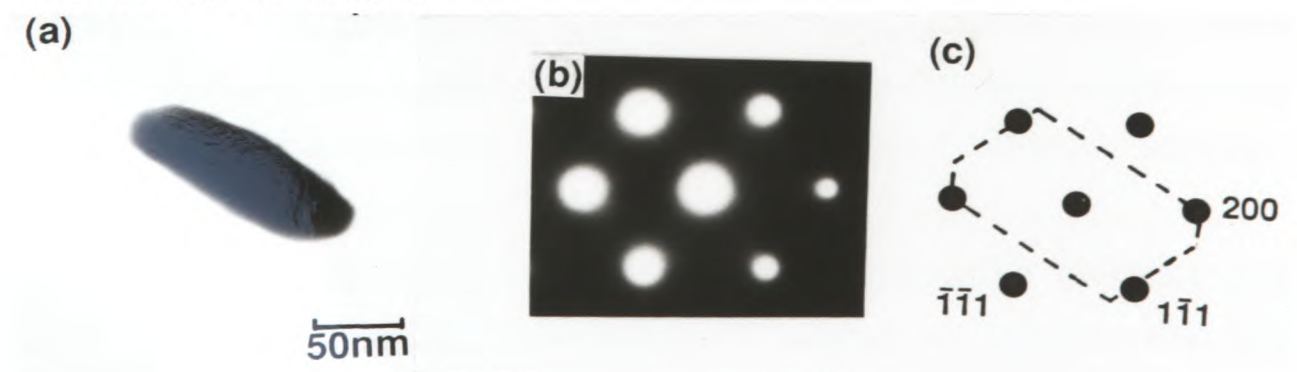


Fig. 5.17: (a) Bright field transmission electron micrograph from melt spun Al-9wt%Cd-1.5wt%Mg after heat treatment for 10^5s at 345°C, showing the elongated cross sectional shape of Cd(Mg) particles normal to the $<110>_{Al(Mg)}$ zone axis; (b) selected area diffraction pattern corresponding to (a), showing the <110> zone of the Al(Mg) matrix; and (c) schematic diffraction pattern and Cd(Mg) particle cross sectional shape.

9wt%Cd-1.5wt%Mg, the Cd(Mg) particle lattice parameters were calculated to be a=0.306nm,and c=0.535nm, corresponding to a composition of Cd-5.7wt%Mg for the Cd(Mg) particles (Pearson, 1958). Cd-5.7wt%Mg is equivalent to Cd-23at%Mg, very close to the stoichiometric composition of Cd_3Mg, so that the Cd(Mg) particles exhibit an ordered hcp DO_{19} structure, as indicated by the superlattice diffraction spots in Figs. 5.14(b) and 5.15(b). X-ray microprobe analysis showed that the ternary alloy composition was Al-8.79wt%Cd-1.45wt%Mg. With the measured Cd(Mg) particle composition of Cd-5.7wt%Mg, this corresponded to an Al(Mg) matrix composition of Al-1.0wt%Mg, equivalent to Al-1.1at%Mg.

In as-melt spun Al-9wt%Cd-1.5wt%Mg, the Cd(Mg) particles were found to have a distorted truncated octahedral shape bounded by $\{111\}_{Al(Mg)}$ and $\{100\}_{Al(Mg)}$ facets. Fig. 5.16(a) shows the characteristic distorted hexagonal cross sectional shape of the Cd(Mg) particles in melt spun Al-9wt%Cd-1.5wt%Mg with the electron beam parallel to a $\langle 110\rangle_{Al(Mg)}$ zone axis. Figs. 5.16(b) and (c) show corresponding selected area and schematic diffraction patterns respectively. As shown in Fig. 4.4(a), with the electron beam parallel to the $\langle 110\rangle_{Al(Mg)}$ zone axis, all the Cd(Mg) particle facets were parallel to the electron beam, so that the observed separation of each pair of opposite facets was equal to the true separation, and from the Gibbs-Wulff theorem was directly proportional to the facet surface energy (Martin and Doherty, 1976, Wulff, 1901). The ratio of the $\{100\}_{Al(Mg)}$ and $\{111\}_{Al(Mg)}//\{0001\}_{Cd(Mg)}$ surface energies was measured from the separations of the corresponding facets, giving a surface energy anisotropy of 1.15 for as-melt spun Al-9wt%Cd-1.5wt%Mg.

After heat treatment for 600s just above the Cd(Mg) particle melting point, ie at 400°C for Al-9wt%Cd-1.5wt%Mg, there was no change in either the Cd(Mg) particle shape, the orientation relationship between the Cd(Mg) particles and the Al(Mg) matrix, or the Cd(Mg) particle lattice parameters. As shown in Fig. 5.17, however, after heat treatment for 10^5s just below the Cd(Mg) particle melting point, ie at 345°C for Al-9wt%Cd-1.5wt%Mg, the Cd(Mg) particles became elongated to increase the surface area and decrease the separation of the two

$\{111\}_{Al(Mg)}//\{0001\}_{Cd(Mg)}$ facets. Fig. 5.17(a) shows the characteristic elongated cross sectional shape of the heat treated Cd(Mg) particles with the electron beam parallel to a $\langle 110\rangle_{Al(Mg)}$ zone axis. Figs. 5.17(b) and (c) show corresponding selected area and schematic diffraction patterns respectively. The ratio of the $\{100\}_{Al(Mg)}$ and $\{111\}_{Al(Mg)}//\{0001\}_{Cd(Mg)}$ surface energies was measured from the separations of the corresponding facets, giving a surface energy anisotropy of 1.90 for heat treated Al-9wt%Cd-1.5wt%Mg.

5.3.2 Cd(Mg) particle solidification

Figs. 5.18(a) and (b) compare typical differential scanning calorimeter traces of Cd(Mg) particle solidification exotherms from melt spun al-4.5wt%Cd and Al-9wt%Cd-1.5wt%Mg respectively. The Cd(Mg) particles in melt spun Al-9wt%Cd-1.5wt%Mg solidified with a broad exotherm extending over a temperature range of 319-353°C, followed by a sharp exotherm at an onset temperature close to 319°C. From the binary phase diagram of the Cd-Mg system (Massalski et al, 1986), the equilibrium melting point of Cd-5.7wt%Mg is 353°C. Therefore, the broad exotherm extended over an undercooling range of 0-34K, and the sharp exotherm was at an undercooling of 34K, below the melting point of the Cd-5.7wt%Mg particles.

5.3.3 Discussion

Differential scanning calorimeter traces such as in Fig. 5.18 give detailed information about the Cd(Mg) particle solidification kinetics in melt spun hypermonotectic Al-9wt%Cd-1.5wt%Mg alloys. The Cd(Mg) particle solidification behaviour can be described as follows. On cooling below the melting point, Cd(Mg) particles containing catalytic trace impurities nucleate and solidify with a variable undercooling, because of the variable catalytic potency of the trace impurities. The number of Cd-5.7wt%Mg particles in Al-9wt%Cd-1.5wt%Mg which are nucleated by catalytic trace impurities is large enough to be detected in the differential scanning calorimeter, producing a broad exotherm extending up to approximately 34K below the 353°C equilibrium melting point,

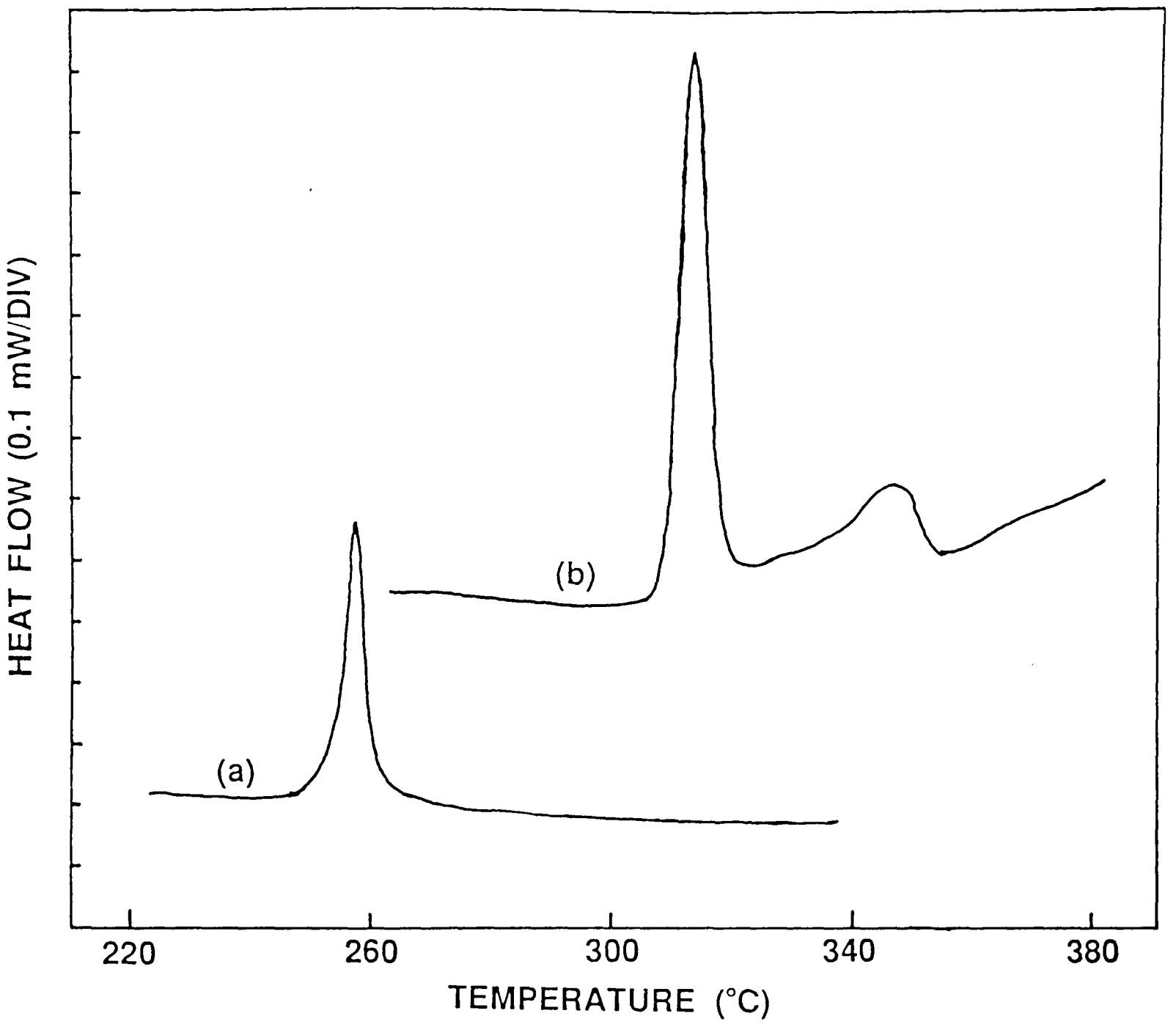


Fig. 5.18: Differential scanning calorimeter traces of Cd(Mg) particle solidification exotherms from (a) melt spun Al-4.5wt%Cd and (b) melt spun Al-9wt%Cd-1.5wt%Mg.

as shown in Fig. 5.18. Below 319°C all the Cd(Mg) particles which have not been nucleated by catalytic trace impurities are heterogeneously nucleated by the surrounding Al(Mg) matrix, with an epitaxial Al(Mg)-Cd(Mg) orientation relationship as shown in Fig. 5.14, and a sharp exotherm in the differential scanning calorimeter as shown in Fig. 5.18.

As shown in Figs. 5.16 and 5.17, equilibrated Cd(Mg) particles exhibit a shape bounded by a pair of elongated flat $\{111\}_{Al(Mg)}//\{0001\}_{Cd(Mg)}$ facets. The ratios of the $\{100\}_{Al(Mg)}$ and $\{111\}_{Al(Mg)}//\{0001\}_{Cd(Mg)}$ surface energies are measured from the equilibrated Cd(Mg) particles to be 1.90, which is larger than the ratio of the $\{100\}_{Al}$ and $\{111\}_{Al}//\{0001\}_{Cd}$ surface energies in Al-4.5wt%Cd, indicating that the addition of Mg to Cd particles embedded in Al increases the anisotropy of the surface energy. The epitaxial Al(Mg)-Cd(Mg) orientation relationship and the anisotropy of the Al(Mg)-Cd(Mg) surface energy indicate that the nucleation of Cd(Mg) solidification can take place on the $\{111\}_{Al(Mg)}$ facets. These facets are expected to survive above the Cd(Mg) melting point, in a similar way to Cd particles in binary Al-Cd discussed in Chapter 4.

The differential scanning calorimeter traces in Fig. 5.18 show that an undercooling of 34K is required to initiate the heterogeneous nucleation of Cd-5.7wt%Mg particle solidification by the {111} matrix facets of Al-1.0wt%Mg, 22K smaller than the undercooling of 56K required to initiate the heterogeneous nucleation of Cd particle solidification by the {111} matrix of Al. In other words, {111} Al facets are a less efficient solidification nucleant for Cd than {111} Al-1.0wt%Mg facets for Cd-5.7wt%Mg. However, the electron diffraction patterns in Figs. 5.14 and 5.15 show lattice disregistries between the Cd(Mg) particles and the Al(Mg) matrix on the $\{111\}_{Al(Mg)}//\{0001\}_{Cd(Mg)}$ facets of 4% and 7% for Al-4.5wt%Cd and Al-8wt%Cd-1.5%Mg respectively. Addition of Mg to Cd particles embedded in Al increases the lattice disregistry on the $\{111\}_{Al(Mg)}//\{0001\}_{Cd(Mg)}$ facets, but decreases the undercooling before the onset of Cd(Mg) particle solidification. Chemical interactions clearly dominate over structural lattice disregistry in determining the catalytic efficiency of nucleating solidification in Al-Cd-

Mg alloys.

5.4 Effect of Ge on the Heterogeneous Nucleation of Pb Solidification by Al

5.4.1 Microstructures

Figs. 5.19(a)-(d) show typical bright field transmission electron micrographs of the microstructures of the melt spun hypermonotectic Al-Pb-Ge alloys after heat treatment for 600s at 380°C in the differential scanning calorimeter. In all cases the Al-Pb-Ge alloy microstructure consisted of 5-150nm Pb particles embedded in an Al(Ge) matrix. At Ge concentrations less than or equal to 1wt%, the Ge atoms were fully dissolved in the Al matrix, whereas at Ge concentrations greater than or equal to 1.5wt%, the Ge atoms were not fully dissolved in the Al matrix, and 50-200nm Ge precipitates appeared in the resulting microstructures, as can be seen arrowed in Figs. 5.19(c) and (d).

Figs. 5.20(a) and (b) show typical selected area electron diffraction patterns from Al-5wt%Pb and Al-5wt%Pb-1.5wt%Ge respectively, and Fig. 5.20(c) shows a corresponding schematic analysis of the diffraction patterns. Figs. 5.20(a) and (b) show superimposed Pb and Al(Ge) ‹110› zones, indicating a cube-cube orientation relationship between the Pb particles and the Al(Ge) matrix (Moore et al, 1987). Fig. 5.21(a) shows a bright field transmission electron micrograph from Al-5wt%Pb-2wt%Ge, and Fig. 5.21(b) shows a dark field transmission electron micrograph from the same area formed with a $\{111\}_{Pb}$ diffraction spot. All the Pb particles in the bright field image in Fig. 5.21(a) were illuminated in the dark field image in Fig. 5.21(b), including the Pb particle in contact with a Ge precipitate as marked by the arrows in Fig. 5.21(a). In other words, contact with Ge precipitates did not affect the cube-cube orientation relationship between the Pb particles and the Al(Ge) matrix.

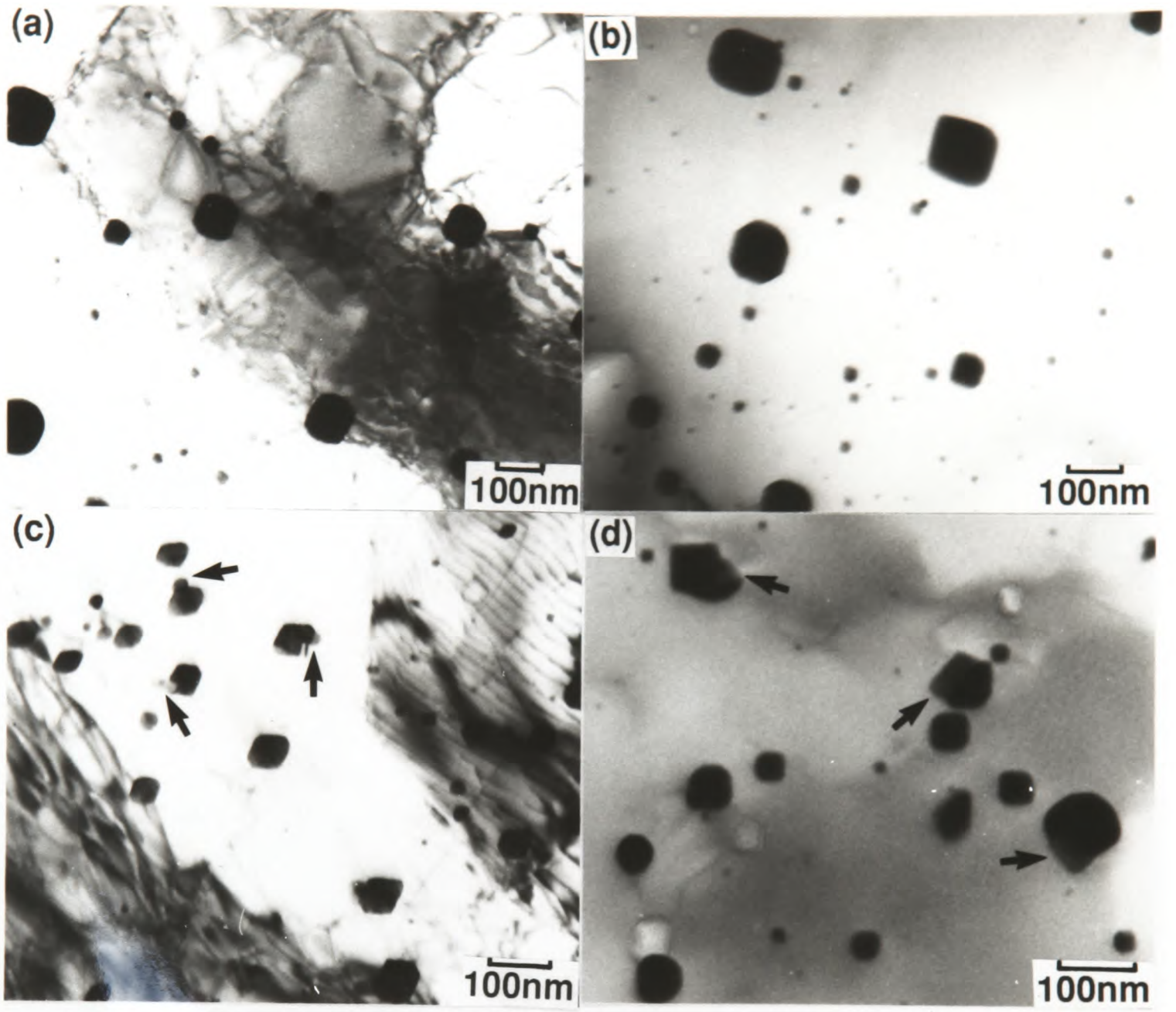


Fig. 5.19: Bright field transmission electron micrographs of the microstructure of melt spun Al-Pb-Ge alloys after heat treatment for 600s at 380°C as a function of Ge concentration: (a) Al-5wt%Pb-0.5wt%Ge; (b) Al-5wt%Pb-1wt%Ge; (c) Al-5wt%Pb-1.5wt%Ge; and (d) Al-5wt%Pb-2wt%Ge. Ge precipitates are arrowed.

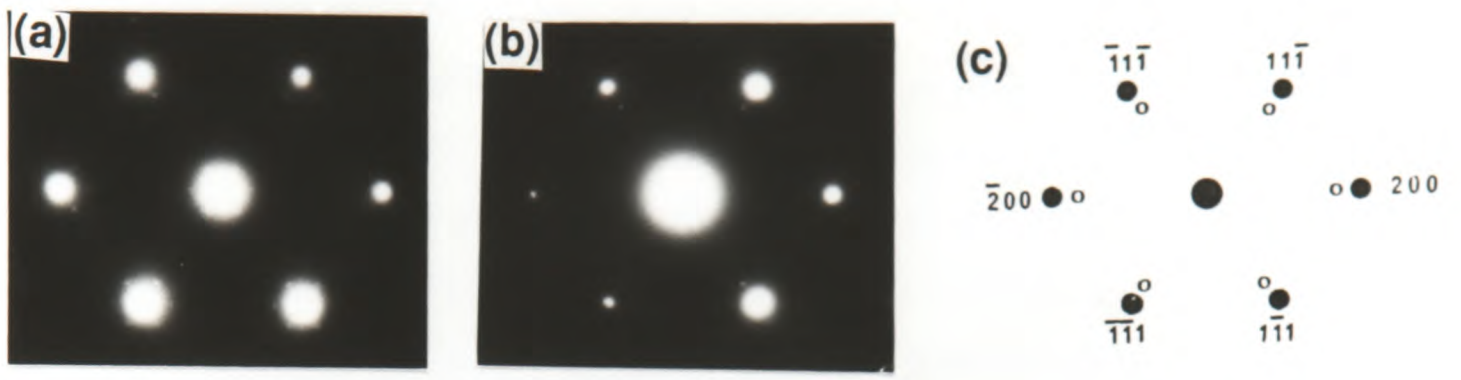


Fig. 5.20: Selected area diffraction patterns from melt spun Al-Pb-Ge alloys after heat treatment for 600s at 380°C, showing superimposed <110> zones from the Pb particles and the Al(Ge) matrix: (a) Al-5wt%Pb; (b) Al-5wt%Pb-1.5wt%Ge; (c) corresponding schematic analysis. Filled circles correspond to Al(Ge) matrix, open circles correspond to Pb particles.

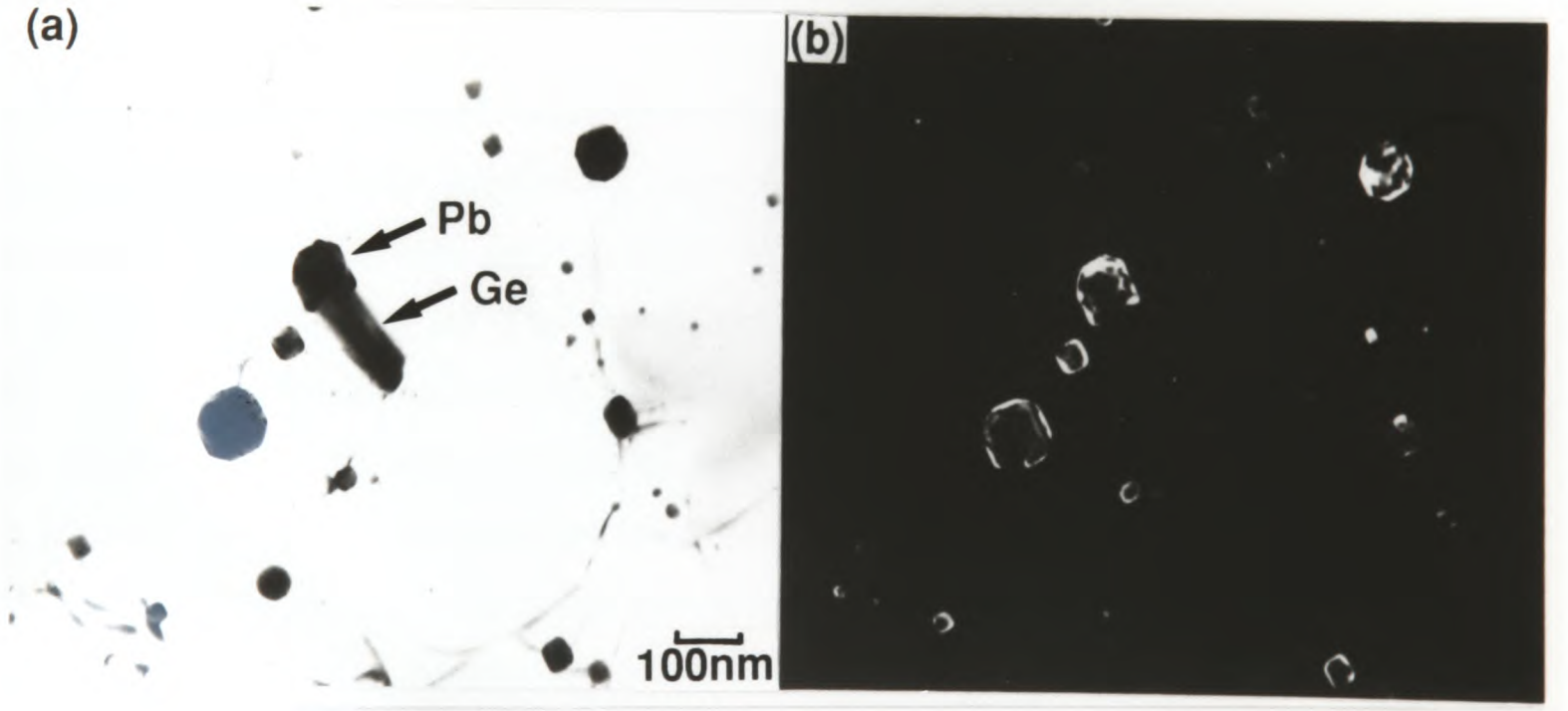


Fig. 5.21: (a) Bright field transmission electron micrograph from melt spun Al-5wt%Pb-2wt%Ge after heat treatment for 600s at 380°C; and (b) dark field transmission electron micrograph from the same area as (a), formed with a $\{111\}_{Pb}$ diffraction spot corresponding to cube-cube Al(Ge)-Pb orientation relationship.

Figs. 5.22(a) and 5.23(a) show bright field transmission electron micrographs of Al-5wt%Pb-0.5wt%Ge and Al-5wt%Pb-2wt%Ge respectively, and Figs. 5.22(b) and (c) and 5.23(b) and (c) show corresponding selected area and schematic diffraction patterns with the electron beam parallel to the $\langle 110 \rangle_{Al(Ge)}$ zone axis. Pb particles which were not in contact with Ge precipitates exhibited a distorted hexagonal cross sectional shape perpendicular to the $\langle 110 \rangle_{Al(Ge)}$ zone axis, as shown in Fig. 5.22(a), indicating a regular truncated octahedral Pb particle shape bounded by {100} and {111} facets (Moore et al, 1987). However, Pb particles which were in contact with Ge precipitates exhibited more irregular cross sectional shapes perpendicular to the $\langle 110 \rangle_{Al(Ge)}$ zone axis as shown in Fig. 5.23(a), indicating that the Pb particle shapes were not fully truncated octahedral. Another non-truncated octahedral Pb particle which was in contact with a Ge precipitate is marked by an arrow in Fig. 5.21(a).

5.4.2 Pb particle solidification

Figs. 5.24(a)-(e) show typical differential scanning calorimeter traces of the Pb particle solidification exotherms from the melt spun Al-Pb-Ge alloys as a function of Ge concentration. At Ge concentrations less than or equal to 1wt%, the Pb particles in the Al-Pb-Ge alloys solidified with a single sharp exotherm. The onset temperature of the solidification exotherm decreased from 305°C to 284°C as the Ge concentration increased from 0 to 1wt%, as shown in Figs. 5.24(a)-(c). At Ge concentrations greater than or equal to 1.5wt%, the Pb particles in the Al-Pb-Ge alloys solidified with two sharp exotherms. The onset temperature of the higher temperature exotherm was constant at 282°C, independent of Ge concentration, whereas the onset temperature of the lower temperature exotherm decreased from 274°C to 267°C as the Ge concentration increased from 1.5wt% to 2wt%, as shown in Figs. 5.24(d) and (e). Fig. 5.25 shows the variation of the onset temperature of the Pb particle solidification exotherm as a function of Ge concentration.

Figs. 5.26(a)-(d) show typical differential scanning calorimeter traces of the Pb particle solidification exotherms from Al-5wt%Pb-2wt%Ge, as a function of

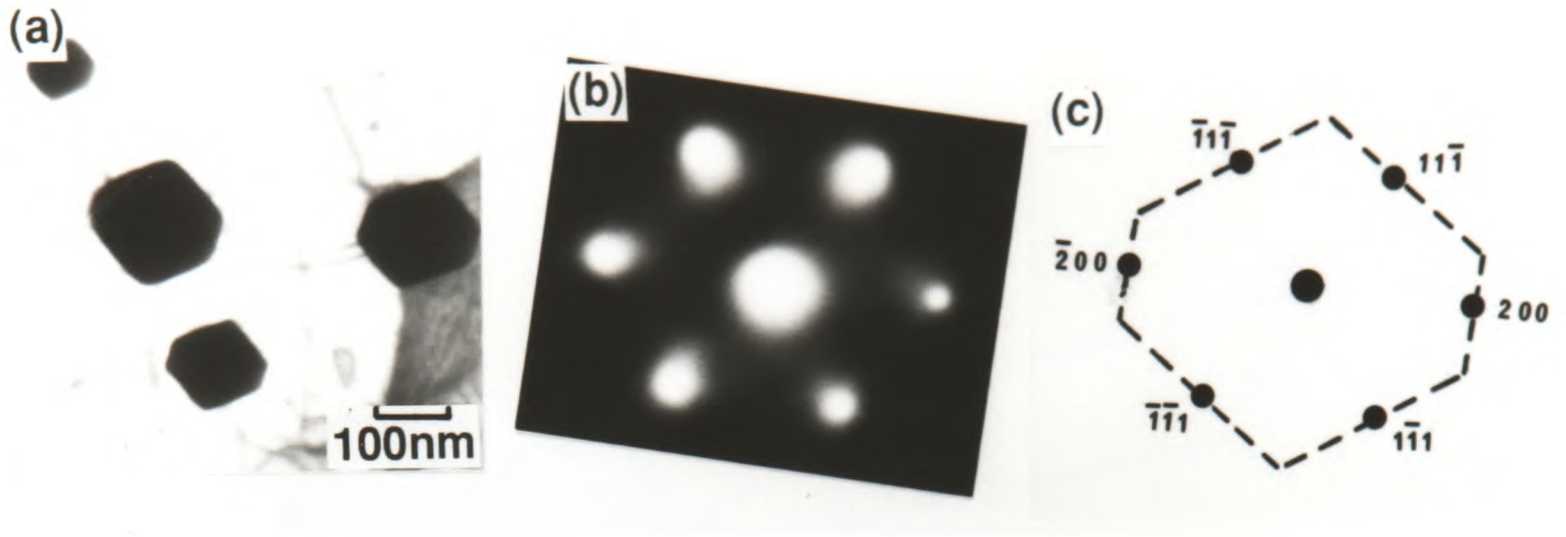


Fig. 5.22: (a) Bright field transmission electron micrograph of Pb particles not in contact with a Ge precipitate, showing a distorted hexagonal cross sectional shape perpendicular to the $<110>_{Al(Ge)}$ zone axis; and (b) and (c) corresponding selected area and schematic diffraction patterns showing the $<110>_{Al(Ge)}$ zone.

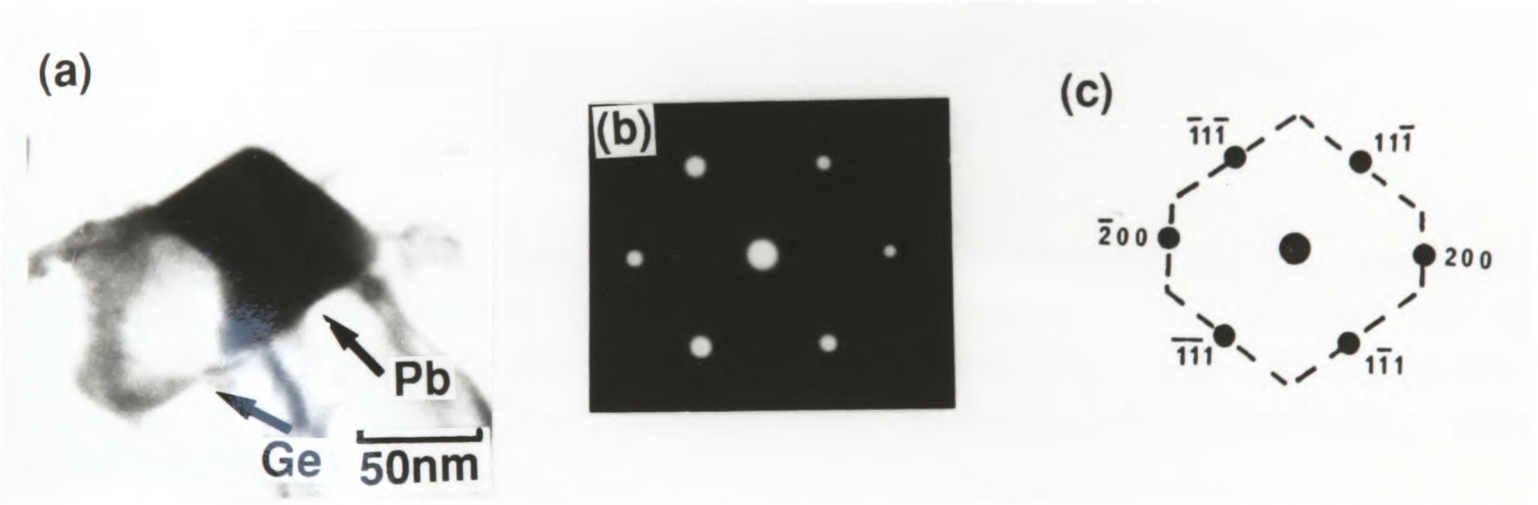


Fig. 5.23: (a) Bright field transmission electron micrograph of a Pb particle in contact with a Ge precipitate, showing an irregular cross sectional shape perperdicular to the $<110>_{Al(Ge)}$ zone axis; (b) and (c) corresponding selected area and schematic diffraction patterns showing the $<110>_{Al(Ge)}$ zone.

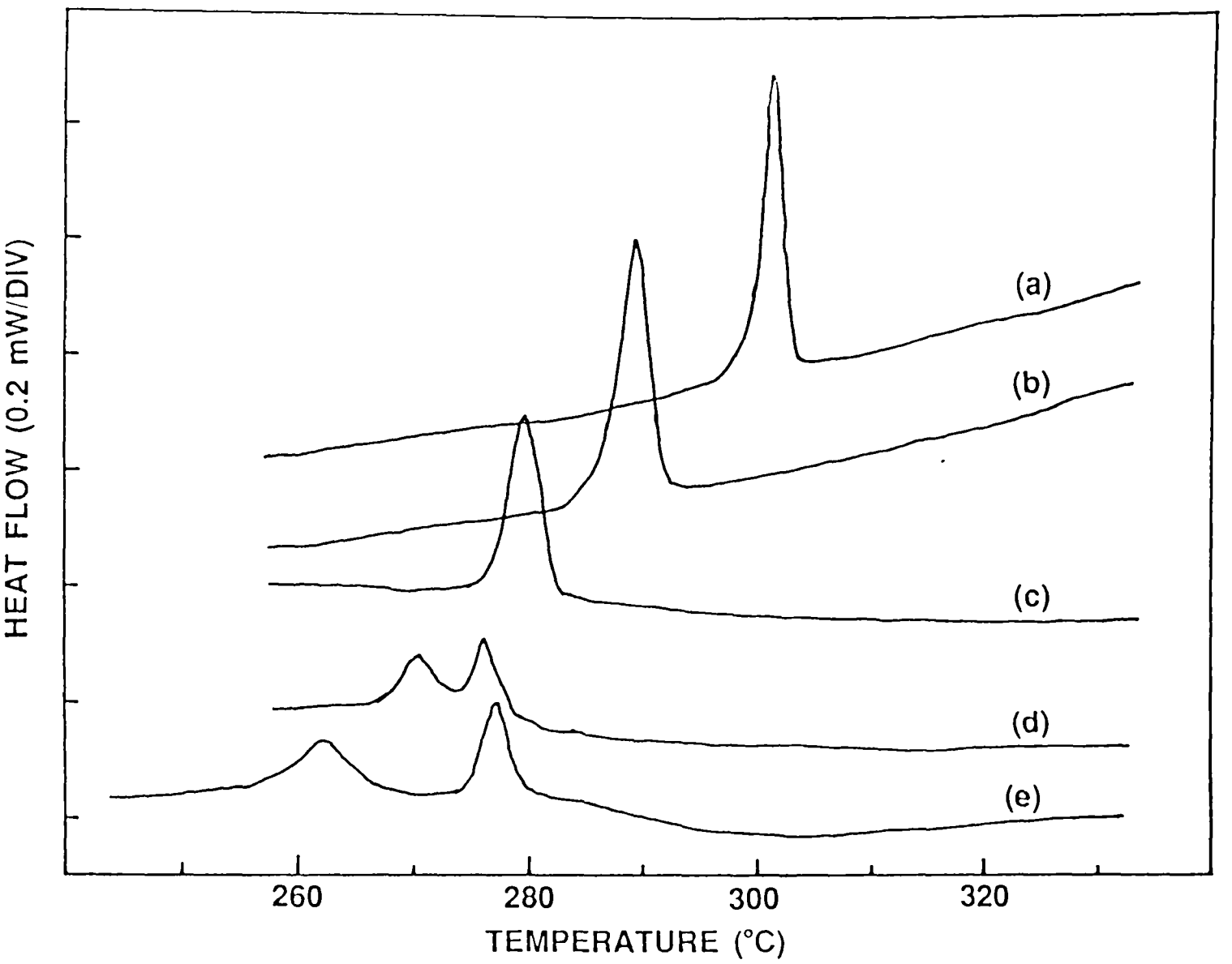


Fig. 5.24: Differential scanning calorimeter traces of Pb particle solidification exotherms from melt spun Al-Pb-Ge alloys as a function of Ge concentration: (a) Al-5wt%Pb; (b) Al-5wt%Pb-0.5wt%Ge; (c) Al-5wt%Pb-1wt%Ge; (d) Al-5wt%Pb-1.5wt%Ge; and (e) Al-5wt%Pb-2wt%Ge.

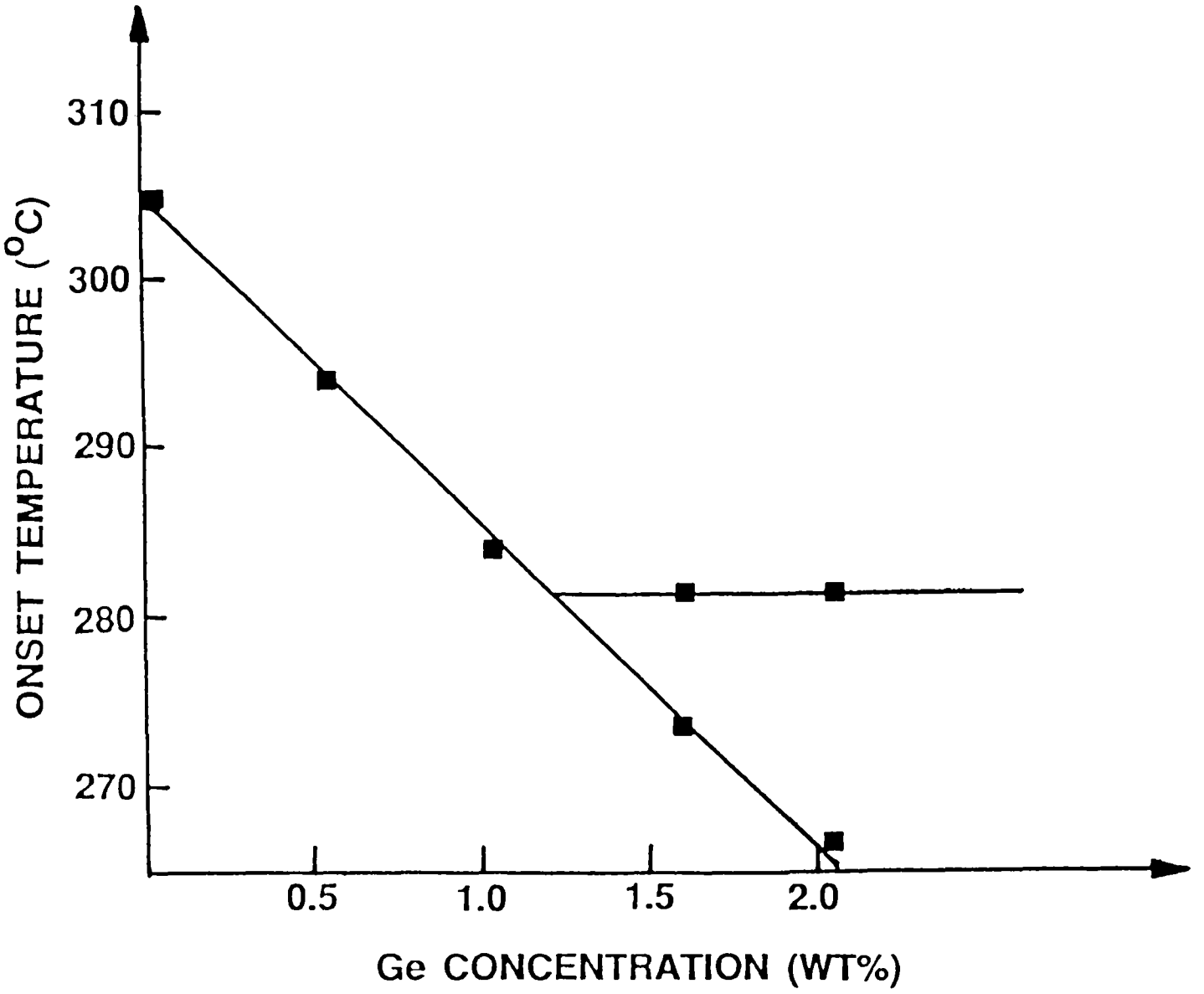


Fig. 5.25: Variation of the onset temperature of Pb particle solidification exotherms during cooling of melt spun Al-Pb-Ge alloys in the differential scanning calorimeter as a function of Ge concentration.

interrupted annealing time at 295°C, i.e. just before the onset of Pb particle solidification, during cooling from 380°C to 200°C. After interrupted annealing at 295°C, the subsequent higher temperature solidification exotherm shifted to slightly higher temperatures, and the lower temperature solidification exotherm broadened. The magnitude of these changes increased with increasing the interrupted annealing time as shown in Figs. 5.26(a)-(d). Fig. 5.27 shows two bright field transmission electron micrographs, comparing the microstructure of Al-5wt%Pb-2wt%Ge after cooling from 380°C to 200°C, (a) without interrupted annealing, and (b) after annealing at 295°C for 2400s. The microstructural effect of interrupted annealing at 295°C was to increase the number of Pb particles which were in contact with Ge precipitates, as shown in Figs. 5.27(a) and (b), indicating that interrupted annealing caused Ge precipitation from supersaturated solid solution in the Al matrix.

5.4.3 Discussion

5.4.3(I) Pb particle solidification

Differential scanning calorimeter traces such as in Figs. 5.24 and 5.26 give detailed information about the Pb particle solidification kinetics in the melt spun hypermonotectic Al-Pb-Ge alloys. At Ge concentrations less than or equal to 1wt%, the Pb particle solidification behaviour can be described as follows. On cooling below the Pb melting point, Pb particles containing catalytic trace impurities nucleate and solidify with a variable undercooling, because of the variable catalytic potency of the trace impurities. The number of Pb particles which are nucleated by catalytic trace impurites is too small to be detected in the differential scanning calorimeter. On cooling below a critical temperature in the range 284°C-305°C, ie an undercooling in the range 22K-43K below the Pb particle melting point, all the Pb particles which have not been nucleated by catalytic trace impurities are heterogeneously nucleated by the surrounding Al(Ge) matrix. Heterogeneous nucleation takes place with an epitaxial Al(Ge)-Pb orientation relationship as shown in Fig. 5.20, and sharp exotherms in the differential scanning calorimeter as shown in Fig. 5.24. As

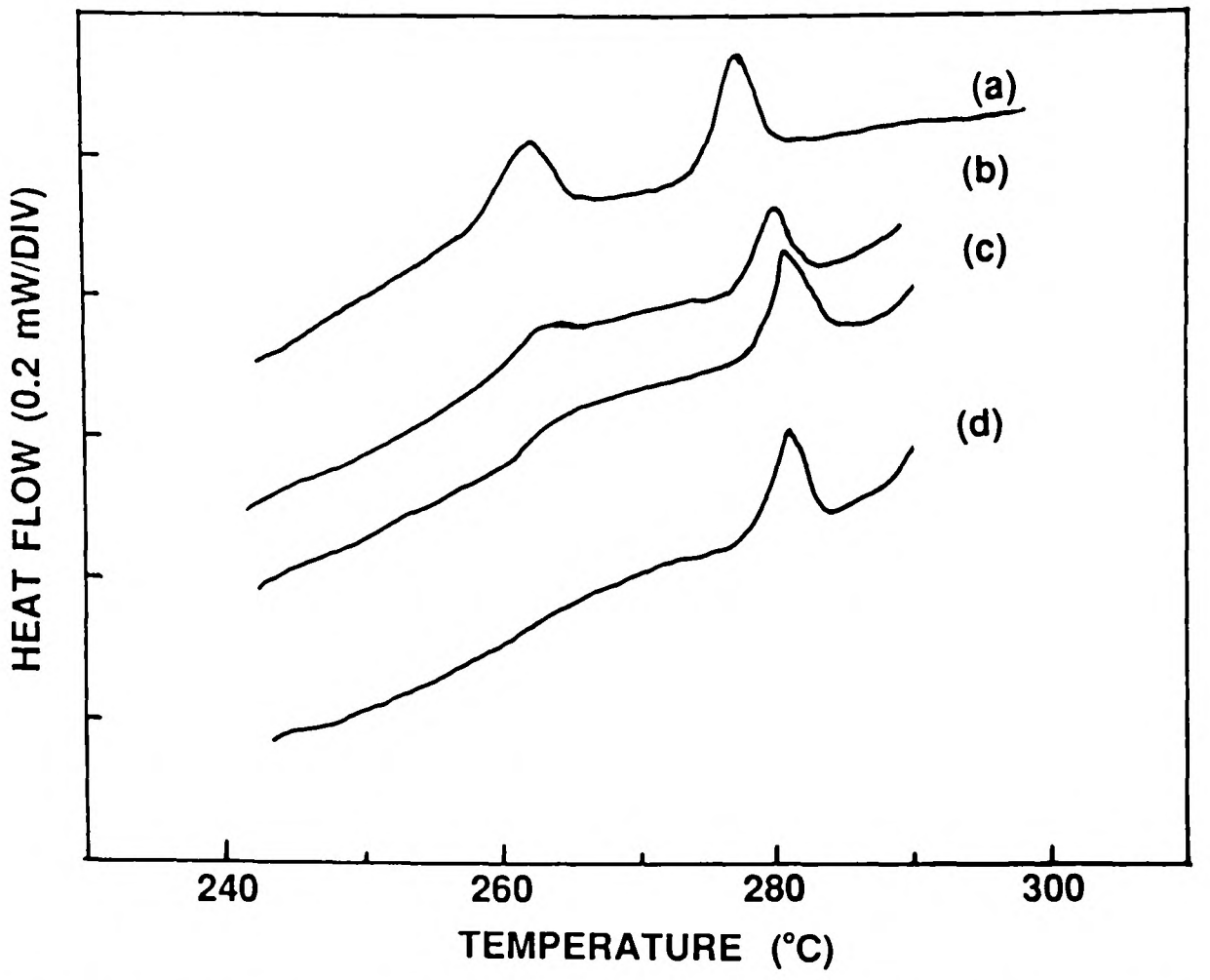


Fig. 5.26: Differential scanning calorimeter traces of Pb particle solidification exotherms from melt spun Al-5wt%Pb-2wt%Ge as a function of interrupted holding time at 295°C during cooling from 380°C to 200°C in the differential scanning calorimeter: (a) no interruption; (b) 1200s; (c) 2400s; and (d) 3600s.

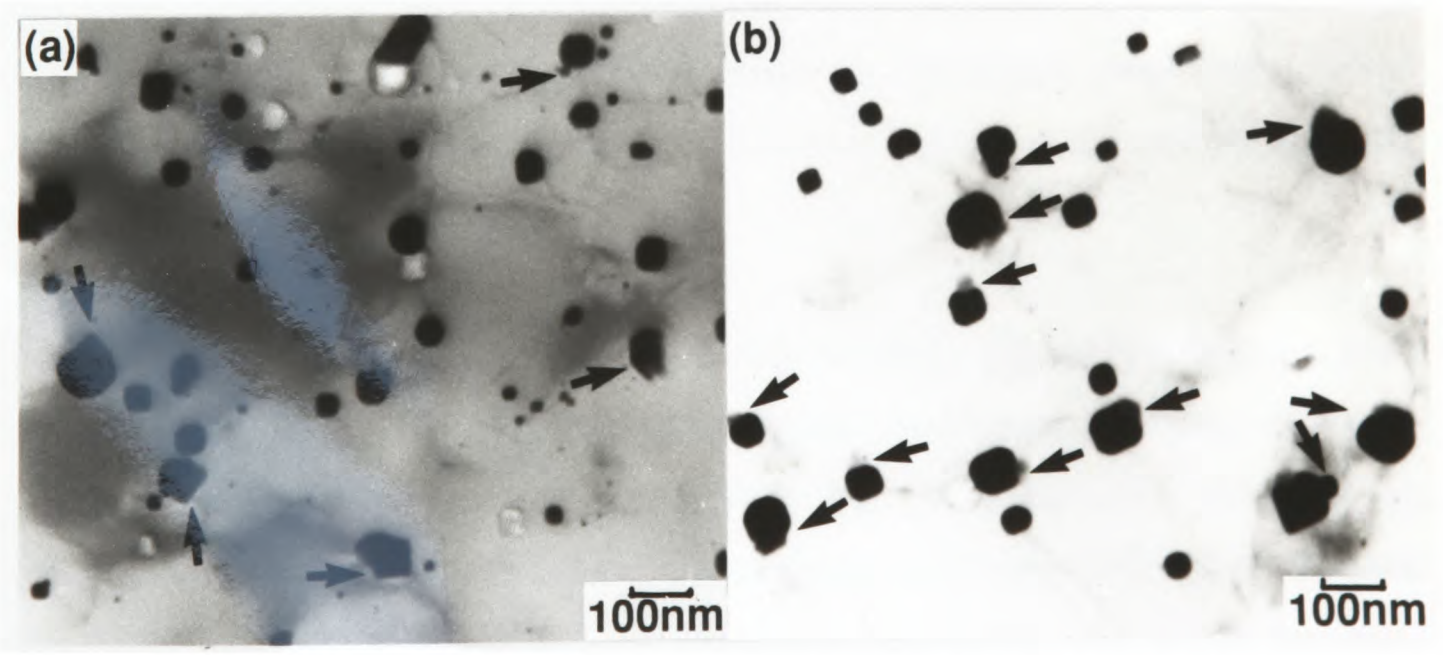


Fig. 5.27: Bright field transmission electron micrographs from melt spun Al-5wt%Pb-2wt%Ge as a function of interrupted holding time at 295°C during cooling from 380°C to 200°C in the differential scanning calorimeter: (a) no interruption; (b) 2400s. Pb particles in contact with Ge precipitates are arrowed.

shown in Fig. 5.22, the Pb particles exhibit a truncated octahedral shape bounded by {100} and {111} facets, and the heterogeneous nucleation of Pb particle solidification can take place on the {111} facets which are expected to survive at temperatures above the Pb melting point, similarly to Pb particles in binary Al-Pb alloys as discussed by Moore et al (1987).

The differential scanning calorimeter traces in Fig. 5.24 show that the onset temperature for Pb particle solidification decreases linearly from 305°C to 284°C, and the corresponding undercooling below the Pb particle melting point increases linearly from 22K to 43K, with increasing Ge concentration from 0 to 1wt% in the Al(Ge) matrix. In other words, the efficiency of the Al(Ge) matrix as a nucleant for Pb solidification decreases with increasing Ge concentration. However, the lattice parameter of the Al(Ge) solid solution increases with increasing Ge concentration, so that the lattice disregistry between the Pb particles and the Al(Ge) matrix on the {111} facets decreases slightly from 18% to 17% as Ge concentration increases from zero to 1wt%, measured from the selected area diffraction patterns such as Figs. 5.20(a) and (b) (Pearson, 1958). Addition of Ge to the Al matrix increases the undercooling before the onset of solidification of Pb particles embedded in an Al matrix, but decreases the lattice disregistry between the Pb particles and the Al matrix. Chemical interactions clearly dominate over structural lattice disregistry in determining the catalytic efficiency of nucleating solidification in Al-Pb-Ge alloys.

At Ge concentrations greater than or equal to 1.5wt%, Pb particles in melt spun Al-Pb-Ge alloys solidify with two exotherms, as shown in Figs. 5.24(d) and (e). After interrupted annealing at 295°C, i.e. just before the onset of Pb particle solidification, the higher temperature exotherm shifts to higher temperatures, and the lower temperature exotherm broadens, as shown in Fig. 5.26. This corresponds to a microstructural change, with Ge precipitation from supersaturated solid solution in the Al(Ge) matrix, and an increase in the number of Pb particles in contact with Ge precipitates, as shown in Figs. 5.27(a) and (b). In other words, the higher temperature exotherms in Figs.

5.26(d) and (e) correspond to the solidification of Pb particles in contact with Ge precipitates; and the lower temperature exotherms correspond to the solidification of Pb particles not in contact with Ge precipitates and surrounded by a supersaturated Al(Ge) matrix.

There are two possible mechanisms for the effect of Ge precipitates on the heterogeneous nucleation of Pb particles embedded in an Al(Ge) matrix:

(1) Solidification of the Pb particles may take place by catalytic nucleation at the Al(Ge) matrix-Ge precipitate interfaces, rather than on the surrounding Al(Ge) matrix. This mechanism is supported strongly by the cube-cube orientation relationship observed between the Pb particles and the surrounding Al(Ge) matrix, independent of the presence of Ge precipitates.

(2) Solidification of the Pb particles may take place by catalytic nucleation on the surfaces of the Ge precipitates, rather than on the surrounding Al(Ge) matrix. To test this possibility further, some additional differential scanning calorimeter experiments were undertaken on specimens of melt spun Ge-5wt%Pb. Fig. 5.28 shows a typical differential scanning calorimeter trace of the resulting Pb particle solidification exotherms. The higher temperature exotherm with an onset temperature of 327°C corresponds to solidification of grain boundary Pb particles, and the Pb particles containing impurities, while the lower temperature exotherm with an onset temperature of 291°C corresponds to solidification of pure Pb particles. This shows that the onset of solidification of Pb particles embedded in a Ge matrix is at an undercooling of 36K below the Pb melting point. This undercooling is lower than the undercooling of the higher temperature exotherm in Figs. 5.24(d) and (e). In other words, Pb particle solidification in the melt spun Al-Pb-Ge alloys is not catalysed directly by the contacting Ge precipitate surfaces, perhaps because of an unsuitable Ge precipitate surface crystallography.

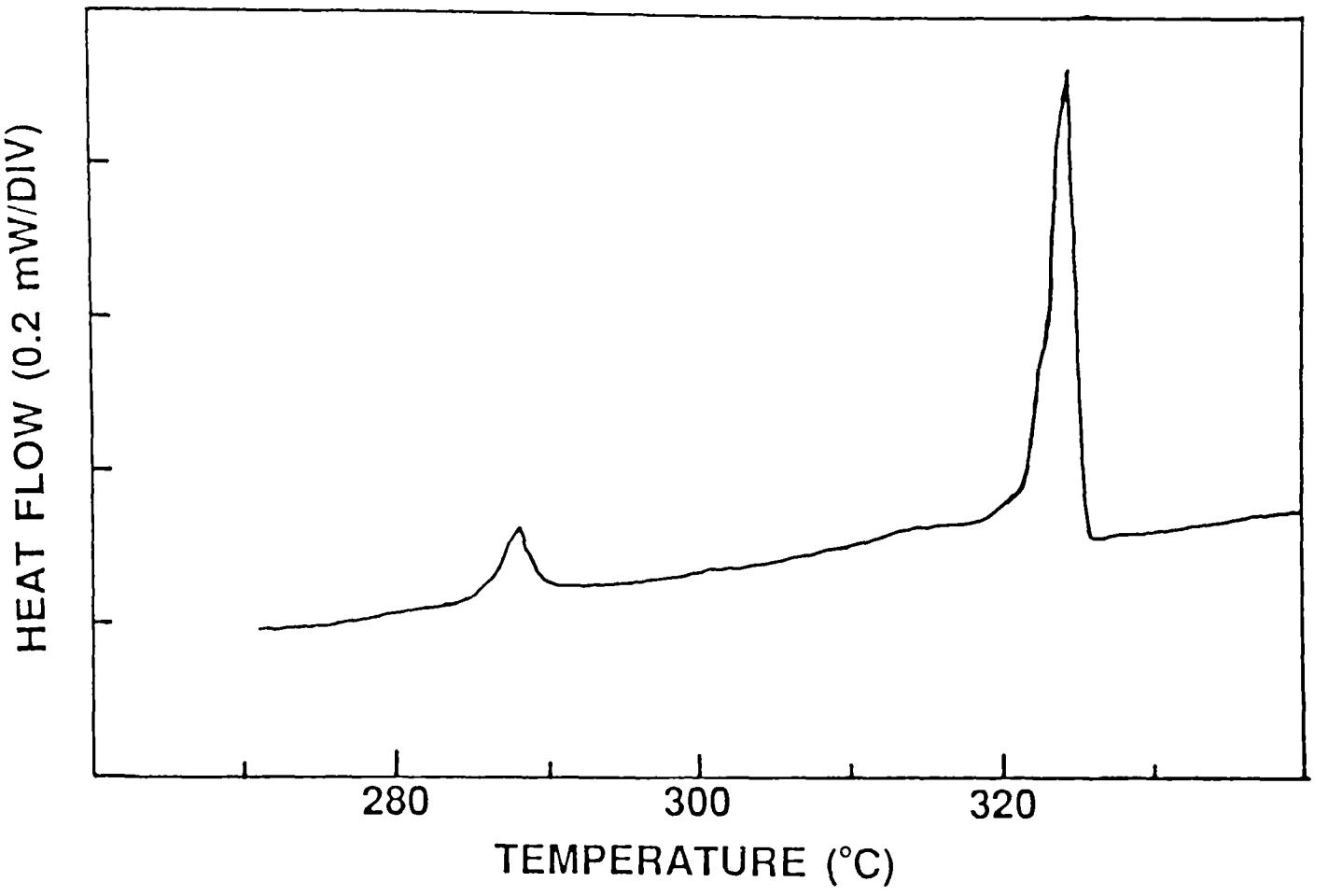


Fig. 5.28: Differential scanning calorimeter trace of Pb particle solidification exotherms from melt spun Ge-5wt%Pb.

5.4.3(II) Nucleation kinetics

Each Pb particle in the ternary Al-Pb-Ge alloys solidifies as a single crystal, as shown in Figs. 5.20 and 5.21, indicating that there is only one nucleation event per Pb particle. In addition, Pb particle solidification takes place at an undercooling in the range 22 to 60K, as shown in Figs. 5.24, indicating that there is a negligible post-nucleation solidification time in each Pb particle. Differential scanning calorimeter traces such as shown in Fig.5.24 can, therefore, be used to calculate the contact angle Θ at the solid Al(Ge)-solid Pb-liquid Pb triple point, by using the analytical method described in section 4.4.5 (Kim et al, 1990). Figs. 5.29(a) and (b) show the cooling rate variations of the Pb particle solidification peak temperature and exothermic peak height respectively, plotted according to equations (4.8) and (4.9) for melt spun Al-5wt%Pb-0.5wt%Ge and Al-5wt%Pb-1wt%Ge respectively. Best fit slopes give values of B from which the contact angles can be calculated, taking σ_{SL}=55mJ/m^2 (Jones, 1974) and L = 250MJ/m^3 (Brandes and Smithells, 1983). Figs. 5.30(a) and (b) show the resulting contact angles as a function of Ge concentration in the Al(Ge) matrix. As expected from the linear decrease in nucleation undercooling, cosΘ decreases linearly with increasing Ge concentration. In other words, the catalytic efficiency of Al(Ge) as a heterogeneous nucleation for Pb solidification decreases linearly with increasing Ge concentration.

5.5 Effect of Si on the Heterogeneous Nucleation of Pb Solidification by Al

5.5.1 Microstructures

Fig. 5.31 shows a typical bright field transmission electron micrograph of the microstructure of melt spun Al-5wt%Pb-0.2wt%Si, after heat treatment for 600s at 380°C in the differential scanning calorimeter. In all the melt spun Al-Pb-Si alloys, with Si content ranging from 0.2-1wt%, the microstructure consisted of a bimodal distribution of Pb particles embedded in an Al(Si)

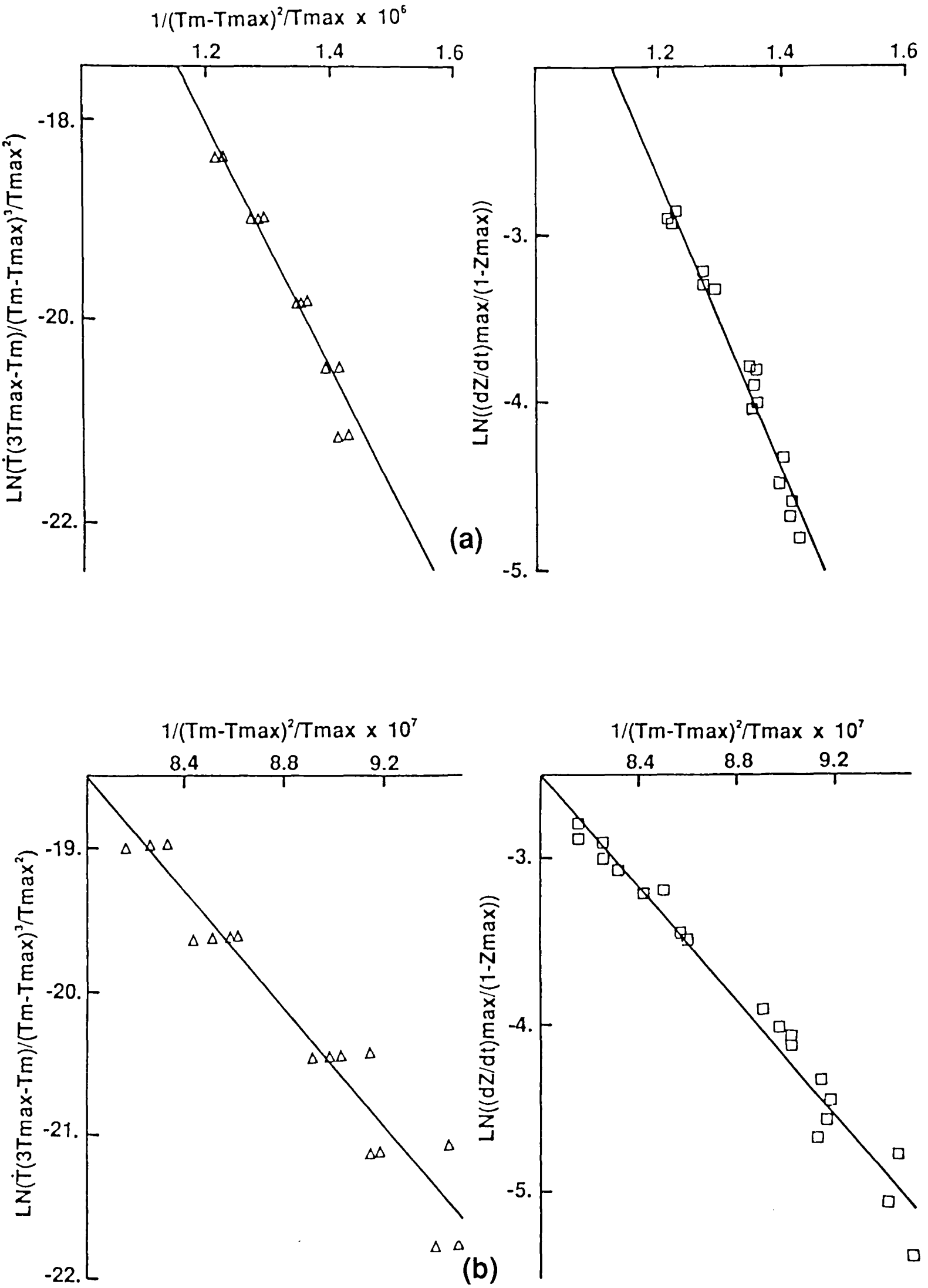


Fig. 5.29: Pb particle solidification peak temperature and exothermic peak height for melt spun Al-Pb-Ge alloys as functions of the cooling rate in the differential scanning calorimeter, plotted according to equations (4.8) and (4.9) in the form: $\ln\{\dot{T}(3T_{max}-T_m)/(T_m-T_{max})^3T_{max}^2\}$ and $\ln\{(dZ/dt)_{max}/(1-Z_{max})\}$ versus $1/(T_m-T_{max})^2T_{max}$ respectively: (a) Al-5wt%Pb-0.5wt%Ge; and (b) Al-5wt%Pb-1wt%Ge.

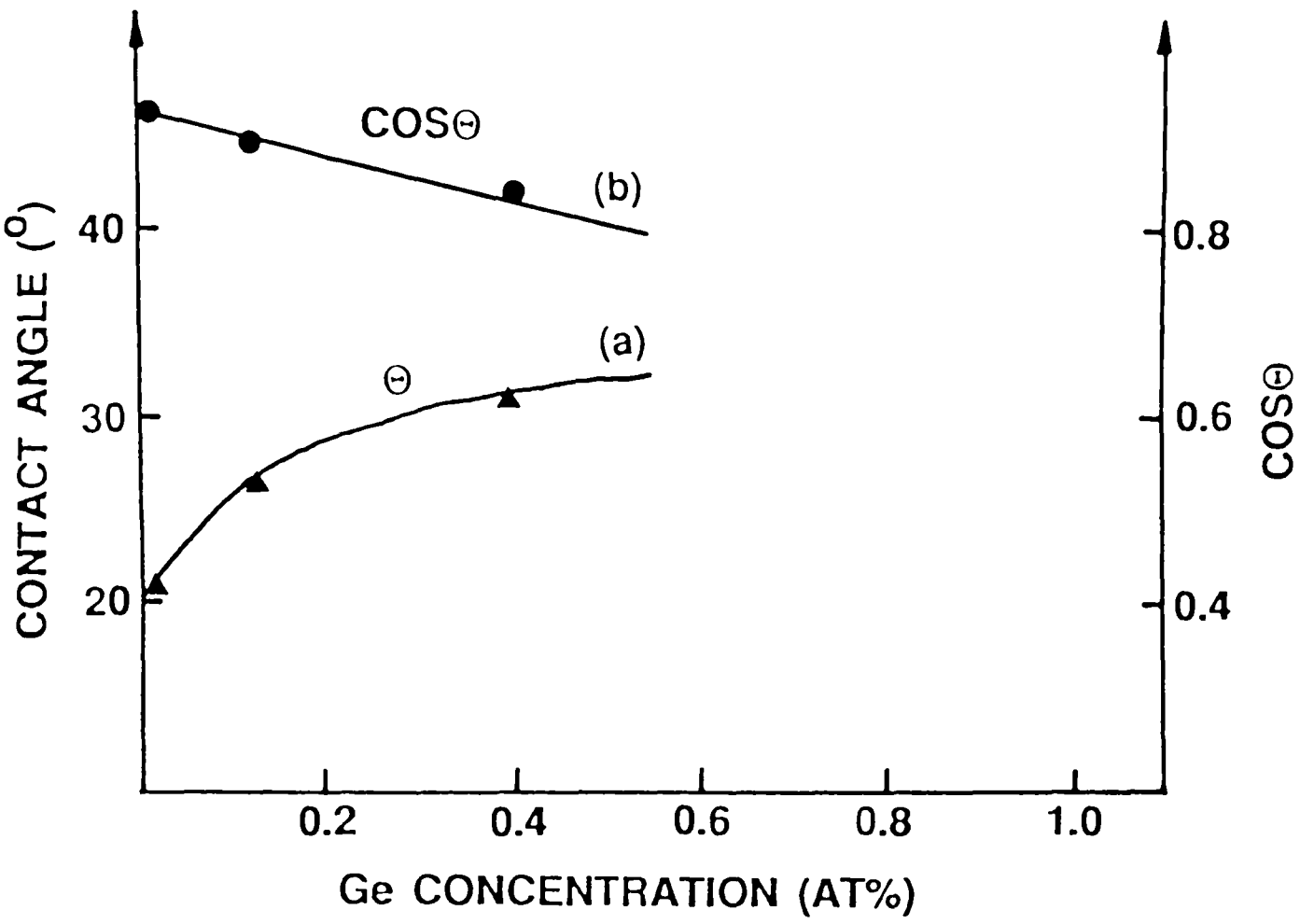


Fig. 5.30: Contact angles Θ at the solid Al(Ge)-solid Pb-liquid Pb triple point, calculated from the Pb particle solidification exotherms from melt spun Al-Pb-Ge alloys, and plotted in the form: (a) Θ and (b) cosΘ versus Ge concentration.

matrix, as shown in Fig. 5.31. The larger Pb particles ranged from 40-200nm in diameter, and the smaller Pb particles ranged from 5-10nm in diameter. Fig. 5.32(a) shows a typical selected area electron diffraction pattern from melt spun Al-5wt%Pb-0.2wt%Si, and Fig. 5.32(b) shows a corresponding schematic analysis of the diffraction pattern. Fig. 5.32(a) shows superimposed Pb and Al(Si) ‹110› zones, indicating a cube-cube orientation relationship between the Pb particles and the Al(Si) matrix (Moore et al, 1987). At Si concentrations less than or equal to 0.2wt%Si, the Si atoms were fully dissolved in the Al matrix, whereas at Si concentrations above 0.2wt%, the Si atoms were not fully dissolved in the Al matrix, and Si precipitates appeared in the resulting microstructures.

Fig. 5.33 shows a high magnification bright field transmission electron micrograph of one of the Pb particles not in contact with a Si precipitate in melt spun Al-5wt%Pb-0.7wt%Si, with the electron beam parallel to the $\langle 110 \rangle_{Al(Si)}$ zone axis. All Pb particles not in contact with a Si precipitate exhibited a distorted hexagonal cross sectional shape perpendicular to the $\langle 110 \rangle_{Al(Si)}$ zone axis, indicating a truncated octahedral Pb particle shape bounded by {100} and {111} facets (Moore et al, 1987). Fig. 5.34(a) shows a high magnification bright field transmission electron micrograph of three large Pb particles in contact with Si precipitates in melt spun Al-5wt%Pb-0.7wt%Si, and Fig. 5.34(b) shows a dark field transmission electron micrograph from the same area formed with an $\{002\}_{Pb}$ diffraction spot corresponding to the cube-cube orientation relationship. The three large Pb particles in Fig. 5.34(a) were in contact with Si precipitates, but were still illuminated in the dark field image in Fig. 5.34(b), indicating that contact with Si precipitates did not affect the cube-cube orientation relationship between the Pb particles and the Al(Si) matrix. However, the Pb particles in contact with Si precipitates exhibited irregular cross sectional shapes as shown in Fig. 5.34(a), indicating that contact with Si precipitates distorted the truncated octahedral Pb particle shape.

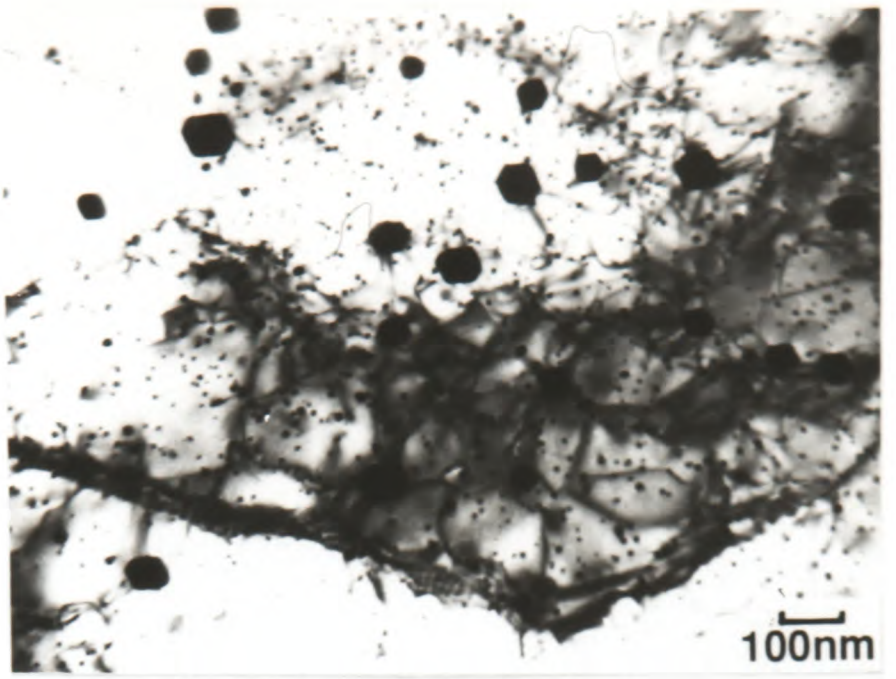


Fig. 5.31: Bright field transmission electron micrograph of the microstructure of melt spun Al-5wt%Pb-0.2wt%Si after heat treatment for 600s at 380°C, showing a bimodal distribution of Pb particles embedded in an Al(Si) matrix.

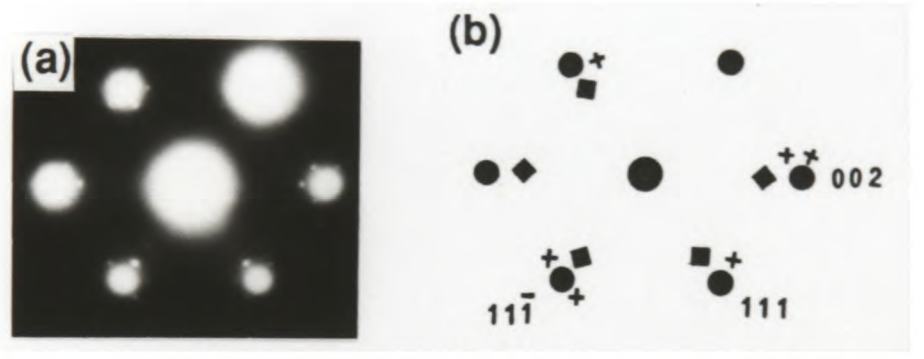


Fig. 5.32: (a) Selected area diffraction pattern showing superimposed <110> zones from the Al(Si) matrix and the Pb paritcles; and (b) corresponding schematic analysis.
Circles - Al(Si); Squares - Pb; Crosses - double diffraction

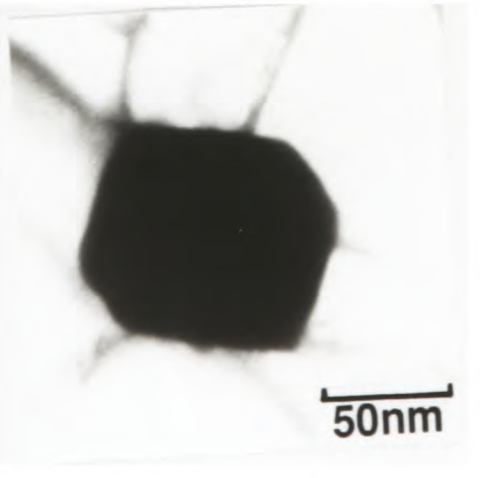


Fig. 5.33: Bright field transmission electron micrograph of a Pb particle not in contact with a Si precipitate, with the electron beam parallel to the $<110>_{Al(Si)}$ zone axis.

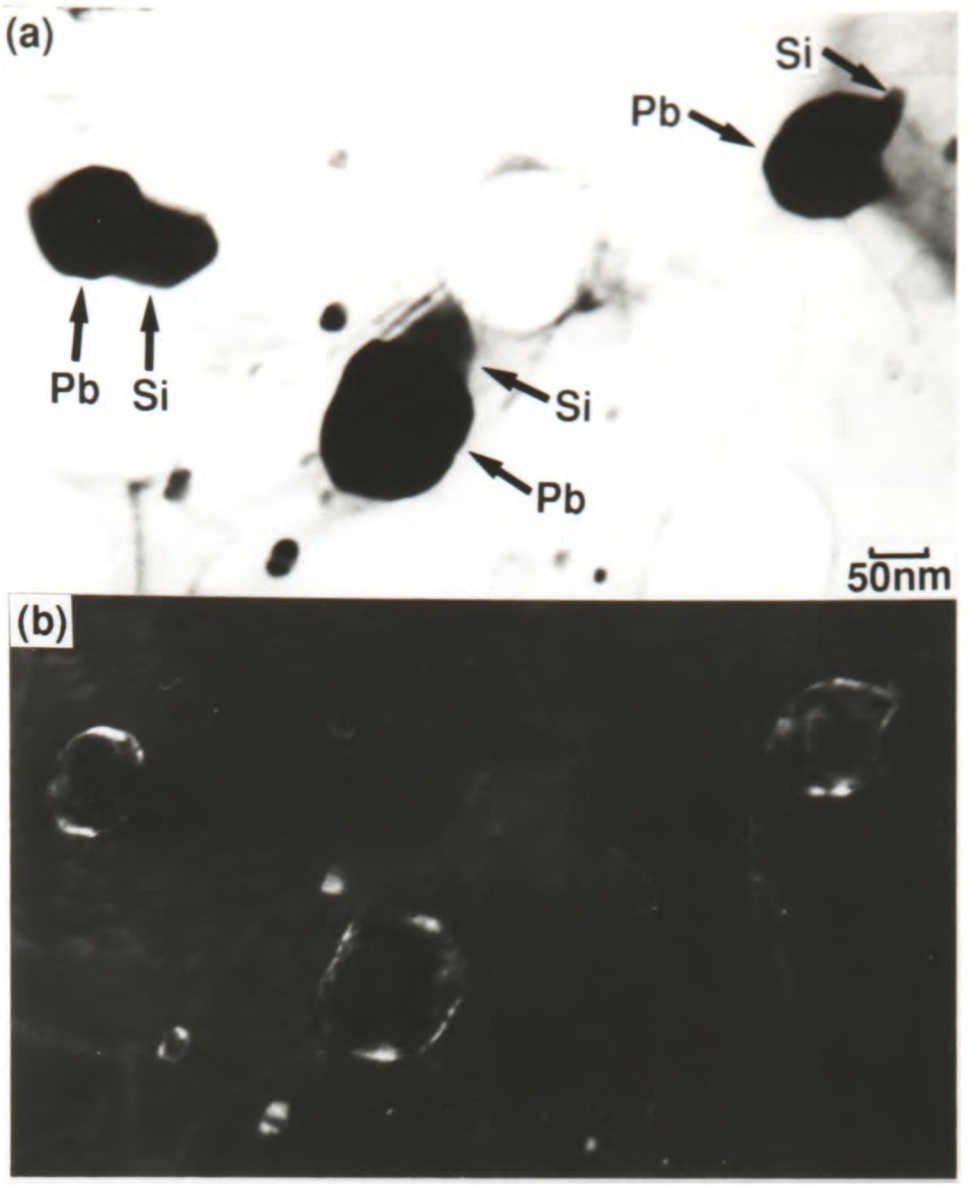


Fig. 5.34: (a) Bright field transmission electron micrograph of Pb particles in contact with Si precipitates; and (b) corresponding dark field transmission electron micrograph formed with an $\{002\}_{Pb}$ diffraction spot corresponding to the cube-cube orientation relationship.

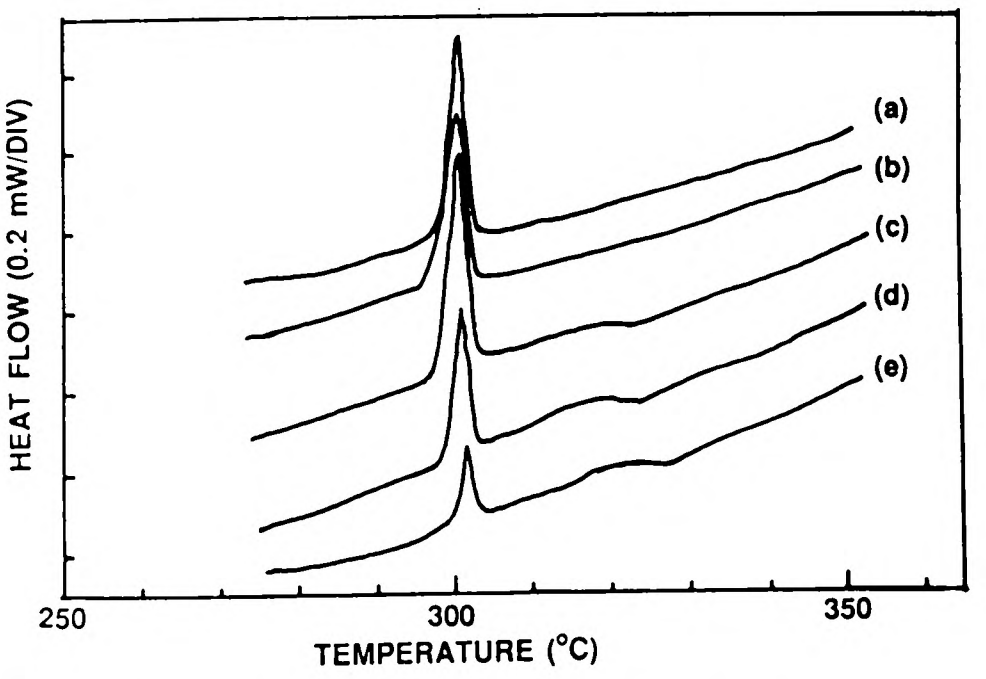


Fig. 5.35: Differential scanning calorimeter traces of Pb particle solidification exotherms from melt spun Al-Pb-Si alloys as a function of Si concentration: (a) Al-5wt%Pb; (b) Al-5wt%Pb-0.2wt%Si; (c) Al-5wt%Pb-0.5wt%Si; (d) Al-5wt%Pb-0.7wt%Si; and (e) Al-5wt%Pb-1wt%Si.

5.5.2 Pb particle solidification

Figs. 5.35(a)-(e) show typical differential scanning calorimeter traces of the Pb particle solidification exotherms from the melt spun Al-Pb-Si alloys as a function of Si concentration. At Si concentrations less than or equal to 0.2wt%, the Pb particles solidified with a single sharp exotherm, at a constant onset temperature of 305°C corresponding to a constant undercooling of 22K, as shown in Figs. 5.35(a) and (b). At Si concentrations above 0.2wt%, the Pb particles solidified with a broad exotherm extending from the Pb melting point of 327°C to a temperature of 305°C, followed by a sharp exotherm at an onset temperature of 305°C. With increasing Si concentration, the sharp exotherm decreased in size and the broad exotherm increased in size, as shown in Figs. 5.35(c)-(e).

5.5.3 Discussion

At Si concentrations less than or equal to 0.2wt%, the Pb particle solidification behaviour can be described as follows. On cooling below the Pb melting point, Pb particles containing catalytic trace impurities nucleate and solidify with variable undercooling because of the variable catalytic potency of the trace impurities. The number of Pb particles which are nucleated by the catalytic trace impurities is too small to be detected in the differential scanning calorimeter. On further cooling below 305°C, all the Pb particles which have not been nucleated by catalytic trace impurities are heterogeneously nucleated by the surrounding Al(Si) matrix, with an epitaxial cube-cube Al(Si)-Pb orientation relationship as shown in Fig. 5.32, and a sharp exotherm in the differential scanning calorimeter as shown in Fig. 5.35. The heterogeneous nucleation of Pb particle solidification by the surrounding Al(Si) matrix takes place at 305°C, ie at an undercooling of 22K, and is not affected by the Si atoms in solid solution, up to the solubility limit of 0.2wt% (Massalski et al, 1986). As shown in Fig. 5.33, Pb particles which are not in contact with Si precipitates exhibit a truncated octahedral shape bounded by {100} and {111} facets, and the heterogeneous nucleation of Pb

particle solidification can take place on the {111} facets which are expected to survive at temperatures above the Pb melting point, similarly to Pb particles in binary Al-Pb alloys as discussed by Moore et al (1987).

At Si concentrations above 0.2wt%, the Pb particles solidify with a broad exotherm between 327°C and 305°C, ie over a 0-22K range of undercoolings, followed by a sharp exotherm at 305°C as shown in Figs. 5.35(c)-(e). At Si concentrations above the solubility limit of 0.2wt%, Si precipitates appear in the microstructure, and are often in contact with the Pb particles, as shown in Fig. 5.32. This indicates that contacts between the Pb particles and the Si precipitates stimulate the nucleation of Pb particle solidification. There are three possible mechanisms for the effect of Si precipitates in stimulating the heterogeneous nucleation of Pb particles embedded in an Al(Si) matrix:

(1) Additions of Si may increase the trace impurity content of the Al-Pb-Si alloys. This is unlikely, since the alloys were manufactured from a Si material of higher purity than the Al and Pb.

(2) Solidification of the Pb particles may take place by catalytic nucleation on the surfaces of the Si precipitates, rather than on the surrounding Al(Si) matrix. To test this possibility further, some additional differential scanning calorimeter experiments were undertaken on specimens of Si-5wt%Pb ingots. Fig. 5.36 shows a typical differential scanning calorimeter traces of the resulting Pb particles solidification exotherm. The onset temperature for solidification of Pb particles embedded in a Si matrix is 302°C, corresponding to an undercooling of 25K below the Pb melting point. This indicates that Si is not a very good catalyst for the Pb solidification, and so that this mechanism is unlikely.

(3) Solidification of the Pb particles may take place by catalytic nucleation at the Al(Si) matrix-Si precipitate interfaces. This mechanism is supported strongly by the cube-cube orientation relationship observed between the Pb

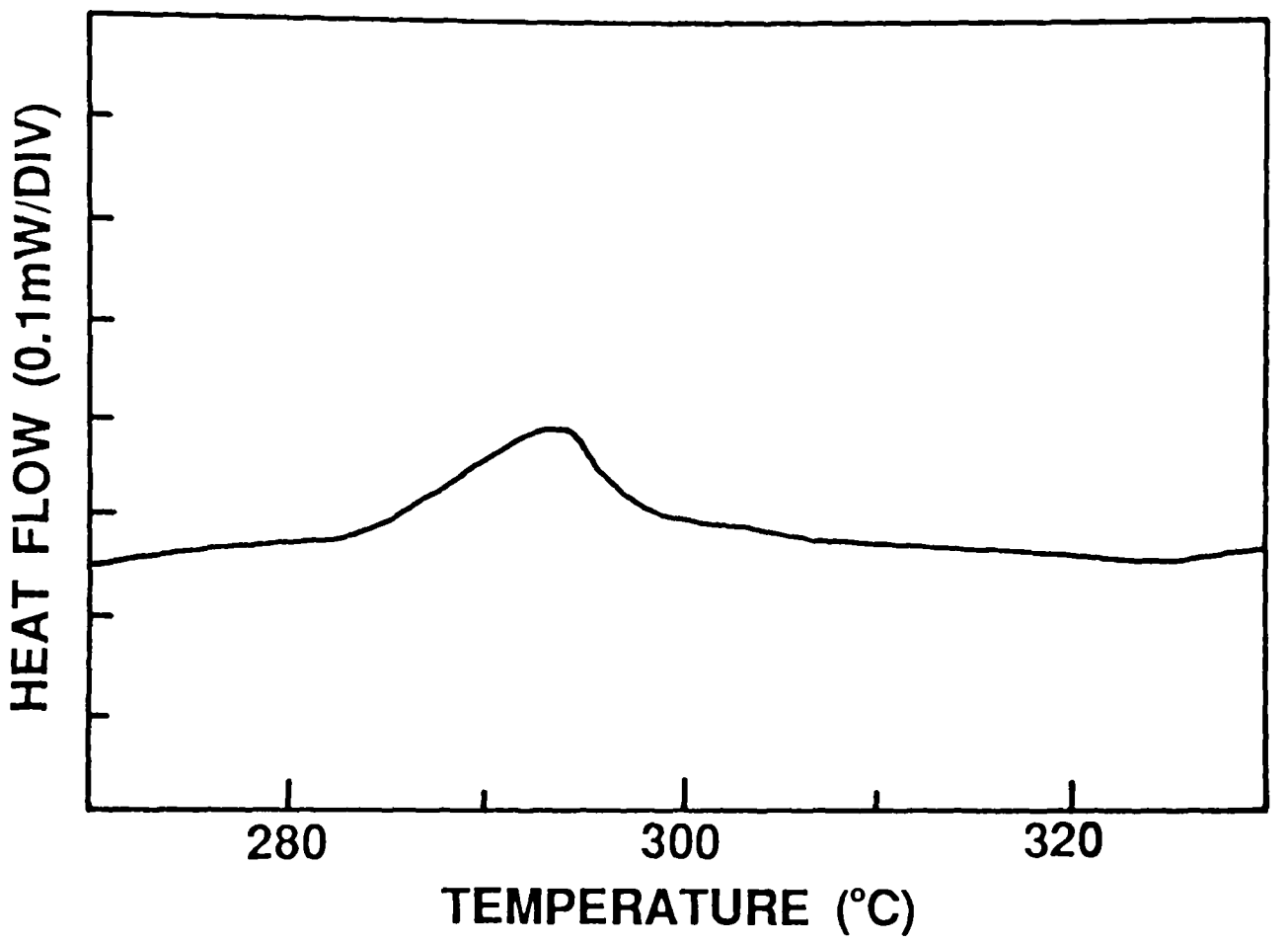


Fig. 5.36: Differential scanning calorimeter traces of Pb particle solidification exotherm from Si-5wt%Pb ingots.

particles and the surrounding Al(Si) matrix, independent of the presence of Si precipitates. The Si precipitates stimulate epitaxial nucleation on the Al(Si) matrix, with solid Pb nuclei forming at the Al(Si) matrix-Si precipitate interfaces.

Chapter 6

Melting Behaviour of Cd, In and Pb Particles Embedded in an Al Matrix

6.1 Introduction

In this chapter, results of the experimental work on melting behaviour of Cd, In and Pb particles embedded in an Al matrix are described and discussed in relation to the current theory of particle melting. The experiments described in this chapter include:

(a) Heating and cooling experiments in the differential scanning calorimeter.

(b) In-situ heating experiments in the transmission electron microscope.

6.2 Melting Behaviour of Cd Particles Embedded in an Al Matrix

6.2.1 Cd particle melting

Figs. 6.1 shows a typical differential scanning calorimeter trace of the Cd particle melting endotherm from melt spun Al-4.5wt%Cd. The Cd particles melted with a single sharp endotherm with onset, peak and end temperatures of 312°C, 321°C and 326°C respectively, as shown in Fig. 6.1. Figs. 6.2(a) shows the volume fraction of molten Cd particles as a function of temperature determined by heating a series of specimens in the calorimeter to different temperatures in the range 312-350°C, i.e. in the range of Cd particle melting, followed by holding for 600s, and then cooling to measure the solidification heats for each annealing temperature. Approximately 45vol% of the Cd particles melted at temperatures in the range 1-9K below the bulk equilibrium Cd melting point of 321°C (Massalski et al, 1986), and all the Cd particles were fully melted at temperatures near 321°C.

Fig. 6.2(b) also shows the volume fraction of molten Cd particles as a function of temperature determined by integrating Cd particle melting

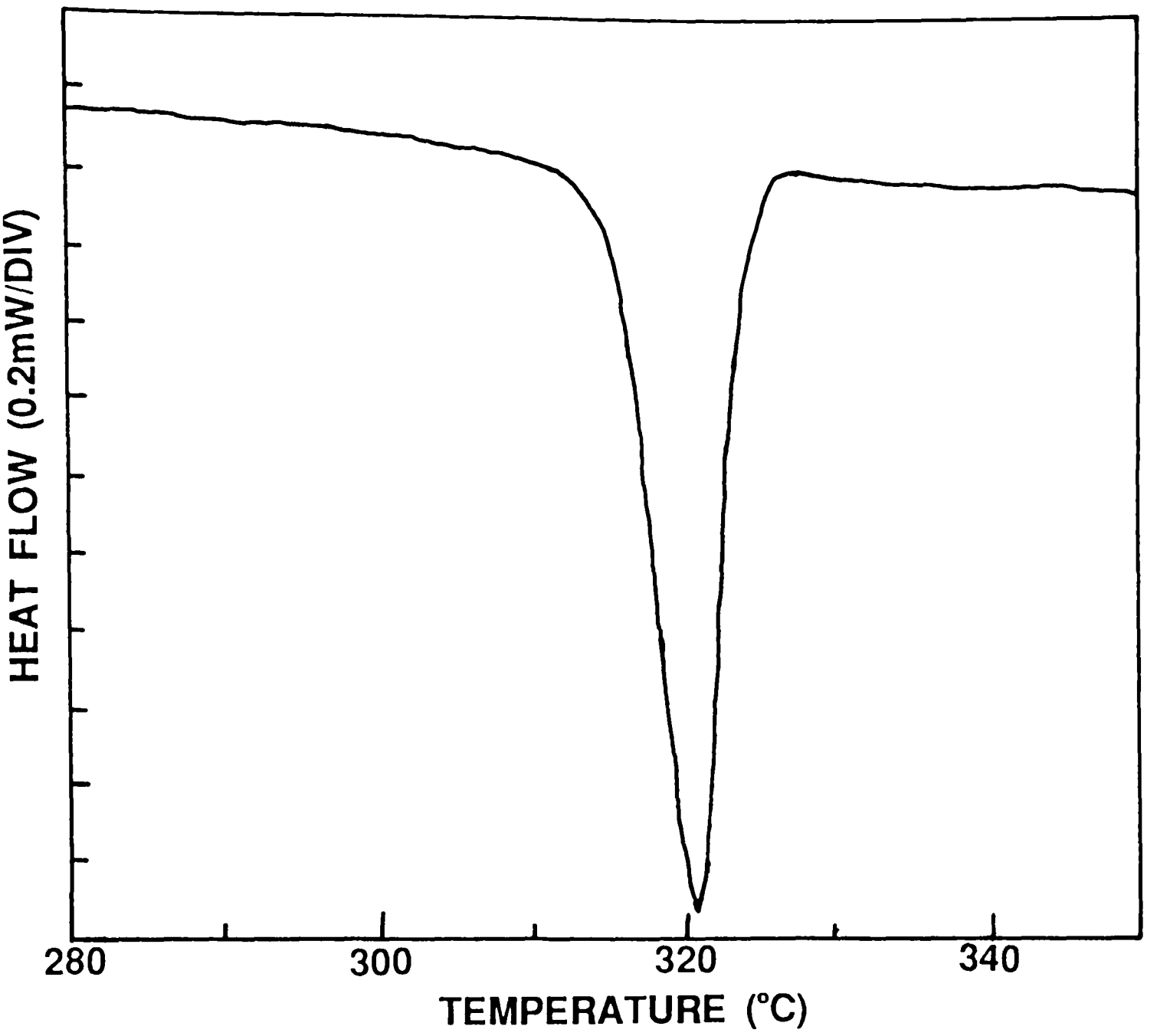


Fig. 6.1: Differential scanning calorimeter trace of the Cd particle melting endotherm from melt spun Al-4.5wt%Cd.

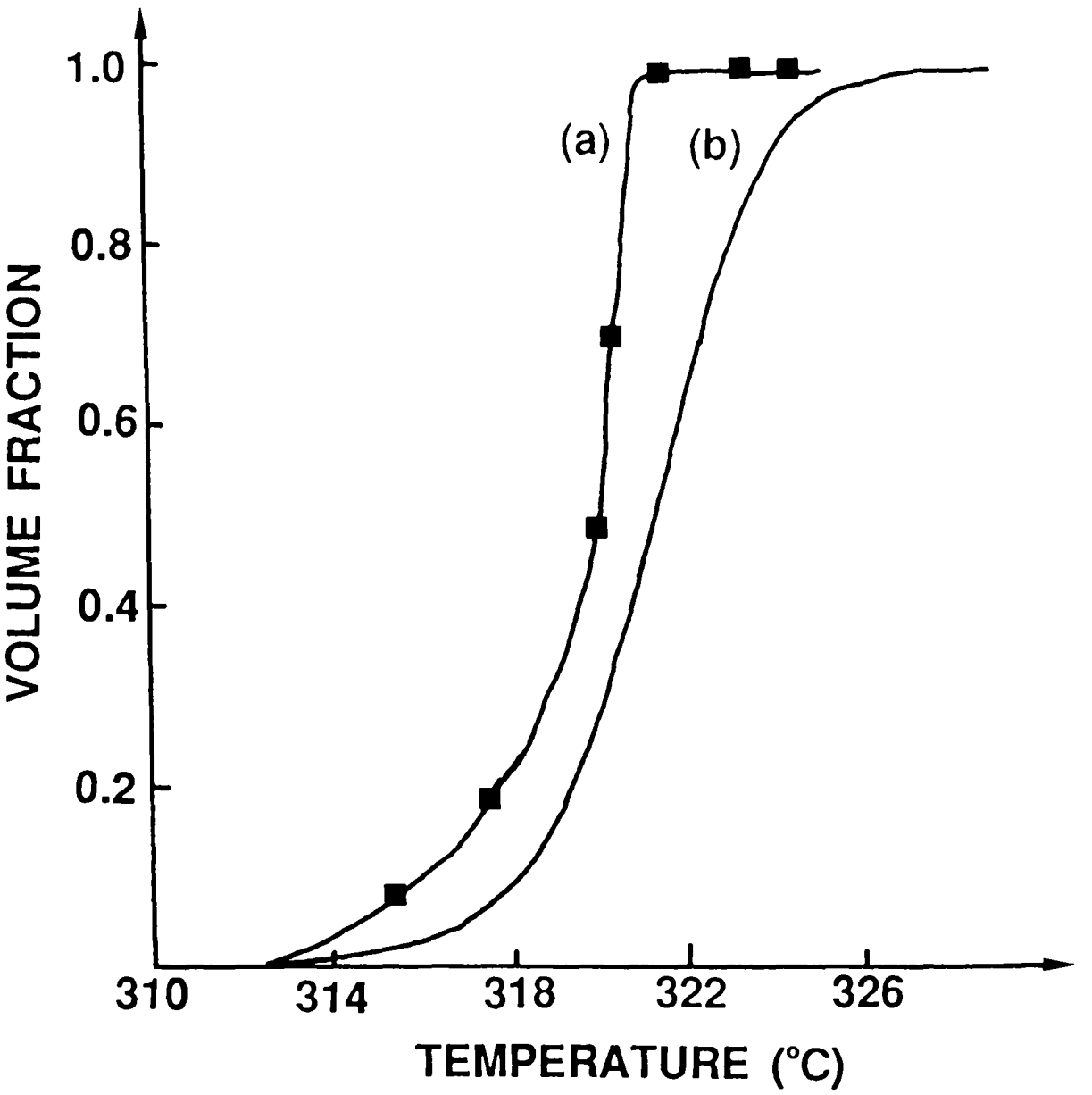


Fig. 6.2: Volume fraction of molten Cd particles as a function of temperature determined by (a) heating a series of specimens in the calorimeter to different temperatures in the range 312-350°C, followed by holding for 600s, and then cooling to measure the solidification heats for each annealing temperature; and (b) integrating the Cd particle melting endotherms.

endotherms such as shown in Fig. 6.1. The curve in Fig. 6.2(a) extends to higher temperature than the curve in Fig. 6.2(b), since it includes kinetic effects which delay particle melting during heating in the calorimeter. However, Fig. 6.2(a) is very similar to Fig. 6.2(b), indicating that there is little thermal lag during continuous heating, and the shapes of the exotherms are not strongly influenced by kinetic effects.

6.2.2 Cd particle solidification

Fig. 6.3 shows differential scanning calorimeter traces of Cd particle solidifcation exotherms from melt spun Al-4.5wt%Cd as a funtion of annealing temperature in the range 312-350°C, i.e. in the range of Cd particle melting. The onset, peak and end temperatures of the Cd particle solidification exotherms were independent of annealing temperature, although the size of the solidification exotherm increased with increasing annealing temperature, as more of the Cd particles melted.

6.2.3 Discussion

The equilibrium melting point of Cd particlesin melt spun Al-4.5wt%Cd may not be the same as the bulk equilibrium Cd melting point of 321°C (Massalski et al, 1986), because of pressure effects caused by differential thermal contraction, solidification shrinkage and capillarity. The combined effects of differential thermal contraction and solidification shrinkage on the Cd particle melting point in an Al matrix can be estimated as follows:

$$\Delta T_1=(V_L K_L-(V_S-s)K_S)T_m/L_V \qquad (6.1)$$

where ΔT_1 is the amount by which the Cd melting point is displaced from the bulk melting point T_m, K_S and K_L are the bulk moduli of solid and liquid Cd, V_S and V_L are the fractional volume changes associated with differential thermal contraction of the solid and liquid Cd particles, and -s is the solidification shrinkage. V_S and V_L can be calculated from:

$$V_S=3(T_m-T_R)(a_{Al}-a_{SCd}) \qquad (6.2)$$

$$V_L=3(T_{mo}-T_m)(a_{Al}-a_{LCd}) \qquad (6.3)$$

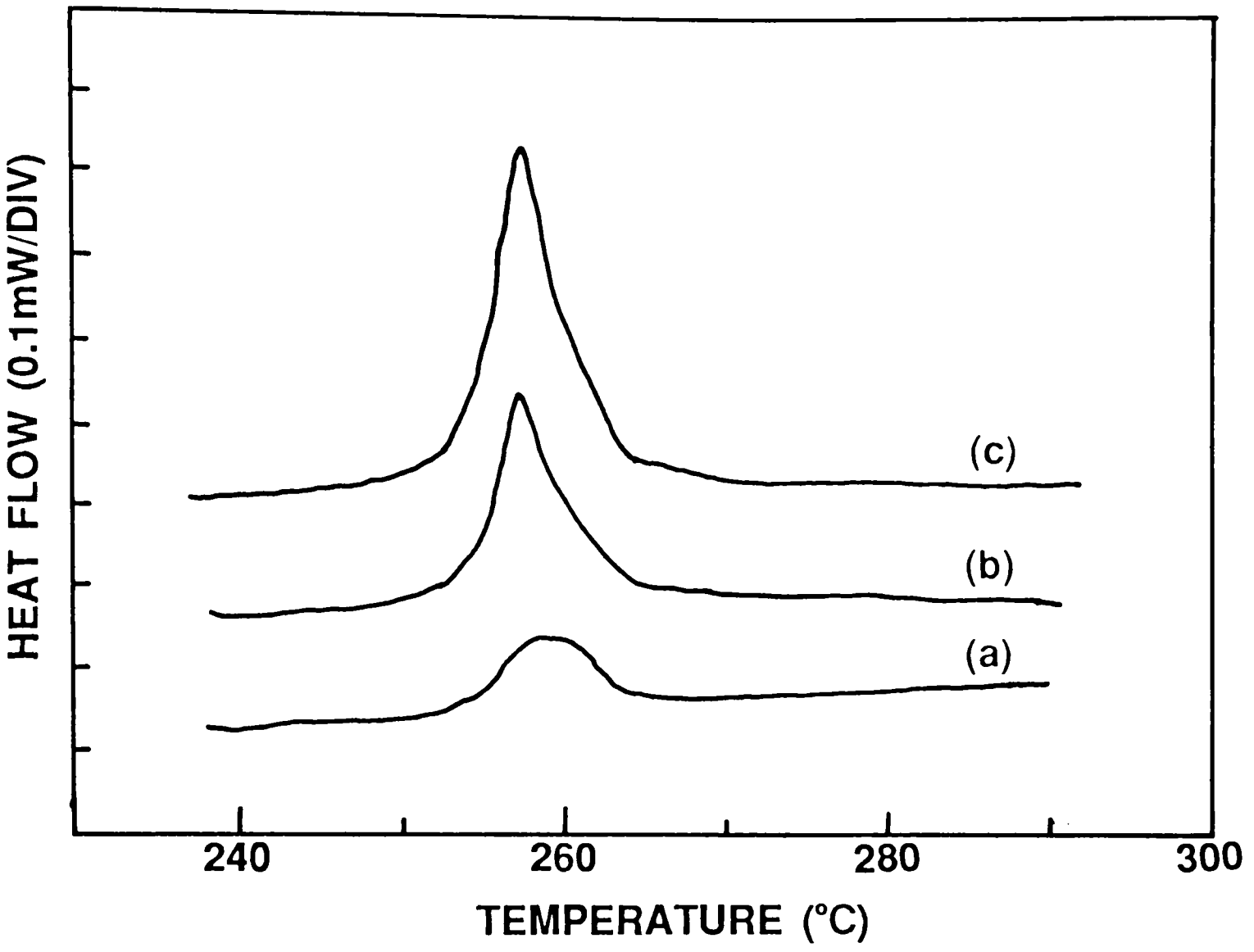


Fig. 6.3: Differential scanning calorimeter traces of Cd particle solidification exotherms from melt spun Al-4.5wt%Cd as a function of annealing temperature in the range of Cd particle melting: (a) 317.4°C; (b) 319.9°C; and (c) 321.3°C.

Where T_{mo} and T_R are the monotectic temperature and room temperature respectively, and a_{Al}, a_{SCd} and a_{LCd} are the linear coefficients of thermal expansion of solid Al, solid Cd and liquid Cd respectively.

In the absence of cavitation, fracture or flow to relieve differential thermal contraction and solidification shrinkage stresses, equation (6.1) predicts that the change in equilibrium melting point ΔT_1 is independent of particle size, and positive or negative depending on the relative magnitudes of the different terms in equation (6.1). Fig. 6.2(a) shows that approximately 55vol% of the Cd particles melt at temperatures less than 1K different from the bulk equilibrium Cd melting point of 321°C, indicating that the differential thermal contraction and solidification shrinkage stresses must be relieved by cavitation, fracture or flow and could be considered to be negligible.

Liquid and solid Cd particles in melt spun Al-4.5wt%Cd are also subject to hydrostatic stresses caused by capillarity forces from the curvature of the particle surfaces. The hydrostatic capillarity stresses are associated with changes in chemical potential in the Cd particles, which also lead to a displacement of the Cd particle melting point from the bulk equilibrium value:

$$\Delta T_2=2(\sigma_L/\rho_L-\sigma_S/\rho_S)T_m\rho_L/L_V r \qquad (6.4)$$

Where ΔT_2 is the amount by which the Cd particle melting point is displaced from the bulk melting point, ρ_L and ρ_S are the densities of liquid and solid Cd respectively, and σ_L and σ_S are the average solid Al-liquid Cd and solid Al-solid Cd surface enegies respectively. The surface energies σ_L and σ_S in equation (6.4) are averages over all of the Cd particle surfaces, inculding contributions from the facets as shown in Fig. 4.5 as well as the facet edges and corners.

Equation (6.4) predictes that the change in equilibrium melting point caused by capillarity ΔT_2 is inversely proportional to particle size and positive or negative depending on the relative magnitude of the two terms in equation (6.4). Previous work on Al-Cd alloys has shown that the equilibrium melting point depression of Cd particles embedded in an Al matrix increases as the Cd

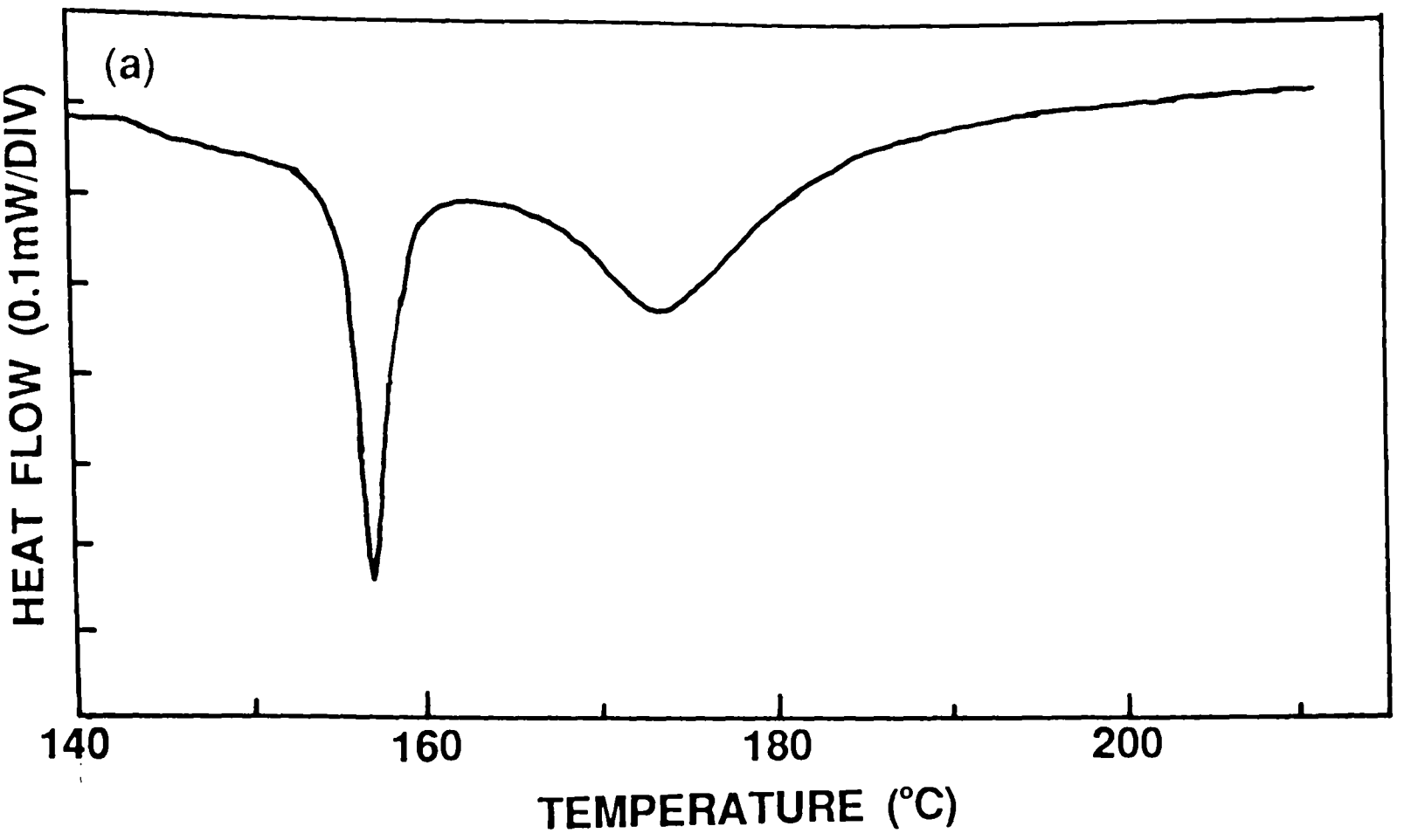
particle size decreases (Kim et al, 1990). As shown in Fig. 6.2(a), the largest depression of melting point in melt spun Al-4.5wt%Cd is 9K corresponding to the smallest particle size of 5nm in diameter. Taking ΔT_2=9K, T_m=594K (Massalski et al, 1986), r=2.5nm, $\rho_L=\rho_S=8.33\times10^6 gm^{-3}$ and $L_v=4.411\times10^8 Jm^{-3}$ (Brandes and Smithell, 1983), equation (6.4) gives the difference in average solid Al-solid Cd and solid Al-liquid Cd surface energies as $\sigma_S-\sigma_L=16.7mJm^{-2}$. It can be seen that σ_S is higher than σ_L, while in chapter 4 it has been shown that σ_{CS} is lower than σ_{CL} for melt spun Al-4.5wt%Cd. This is because that σ_S and σ_L average over all facets and facet edges and corners, whereas σ_{CS} and σ_{CL} are specific to the $\{111\}_{Al}//\{0001\}_{Cd}$ facets. Melting point of only approximately 20vol% Cd particles are depressed for more than 3K, indicating that the effect of capillarity is very small.

Fig. 6.2(a) shows that no superheating is required to initiate Cd melting, indicating that the kinetic barrier on nucleation of Cd melting is negligible. This is understandable considering that Cd particles are surrounded by large area of curved diffusive facets where nucleation of melting can take place easily. Fig. 6.3 shows that the onset, peak and end temperatures of the Cd particle solidification exotherms are independent of annealing temperature, i.e. are independent of Cd particle melting temperature. This suggests that effect of the depression of Cd particle equilibrium melting point on Cd particle solidification exotherms is small.

6.3 Melting Behaviour of In and Pb Particles Embedded in an Al Matrix

6.3.1 In and Pb particle melting

Figs. 6.4(a)-(c) show typical differential scanning calorimeter traces of In and Pb particle melting endotherms from melt spun Al-7wt%In, Al-5wt%Pb and Al-2wt%Pb respectively. The In particles in melt spun Al-7wt%In melted with a sharp endotherm at an onset temperature of 153°C, followed by a broad endotherm over the temperature range 163°C-193°C, as shown in Fig. 6.4(a). The Pb particles in melt spun Al-5wt%Pb melted with a sharp endotherm at an onset



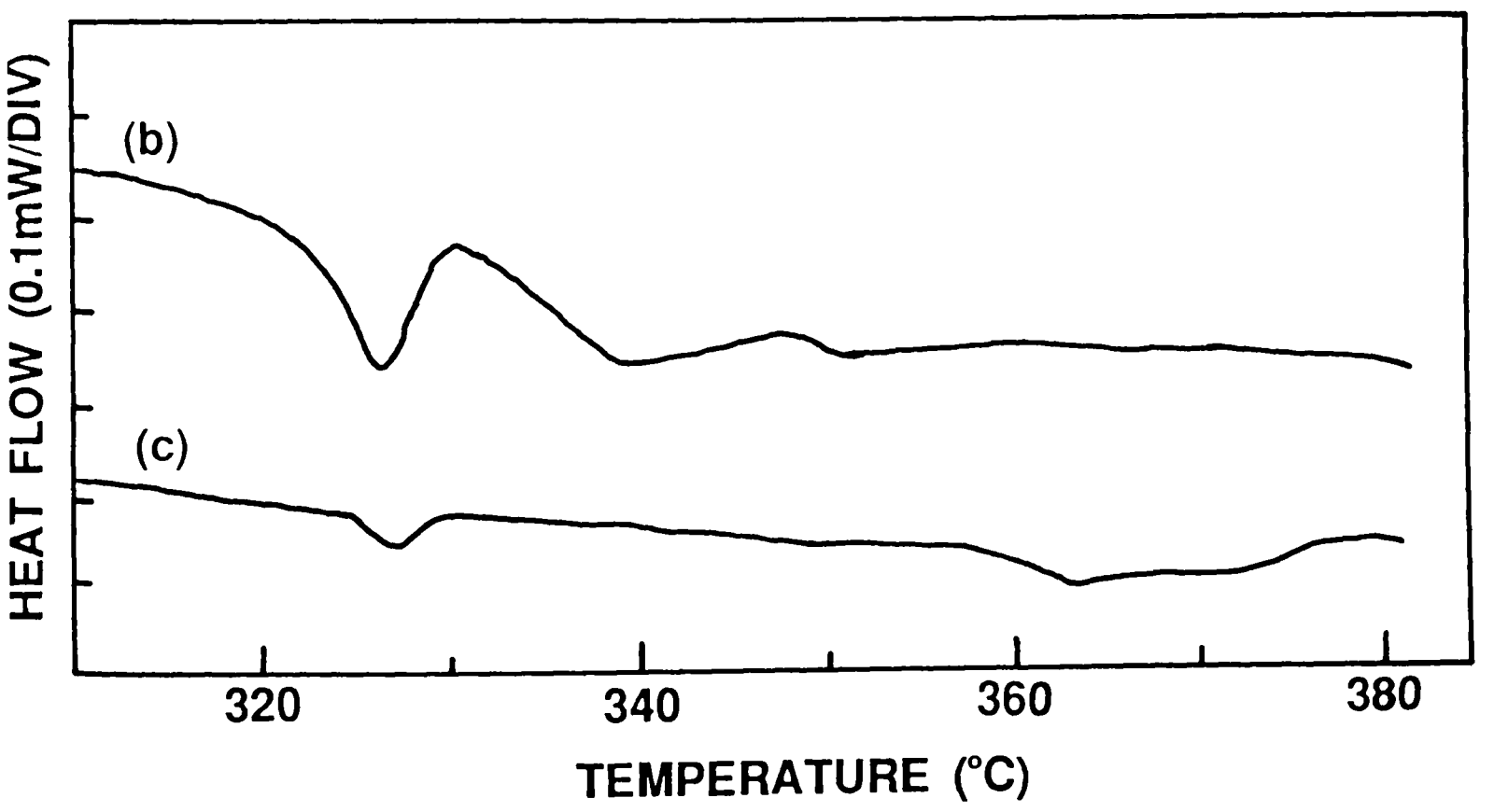


Fig. 6.4: Differential scanning calorimeter traces of the In and Pb particle melting endotherms from (a) melt spun Al-7wt%In; (b) melt spun Al-5wt%Pb; and (c) melt spun Al-2wt%Pb.

temperature of 320°C, followed by two broad endotherms, over the temperature ranges 330-352°C, and 346-370°C, as shown in Fig. 6.4(b). However, the Pb particles in melt spun Al-2wt%Pb melted with a sharp endotherm at an onset temperature of 325°C, followed by a single broad endotherm over the temperature range 358-375°C, as shown in Fig. 6.4(c).

Figs. 6.5(a) and (b) show the volume fraction of molten In and Pb particles as functions of temperature determined by heating a series of specimens in the calorimeter to different temperatures in the range 145-210°C for Al-7wt%In, and 310-380°C for Al-5wt%Pb, i.e. in the range of In and Pb particle melting, followed by holding for 600s, and then cooling to measure the solidification heats for each annealing temperature. As shown in Fig. 6.5(a), melt spun Al-7wt%In had to be heated up to 185°C, i.e. 29K higher than the bulk equilibrium In melting point of 156°C (Massalski et al, 1986), before all the In particles melted. Approximately 5vol% of the In particles melted at temperatures in the range 1-4K below 156°C, and approximately 90vol% of the In particles melted at temperatures in the range 1-39K above 156°C. As shown in Fig. 6.5(b), melt spun Al-5wt%Pb had to be heated up to 365°C, ie 38K higher than the bulk equilibrium Pb melting point of 327°C (Massalski et al, 1986), before all the Pb particles melted. Approximately 15vol% of the Pb particles melted at temperatures in the range 1-6K below 327°C, and approximately 80vol% of the Pb particles melted at temperatures in the range 1-38K above 327°C.

Figs. 6.6(a) and (b) also show the volume fraction of molten In and Pb particles as functions of temperature, determined by integrating In and Pb particle melting endotherms such as shown in Figs. 6.4(a) and (b). The curves in Figs. 6.6(a) and (b) extend to slightly higher temperature than the curves in Figs. 6.5(a) and (b), since they exclude kinetic effects which delay particle melting during heating in the calorimeter. However, Figs. 6.5(a) and (b) are very similar to the corresponding curves in Figs. 6.6(a) and (b), indicating that there is little thermal lag during continuous heating, and the shapes of the endotherms are not strongly influenced by kinetic effect.

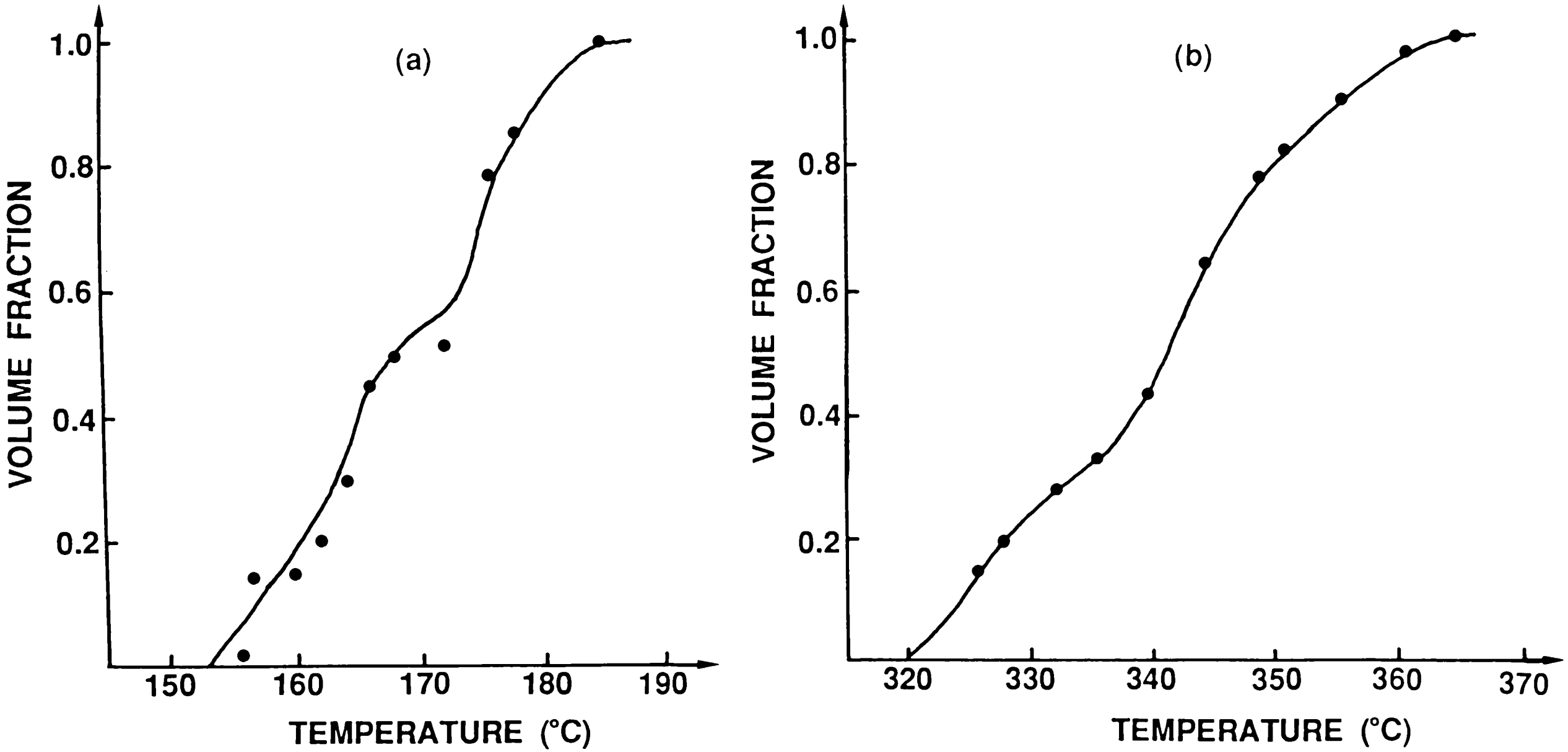


Fig. 6.5: Volume fraction of molten In and Pb particles as functions of temperature; determined by heating a series of specimens in the calorimeter to different temperatures in the range 145-210°C for Al-7wt%In and 310-380°C for Al-5wt%Pb, followed by holding for 600s and then cooling to measure the solidification heats for each annealing temperature: (a) Al-7wt%In; and (b) Al-5wt%Pb.

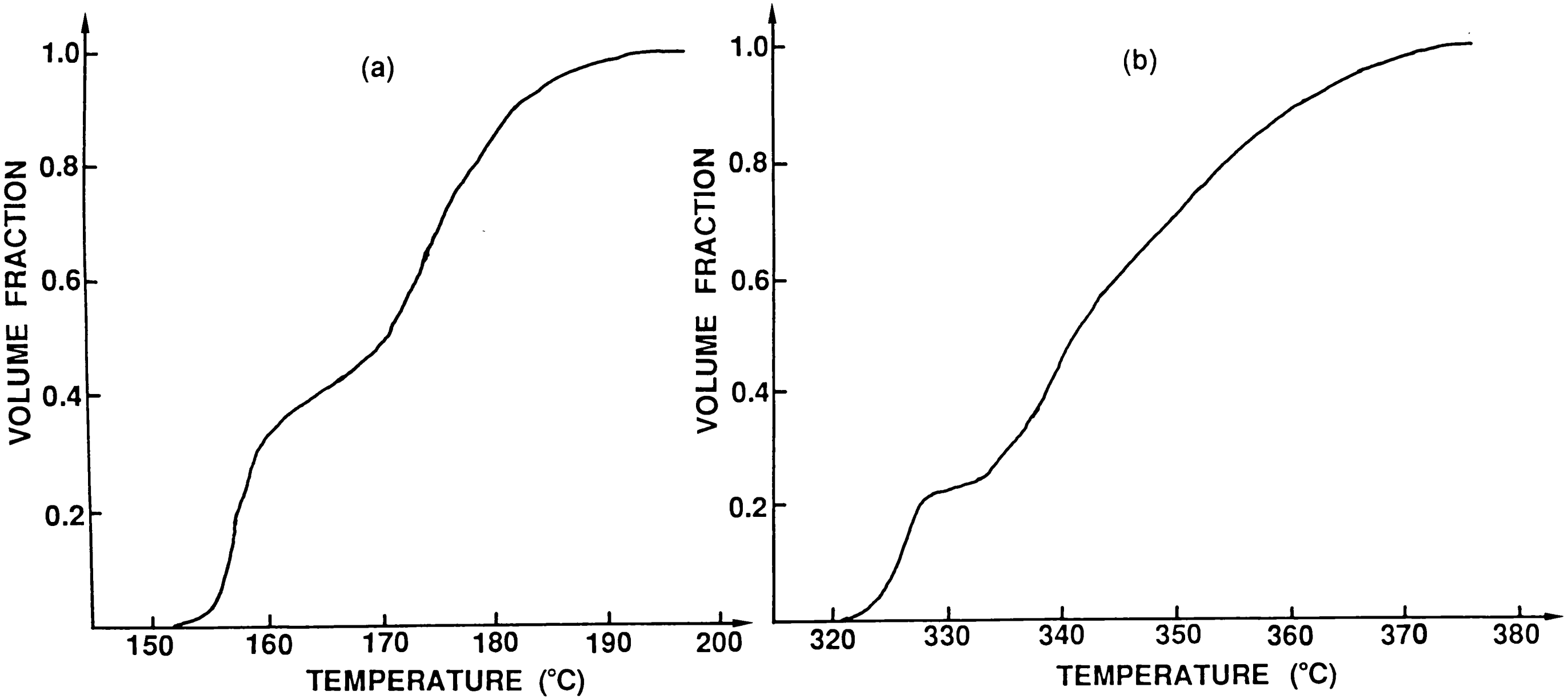


Fig. 6.6: Volume fraction of molten In and Pb particles as functions of temperature, determined by integrating the In and Pb particle melting endotherms: (a) Al-7wt%In; and (b) Al-5wt%Pb.

6.3.2 In-situ heating experiments

Figs. 6.7(a) and (b) show two dark field transmission electron micrographs from the same area of a melt spun Al-7wt%In specimen taken at 150°C and 165°C respectively during in-situ heating in the transmission electron microscope. As shown in Figs. 6.7(a) and (b), the larger In particles marked 1, 2 and 3 melted at temperatures close to 165°C, but none of the other, smaller In melted at 165°C. Fig. 6.8 shows another dark field transmission electron micrograph from melt spun Al-7wt%In taken at 180°C. It can be seen that In particles with sizes smaller than 30nm did not melt at 180°C, while the larger In particles melted.

Figs. 6.9(a)-(c) show three dark field transmission electron micrographs from the same area of a melt spun Al-5wt%Pb specimen, taken at 310°C, 325°C and 330°C respectively during in-situ heating in the transmission electron microscope. As shown in Figs. 6.9(a) and (b), the grain boundary Pb particles (marked 1 and 2) and the largest Pb particle within the Al matrix grain (marked 3) melted at temperatures close to 325°C. As shown in Figs. 6.9(b) and (c), the next largest Pb particle within the Al matrix grain (marked 4) melted at a temperature close to 330°C, while all the other, smaller Pb particles within the Al matrix grain still did not melt. Fig. 6.10 shows another dark field transmission electron micrograph from Al-5wt%Pb taken at 370°C. Once again Fig. 6.10 shows that the smaller Pb particles within the Al matrix grains still did not melt, while the larger Pb particles did melt.

During in-situ heating in the transmission electron microscope, it was also found that (a) each single particle melted almost instantaneously, judging from the fact that the brightness of each particle dark field image disappeared suddenly; and (b) at each annealing temperature, particles with similar size melted at slightly different times, but after a short time the number of particles which melted did not increase with increasing annealing time. This observation was in agreement with the calorimeter results in Figs. 6.5 and 6.6, showing that thermal lag and kinetic effects are small.

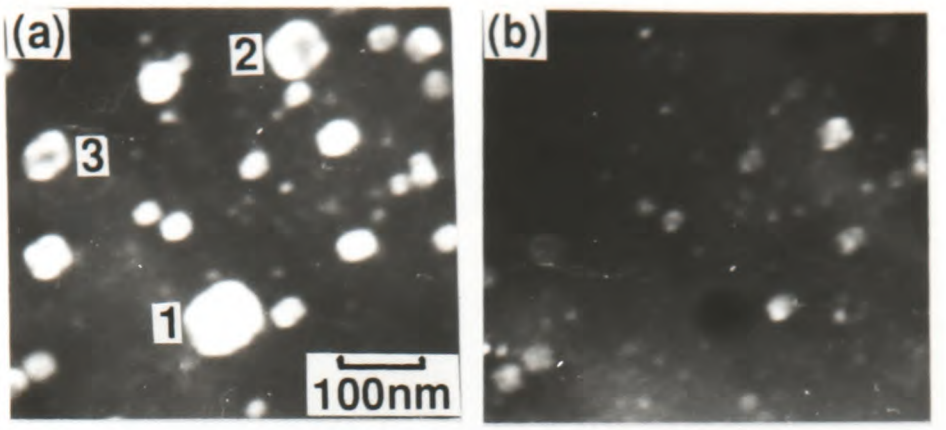


Fig. 6.7: Dark field transmission electron micrographs from the same area of a melt spun Al-7wt%In specimen, taken at (a) 150°C and (b) 165°C during in-situ heating in the transmission electron microscope.

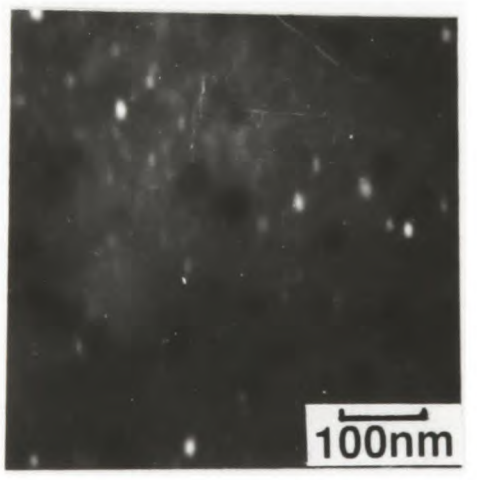


Fig. 6.8: Dark field transmission electron micrograph from melt spun Al-7wt%In, taken at 180°C during in-situ heating in the transmission electron microscope.

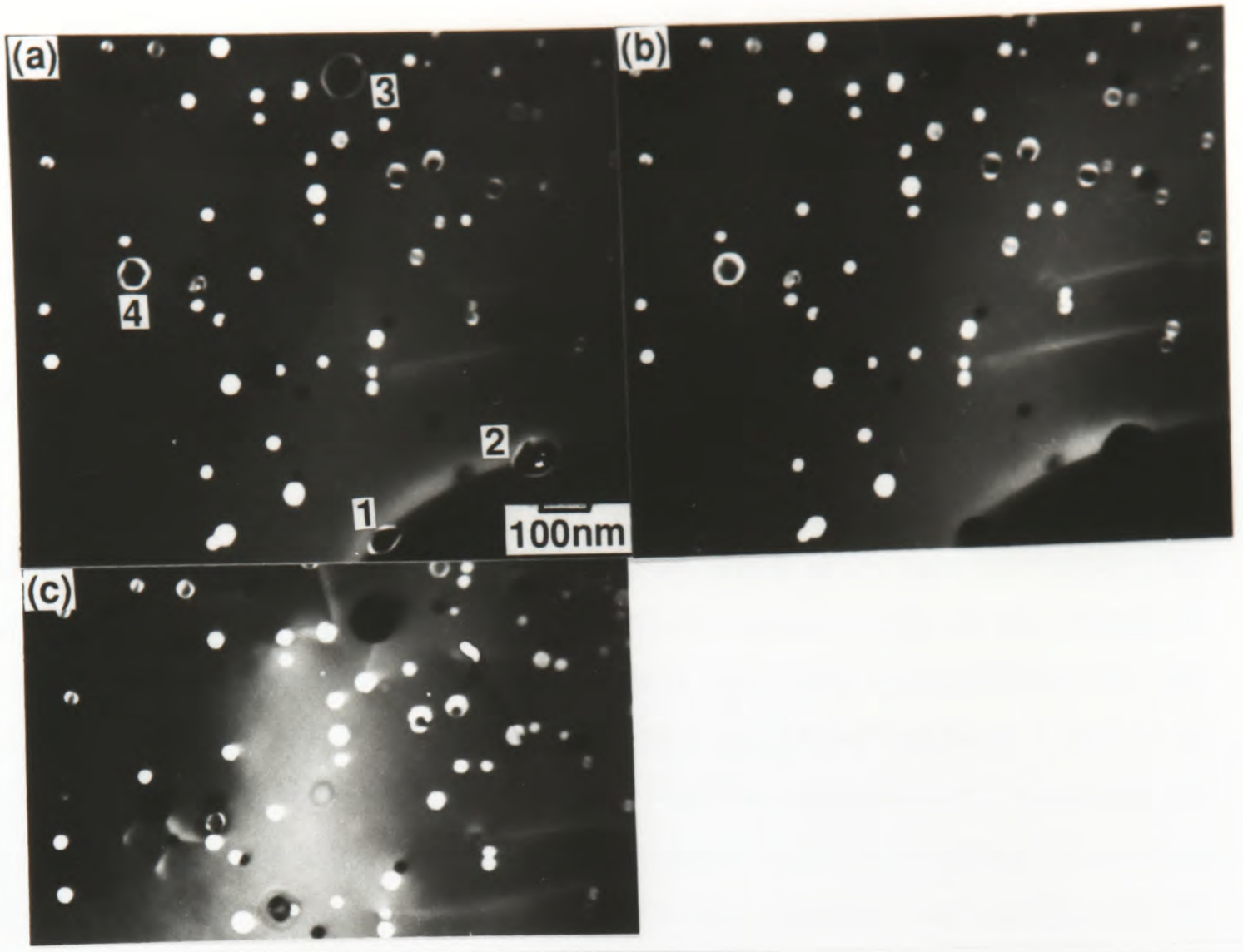


Fig. 6.9: Dark field transmission electron micrographs from the same area of a melt spun Al-5wt%Pb specimen, taken at (a) 310°C; (b) 325°C; and (c) 330°C during in-situ heating in the transmission electron microscope.

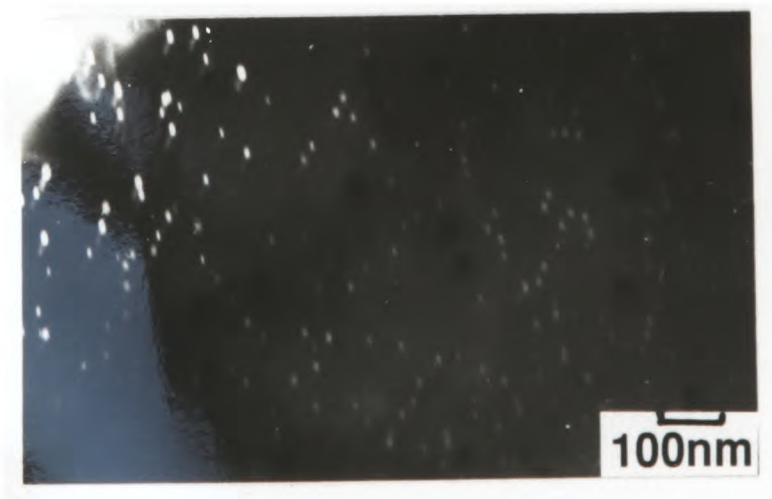


Fig. 6.10: Dark field transmission electron micrograph from melt spun Al-5wt%Pb, taken at 370°C during in-situ heating in the transmission electron microscope.

Unfortunately, these effects could not be recorded with the normal transmission electron microscope camera. The smallest In and Pb particles did not melt until the temperatures was 30-50°C above the bulk equilibrium melting point, in agreement with the calorimeter melting endotherms such as shown in Figs. 6.4(a) and (b).

6.3.3 In and Pb particle solidification

Figs. 6.11(a) and (b) show typical differential scanning calorimeter traces of In and Pb particle solidification exotherms from melt spun Al-7wt%In and Al-5wt%Pb respectively as functions of annealing temperature in the range of In and Pb particle melting. The onset, peak and end temperatures of the undercooled In and Pb particle solidification exotherms (marked 1 and 3 on Figs. 6.11(a) and (b)) were independent of annealing temperature, although the size of the solidification exotherms increased with increasing annealing temperature, as more of the In and Pb particles melted. For Al-7wt%In the size and the shape of the high temperature In particle solidification exotherm (marked 2 on Fig. 6.11(a)) were both independent of annealing temperature, when the annealing temperature was above 160°C, as shown in Fig. 6.11(a). This indicated that the high temperature exotherm corresponded to the solidification of only those In particles which melted at temperatures below 160°C.

6.3.4 Discussion

Differential scanning calorimeter traces such as Figs. 6.4(a)-(c) and transmission electron micrographs during in-situ heating such as Figs. 6.7-6.10 give qualitative and quantitative information about In and Pb particle melting in melt spun Al-7wt%In, Al-5wt%Pb and Al-2wt%Pb alloys. Different In and Pb particles melt at different temperatures. Dark field transmission electron micrographs such as Figs. 6.7-6.10 show that: (a) the grain boundary Pb particles melt at the lowest temperatures close to its bulk equilibrium melting point; (b) the large In and Pb particles within the Al matrix grains

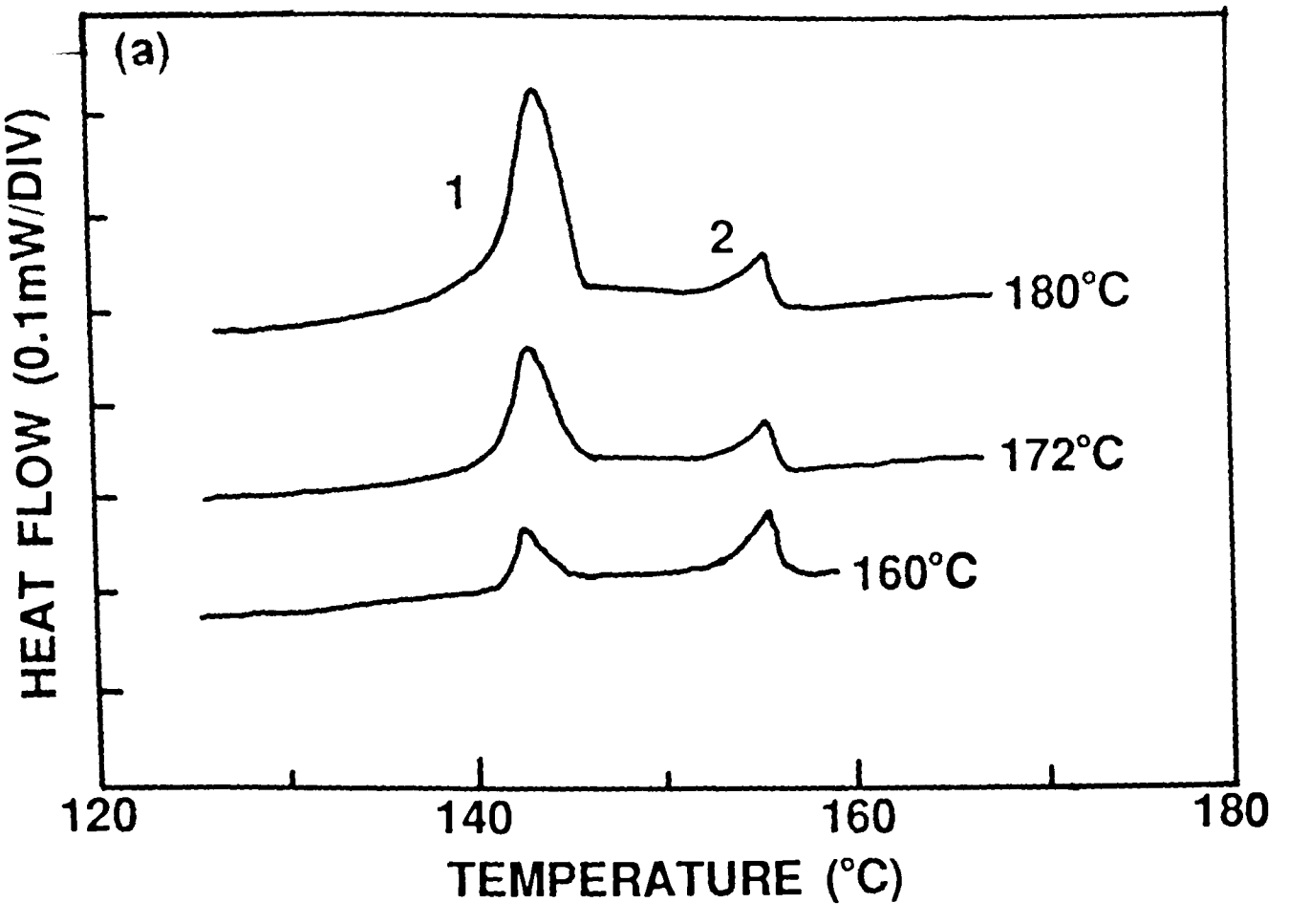
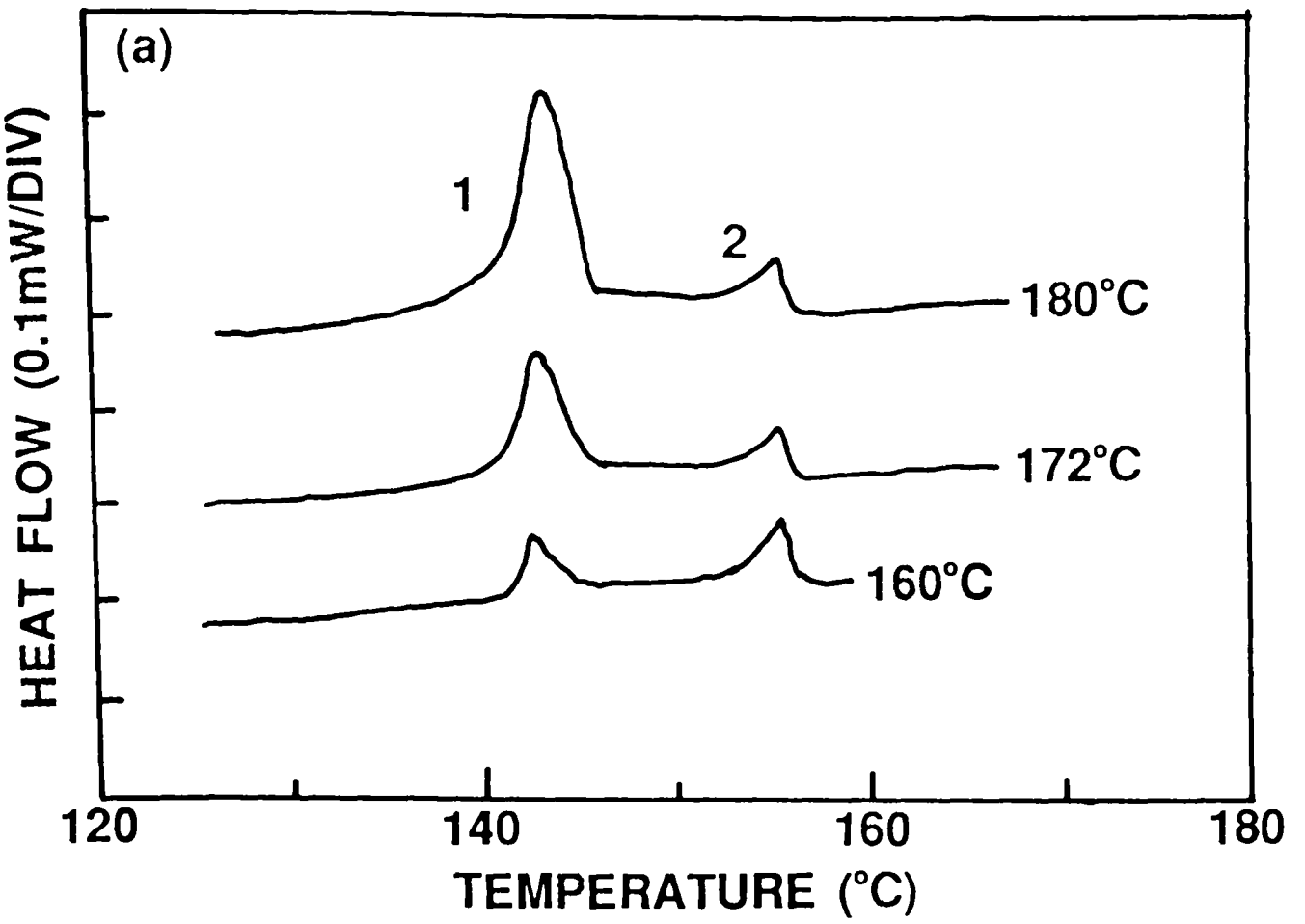


Fig. 6.11: Differential scanning calorimeter traces of In and Pb particle solidification exotherms from (a) melt spun Al-7wt%In and (b) melt spun Al-5wt%Pb as functions of annealing temperature in the range of In and Pb paeticle melting.



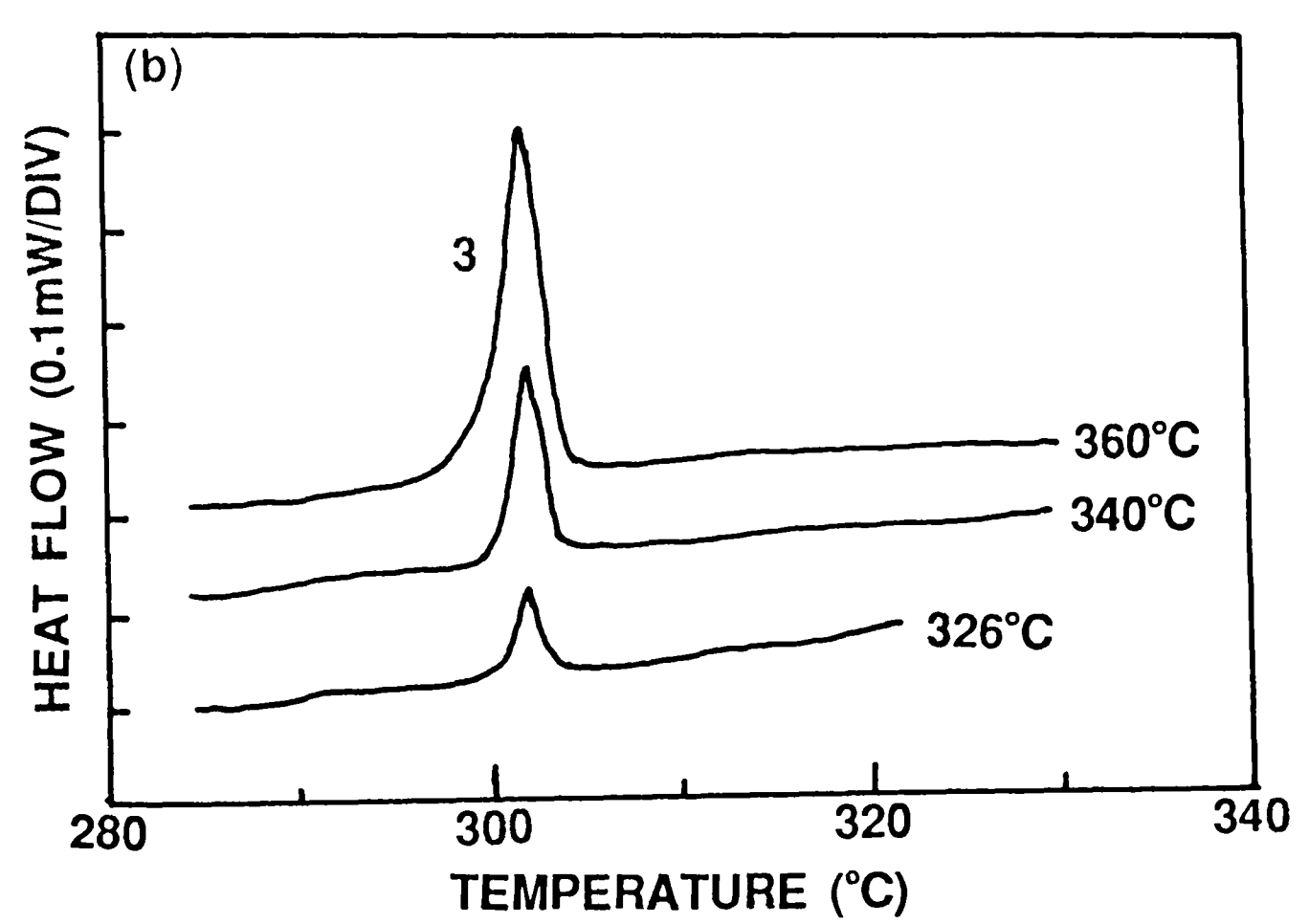


Fig. 6.11: Differential scanning calorimeter traces of In and Pb particle solidification exotherms from (a) melt spun Al-7wt%In and (b) melt spun Al-5wt%Pb as functions of annealing temperature in the range of In and Pb paeticle melting.

melt at higher temperatures 0-10K above their equilibrium melting points; and (c) the small In and Pb particles within the Al matrix grains melt at even higher temperatures, 20-40K above their euilibrium melting points. These in-situ heating results are confirmed by comparing the differential scanning calorimeter traces of Pb particle melting endotherms from hypermonotectic Al-5wt%Pb and near monotectic Al-2wt%Pb, such as shown in Figs. 6.4(b) and (c). The number of large 30-150nm Pb particles in the microstructure of melt spun Al-2wt%Pb is very small compared to Al-5wt%Pb. The absence of an endotherm over the temperature range 330-352°C and the presence of an endotherm over the temperature range 356-375°C in Al-2wt%Pb indicates therefore that the highest temperature endotherm corresponds to the small 5-30nm Pb particles. In another words, the 5-30nm Pb particles are clearly superheated by at least 29K.

Figs. 6.5(a) and (b) show that the melting point of approximately 5vol% In particles and 15vol% particles are depressed by 1-3K and 1-7K respectively. In-situ heating shows that the grain boundary Pb particles melt at the lowest temperatures. The In particle solidification exotherms at different annealing temperatures in Fig. 6.11(a) show that the In particles which melt at the lowest temperatures are those particles containing catalytic trace impurities which are also very likely to be the grain boundary In particles. In other words the melting point of some of the grain boundary In and Pb particles are depressed by 1-3k and 1-7K respectively. The depression of melting point in these grain boundary particles may be caused by capillarity effects similar to the Cd particles discussed in section 6.2, but in any case, the melting point depression is not large.

Saka et al (1988) have investigated In particle melting behaviour in rapidly solidified Al-In alloys by in-situ heating in a transmission electron microscope. Grabaek et al (1990) have investigated Pb precipitate melting behaviour in Al single crystals implanted with Pb^+ by in-situ X-ray diffraction. Their results are in agreement with the present results, with a large amount of superheating in the small In and Pb particles which increases

with decreasing particle size. Grabaek et al did not discuss the superheating results in detail. Saka et al attributed the superheating of the In particles to an increase in equilibrium melting point with decreasing particle size, because the solid Al-liquid In surface energy is higher than the solid Al-solid In surface energy. There are two main difficulties with this interpretation:

(1) The solid-solid surface energy is likely to be higher than the solid-liquid surface energy in systems such as Al-In and Al-Pb. Chemical contributions to the surface energy are similar for both type of surface, with strong repulsive interaction between unlike atoms. However, the solid-solid surface energy will include an additional structural contribution, with a high mismatch between the different solid crystal structures. From the Gibbs-Thomson equation, this leads to a depression in melting point for small particles, rather than the superheating seen in the present work and by Saka et al and Grakaek et al. In section 6.2, solid Al-solid Cd surface energy has been shown to be higher than the solid Al-liquid Cd surface energy for Cd particles embedded in an Al matrix by the depression of Cd particle equilibrium melting point. Solid Al-solid Sn surface energy has also been shown to be higher than the solid Al-liquid Sn surface energy for Sn particles embedded in an Al matrix (Kim et al, 1990).

(2) The In and Pb particle solidification exotherms in Figs. 6.11(a) and (b) show clearly that the solidification onset temperatures are independent of In and Pb particle size. More detailed analysis in chapter 4 of In and Pb particle solidification exotherms such as in Figs. 6.11(a) and (b) shows that (a) the solidification onset temperatures retain constant to within the experimental error of +/-0.2-0.3K, and (b) the solidification peak and finish temperature decrease by 2-3K with increasing cooling rate, in agreement with predictions from the classical theory of nucleation, These results are only consistent with an equilibrium particle melting point which is independent of particle size (Kim et al, 1990).

An alternative interpretation of the superheating of In and Pb particle melting is that it is associated with a kinetic difficulty of nucleating melting in the embedded In and Pb particles. The melting of In and Pb particles embedded in an Al matrix must initiate from the interface between the particles and the matrix (Cahn, 1986, Saka et al, 1987). However, it is more difficult for nucleation of melting to take place directly on the ordered {111} and {100} facets than on disordered regions of the interface such as pores, dislocations, edges between adjacent facets, and corners between adjacent edges. The smaller In and Pb particles have sharper edges and corners than the larger In and Pb particles. In addition, the smaller In and Pb particles are more likely to be free from defects such as pores and dislocations. Therefore the nucleation of melting is more difficult in smaller In and Pb particles, because there is little or no disordered interface available. When the particle size is as small as 5-30nm, the area of disordered interface is so small that superheating of 20-40K is required as a driving force to overcome the kinetic barrier to melting. Once melting is nucleated in a particle, it proceeds very quickly until the whole particle melt, as shown by the in-situ heating experiments in the transmission electron microscope.

Chapter 7

Heterogenous Nucleation of Solidification of Si by Solid Al in Hypoeutectic Al-Si Alloys

7.1 Introduction

In this chapter, results of the experimental work on heterogeneous nucleation of solidification of Si by solid Al in hypoeutectic Al-Si alloys are described and discussed in relation to current theories of nucleation. The experiments described in this chapter include:

(a) Quenching experiments.

(b) Heating and cooling experiments in a differential scanning calorimeter.

(c) Transmission electron metallography to investigate the as-rapidly solidified and heat treated microstructures of melt spun binary and ternary Al-Si alloys.

7.2 Microstructures

Figs. 7.1(a)-(d) show typical transmission electron micrographs of the microstructures of the as-melt spun alloys: (a) binary Al-3wt%Si with 99.999% pure Al; (b) binary Al-3wt%Si with 99.9999% pure Al; (c) ternary Al-3wt%Si-0.3%Sr; and (d) ternary Al-3wt%Si-Na. The as-melt spun microstructures all consisted of 0.1-0.8μm Si particles distributed along the cell boundaries in an α-Al matrix.

Figs. 7.2(a)-(d) show transmission electron micrographs of the alloy microstructures corresponding to Figs. 7.1(a)-(d) after annealing for 10 minutes at 595°C, 18K above the Al-Si eutectic temperature of 577°C, followed by quenching into water. The annealed microstructures all consisted of spherical 1-6μm two phase Al-Si eutectic particles distributed homogeneously throughout an α-Al matrix. Fig. 7.3(a) shows a higher magnification transmission electron micrograph of one of the quenched Al-Si eutectic

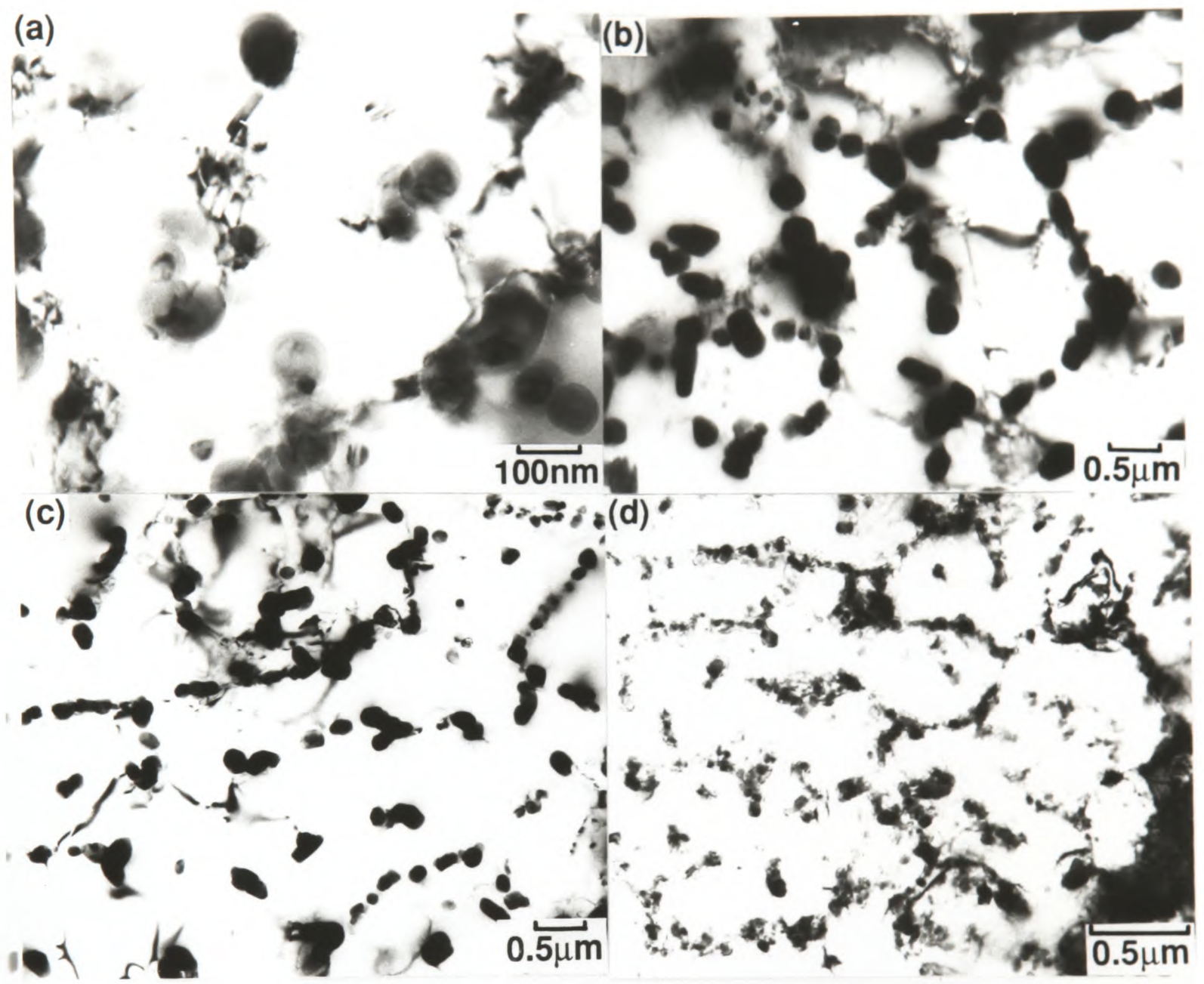


Fig. 7.1: Bright field transmission electron micrographs of the microstructures of as-melt spun Al-Si alloys: (a) binary Al-3wt%Si with 99.999% pure Al; (b) binary Al-3wt%Si with 99.9999% pure Al; (c) ternary Al-3wt%Si-Na; and (d) ternary Al-3wt%Si-0.3wt%Sr.

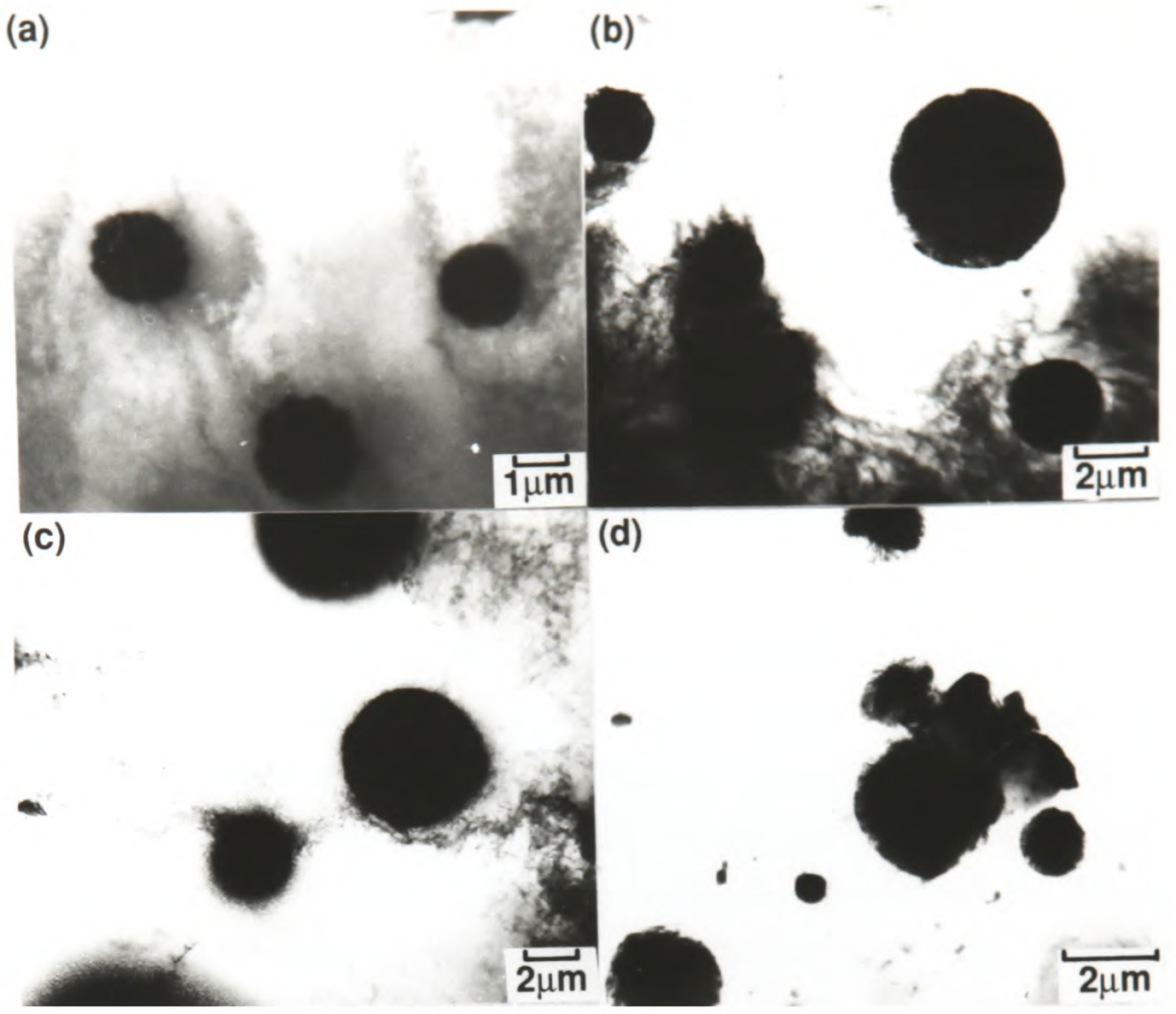


Fig. 7.2: Bright field transmission electron micrographs of the microstructures of melt spun Al-Si alloys after annealing for 10 minutes at 595°C followed by quenching into water: (a) binary Al-3wt%Si with 99.999% pure Al; (b) binary Al-3wt%Si with 99.9999% pure Al; (c) ternary Al-3wt%Si-Na; and (d) ternary Al-3wt%Si-0.3wt%Sr.

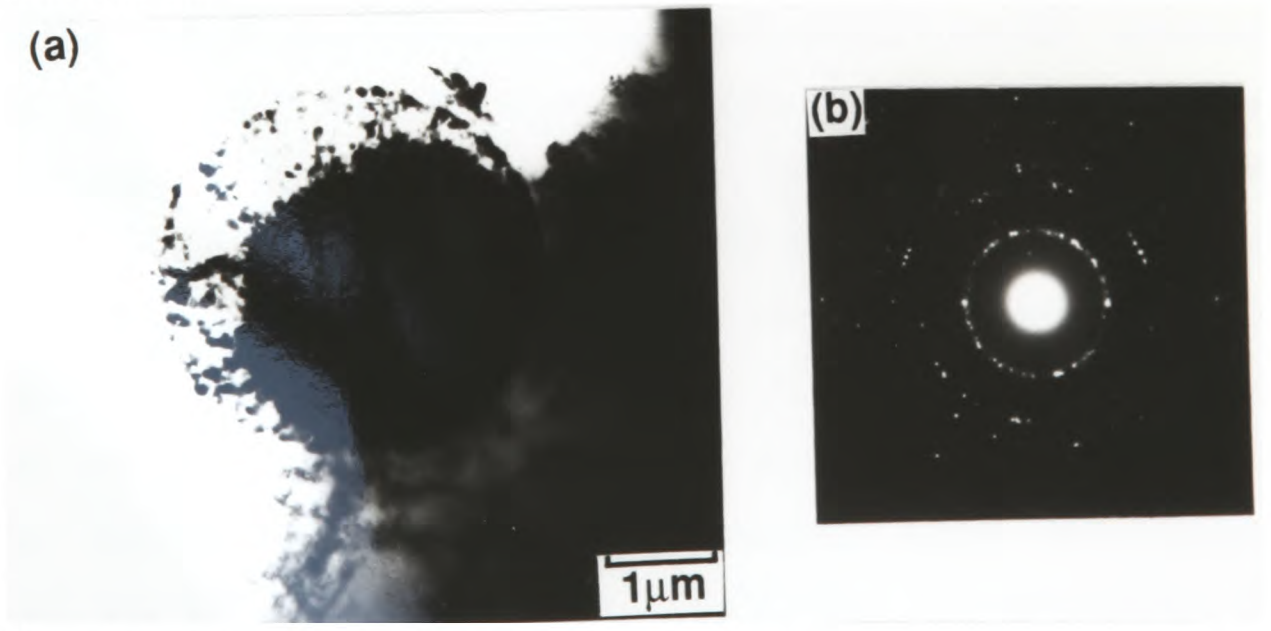


Fig. 7.3: (a) Bright field transmission electron micrograph of the microstructure of melt spun 99.999% pure Al-3wt%Si after annealing for 10 minutes at 595°C followed by quenching into water; and (b) selected area diffraction pattern corresponding to (a), showing ring patterns from Si particles.

droplets in melt spun 99.999% pure Al-3wt%Si, and Fig. 7.3(b) shows the corresponding selected area diffraction pattern. Fig. 7.3(b) shows a ring diffraction pattern from Si, indicating that the quenched eutectic droplets consisted of clusters of Si particles embedded in Al. Comparison of Figs. 7.1 and 7.2 shows that coarsening of the eutectic liquid droplets took place during annealing above the eutectic temperature. As the distance between the droplets increased, the rate of coarsening decreased, and the droplet sizes remained approximately constant and independent of further annealing beyond 10 minutes at 595°C.

Fig. 7.4 shows a typical bright field transmission electron micrograph of the microstructure of melt spun 99.995% pure Al-3wt%Si, after annealing for 10 minutes at 595°C, followed by slow cooling at 10K/min in the calorimeter. With 99.995% Al purity, each eutectic liquid droplet solidified to form a regular faceted single crystal Si particle. Fig. 7.5 shows a typical bright field transmission electron micrograph of the microstructure of melt spun 99.999% pure Al-3wt%Si, after annealing for 10 minutes at 595°C followed by slow cooling at 10K/min in the calorimeter. With 99.999% Al purity, only a few of the eutectic liquid droplets solidified to form regular faceted single crystal Si particles, as arrowed in Fig. 7.5, and most of the droplets solidified by a different mechanism to form irregular non-faceted Si particles. The irregular non-faceted Si particles sometimes exhibited internal twinning, as shown in Figs. 7.6(a)-(c). Fig. 7.7 shows a typical bright field transmission electron micrograph of the microstructure of melt spun 99.9999% pure Al-3wt%Si, after annealing for 10 minutes at 595°C followed by slow cooling at 10K/min in the calorimeter. Most of the eutectic liquid droplets solidified to form clusters of Si particles embedded in Al, similar to the quenched droplets shown in Fig. 7.3. Unlike the lower purity alloys, the spherical shape of the eutectic liquid droplets remained after solidification, indicating that the droplets were rapidly solidified. In some cases, the Si particles were found to be distributed along the periphery of the solidified droplets, as shown in Fig. 7.7(b), indicating that the Si phase nucleated heterogeneously on the interface between the droplets and the surrounding Al

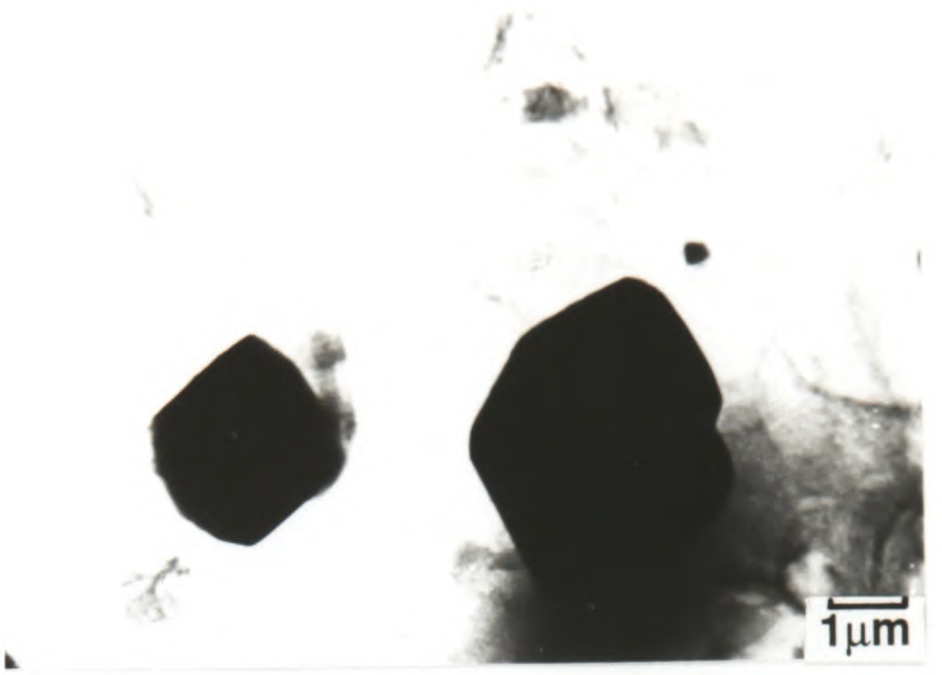


Fig. 7.4: Bright field transmission electron micrograph of the microstructure of melt spun 99.995% pure Al-3wt%Si, after annealing for 10 minutes at 595°C followed by slow cooling at 10K/min.

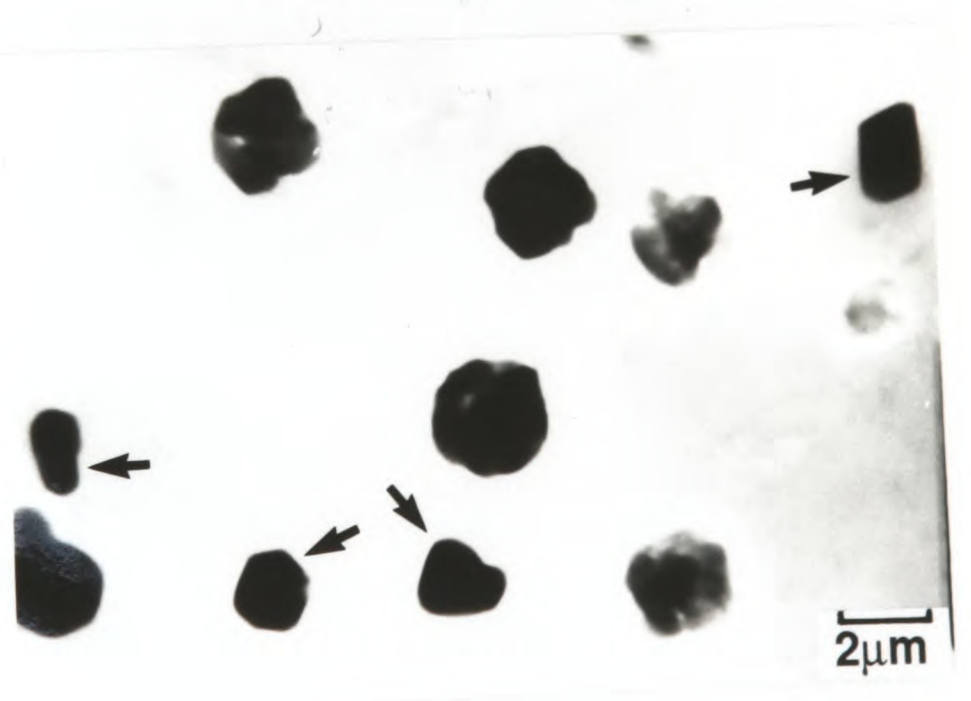


Fig. 7.5: Bright field transmission electron micrograph of the microstructure of melt spun 99.999% pure Al-3wt%Si, after annealing for 10 minutes at 595°C followed by slow cooling at 10K/min.

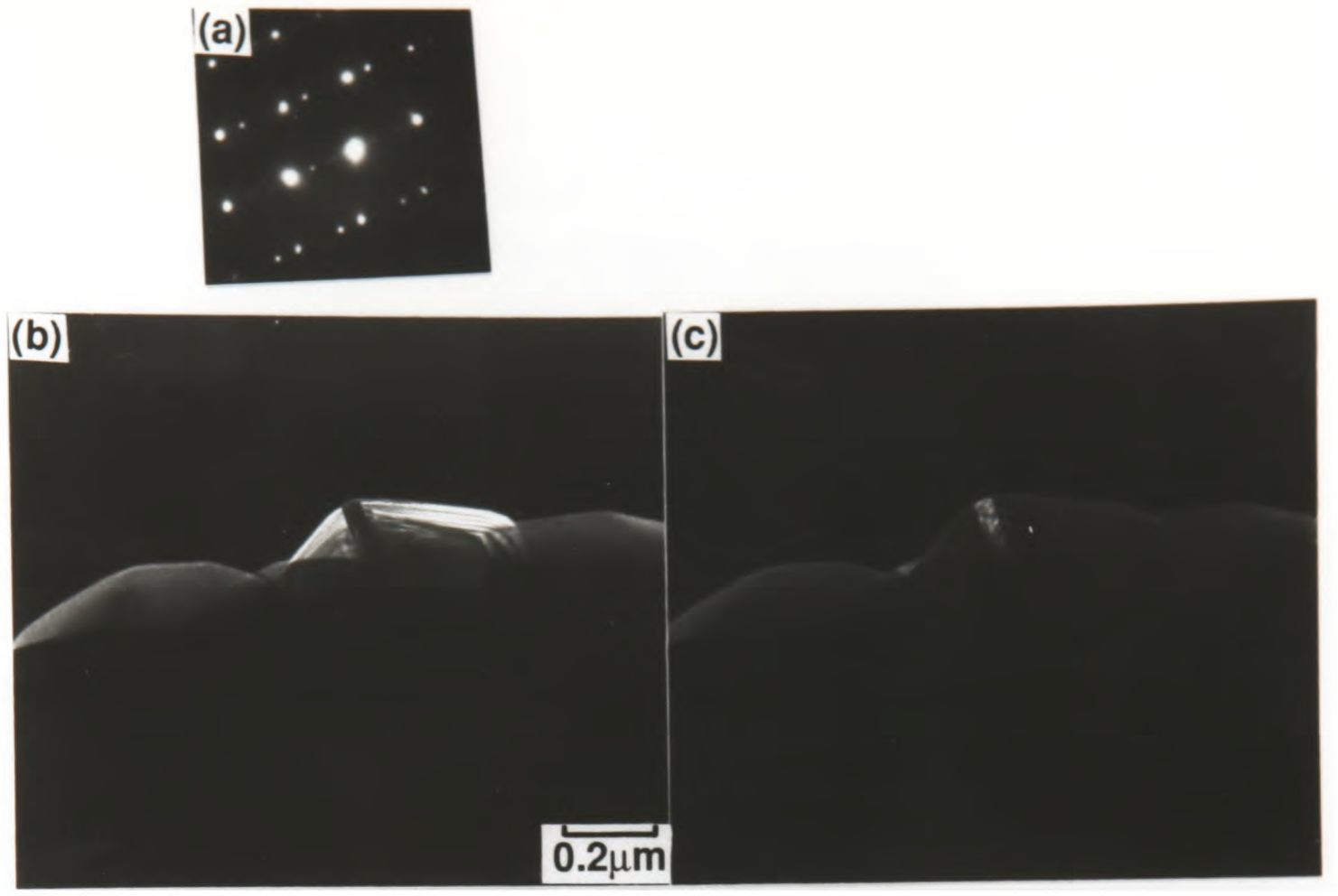


Fig. 7.6: (a) Selected area electron diffraction patterns from a Si particle in melt spun 99.999% pure Al-3wt% after annealing for 10 minutes at 595°C followed by slow cooling at 10K/min; (b) and (c) dark field transmisssion electron micrographs corresponding to (a), showing twins in the Si particles.

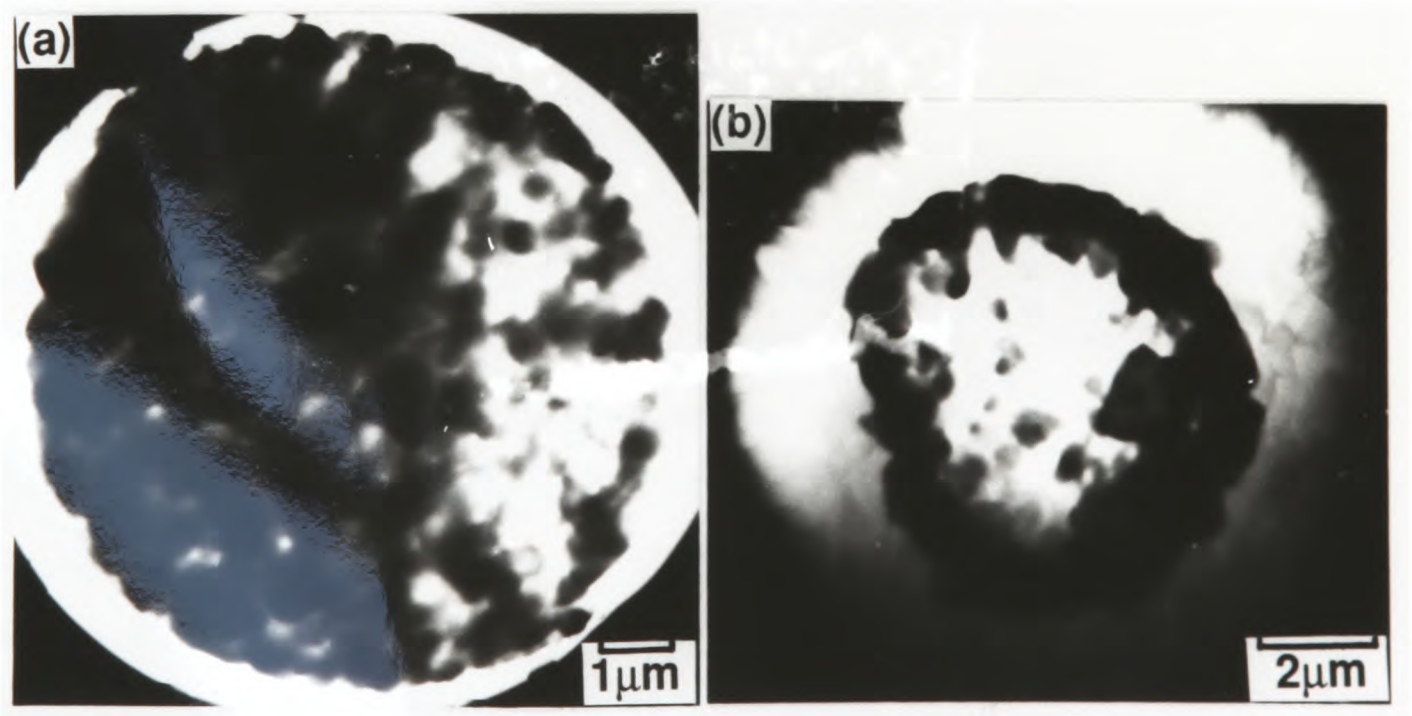


Fig. 7.7: Bright field transmission electron micrographs of the microstructure of melt spun 99.9999% pure Al-3wt%Si, after annealing for 10 minutes at 595°C followed by slow cooling at 10K/min.

rich matrix.

Fig. 7.8 shows a typical transmission electron micrograph of the microstructure of melt spun Al-3wt%Si-Na after annealing for 10 minutes at 595°C followed by slow cooling at 10K/min in the calorimeter. Most of the eutectic liquid droplets in this alloy solidified to form clusters of Si particles embedded in Al, and retained their spherical shape, similar to the droplets in the 99.9999% pure binary Al-3wt%Si alloy. Figs. 7.9 and 7.10 show typical transmission electron micrographs and corresponding selected area diffraction patterns of the microstructures of melt spun Al-3wt%Si-0.15wt%Sr and Al-3wt%-0.3wt%Sr respectively, after annealing for 10 minutes at 595°C followed by slow cooling at 10K/min in the calorimeter. With 0.15wt%Sr addition, each of the eutectic liquid droplets solidified to form a faceted single crystal Si particle, as indicated by the analysis of selected area electron diffraction patterns such as in Fig. 7.9(b). With 0.35wt%Sr addition, some of the droplets solidified to form faceted single crystal Si particles, whereas other droplets solidified to form a mixture of Al_4Sr and Si particles, as indicated by the analysis of selected area diffraction patterns such as in Figs. 7.10(b) and (c).

7.3 Solidification of Al-Si Eutectic Liquid Droplets

Figs. 7.11(a)-(c) show typical differential scanning calorimeter traces of Al-Si eutectic liquid droplet solidification exotherms from the melt spun binary Al-3wt%Si alloys as a function of Al purity. For each of the calorimeter traces in Fig. 7.11, the melt spun Al-3wt%Si alloy specimen was heat treated in the calorimeter for 10 minutes at 595°C and then cooled at 10K/min to solidify the Al-Si eutectic liquid droplets. In all cases, the Al-Si eutectic liquid solidified in two stages, a sharp exotherm at an onset temperature close to 574°C, followed by a broad exotherm at a lower temperature. For each level of Al purity and annealing time and cooling rate in the calorimeter, the onset and peak temperatures of the exotherms were reproducible to within +/- 1K. Fig. 7.11 shows that the onset temperature of the high temperature

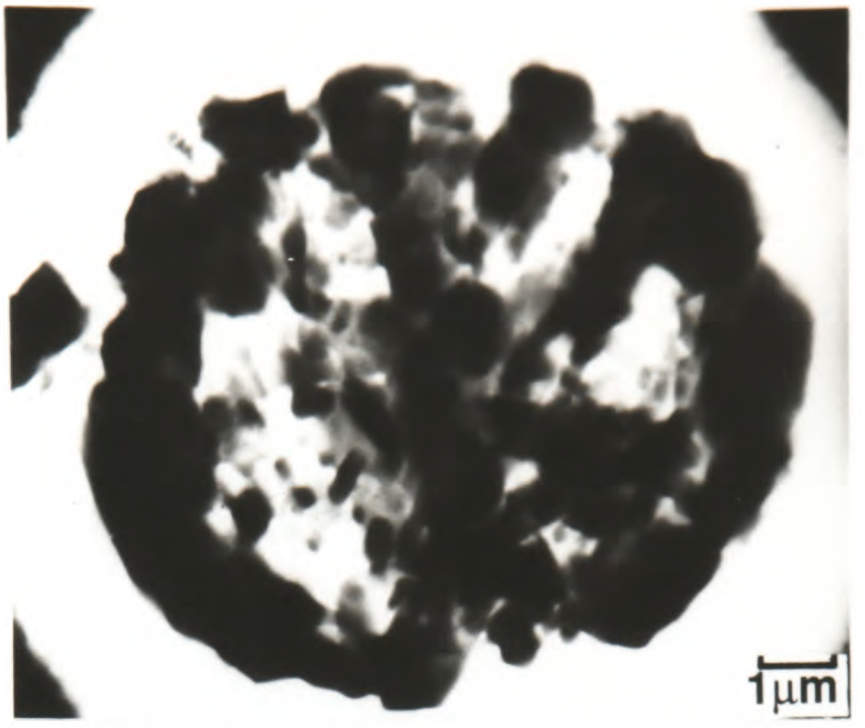


Fig. 7.8: Bright field transmission electron micrograph of the microstructure of melt spun Al-3wt%Si-Na, after annealing for 10 minutes at 595°C followed by slow cooling at 10K/min.

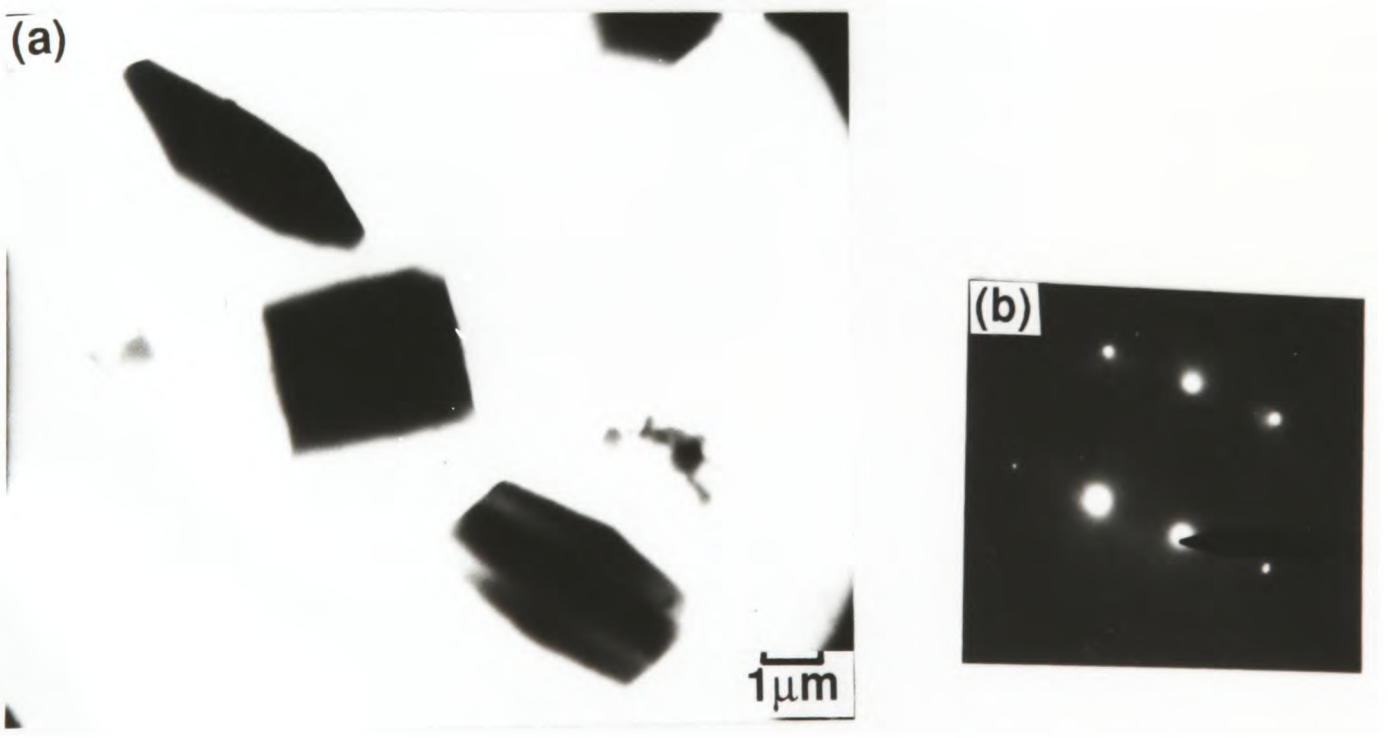


Fig. 7.9: (a) Bright field transmission electron micrograph of the microstructure of melt spun Al-3wt%Si-0.15wt%Sr, after annealing for 10 minutes at 595°C followed by slow cooling at 10K/min; and (b) selected area electron diffraction patttern from one of the Si particles in the microstructure.

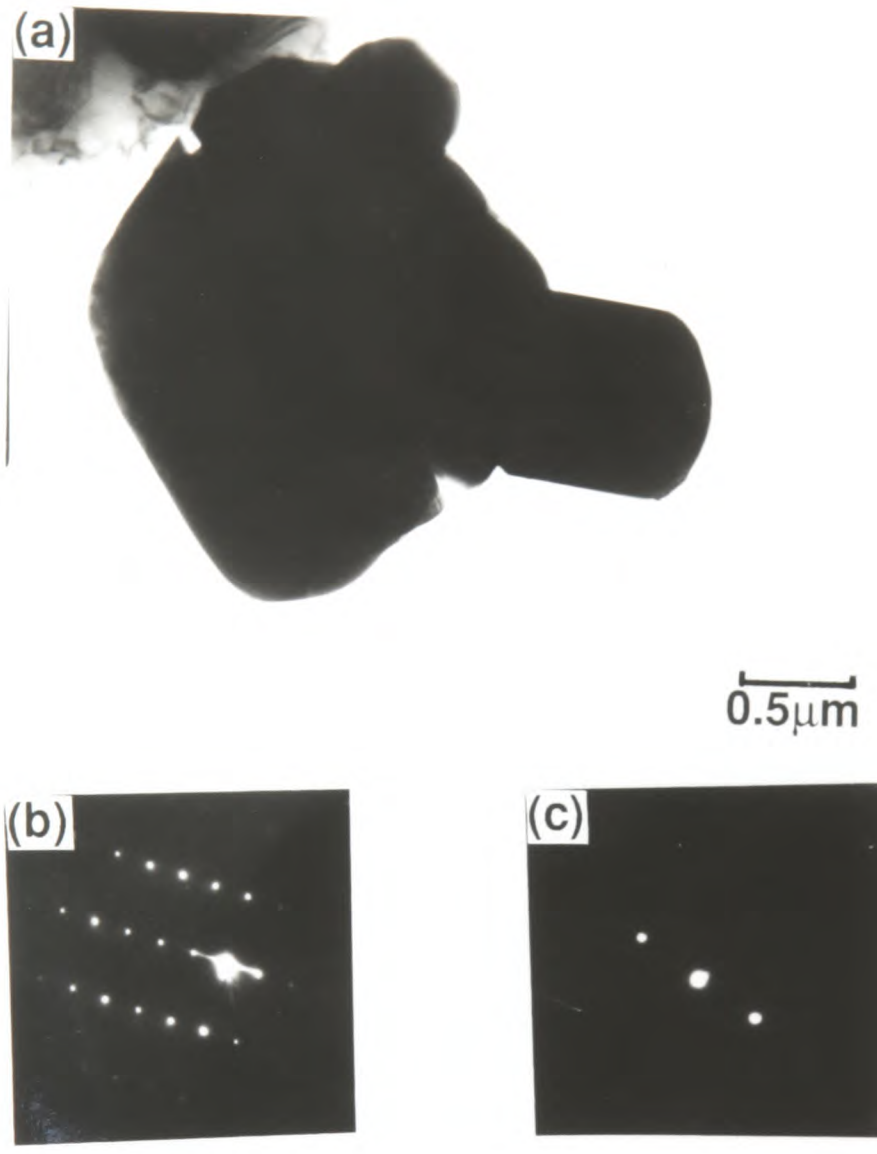


Fig. 7.10: (a) Bright field transmission electron micrograph of the microstructure of melt spun Al-3wt%Si-0.3wt%Sr after annealing for 10 minutes at 595°C followed by slow cooling at 10K/min; and (b) and (c) selected area electron diffraction patterns corresponding to (a), from Al_4Sr and Si particles respectively.

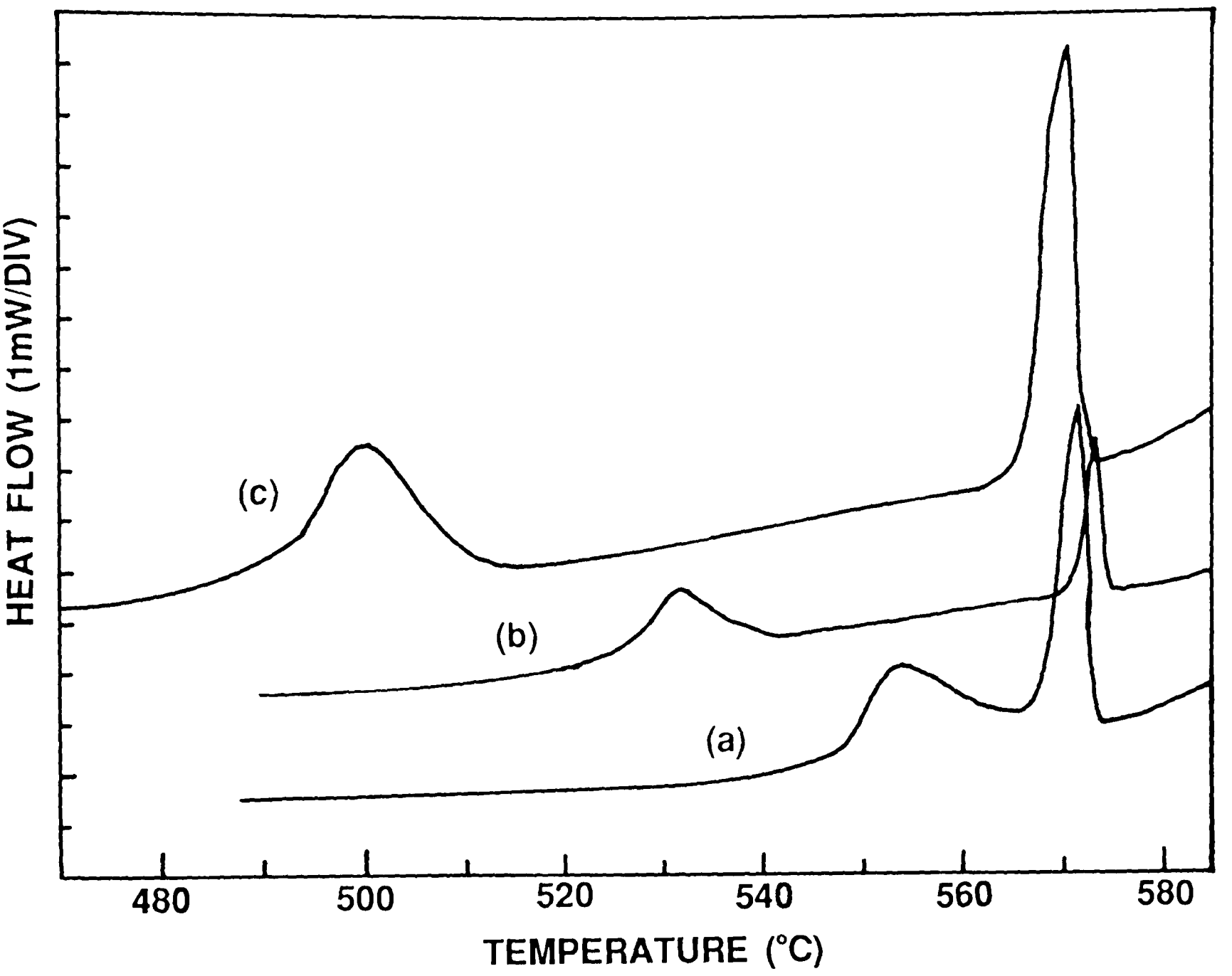


Fig. 7.11: Differential scanning calorimeter traces of Al-Si eutectic liquid solidification exotherms from melt spun binary Al-3wt%Si alloys as a function of Al purity: (a) 99.995%; (b) 99.999%; and (c) 99.9999%.

exotherm was independent of Al purity, but the onset temperature of the low temperature exotherm decreased from 568°C to 540°C and then to 514°C as the Al purity increased from 99.995% to 99.999% and then to 99.9999%.

Quenching experiments showed that the high temperature exotherms corresponded to solidification of the grain boundary eutectic liquid, and the low temperature exotherms corresponded to the solidification of the droplets. Fig. 7.12 shows a transmission electron micrograph of the microstructure of melt spun 99.999% pure Al-3wt%Si, after annealing for 10 minutes at 595°C followed by slow cooling to 560°C and then quenching into water. The eutectic droplets exhibited a fine scale quenched microstructure similar to that shown in Fig. 7.2, while the grain boundary eutectic exhibited a coarser, slow cooled solidification structure. This indicated that the grain boundary eutectic liquid solidified before quenching.

The annealing time at 595°C had different effects on the Al-Si eutectic liquid solidification exotherms in the binary Al-3wt%Si alloys, depending upon the level of Al purity. When the Al purity was 99.995%, the onset temperatures of both the high and low temperature exotherms were independent of annealing time, but the size of the high temperature exotherm decreased with increasing annealing time, and disappeared completely after 60 minutes, as shown in Fig. 7.13. When the Al purity was 99.999%, the onset temperature of the high temperature exotherm was again independent of annealing time, but the onset and peak temperatures of the low temperature exotherm decreased from 540 to 528°C and from 528 to 518°C respectively as the annealing time increased from 5 to 60 minutes. After annealing for 60 minutes, the low temperature exotherm stabilised, and was independent of further annealing, as shown in Fig. 7.14(a). When the Al purity was 99.9999%, the onset temperature of the high temperature exotherm was again independent of annealing time, but the low temperature exotherm broadened, with onset and peak temperatures which increased from 514 to 529°C and from 499 to 506°C respectively as the annealing time increased from 10 to 60 minutes. After annealing for 60 minutes, the low temperature exotherm again stabilised, and was independent of further

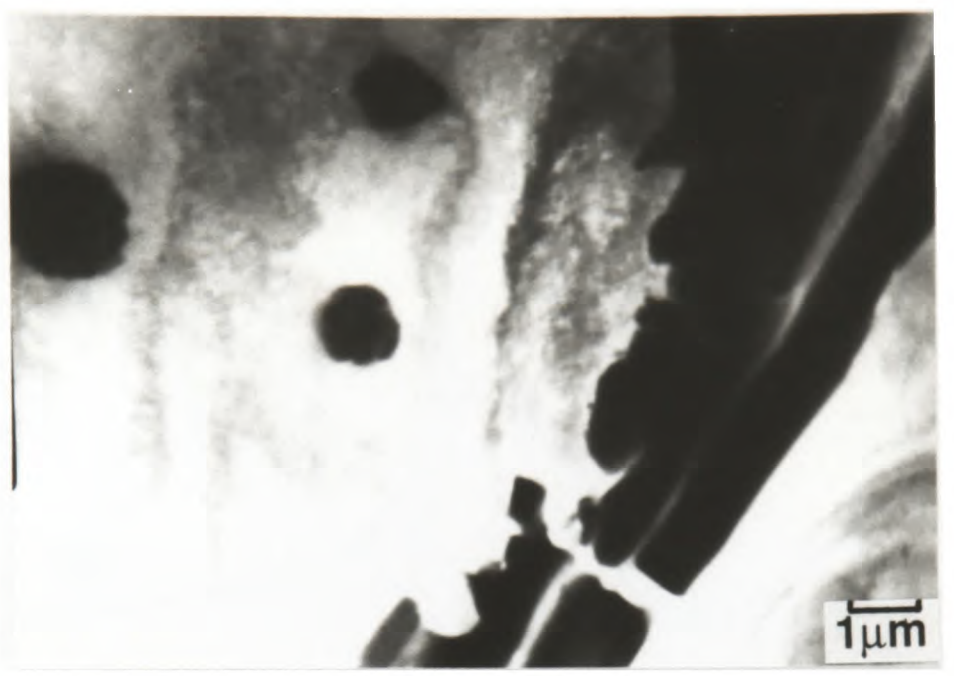


Fig. 7.12: Bright field transmission electron micrograph of the microsctructure of melt spun 99.999% pure Al-3wt%Si after annealing for 10 minutes at 595°C followed by slow cooling to 560°C, and then quenching into water.

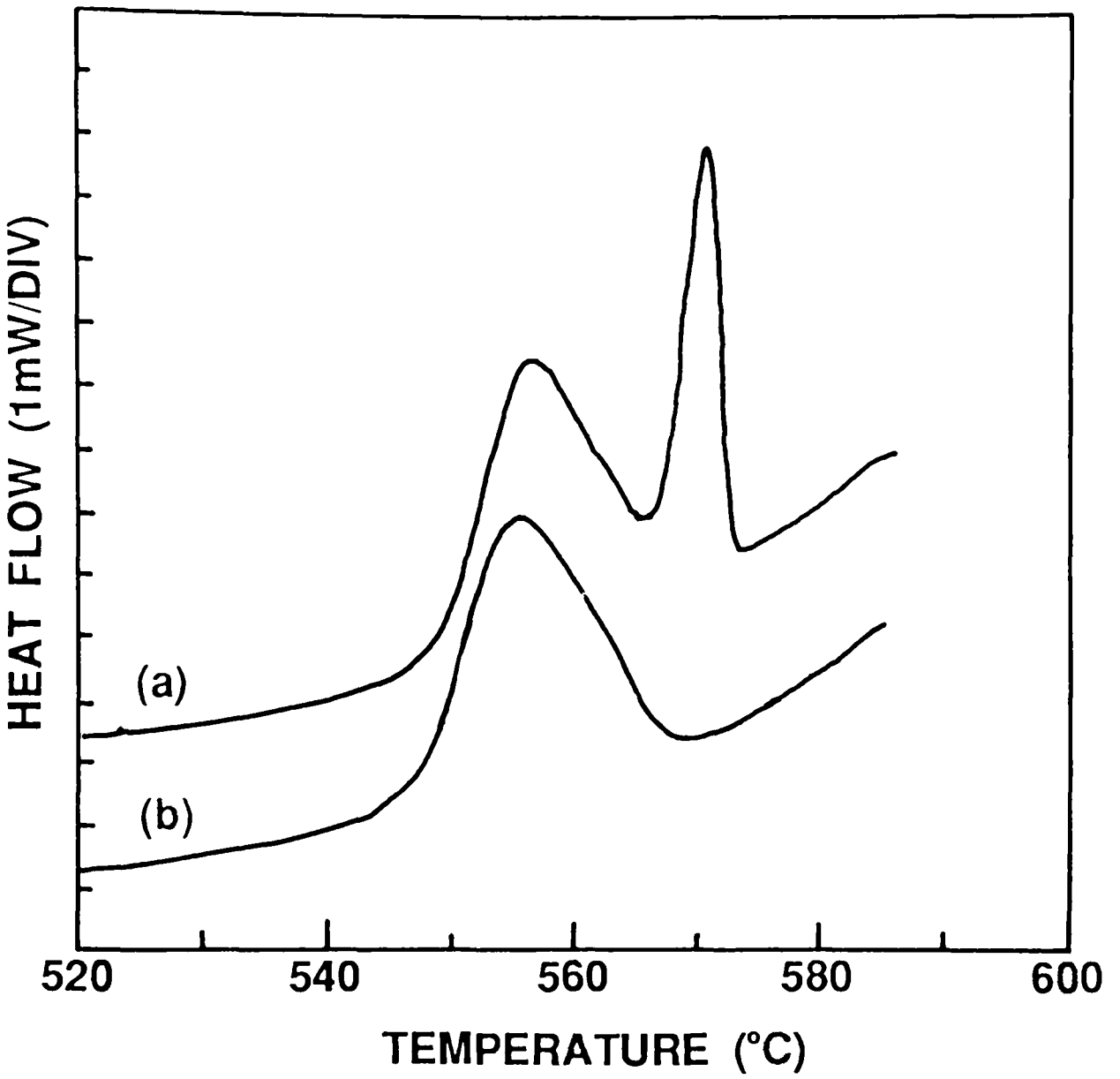


Fig. 7.13: Differential scanning calorimeter traces of Al-Si eutectic liquid solidification exotherms from melt spun 99.995% pure Al-3wt%Si: (a) annealing for 10 minutes at 595°C; and (b) annealing for 60 minutes at 595°C.

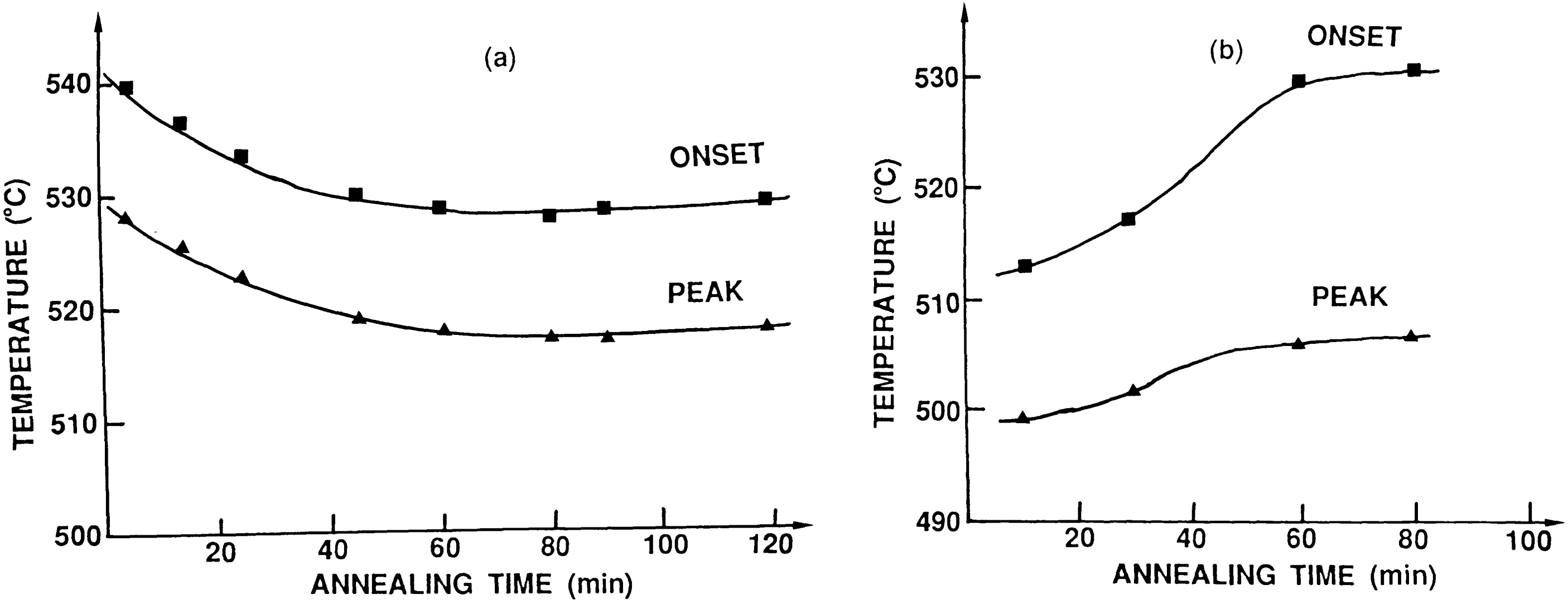


Fig. 7.14: Onset and peak temperatures of the low temperature Al-Si eutectic liquid solidification exotherm from melt spun binary Al-Si alloys as a function of annealing time at 595°C: (a) 99.999% pure Al-3wt%Si; and (b) 99.9999% pure Al-3wt%Si.

annealing, as shown in Fig. 7.14(b).

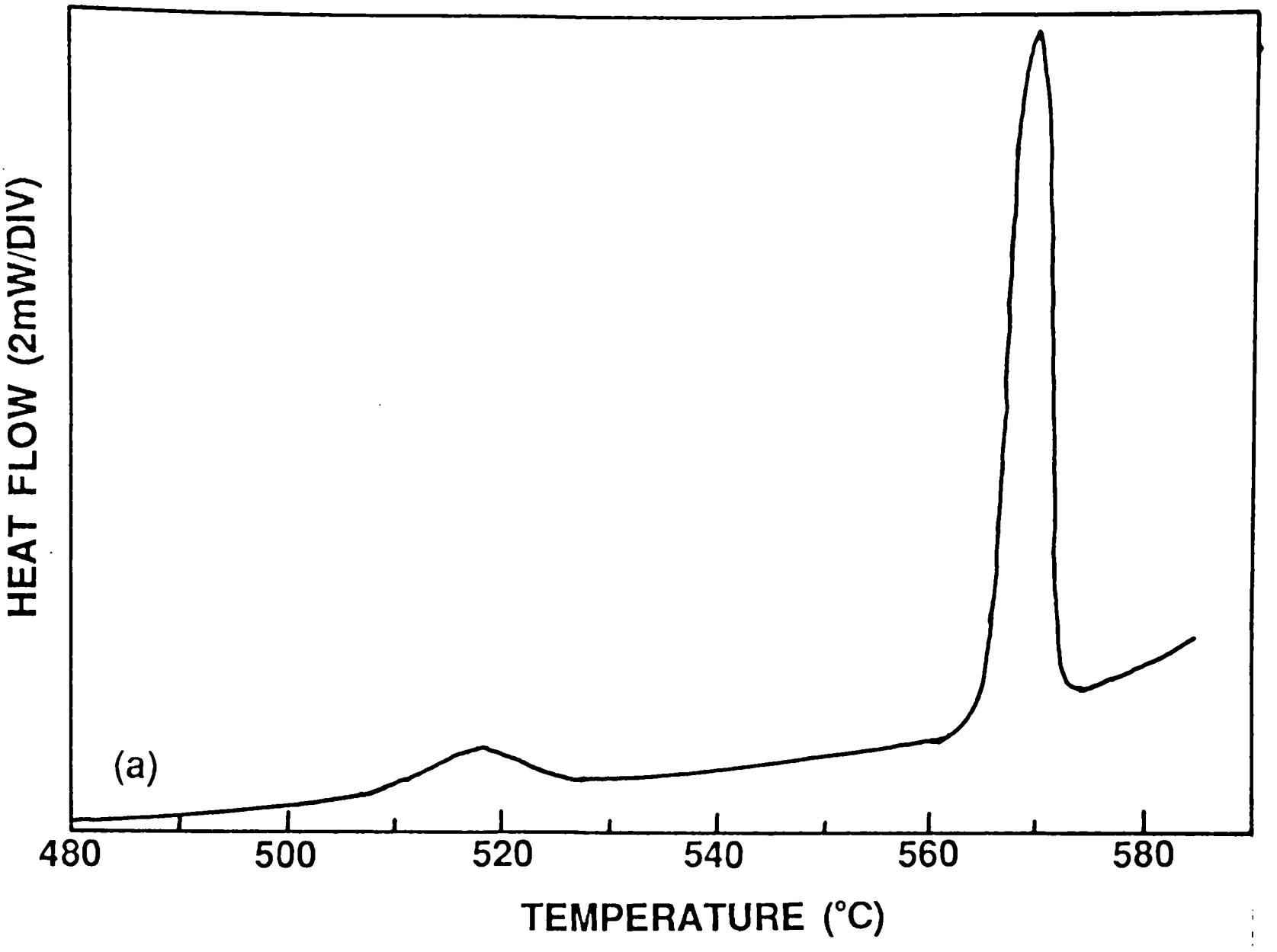
Figs. 7.15(a)-(c) show typical differential scanning calorimeter traces of Al-Si eutectic liquid droplet solidification exctherms from the melt spun ternary Al-Si-Na and Al-Si-Sr alloys. For each of the calorimeter traces in Fig. 7.15, the melt spun ternary alloy specimen was heat treated in the calorimeter for 10 minutes at 595°C and then cooled at 10K/min to solidify the Al-Si eutectic liquid droplets. With a small Na addition, the Al-Si eutectic liquid solidified with a sharp exotherm at an onset temperature close to 574°C, followed by a small broad exotherm at an onset temperature close to 527°C, as shown in Fig. 7.15(a). With 0.35wt%Sr addition, the Al-Si eutectic liquid solidified with only one sharp exotherm at an onset temperature close to 574°C, as shown in Fig. 7.15(c). With 0.15wt%Sr additon, the Al-Si eutectic liquid solidified with a sharp exotherm at an onset temperature close to 574°C, followed by a small broad exotherm at an onset temperature close to 568°C, as shown in Fig. 7.15(b). The ternary alloy exotherms were independent of annealing time above the eutectic temperature.

7.4 Discussion

7.4.1 Solidification of binary Al-Si droplets

In all three melt spun binary Al-3wt%Si alloys, the Al-Si eutectic liquid droplets solidify with two exotherms. The high temperature exotherm is at 3-4K undercooling below the eutectic temperature and is independent of Al purity, while the low temperature exotherm is at an undercooling which increases from 9 to 63K as the Al purity increases from 99.995% to 99.9999%.

In the heat treated 99.999% pure Al-3wt%Si alloy, large flakes of Si are observed in the grain boundaries as shown in Fig. 7.12 , indicating that there is quite a large volume fraction of Al-Si liquid along the grain boundary. In the heat treated 99.995% pure Al-3wt%Si alloy, however, Si flakes are not observed at the grain boundaries, and at the same time the higher temperature



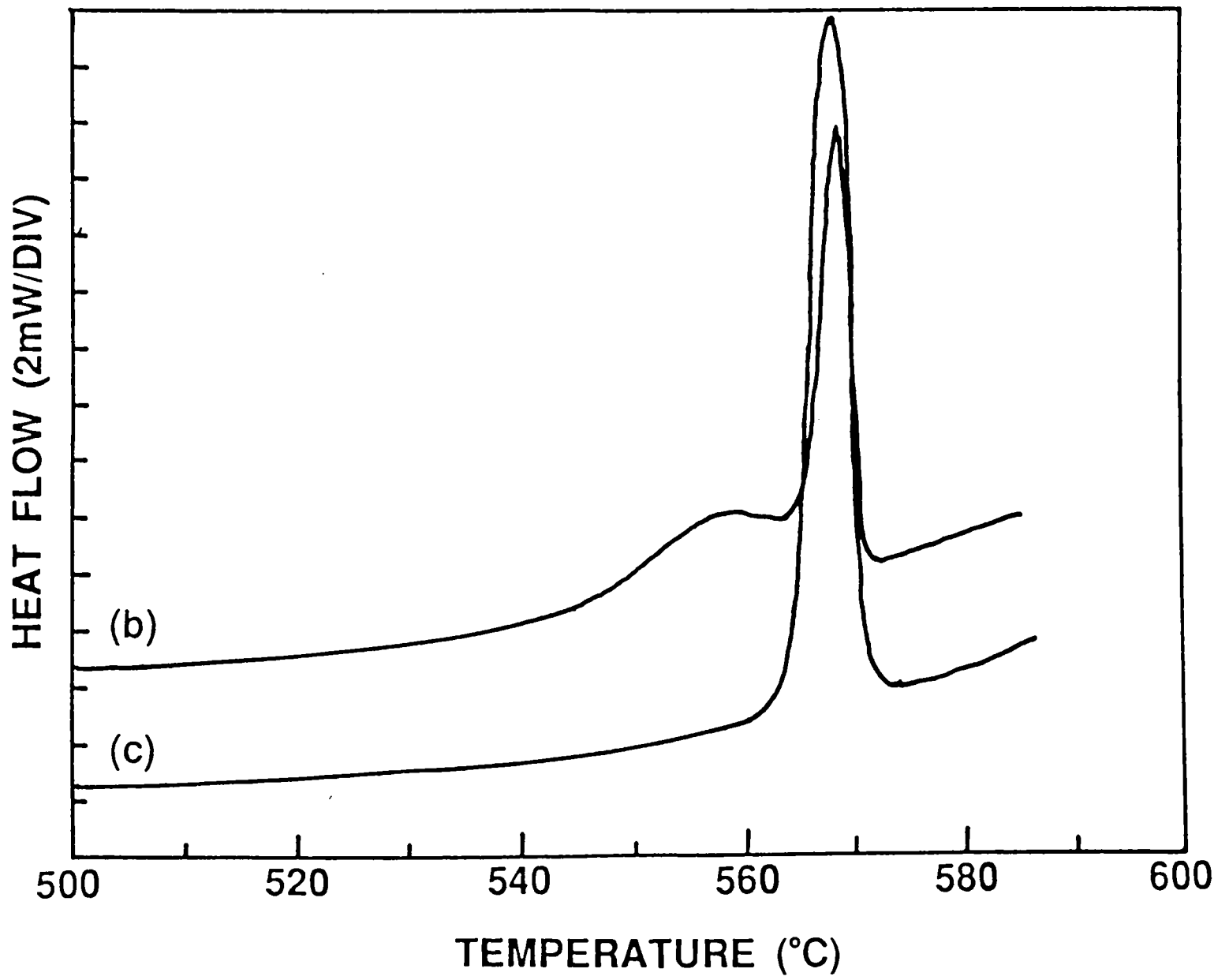


Fig. 7.15: Differential scanning calorimeter traces of Al-Si eutectic liquid solidification exotherms from melt spun ternary Al-Si alloys (a) Al-3wt%Si-Na; (b) Al-3wt%Si-0.15wt%Sr; and (c) Al-3wt%Si-0.3wt%Sr.

exotherm disappeared completely. This may be because the continuous grain boundary eutectic liquid breaks into liquid droplets during annealing, so that the volume of liquid containing effective catalytic trace impurities decreases below the detection level of the calorimeter.

The increase in Si nucleation undercooling in the Al-Si eutectic liquid droplets with increasing Al purity agrees well with the previous results of Southin (1970) using Al-Si alloy ingots. Southin suggested that Si does not nucleate on the interface between the liquid droplets and the surrounding Al matrix, but nucleates instead on the surface of inclusions in the liquid droplets. This suggestion was based on the observation of Al-Si eutectic microstructures radiating from the centre of the solidified droplets. In the present more detailed transmission electron microscope investigation, the solidified droplets do not exhibit radiating eutectic structures, and no inclusions are observed. In fact, the clustered Si particle microstructures in the highest purity 99.9999% Al-3wt%Si, as shown in Fig. 7.7(b), suggest strongly that Si nucleation takes place on the interface between the droplets and the surrounding Al rich matrix. The spherical droplet shapes in 99.9999% pure Al-3wt%Si, such as shown in Fig. 7.7, indicates that no facets develop during slow cooling in the calorimeter, and that there are no places on the interface where preferential Si nucleation takes place.

Fig. 7.11 shows that increasing Al purity leads to an increased undercooling to initiate droplet solidification, i.e. to an decreased catalytic efficiency of the Al matrix for nucleation of Si solidification. Experiments on the effects of Mg on nucleation of Cd solidification by Al, and of Ge on nucleation of Pb solidification by Al, have clearly shown that ternary additions can strongly influence the catalytic efficiency of Al as a solidification nucleant. Similarly, impurity elements seem to have a sensitive effect on the catalytic efficiency of Al for nucleating the solidification of Si. Increased annealing time at 595°C increases the Si nucleation undercooling in 99.999% pure Al-Si, but decreases the Si nucleation undercooling in 99.9999% pure Al-Si, as shown in Figs. 7.14(a) and (b). However, the onset

temperature for Si nucleation in both cases stablises close to 529°C. This indicates the presence of a common catalytic impurity element. With long enough annealing time, the distribution of this catalytic impurity elements equilibrates in both alloy purities, so that the effect is similar in both cases.

7.4.2 Solidification of ternary Al-Si alloys

Compared with binary 99.995% pure Al-3wt%Si, Na and Sr additions do not affect the onset temperature of the high temperature exotherm, but do affect the onset temperature of the low temperature exotherm, in a different way for each element. With a low level of Na addition, the onset temperature of the low temperature exotherm decreases from 568 to 527°C, i.e. the nucleation undercooling for Si solidification on the surrounding Al matrix increases from 9 to 50K. With 0.15wt%Sr addition, the onset temperature of the low temperature exotherm does not change, but with 0.35wt%Sr addition, the lower temperature exotherm disappears, i.e. the nucleation undercooling for Si solidification on the surrounding Al matrix decreases from 9K to 3-4K.

The effect of Na on the Si nucleation temperature is in agreement with that reported by Southin (1970). Southin suggested that the increased Si nucleation undercooling results from fewer external nucleants, because of reactions between the Na addition and impurity elements such as P. The present investigation shows that Si nucleates on the Al matrix and not on external inclusions, so that Southin's mechanism is not possible. Addition of Na can reduce the catalytic efficiency of the Al matrix by several possible mechanisms: (a) by segregating at the interface between the eutectic liquid and the matrix, or (b) by reacting with other impurities which stimulate Si nucleation, and removing them from the interface between the eutectic liquid and the matrix. Unfortunately, Na contents were below the 0.05wt% detection level of the microprobe analyser, making it difficult to determine the precise mechanism.

Unlike Na, addition of Sr stimulates the nucleation of Si solidification. The appearance of high temperature intermetallic phases such as Al_4Sr in the microstructure of heat treated Al-3wt%Si-0.3wt%Sr, often in the form of particles in contact with Si, suggests that Si nucleation is stimulated by these high temperature phases. The Si nucleation temperature is not affected by 0.15wt%Sr.

7.4.3 Undercooling and microstructure

The solidified microstructures of the Al-Si eutectic droplets in the binary and ternary melt spun Al-3wt%Si alloys depend upon the Si nucleation temperature, as shown in Figs. 7.4-7.10. When Si nucleates at high temperature, i.e. at low undercooling, the droplet microstructures consist of coarse and faceted Si particles. However, when Si nucleates at low temperature, i.e. at high undercooling, the droplet microstructures consist of a fine-scale nonfaceted two phase eutectic structures. Because of recalesence, the Si growth temperature may be somewhat higher than the nucleation temperature measured from the calorimeter traces. In low purity binary Al-3wt%Si, and in ternary Al-Si-Sr, the nucleation undercooling is only ~10K below the eutectic temperature, and the Si growth temperature is close to the eutectic temperature. However, in high purity binary Al-Si and in ternary Al-Si-Na alloys, the nucleation undercooling is 40-70K below the eutectic temperature, and the Si growth temperature is also well below the eutectic temperature. Clearly, the Si growth morphology depends upon its nucleation and therefore its growth temperature, as suggested previously by Southin (1970) and Kim and Heine (1963-64). Southin used the mechanism proposed by Cahn et al (Cahn, 1960, Cahn et al, 1964) to explain the change in Si growth morphology with increasing undercooling. At low undercooling, under normal conditions, Si grows by faceted lateral growth, but at high undercooling, Si grows by non-faceted normal uniform growth. This mechanism is also supported by the similar investigation into the structure of eutectic liquid droplets in Al-Ge and Pb-Sb alloys (Southin, 1970).

As shown in Figs. 7.4 and 7.7, one droplet can solidify to produce either just one single Si crystal or many Si crystals depending on the conditions, indicating that either single nucleation or multiple nucleation of Si occurs in one droplet. Multiple nucleation has been reported for the solidification of atomised Al-Si eutectic powders (Levi and Mehrabian, 1982) and in other powders (Perepezko et al, 1987). At very high liquid undercooling, multiple nucleation is possible, because of slow atomic transport and therefore the growth kinetics. The present case is slightly different from the solidification of atomised powders, because nucleation is heterogeneous. However, with high nucleation undercooling, i.e. low nucleation temperature, atomic transport and growth may again be slow, so that a similar mechanism may possibly be operative.

7.4.4 Modification of Al-Si by Na and Sr

Na and Sr additions both lead to modification of Al-Si eutectic structure in conventional castings (Kanani and Abbaschian, 1984, Hanna et al, 1984). However, the present work shows that Na and Sr additions have different effects on the catalytic nucleation of Si solidification by Al. Na decreases the Si nucleation temperature and modifies the Si morphology to produce a fine scale eutectic structure. However, 0.15wt%Sr addition does not affect the Si nucleation temperature or morphology. This indicates that a change in nucleation mechanism is not the only mechanism for producing modification of Al-Si alloys.

The present results of effect of Na additions on the Si nucleation temperature support previous suggestions (Southin, 1970, Flood and Hunt, 1987) that Na additions modify the Si morphology in two stages: (a) decreasing Si nucleation temperature, and (b) changing Si growth mode. However. the present result for the effect of Sr on the Si nucleation temperature proves that the role of Sr additons in modifying the Si morphology is only by changing the Si growth mode, probably by the twinning mechanism as suggested by Hellawell and co-workers (Day and Hellawell, 1968, Hanna et al, 1984) and Hogan and co-workers (Kobayashi and Hogan, 1985, Shamsuzzoha and Hogan, 1986).

Chapter 8

Conclusions

8.1 General Comments

Before the conclusions drawn from the present work are summarised, it is interesting to compare some of the results obtained in this study with corresponding results obtained in previous work on heterogeneous nucleation of solidification. In the present work, it has been shown that 56, 13, 22 and 63K undercoolings are required to initiate the solidification of Cd, In, Pb and Si on Al respectively. These results are only a few degrees different from the corresponding undercoolings reported by Southin and Chadwick (1978). Considering that in the present work differential scanning calorimetry is used instead of differential thermal analysis, and that onset temperatures of the exotherms instead of peak temperatures are used to calculate the undercoolings, the results in the present work are in very good agreement with Southin and Chadwick's results. This indicates: (a) that the Cantor et al's refinements of the entrained particle technique (Moore et al, 1990, Kim and Cantor, 1990) do not affect the results adversely, but only give more information; and (b) that the entrained particle technique is very reliable for heterogeneous nucleation experiments. In the present work, not many alloys have been examined, and therefore the non-reciprocal principle of heterogeneous nucleation can not be tested directly. However, considering the good agreement between the present work and Southin and Chadwick's results, the present work supports Southin and Chadwick's conclusion that the non-reciprocal principle is not correct.

As for the factors controlling the catalytic efficency of a solidification nucleant for specific metals, the results of doping experiments clearly contradict Turnbull and Vonnegut's theory (1952) that structural factors such as lattice disregistry acrossing the nucleus-nucleant interfaces are dominating factors in determining the catalytic effeciency. The results of doping Ge into Al-Pb alloys and Mg into Al-Cd alloys show that without

changing the structural relationship between the solid nuclei and the nucleant, the required undercooling for heterogeneous nucleation can be changed significantly by changing the chemical bonding. In addition, Southin and Chadwick's conclusion (1978) that similar crystal structure and bonding type between nuclei and nucleant are necessary for efficacious heterogeneous nucleation is doubtful.

8.2 Conclusions

The conclusions of the present work are summarised as follows.

1. The as-solidified microstructures of melt spun hypomonotectic Al-4.5wt%Cd and Al-7wt%In consist of homogeneous distributions of faceted Cd and In particles embedded in an Al matrix. The as-melt spun Cd particle sizes range from 5-120nm in diameter, with an average particle size of 20nm in diameter. The as-melt spun In particles size range from 10-200nm in diameter, with a average particle size decreasing from 70-30nm in diameter as the wheel speed increases from 7-65m/s.

2. The Cd and In particles are formed during monotectic solidification of the Al matrix, and have irregular monotectic microstructures consistent with a relatively low value of ~100Ks/mm^2 of the ratio of thermal gradient to solidification velocity.

3. The Cd particles in melt spun hypomonotectic Al-4.5wt%Cd exhibit an orientation relationship with the Al matrix of $\{111\}_{Al}//\{0001\}_{Cd}$ and $\langle 110\rangle_{Al}//\langle 11\bar{2}0\rangle_{Cd}$. In each Al grain, there are four Cd particle variants depending upon which $\{111\}_{Al}$ plane is parallel to $\{0001\}_{Cd}$. The Cd particles exhibit a distorted truncated octahedral shape, bounded by six curved $\{100\}_{Al}//\{20\bar{2}3\}_{Cd}$ facets, six curved $\{111\}_{Al}//\{40\bar{4}3\}_{Cd}$ facets, and two flat $\{111\}_{Al}//\{0001\}_{Cd}$ facets. The as-melt spun Cd particles are metastable, and equilibrate during heat treatment just below the Cd melting point, becoming elongated to increase the surface area and decrease the separation of the

$\{111\}_{Al}//\{0001\}_{Cd}$ facets.

4. The In particles in melt spun hypomonotectic Al-7wt%In exhibit an orientation relationship with the Al matrix which can be described as $\{111\}_{Al}//\{111\}_{In}$ and $\langle 110\rangle_{Al}//\langle 110\rangle_{In}$, using a face centred tetragonal representation for In. The In particles exhibit a truncated octahedral shape bounded by $\{111\}_{Al}$ and $\{100\}_{Al}$ facets. The as-melt spun In particles are metastable, and equilibrate during heat treatment just below the In melting point, becoming elongated to increase the area and decrease the separation of the low energy $\{111\}_{Al}//\{111\}_{In}$ facets.

5. The solid Al-solid Cd surface energy anisotropy is constant over the temperatue range between room temperature and the Cd melting point of 321°C, with the $\{100\}_{Al}//\{20\bar{2}3\}_{Cd}$ surface energy on average 40% greater than the $\{111\}_{Al}//\{0001\}_{Cd}$ surface energy. and 10% greater than the $\{111\}_{Al}//\{40\bar{4}3\}_{Cd}$ surface energy. The $\{100\}_{Al}//\{20\bar{2}3\}_{Cd}$ facets disappear, and the $\{111\}_{Al}//\{40\bar{4}3\}_{Cd}$ and $\{111\}_{Al}//\{0001\}_{Cd}$ surface energies become equal when the Cd particles melt, and the surface energy anisotropy decreases gradually from 1.1 to 1 as the temperature increases above the Cd melting point from 321°C to ~450°C.

6. The solid Al-solid In surface energy anisotropy is constant over the temperature range between room temperature and the In particle melting temperature, with the $\{100\}_{Al}$ surface energy on average 36% greater than the $\{111\}_{Al}//\{111\}_{In}$ surface energy and 25% greater than the other $\{111\}_{Al}$ surface energy. The $\{100\}_{Al}$ facets disappear and all the $\{111\}_{Al}$ surface energies become equal when the In particles melt, and the surface energy anisotropy decreases gradually from 1.25 to 1 as the temperature increases above the In melting point.

7. Solidification of Cd particles embedded in an Al matrix is nucleated catalytically by the surrounding Al matrix on the $\{111\}_{Al}$ faceted surfaces with an undercooling of 56K and a contact angle of 42°, in good agreement with the

spherical cap model of heterogeneous nucleation.

8. Solidification of In particles embedded in an Al matrix is nucleated catalytically by the surrounding Al matrix on the $\{111\}_{Al}$ facets with an undercooling of 13K and a contact angle of 27°.

9. Solidification of Pb particles embedded in an Al matrix is nucleated catalytically by the surrounding Al matrix on the $\{111\}_{Al}$ facets with an undercooling of 22K and a contact angle of 21°.

10. Doping of Zn in the Al-Cd alloy does not affect the catalytic efficiency of Al as a heterogeneous nucleant for Cd soldification; doping of Ga, Ge and Cu in the Al-Cd alloy decreases the catalytic efficiency of Al as a heterogeneous nucleant for Cd solidification. Doping of Zn and Cu in the Al-Pb alloy does not affect the catalytic efficiency of Al as a heterogeneous nucleant for Pb solidification; doping of Ga in the Al-Pb alloy decreases the catalytic efficiency of Al as a heterogeneous nucleant for Pb solidification.

11. Melt spun hypermonotectic Al-9wt%Cd-1.5wt%Mg exhibits a microstructure consisting of a homogeneous distribution of faceted Cd(Mg) particles embedded in an Al(Mg) matrix. The as-melt spun Cd(Mg) particles exhibit an orientation relationship of $\{111\}_{Al(Mg)}//\{0001\}_{Al(Mg)}$ and $\langle 110\rangle_{Al(Mg)}//\langle 11\bar{2}0\rangle_{Cd(Mg)}$ with the Al(Mg) matrix, and have a distorted truncated octahedral shape bounded by $\{111\}_{Al(Mg)}$ and $\{100\}_{Al(Mg)}$ facets. After equilibration by heat treatment, just below the Cd(Mg) melting point, the Cd(Mg) particles become elongated to increase the surface area and decrease the separation of the two $\{111\}_{Al(Mg)}//\{0001\}_{Cd(Mg)}$facets. The lattice disregistries between the Cd(Mg) particles and the Al(Mg) matrix on the $\{111\}_{Al(Mg)}//\{0001\}_{Al(Mg)}$ facets are 4% and 7% in Al-4.5wt%Cd and Al-9wt%Cd-1.5wt%Mg respectively.

12. The solidification of Cd(Mg) particles in melt spun Al-9wt%Cd-1.5wt%Mg is catalytically nucleated by the {111} planes of the surrounding Al(Mg) matrix, at an undercoolings of 34K below the Cd(Mg) particle melting point. Addition

of Mg to Cd particles embedded in Al increases the lattice disregistry, but decreases the undercooling before the onset of Cd(Mg) particle solidification, indicating that chemical interactions dominate over structural factors in determining the catalytic efficiency of nucleating solidification in Al-Cd-Mg alloys.

13. The microstructures of melt spun hypermonotectic Al-5wt%Pb alloys containing ternary additions of 0-2wt%Ge consist a distribution of a 5-150nm diameter Pb particles embedded in an Al(Ge) matrix. At Ge concentrations less than or equal to 1wt%, the Ge atoms are dissolved in the Al matrix, whereas at Ge concentrations greater than or equal to 1.5wt%, the Ge atoms are not fully dissolved in the Al matrix, and Ge precipitates appear in the melt spun alloy microstructures.

14. The Pb particles in melt spun hypermonotectic Al-Pb-Ge alloys exhibit a cube-cube orientation relationship with the Al(Ge) matrix. Pb particles which are not in contact with Ge precipitates, ie which are surrounded fully by the Al(Ge) matrix, exhibit a regular truncated octahedral shape bounded by {100} and {111} facets. However, Pb particles which are in contact with Ge precipitates exhibit more irregular and non-truncated octahedral shapes.

15. At Ge concentrations less than or equal to 1wt%, Pb particle solidification is catalytically nucleated by the {111} planes of the surrounding Al(Ge) matrix. As the Ge concentration in the Al(Ge) matrix increases from 0 to 1wt%, the nucleation temperature decreases linearly from 305°C to 284°C, the nucleation undercooling increases linearly from 22K to 43K, and the cosine of the contact angle Θ decreases linearly from 0.93 to 0.84. Addition of Ge to Al increases the undercooling before the nucleation of Pb solidification on the $\{111\}_{Al(Ge)}$ planes, but also decreases the lattice disregistry across the $\{111\}_{Al(Ge)}//\{111\}_{Pb}$ nucleating planes. In other words, chemical factors dominate over structural factors in determining the catalytic efficiency of Al(Ge) as a heterogeneous nucleant for the solidification of Pb.

16. At Ge concentrations greater than or equal to 1.5wt%, Pb particle solidification takes place by two mechanisms. (a) The solidification of Pb particles not in contact with Ge precipitates is catalytically nucleated by the {111} planes of the surrounding Al(Ge) matrix, at an undercooling which increases from 53K to 60K as the Ge concentration increases from 1.5wt% to 2.0wt%. (b) The solidification of Pb particles in contact with Ge precipitates is catalytically nucleated by the Al(Ge) matrix-Ge precipitate interfaces at a constant undercooling of 45K.

17. The microstructures of melt spun hypermonotectic Al-5wt%Pb alloys containing ternary additions of 0-1wt%Si consist of a bimodal distribution of Pb particles embedded in an Al(Si) matrix. The larger Pb particles range from 40-200nm in diameter, and the smaller Pb particles range from 5-10nm in diameter. At Si concentrations less than or equal to 0.2wt%, the Si atoms are dissolved in the Al matrix, whereas at Si concentrations above 0.2wt%, the Si atoms are not fully dissolved in the Al matrix, and Si precipitates appear in the melt spun alloy microstructures.

18. The Pb particles in the melt spun hypermonotectic Al-Pb-Si alloys exhibit a cube-cube orientation relationship with the Al(Si) matrix. Pb particles which are not contact with Si precipitates, ie which are surrounded fully by the Al(Si) matrix, exhibit a regular truncated octahedral shape bounded by {100} and {111} facets. Pb particles which are in contact with Si precipitates exhibit more irregular and non-truncated octahedral shapes.

19. The solidification of Pb particles not in contact with Si precipitates is catalytically nucleated by the {111} planes of the surrounding Al(Si) matrix at an undercooling of 22K, and is independent of Si content up to the solubility limit. The solidification of Pb particles in contact with Si precipitates is catalytically nucleated by the Al(Si) matrix-Si precipitate interfaces, at undercoolings in the range 0-22K.

20. The equilibrium melting point of small Cd particles in melt spun Al-4.5wt%Cd is depressed because of capillarity, and the depression of the equilibrium melting point increases with decreasing particle size. For the smallest 5nm diameter Cd particles, the equilibrium melting point is depressed by 9K.

21. In melt spun Al-7wt%In and Al-5wt%Pb, most of the In and Pb particles embedded within the Al matrix grains melt at superheatings in the range of 0-40K, and the superheatings increases with decreasing particle size. The In and Pb particles along the grain boundaries of the Al matrix melt without any superheating, and the melting point of some of the grain boundary In and Pb particles is depressed by 1-3K and 1-7K respectively.

22. The superheating of In and Pb particle melting within the Al matrix grains is due to a kinetic difficulty of nucleating melting, which increases with decreasing In and Pb particle size.

23. The as-solidified microstructures of melt spun Al-3wt%Si alloys without and with ternary additions of Na and Sr consist of a homgeneous distribution of 0.1-0.8μm Si particles distributed along the cell boundaries in an α-Al matrix.

24. The heterogeneous nucleation temperature for solidification of Si in contact with the surrounding Al matrix depends sensitively on the purity of the Al, with a nucleation undercooling which increases from 9K to 63K below the Al-Si eutectic temperature as the average Al purity increases from 99.995% to 99.9999%. With an Al purity of 99.995%, the Si nucleation temperature is independent of annealing time above the eutectic temperature; with an Al purity of 99.999%, the Si nucleation temperature decreases with annealing time above the eutectic temperature; and with the highest Al purity of 99.9999%, the Si nucleation temperature increases with annealing time above the eutectic temperature.

25. Na and Sr have different effects on the Si nucleation temperature. With an Al purity of 99.995%, Na addition increases the Si nucleation undercooling from 9K to 50K, 0.15wt%Sr addition does not affect the Si nucleation temperature, and 0.3wt%Sr addition decreases the Si nucleation undercooling from 9K to 3-4K.

26. The solidified microstructure of liquid Al-Si eutectic droplets embedded in an Al matrix is affected by the Si nucleation undercooling. With low Si nucleation undercooling, each Al-Si eutectic liquid droplet solidifies to form one faceted Si particle; however, with high Si nucleation undercooling, each Al-Si eutectic droplets solidifies to form a large number of non-faceted Si particles embedded in Al. There is no clear orientation relationship between the Al matrix and the solidified Si.

27. The chemical effect of trace impurities on the heterogeneous nucleation of Si solidification is important in industrial casting hypoeutectic Al-Si alloys. Na and Sr additions have different effects on the Si nucleation temperature, and work in different ways to modify the resulting eutectic Al-Si structure.

8.3 Future Work

Based on the present and previous published work on heterogeneous nucleation of solidification, the following are proposed for future studies of heterogeneous nucleation.

1. Other binary monotectic systems should be examined with the modified entrained particle technique used in the present work, so as to establish a data base for heterogeneous nucleation of solidification.

2. The doping experiments used in the present work should be applied to other appropriate monotectic systems to explore further the factors controlling the catalytic efficiency of solidification nucleants.

3. Other binary eutectic system should be examined with the modified entrained particle technique used in the present work, to examine the effect of nucleation undercooling on the soldified eutectic structures.

4. Thermodynamic and phase diagram data should be used to construct models to attempt to (1) predict nucleation undercooling and (2) explain the effect of ternary elements on the heterogenous nucleation of metal solidification.

References

Chapter 1

Kim W. T. and Cantor B., 1990, J. Mat. Sci., in press

Moore K. I., Zhang D. L. and Cantor B., 1990, Acta Metall. Mater., 38, 1327

Turnbull D., 1950, J. Appl. Phys., 21, 1022

Wang C. C. and Smith C. S., 1950, Trans. Metall. Soc. AIME, 188, 136

Chapter 2

Anderson I. E. and Perepezko J. H., 1983, in "Grain Refinement in Casting and Welds" G. J. Abbaschian (ed.), TMS-AIME, Warrendale, PA

Baster field J., Miller W. A. and Weatherley G. C., 1970, Can. met., 131

Becker R. and Doring W., 1935, Ann. Physik, (5), 24, 719

Berman A. P. and Curzon A. E., 1974, Can. J. Phys., 52, 923

Bosio L., Defrain A. and Epelboin I., 1961, C .R. Acad. Sci., 523, 2343

Boswell P. G. and Chadwick G. A., 1980 Acta Metall., 28, 209

Boswell P. G., Chadwick G. A., Elliot R. and Sale F. R., 1979, in "Solidification and Casting of Metals ", Metal Society, London, P.611

Bradshaw F. J., Gasper M. E. and Pearson S., 1958-1959, J. Inst. of Metals, 87, 15

Cahn J. W., 1977, J. Chem. Phys., 66, 3667

Cahn J. W., 1979, Met. Trans., 10A, 119

Camel D., Simon J. P. and Eustathopoulos N., 1980, Scripta Metall., 41, 1101

Cantor B., to be published

Cantor B. and Doherty R. T., 1979, Acta Met., 27, 33

Carlgerg T. and Bergman A., 1985, Scripta Metall., 19, 333

Chadwick G. A., 1962, J. Inst. Metals, 91, 169

Chadwick G. A., 1965(1), J. Aus. Inst. Met., 10, 178

Chadwick G. A., 1965(2), Br. J. App. Phys., 16, 1095

Chadwick G. A., 1969 in "Interfaces", R. C. Gifkins (ed), Butterworths, London, P.101

Chattopadhyay K. and Ramachandrarao P., 1980, J. Mat. Sci., 15, 685

Christian J. W., 1975, "The Theory of Transformation in Metals and Alloys", Pergamon, Oxford

Chu M. G., Shiohara Y. and Flemings M. C., 1984, Met. Trans., 15A, 1303

Cibula A., 1949, J. Inst. Metals, 17, 321

Cladkihk N. T., Lavin U. I., Severin V. M. and Khokevich V. T., 1973, in "Kinetika i Mekhanika Kinstall", Nauka i Technika, Minska, P.126

Clark J. N. and Elliott R., 1976(1), Metal Sci., 10, 101

Clark J. N. and Elliott R., 1976(2), J. Crys. Growth, 33, 169

Coombes C. J., 1972, J. Phys. F. (Met. Phys.), 2, 441

Cooper K. P., Anderson I. E. and Perepezko J. H., 1982, "Rapidly Quenched Metals", T. Masumato and K. Suzaki (eds.), The Japan Institute of

Metals, P.107

Crossley P. B. and Mondolfo L. F., 1951, Trans. Met. Soc. AIME, 14, 143

Crossley P. B., Doughlas A. W. and Mondolfo L. F., 1968, in "The Solidification of Metals", Iron and Steel Institute Publication No.110, P.10

Davies I. G., Dennis J. M. and Hellawell A., 1970, Met. Trans., 1A, 275

Day M. G. and Hellawell A., 1968, Proc. Roy. Soc. Lond., 305A, 473

Derby B., 1984, Scripta Metall., 8, 169

Derby B. and Favier J. J., 1983, Acta Metall., 31, 1123

Derby B., Camel D. and Favier J., 1983, J. Crys. Growth, 65, 280

Doherty R. D., 1978, Scripta Metall., 12, 591

Eborall M. D., 1949, J. Inst. Metals, 76, 295

Elliot R., 1983, "Eutectic Solidification Processing", Butterworth, London

Eustathopoulos N., 1983, Int. Met. Rev. 28, 189

Eustathopoulos N., Coudurier L., Joud J. C. and Desre P., 1974, J. Chem. Phys., 71, 1465

Eustathopoulos N., Condurier L., Joud J. C. and Desre P., 1976, J. Crys. Growth, 33, 105

Falkenhagen G. and Hofmann W., 1952, Z. Metallkd, 43, 69

Fisher D. J. and Kurz W., 1980, Acta Metall., 28, 777

Fisher D. J. and Kurz W., 1981, Met. Trans., 12A, 669

Flood S. C., 1985, D. Phil. Thesis, University of Oxford, England

Flood S. C. and Hunt J. D., 1981, Metal Sci., 15, 387

Glicksman M. E. and Childs W. J., 1962, Acta Metall., 10, 925

Glicksman M. E. and Vold C. L., 1969, Acta Metall., 17, 1

Glicksman M. E. and Vold C. L., 1971, Scripta Metall., 5, 493

Grugel R. N. and Hellawell A., 1981, Met. Trans., 12A, 669

Grugel R. N., Lograsso T. A. and Hellawell A., 1984, Met. Trans., 15A, 1003

Gunduz M., 1984, D. Phil. Thesis, University of Oxford, England

Hanna M. D., Lu S. Z. and Hellawell A., 1984, Met. Trans. 15A, 459

Hanszen K. J., 1960, Z. Phys., 157, 523

Hellawell A. and Grugel R., 1978, in "Proc. Conf. on In-Situ Composites" Boston, Mass., USA, P.39

Hogan L. M. and Song H., 1987, Acta Metall., 35, 677

Hogan L. M. L. M. and Shamsuzzoha M., 1987, in "Solidification Processing in

1987" J. Beech and H. Johns (eds.), Institute of Metals, London, P.22

Hollomon J. H. and Turnbull D., 1951, Trans. Met. Soc. AIME, 191, 803

Hunt J. D. and Jackson K. A., 1966, Trans. Met.Soc. AIME, 236, 843

Hunter M. J. and Chadwick G. A., 1972, J. Iron Steel Inst., 210, 707

Jackson K. A., 1965, Ind. Eng. Chem., 57, 29

Jackson K. A. and Hunt J. D., 1966, Trans. Met. Soc. AIME, 236, 1129

Jones D. R. H.,1974, J. Mater. Sci., 9, 1

Kanani N. and Abbaschian G. R., 1984, Aluminium, 60, (8), E505

Kattamis T. Z. and Flemings M. C., 1970, Met. Trans., 1A, 1449

Kim W. T. and Cantor B., 1990, J. Mat. Sci., in the press

Kobayashi K. F. and Hogan L. M., 1985, J. Mat. Sci., 20, 1961

Levi C. G., 1986, in "Modelling of Casting and Welding Processes III" Kon and R. Mehrabian (eds.), ASM

Levi C. G. and Mehrabian R., 1982(1), Met. Trans., 13A, 13

Levi C. G. and Mehrabian R., 1982(2), Met. Trans., 13A, 221

Lu S. Z. and Hellawell A., 1985, J. Crys. Growth, 73, 316

Lu S. Z. and Hellawell A., 1987, in "Solidification Processing in 1987", J. Beech, H. Jons (eds.), Institute of Metals, London, P.26

McCormick M. A., Evans E. B. and Erb U., 1986, Phil. Mag., A53, L27

Miller W. A. and Chadwick G. A.,1968, in " Solidification of Metals", The Iron and Steel Institute, London, P.48

Miller W. A. and Chadwick G. A., 1969, Proc. R. Soc., A312, 257

Minkoff I., 1986, "Solidification and Cast Structure", John Wiley & Sons, Chichester

Miyazawa Y. and Pound G. M., 1974, J. Crys. Growth, 23, 45

Mondolofo L. F., 1989, Mat. Sci. Tech., 5, 118

Mondolfo L. F., Parisi N. L. and Kardys G. J., 1984-1985, Mat. Sci. Eng., 68, 249

Moore K. I., 1986, D. Phil. Thesis, University of Oxford, England

Moore K. I. and Cantor B., 1987, in "Solisification Processing in 1987", J. Beech and H. Jones (eds), Institute of Metals, London, P.515

Moore K. I., Chattopadhyay K., Cantor B., 1987, Proc. R. Soc., A414, 497

Moore K. I., Zhang D. L. and Cantor B., 1990, Acta Metall. Mater., 38, 1327

Mullins W. W., 1963, in "Metals Surfaces", ASM, Ohio, P.17

Naidich Yu. V., Grigorenko N. F. and Perevertaito V. M., 1983, J. Crys.

Growth, 53, 261

Ojho S. N. and Chattopadhyay K., 1978, Trans. Indian Inst. of Metals, 31, No. 3, 208

Pacz A., 1921, US Patent No. 1387900

Passerone A., 1979, Metall. Ital., 27, 33

Passerone A., 1981, D. Phil. Thesis, Grenove, France

Passerone A. and Eustalathopoulos N., 1980, J. Crys. Growth, 49, 757

Passerone A. and Eustathopoulos N., 1982, Acta Metall., 30, 349

Passerone A., Eustathopoulos N. and Desre P., 1977, J. Less-common Metals, 52, 37

Passrone A., Sangiorgi R., Eustathopoulos N. and Desre P., 1979, J. Mat. Sci., 13, 359

Perepezko J. H., 1979, 17th Aerospace Science Meeting, New Orleans, LA.

Perepezko J. H., 1984, Mat. Sci. Eng., 65, 125

Perepezko J. H. and Rasmussen D. H., 1978, Met. Trans., 9A, 1490

Perepezko J. H. and Paik J. S., 1982, in "Proc. of Mat. Res. Soc. Symposium Rapidly Solidified Amorphous and Crystalline Alloys", B. H. Kear and B. C. Giessen (eds.), North Holland, New YorK

Perepezko J. H. and Paik J. S., 1984, J. Non. Cryst. Solids, 61 and 62, 113

Perepezko J. H., Rasmussen D. H., Anderson I. E. and Loper Jr. C. K., 1979, in "Solidification and Casting of Metals ", Metal Soc., London, P.169

Perepezko J. H., Shiohara Y., Paik J. S. and Flemings M. C., 1982, in "Proc. 3rd Int. Con. on R. S. P. Principle and Technologies", National Bureau of Standards, Washington D. C.

Perepezko, J. H., Mueller B. A., Richmond J. J. and Cooper K. P., 1985 in "Rapidly Quenched Metals", S. Steeb, H. Warlimont (eds), Elserser Sicence Publisher, B. V., P.43

Perepezko J. H., Mueller B. A. and Ohsaka K., 1986, in "Undercooled Alloy Phases", E. W. Collings and C. C. Koch (eds.), TMS, Warrendale, PA, P.289

Perepezko J. H., Galaup C. and Cooper P., 1982, in "Proc. Mat. Res. Soc. Symposium: Material Processing Research in the Reduced Gravity Evironment of Space", Guy Z. Rindone (ed.), North Holland, N. Y.

Pound G. M. and LaMer V. K., 1952, J. Amer. Chem. Soc., 74, 2323

Powell G. L. F. and L. M. Hogan, 1965, J. Inst. Metals, 93, 505

Powell G. L. F. and Colligan G. A., 1969(1), Trans. Met. Soc. AIME, 245, 1913

Powell G. L. F. and Colligan G. A. 1969(2), J. Inst. Metals, 97, 319

Quinson J. F., Brun M. and Eyraud C., 1979, J. Chim. Phys., 76, 857

Rasmussen D. H. and Loper Jr. G. R., 1975, Acta Metall., 23, 1215

Reiss H. and Wilson I. B., 1948, J. Colloid Sci., 3, 551

Reynolds J. A. and Tottle G. R., 1951, J. Inst. Metals, 80, 93

Samples J. R., 1971, Proc. R. Soc., A324, 339

Sang H. and Miller W. A., 1970, J. of Crys. Growth, 6, 303

Sato T. and Sagama Y., 1974, J. Crys. Growth, 22, 259

Scripov V. P., 1977, in "Crystal Growth and Materials", E. Kaldis and H. Scheel (eds.), North Holland, P.327

Scripov V. P., Koverda V. P. and Butorin G. T., 1973, in "Kinetika i Mekhanika Kvistall", Nauka i Tekhnika, Minsk, P.65

Scripov V. P., Koverda V. P. and Skokor V. N., 1981, Phys. Status Solids, 60, 109

Shamsuzzoha M. and Hogan L. M., 1986(1), Phil. Mag., A 54, 459

Shamsuzzoha M. and Hogan L. M., 1986(2), J. Crys. Growth, 76, 429

Shamsuzzoha M. and Hogan L. M., 1989(1), J. Mat. Sci., 24, 2849

Shamsuzzoha M. and Hogan L. M., 1989(2), Metallography, 22, 37

Shiohara Y. and Flemings M. C., 1984, in "Modelling of Casting and Welding Processes II" J. A. Dantzig and J. T. Berrg (eds.), ASM

Skapski A. S., 1956, Acta Metall., 4, 576

Southin R. T. 1970, D. Phil. Thesis, Cambridge University, England

Southin R. T. and Chadwick G. A., 1978, Acta Metall., 26, 223

Steen H. A. H. and Hellawell A., 1972, Acta Metall., 20, 363

Steen H. A. H. and Hellawell A., 1975, Acta Metall., 23, 529

Stowell M. J., 1970, Phil. Mag., 22, 1

Sundquist B. E., 1963(1), Acta Met., 11, 630

Sundquist B. E., 1963(2), Acta Met., 11, 1002

Sundquist B. E., 1964, Acta Metall., 12, 67

Sundquist B. E. and Mondolfo L. F., 1961(1), Trans. Met. Soc. AIME, 221, 157

Sundquist B. E. and Mondolfo L. F., 1961(2), Trans. Met. Soc. AIME, 221, 607

Takagi M., 1954, J. Phys. Soc. Jpn., 9, 259

Tassa M. and Hunt J. D., 1976, J. Crys. Growth, 34, 38

Tiller W. A. and Takahashi T., 1969, Acta Metall., 17, 483

Toloui B. and Hellawell A., 1976, Acta Metall., 24, 565

Toloui B., McLeod A. J. and Double D. D., 1984, in "Proc. Conf. In-Situ Composites", Boston, Mass., USA, P.253

Turnbull D., 1950(1), Trans. Met. Soc. AIME, 188, 1144

Turnbull D., 1950(2), J. Appl. Phys., 21, 1022

Turnbull D., 1952, J. Chem. Phys., 20, 411

Turnbull D., 1981, Prog. in "Mat. Sci. Chalmer Anniversary Volume"

Turnbull D. and Fisher J. C., 1949, J. Chem. Phys., 17, 71

Turnbull D. and Cech R. E., 1950, J. Appl. Phys., 21, 804

Turnbull D. and Cormin R., 1960, J. Chem. Phys., 34, 820

Turnbull D. and Vonnegut B., 1952, Ind. Eng. Chem., 44, 1292

Volmer M. and Weber A., 1925, Z. Phys. Chem., 119, 227

Vonnegut B., 1948, J. Colloid Sci., 3, 563

Wagner R. S., 1962, in "Metalurgy of Advanced Electron Materials, AIME Conference 19", Pub. Interscience, P. 239

Wang C. C. and Smith C. S., 1950, Trans. Met. Soc. AIME, 188, 136

Woodruff D. P., 1973, "The Solid-Liquid Interface", Cambridge University Press, Cambridge

Wronski C. R. W., 1967, Br. J. Appl. Phys., 18, 1731

Wulff G., 1901, Z. Crystallogr, 53, 440

Chapter 3

Gillen A. G. and Cantor B., 1985, Acta Metall., 33, 1813

Chapter 4

Brandes E. A. and Smithells C. J., 1983, in "Metals Reference Handbook" 6th Edition, Butterworth, London

Camel D., Simon J. P. and Eustathopoulos N., 1980, Scripta Metall., 14, 1101

Cantor B. and Doherty R. D., 1979, Acta Metall., 27, 33

Derby B., 1984, Sripta Metall., 18, 169,

Derby B. and Favier J. J., 1983, Acta Metall., 31, 1123

Hume-Rothery W., Smallman R. E. and Haworth C. W., 1969, "Structure of Metals and Alloys", The Institute of Metals, London

Johns D. R. H., 1974, J. Mat. Sci., 9, 1

Kim W. T. and Cantor B., 1990, J. Mat. Sci., in the press

Kim W. T., Zhang D. L. and Cantor B., 1990, submitted to Met. Trans. A

Martin J. W. and Doherty R. D., 1976, "Stability of Microstructure in Metallic Systems", Cambridge University Press, Cambridge

Massalski T. B. et al, 1986, in "Binary Phase Diagrams",ASM, Ohio

Mondolfo L. F., Parist N. L. and Kardys G. J., 1984-1985, Mat. Sci. Eng., 9, 1

Moore K. I., Chattopadhyay K. and Cantor B., 1987, Proc. R. Soc., A414, 497

Shewmon P. G., 1963, "Diffusion in Solids", McGraw-Hill Book Company, Wiley

Sundquist B. E., 1964, Acta Metall., 12, 67

Turnbull D., 1950, J. Appl. Phys., 21, 1022

Wulff G., 1901, Z. Crystallogr., 53, 440

Chapter 5

Brandes E. A. and Smithells C. J., 1983, in "Metals Reference Handbook" 6th Edition, Butterworth, London

Johns D. R. H., 1974, J. Mat. Sci., 9, 1

Kim W. T., Zhang D. L. and Cantor B., 1990, submitted to Met. Trans. A

Martin J. W. and Doherty R. D., 1976, "Stability of Microstructure in Metallic Systems", Cambridge University Press, Cambridge

Massalski T. B. et al, 1986, in "Binary Phase Diagrams", ASM, Ohio

Moore K. I., Chattopadhyay K. and Cantor B., 1987, Proc. R. Soc., A414, 497

Pearson W. B., 1958, "A Handbook of Lattice Spacings and Structures of Metals and Alloys", Pergamon, London

Wulff G., 1901, Z. Crystallogr., 53, 440

Chapter 6

Brandes E. A. and Smithells C. J., 1983, in "Metals Reference Handbook" 6th Edition, Butterworth, London

Cahn R. W., 1986, Nature, 323, 668

Grabaek L. et al, 1990, Phys. Rev. Lett., 64, 934

Kim W. T., Zhang D. L. and Cantor B., to be published

Massalski T. B. et al, 1986, in "Binary Phase Diagrams", ASM, Ohio

Saka H., Nishikawa Y. and Imura T., 1987, Phil. Mag. Lett., 55, 163

Saka H., Nishikawa Y. and Imura T., 1988, Phil. Mag, 57A, 895

Chapter 7

Cahn J. W., 1960, Acta Metall., 8, 554

Cahn T. W., Hillig W. B. and Sears G. W., 1964, Acta Metall., 12, 1421

Day M. G. and Hellawell A., 1968, Proc. Roy. Soc. Lond., 305A, 473

Flood S. C. and Hunt J. D., 1981, Metal Sci., 15, 287

Hanna M. D., Lu S. Z. and Hellawell A., 1984, Met. Trans., 15A, 459

Kim C. B. and Heine R. W., 1963-64, J. Inst. Metals, 92, 367

Kobayashi K. F. and Hogan L. M., 1985, J. Mat. Sci., 20, 1961

Levi C. G. Mehrabian R., 1982, Met. Trans., 13A, 13

Perepezko J. H., Mueller B. A. and Ohsaka K., 1987, in "Undercooled Alloy Phases", E. W. Collings and C. C. Koch (eds), TMS, Warrendale, PA P.289

Shamsuzzoha M. and Hogan L. M., 1986, Phil Mag., 54A, 459

Southin R. T., 1970, D. Phil. Thesis, University of Cambridge, Cambridge

Chapter 8

Southin R. T. and Chadwick G. A., 1978, Acta Metall., 26, 223

Turnbull D. and Vonnegut B., 1952, Ind. Eng. Chem., 44, 1292